Density Functional Theory Studies of Electrochemical Processes

Hansen, Heine Anton

Publication date:
2009

Document Version
Early version, also known as pre-print

Density Functional Theory Studies of Electrochemical Processes

Heine Anton Hansen

Ph.D. Thesis
September 2009
Center for Atomic-scale Materials Design
Department of Physics
Technical University of Denmark
DK-2800 Kgs. Lyngby, Denmark

Contents

Preface

This thesis is submitted in the candidacy for the Ph.D. degree from the Technical University of Denmark (DTU). The work has been carried out over the last 3 years at the Center for Atomic-scale Materials Design (CAMD), Department of Physics, DTU, with Professor Jens K. Nørskov as supervisor and Assistant Professor Jan Rossmeisl as co-supervisor. Financial support was provided by DTU.

First of all I would like to thank my supervisors for good discussions and guidance during the last three years. I would also like to thank Jeppe Gavnholt, Thomas Olsen, Vivien Petzold and Carsten Rostgaard for a pleasant and helpful working environment at our office during the last three years. In addition I would like to thank all present and past collaborators for inspiring discussions. Especially I would like to thank Heinz Pitsch and Venkat Viswanathan for their hospitality during my visit to Stanford.

I would also like to thank Venkat Viswanathan, Ifan Stephens, Carsten Rostgaard, Ask Larsen and Duncan Mowbray for proofreading of the thesis.

Kgs. Lyngby, September, 2009.
Heine Anton Hansen

Abstract

In this thesis density functional theory (DFT) is applied to study surface structures and reaction intermediates in electrochemistry.

We have calculated surface stability diagrams for Ni(111) and Ag(111) in equilibrium with water, protons and electrons as a function of pH and potential. We then consider the oxygen reduction reaction (ORR) on the most stable surfaces.

For Pt(111) we have simulated the potential dependent adsorption of O and OH using DFT calculated formation energies and interaction potentials as input to Monte Carlo simulations. The simulations show reasonable agreement with charge transfer obtained from cyclic voltammograms and OH and O coverages obtained from electrochemical XPS.

We present the results of a computational screening for Pd and Pt catalysts active for the ORR. The study suggests that alloys based on Pd or Pt in combination with an early transition metal may have good activity. Experiments show that these alloys are indeed more active than Pt. The high activity of these alloys is surprising, because they have a larger lattice constant than Pt. The ability to predict new materials is stong evidence in support for the underlying model. The free energy of the reaction intermediates are calculated on Pt_3Y (111) and Pt_3Sc(111) surfaces with a Pt skin. The role of subsurface alloy structure is briefly discussed based on the available experimental and calculated data.

The free formation energy of bulk rutile dioxides is calculated for a wide range of transition metals. We show that DFT describes the trend in formation energies surprisingly well. We then suggest a simple model to explain the observed trend in formation energy.

Finally we consider chlorine evolution from rutile 110 surfaces. Oxidation of water at the catalyst sites competes with chlorine adsorption and modifies the nature and availability of the active sites. We show, the chlorine adsorption energy and oxygen adsorption energy at the cus site are linearly correlated. Based on this, we suggest a model describing both water oxidation and chlorine evolution using the oxygen binding energy as a descriptor. The model explains why the potential for chlorine evolution is lower than the potential for oxygen evolution.

Resume

I denne afhandling bliver tæthedsfunktionalteori (DFT) anvendt i studier af overfladestrukturer og reaktionsintermediære i elektrokemi.

Vi har beregnet overfladestabilitetsdiagrammer for Ni(111) og Ag(111) i ligevægt med vand, protoner og elektroner som funktion af potential og pH. Vi betragter derpå iltreduktion på den mest stabile overfladestruktur.

For Pt(111) har vi simuleret den potentialafhængige adsorption af O og OH ved hjælp af Monte Carlo-simuleringer. Monte Carlo-simuleringerne er baseret på formationsenergier og vekselvirkningspotentialer beregnet med DFT. Simuleringerne er i rimelig overensstemmelse med ladningsoverførslen i CV-eksperimenter samt dækningsgraderne af O og OH målt med elektrokemisk XPS.

Vi præsenterer resultaterne af en systematisk computerbaseret søgen efter Pd- og Pt-katalysatorer til iltreduktion. Studiet finder at legeringer baseret på Pd eller Pt samt et tidligt overgangsmetal sandsynligvis har gode katalytiske egenskaber. Eksperimenter har eftervist at disse legeringer er mere aktive end Pt. Den høje aktivitet af disse legeringer er overraskende, fordi de har en større gitterkonstant end Pt. Det er et vigtigt indicium for den bagvedliggende model for iltreduktion, at den kan forudsige aktiviteten af nye ukendte materialer. Den frie energi af de intermediære tilstande i iltreduktionsreaktionen er beregnet på $Pt_3Y(111)$- og $Pt_3Sc(111)$-overflader termineret med et overfladelag af Pt. Betydningen af legeringens struktur i overfladeregionen bliver kort diskuteret baseret på de tilgængelige eksperimentelle og beregnede data.

Den frie formationsenergi af rutiloxider er beregnet for en bred vifte af overgangsmetaller. Vi viser, at DFT beskriver trenden i formationsenergier overraskende godt. Vi foreslår derpå en simpel model, som forklarer observationerne.

Til slut betragter vi klorudvikling fra rutil-110-overflader. Oxidation af vand på katalysatorens aktive centre påvirker adsorptionen af klor og modificerer de aktive centre. Vi viser, at adsorptionsenergien af klor korrelerer med iltbindingsenergien på cus-centret og foreslår derp en model som beskriver elektrokemisk vandsplitning og klorudvikling ved hjælp af iltbindingsenergien som den en enkelt parameter. Modellen forklarer hvorfor potentialet påkrævet for klorudvikling er mindre end potentialet for iltudvikling.

List of Included Papers

P1

Surface Pourbaix Diagrams and Oxygen Reduction Activity of Pt, Ag and Ni(111) Surfaces Studied by DFT
H. A. Hansen, J. Rossmeisl and J. K. Nørskov
Phys. Chem. Chem. Phys., **10**, 37223730 (2008)

P2

Alloys of Platinum and Early Transition Metals as Oxygen Reduction Electrocatalysts
J. Greeley, I. E. L. Stephens, A. S. Bondarenko, T. P. Johansson, H. A. Hansen, T. F. Jaramillo, J. Rossmeisl, I. Chorkendorff and J. K. Nørskov
Accepted for publication in Nature Chemistry

P3

Scaling Relationships for Adsorption Energies on Transition Metal Oxide, Sulfide, and Nitride Surfaces
E. M. Fernandez, P. G. Moses, A. Toftelund, Heine A. Hansen, J. I. Martinez, F. Abild-Pedersen, J. Kleis, B. Hinnemann, J. Rossmeisl, T. Bligaard, and J. K. Nørskov
Angew. Chem. Int. Ed., **47**, 4683-4686 (2008)

P4

Formation Energies of Rutile Metal Dioxides Using Density Functional Theory
J. I. Martinez, H. A. Hansen, J. Rossmeisl, and J. K. Nørskov
Phys. Rev. B., **79**, 045120 (2009)

P5

Electrochemical Chlorine Evolution at Rutile Oxide 110 Surfaces
H. A. Hansen, I. C. Man, F. Studt, F. Abild-Pedersen, T. Bligaard and J. Rossmeisl
Accepted for publication in Phys. Chem. Chem. Phys.

P6

Volcano Relation for the Deacon Process over Transition-metal Oxides
F. Studt, F. Abild-Pedersen, H. A. Hansen, I. C. Man, J. Rossmeisl and T. Bligaard
Accepted for publication in ChemCatChem

Chapter 1

Introduction

Electrochemistry has a long history going back to the end of the 18th and the beginning of the 19th century. Key discoveries were made by Galvani, Volta and Faraday, just to name a few [1]. While some fundamental principles and concepts, such as Marcus theory for outer sphere redox reactions [2], are understood, many quantitative descriptions of specific systems and reactions are mostly mechanistic. As such, we have only a limited understanding of the important processes at the atomic level. However, recent developments in experimental and computational techniques have begun to change this [3].

Electrochemistry is important for all processes that convert energy between electric energy and chemical energy. However, from a technological point of view, much recent research has focused on energy conversion. In a hydrogen based energy economy, excess electric energy from renewable energy sources such as wind or solar power is stored as chemical energy in hydrogen and oxygen by means of water electrolysis. This chemical energy can then be used for transportation or in stationary power plants when there is a shortage of power from renewable sources.

However, the use of oxygen electrodes in fuel cells is not limited to systems that use hydrogen as an energy carrier. Oxygen may also be used as an oxidizing agent in systems based on alcohols, for example. The advantages of fuel cells with oxygen electrodes are firstly that fuel cells are not limited by the Carnot efficiency. They may therefore obtain greater efficiency than combustion engines or other heat engines. Secondly, oxygen based fuel cell systems may obtain a lower weight than, for example, a chlorine based fuel cell. This is because oxygen may be extracted from air and the generally harmless emission products may be let out into the atmosphere.

There are significant energy losses associated with the electrochemical splitting of water in electrolyzers and the oxygen reduction reaction in fuel cells. These losses are primarily caused by the slow kinetics at the oxygen electrode and prevent the widespread usage of these technologies. Moreover, the most efficient catalysts for oxygen electrodes are based on scarce and expensive platinum-group metals such as Pt, Ru and Ir. Development of more active and cheaper oxygen electrodes is therefore required [4].

For rather simple reactions, materials with desirable properties have been discovered based on Density Functional Theory (DFT) calculations [5, 6]. With improved computational tools the future will hopefully bring new discoveries.

In the descriptor based approach to catalyst design, the catalyst reaction must first be understood in detail on a single to a few materials. The next step is to identify descriptors that determine activity, selectivity, stability or other important properties for a class of related catalysts. Scaling relations between the adsorption energies of different adsorbates [7, 8] and BEP relations between reaction barriers and reaction energies [9] allow simple reactions to be well described by a few independent parameters. In this case, the descriptor based approach therefore also leads to a model of the activity. When a suitable set of descriptors have been identified, a list of

catalyst candidates may be generated and the descriptors are calculated or estimated for each candidate. This identifies catalysts which are most likely to have the desired properties. These candidates can subsequently be tested in experiments.

DFT calculations of electrochemical reactions are complicated by the presence of a liquid in contact with the catalyst surface. In calculations there is direct control of the number of valence electrons and ion cores in the calculation. In contrast, a real catalyst surface is an open system that may exchange particles with the surroundings. There is little or no direct microscopic control over electrons and atoms. The state of a surface in equilibrium within the electrochemical environment is determined by the potential and the electrolyte, which in turn determine the chemical potentials of electrons and ions. This makes it difficult to calculate potential dependent reaction barriers accurately for extended surfaces [10]. The potential also has a strong thermodynamic effect on the equilibrium adsorbate structure.

Outline

In this work we employ a thermodynamic approach to estimate activity and consider only the free energy of intermediates along a given reaction path.[11] At the very least, this approach can identify the worst catalysts for a given reaction. Chapter 2 deals with electronic structure theory, in particular Density Functional Theory. This is the most wide spread methodology for solving the electronic structure problem [12]. Chapter 3 describes the thermodynamic method which is used to calculate reaction free energies and phase diagrams. In chapter 4 we employ this method to study the oxygen reduction reaction (ORR) on Ag(111) and oxygen covered Ni(111) in alkaline solution. In detail, we model how OH and O coverage increase with potential and how this affects the stability of the ORR intermediates. In chapter 5 we present the results of a descriptor based screening for catalysts active for the ORR. This screening is based on the thermodynamic model from Ref. [11]. Despite the apparent limitations, the model successfully identifies a new class of Pt and Pd based catalysts. Initial experiments performed by I. Chorkendorff and co-workers have subsequently confirmed these alloys have improved activity over Pt.

While kinetic mean field modeling has been used with some success for the ORR [13, 14], it is desirable to go beyond the mean field approximations to check the validity of mean field results. For the ORR, attractive interactions between adsorbed OH or effective adsorbate-adsorbate repulsions may play a signficant role. In chapter 6 we simulate potential dependent OH and O formation on Pt(111) based on formation energies and interaction energies calculated with DFT. The MC simulations have been performed in collaboration with V. Viswanathan T. F. Jaramillo and H. Pitsch.

At positive (oxidizing) potentials, stability is a major issue for electrocatalysts. In chapter 7 we calculate formation energies of rutile dioxides, which are used as anodes in electrolyzers. We aim to test whether the methodology that has successfully been applied to ORR also can be applied to other materials and other reactions. [11] In chapter 8 we therefore use the thermodynamic method to study the technologically important chlorine evolution reaction (ClER) on rutile (110) model surfaces. Using linear relations, we establish a unified descriptor based model for ClER activity and oxygen evolution activity. Based on this model we are able to explain experimentally observed correlations. Finally, chapter 9 presents an overall summary of results and an outlook for future work.

Chapter 2

Electronic Structure Calculations

The formation of chemical bonds in solids, molecules and at surfaces is controlled by the electronic structure of the system under consideration. The fundamental laws of quantum mechanics that determines the electronic structure are well known. However, an exact solution of the problem is only possible for the most simple cases. With the advent of modern computers and improved theoretical methods, it has become possible to solve the electronic structure problem within an acceptable accuracy for realistic model systems.

2.1 The Manybody Wavefunction

In quantum mechanics all information about a system is contained in the wave function $\Psi = \Psi(\mathbf{r_1}, \ldots \mathbf{r_N};, \mathbf{R_1}, \ldots \mathbf{R_K}; \mathbf{t})$[15], which is a function of time t, electron coordinates $\{\mathbf{r_1}, \ldots \mathbf{r_N}\}$ and nuclei coordinates $\{\mathbf{R_1}, \ldots \mathbf{R_K}\}$ including the spin coordinate. The wave function satisfies the time dependent non-relativistic Schrödinger equation

$$\hat{H}\Psi = i\frac{\partial}{\partial t}\Psi, \tag{2.1}$$

where $\hat{H}$ is the Hamiltonian operator. In coordinate representation this is[1]

$$\hat{H} = -\frac{1}{2}\sum_{i=1}^{N}\nabla_i^2 - \sum_{k=1}^{K}\frac{1}{2M_k}\nabla_k^2 - \sum_{i=1}^{N}\sum_{k=1}^{K}\frac{Z_k}{|\mathbf{r_i} - \mathbf{R_k}|} \tag{2.2}$$

$$+ \frac{1}{2}\sum_{i\neq j}^{N}\frac{1}{|\mathbf{r_i} - \mathbf{r_j}|} + \frac{1}{2}\sum_{k\neq l}^{K}\frac{Z_k Z_l}{|\mathbf{R_k} - \mathbf{R_l}|}. \tag{2.3}$$

The first term is the kinetic energy of the electrons, the second term is the kinetic energy of the nuclei, the third term is the interaction between the electrons and the nuclei, the fourth term is the electron electron interaction and the fifth term is the interaction between the nuclei. As the nuclei are 3 to 4 orders of magnitude heavier than the electrons, electron structure calculations usually employ the Born-Oppenheimer (BO) approximation, where it is assumed that the electrons respond instantaneously to the movements of the nuclei. This allows a separation of the problem into the electronic structure problem and the nuclear motion. Focusing on stationary solutions to the electronic structure problem, the time independent electronic wave function $\Phi = \Phi(\mathbf{r_1}, \ldots \mathbf{r_N})$ satisfies the Schrödinger equation

$$E\Phi = \left\{\hat{T}_e + \hat{V}_{en} + \hat{V}_{ee}\right\}\Phi, \tag{2.4}$$

[1] The Hamiltonian is written in atomic units.

where $\hat{T}_e$ is the kinetic energy operator for the electrons, $\hat{V}_{en}$ is the electron nucleus interaction and $\hat{V}_{ee}$ is the electron electron interaction.

2.2 Density Functional Theory

In Density Functional Theory (DFT) the search for the N-particle wavefunction is replaced by a search for the electron density $n(\mathbf{r})$. In so doing, the problem is simplified from one in terms of $3N$ variables to one with 3 variables. From a physical point of view it is evident that the ground state is uniquely defined by the external potential and the number of electrons in the potential, since the external potential specifies the Hamiltonian.

In 1964 Hohenberg and Kohn showed that the converse is also true: the external potential is uniquely determined by the ground state density $n(\mathbf{r})$[16]. As the external potential determines the Hamiltonian, the groundstate N-particle wavefunction and all observables of the ground state are in principle functionals of the density $n(\mathbf{r})$. In particular, the ground state energy is a functional of the density $E[n(\mathbf{r})]$.

Using variational principles it may be shown [12], that the ground state density $n(\mathbf{r})$ minimizes the energy, $E[n(\mathbf{r})]$. If the ground state is degenerate, then any groundstate density minimizes $E[n(\mathbf{r})]$. Following the "constrained search" approach by Lieb and Levy [17, 18] the groundstate energy may be obtained by minimizing the energy over all possible wavefunctions with the density $n(\mathbf{r})$, and then minimizing over all densities. The ground state energy may then be written formally as

$$E_0 = \min_{n(\mathbf{r})} E[n((r))] = \min_{n(\mathbf{r})} \left\{ F[n(\mathbf{r})] + \int v_{ext}(\mathbf{r}) n(\mathbf{r}) \mathrm{d}\mathbf{r} \right\} , \tag{2.5}$$

where v_{ext} is the external potential and $F[n(\mathbf{r})]$ is a universal but unknown functional obtained by minimizing over all wavefunctions with density $n(\mathbf{r})$

$$F[n(\mathbf{r})] = \min_{\Psi \to n(\mathbf{r})} \langle \Psi | \, \hat{T}_e + \hat{V}_{ee} \, | \Psi \rangle \, . \tag{2.6}$$

The energy functional may thus be expressed as

$$E[n((r))] = F[n(\mathbf{r})] + V_{ext}[n(\mathbf{r})], \tag{2.7}$$

where $V_{ext}[n(\mathbf{r})] = \int v_{ext}(\mathbf{r}) n(\mathbf{r}) \mathrm{d}\mathbf{r}$. The first term is independent of the external potential and thus the same for *all* systems of electrons interacting through the Coulomb potential. The second term is easily evaluated and depends on the system. The relation in equation (2.7) is only formal and the Hohenberg-Kohn (HK) theorem only proves the energy is a functional of the density. It does not describe a scheme for obtaining this functional. An approximate scheme for obtaining the functional was proposed by Kohn and Sham in 1965.

2.2.1 The Kohn Sham Equations

Kohn and Sham realized that if they had a system of non-interacting electrons in an effective potential v_{eff} and a system of interacting electrons, then, by the HK theorem, if the density of the two systems are the same then their energy is also the same - as all other observables of the groundstate.

In Kohn-Sham (KS) theory the electrons are treated as noninteracting particles moving in an effective potential v_{eff}. If the effective potential is constructed such that the Kohn-Sham electrons have the exact same density as the (real) interacting electrons, then the HK theorem states that the Kohn-Sham electrons also have the same energy as the interacting electrons.

The KS total energy is

$$E\left[n(\mathbf{r})\right] = T_s\left[n(\mathbf{r})\right] + V_H\left[n(\mathbf{r})\right] + E_{xc}\left[n(\mathbf{r})\right] + V_{ext}\left[n(\mathbf{r})\right] \tag{2.8}$$

[19] where $T_s[n(\mathbf{r})]$ is the kinetic energy of a noninteracting electron gas with density $n(\mathbf{r})$, and $V_H[n(\mathbf{r})]$ is the Hartree energy

$$V_H[n(\mathbf{r})] = \frac{1}{2}\int\int \frac{n(\mathbf{r}')n(\mathbf{r})}{|\mathbf{r}-\mathbf{r}'|}\mathrm{d}\mathbf{r}'\mathrm{d}\mathbf{r}. \tag{2.9}$$

The exchange correlation energy functional $E_{xc}[n]$ is introduced as a correction that contains electron exchange and correlation. The exchange correlation functional is not known exactly, and the strength of DFT relies on accurate but efficient approximations to E_{xc}.

Variations with respect to the density requiring that N is fixed yield the KS equations

$$\left[-\frac{1}{2}\nabla^2 + v_{eff}\right]\phi_j(\mathbf{r}) = \epsilon\phi_j(\mathbf{r}), \tag{2.10}$$

where the effective potential is

$$v_{eff}(\mathbf{r}) = v_{ext}(\mathbf{r}) + \int \frac{n(\mathbf{r}')}{|\mathbf{r}-\mathbf{r}'|}\mathrm{d}\mathbf{r}' + v_{xc}(\mathbf{r}), \tag{2.11}$$

and the exchange correlation potential is the functional derivative of E_{xc}

$$v_{xc}(\mathbf{r}) = \frac{\delta E_{xc}}{\delta n(\mathbf{r})}, \tag{2.12}$$

$$\left[-\frac{1}{2}\nabla^2 + v_{ext}(\mathbf{r}) + \int \frac{n(\mathbf{r}')}{|\mathbf{r}-\mathbf{r}'|}\mathrm{d}\mathbf{r}' + v_{xc}(\mathbf{r})\right]\phi_j(\mathbf{r}) = \epsilon_j\phi_j(\mathbf{r}), \tag{2.13}$$

$$n(\mathbf{r}) = \sum_{j\in occupied} |\phi_j(\mathbf{r})|^2. \tag{2.14}$$

The KS equations describe noninteractiong electrons in a fictitious potential which results in the same density as the interacting electrons. Since the effective potential v_{eff} depends on $n(\mathbf{r})$, the Kohn-Sham equations (2.10) and (2.11) must be solved iterately until a selfconsistent density is obtained.

2.2.2 Exchange Correlation Functionals

The most simple approximation to the exchange correlation functional (xc-functional) was proposed by Kohn and Sham[19], who assumed the exchange correlation energy at density n is the same as for the homogeneous electron gas at the same density. This is known as the local-density approximation, LDA,

$$E_{xc}^{LDA} = \int \epsilon_{xc}^{hom}(n(\mathbf{r}))n(\mathbf{r})\mathrm{d}\mathbf{r}, \tag{2.15}$$

where $\epsilon_{xc}^{hom}(n(\mathbf{r}))$ is the energy of the exchange correlation hole in the homogeneous electron gas of density n. LDA extended to spin-polarized systems is known as the local spin density approximation LSDA. LDA is in principle unique, but different parametrizations of ϵ_{xc}^{hom} exist [20, 21, 22]. Despite the simplicity, LDA describes properties such as lattice constants, vibrational frequencies and equilibrium geometries of physical systems surprisingly well. Dissociation energies of molecules and cohesive energies of solids are predicted within 10-20% and bond geometries are often predicted within 1%. The success of LDA is partly rationalized by the fact that the

exchange correlation hole is normalized as in all real systems and that it is exact in the limit of high density and the slowly varying limit.

Although local density approximations often are sufficiently accurate in solid state physics, DFT did not become popular in quantum chemistry until the development of the Generalized Gradient Approximations (GGA). In a GGA the exchange correlation energy depends on the gradient of the density as well as the density,

$$E_{xc}^{GGA}\left[n(\mathbf{r})\right] = \int \epsilon_{xc}^{GGA}\left(n(\mathbf{r}), \nabla n(\mathbf{r})\right) \mathrm{d}\mathbf{r}. \tag{2.16}$$

Contrary to ϵ_{xc}^{hom}, ϵ_{xc}^{GGA} is not uniquely defined and several GGA's have been suggested, for example PW91[23], PBE[24, 25] and RPBE[26]. The best choice of functional will depend on the system of interest. In hybrid methods, exact Hartree-Fock exchange is mixed with the correlation energy from e.g. the PBE functional to improve accuracy. In meta-GGAs Laplacians of the density or the kinetic energy density are also used in the calculation of E_{xc}. [27, 28]

2.3 Calculational Details

All DFT calculations in this thesis have been done in the plane wave code DACAPO within the ASE environment [29, 30, 31]. The ionic cores are described by ultrasoft pseudopotentials [32], and the Kohn-Sham valence states are expanded in a plane wave basis. Exchange and correlation effects are approximated by the PBE or the RPBE xc-functional[25, 26]. The Kohn-Sham Hamiltonian is diagonalized iteratively using Pulay mixing of the density and Fermi-Dirac occupation of one-electron states [33]. Unless something else is specified, we use $k_BT = 0.1$ eV for bulk systems and slabs and $k_BT = 0.01$ eV for molecules. Total energies are extrapolated to $k_BT = 0$ eV. Adsorption energies are calculated using asymmetric slabs. The energies are corrected for the dipole interaction between the periodically repeated slabs [34, 35].

Chapter 3

Surface Pourbaix Diagrams

The majority of the work presented in this thesis is related to surfaces in an *electrochemical environment* at potentials *near* the reversible potential of the O_2/H_2O couple i.e. around 1.23 V at room temperature and atmospheric pressure. A surface in this environment is an open system, which may exchange neutral molecules, ions and and electrons with its surroundings. As a further complication there may even be an electrolyte in the vicinity of the surface that affects the adsorbate structures formed on the surface.

At normal surfaces at the solid-gas interphase only atoms and molecules may be exchanged with the surroundings of the surface. Even for this simple case, there may be a discrepancy between the surface structure under ultra high vacuum (UHV) conditions and the structure of the real catalyst *in situ*[36, 37, 38]. Further, the activity obtained from single crystal experiments in UHV may not be extrapolated to industrial conditions, where the reaction takes place at elevated temperature and pressure on supported catalysts. This has been coined the material and pressure gap. Theoretical calculations are "routinely" done on model systems consisting of a metal slab with a few adsorbates. This effectively models an extended surface in vacuum in the limit of low adsorbate coverage[1]. Calculations of this type have both contributed to the understanding of surface dynamics[39], and complemented UHV experiments in the interpretation of microscopic and spectroscopic data[40]. Further, model calculations have been able to describe trends in catalytic activities and even identified novel promising catalysts[41]. DFT calculations have been perfomed to bridge the temperature and pressure gap, to identify the thermodynamically stable phases at elevated temperature end pressure[42, 43]. Using DFT calculated adsorption energies and reaction rates as input for Monte Carlo simulations, surface dynamics at more realistic reaction conditions may also be simulated[44, 45].

In this chapter we derive equations for the construction of surface phase diagrams in electrochemical environments from *first-principles* simulations. The resulting equations bear, naturally, a close resemblance to the *ab initio* thermodynamics by Scheffler and co-workers[46, 47] but with the chemical potentials being determined by potential, pH and concentrations rather than partial pressures. We will show that the change in free energy from an adsorption process within certain approximations may be written as

$$\Delta G = \Delta G^\circ + \Delta G(U) + \Delta G\left(\{a_i\}\right) \tag{3.1}$$

where ΔG° may be calculated from a gas phase adsorption process, $\Delta G(U)$ is a potential dependent correction, whose dominant contribution in many cases may be derived from the nominal charge transfer upon adsorption, and $\Delta G\left(\{a_i\}\right)$ are corrections for deviations from the chemical standard state. Electrochemical surface stability

[1] In many cases the coverage is not well defined as it may change during the simulations as a result of reactions taking place at the surface. If the super cell is sufficiently large, however, there will be no interactions between the adsorbates in different super cells, and the low coverage limit is achieved.

diagrams have been constructed based on experimental data for Cu assuming non-interacting adsorbates[48], and for S adsorption on Fe[49]. Theoretical electrochemical surface stability diagrams have also been constructed by Neurock and co-workers for a range of metals[50, 51, 52], by Jacob [53] and by our group [54, P1,P5].

Two macroscopic parameters of interest, especially for corrosion, is the potential of the surface and the pH of the solution. For bulk systems, potential-pH stability diagrams are known as Pourbaix diagrams [55]. We will occasionally refer to the surface diagrams in pH and potential as surface Pourbaix diagrams [56].

3.1 The Thermodynamic Potential Scale

An electrode surface at equilibrium in an electrochemical environment is an open system, which may exchange electrons with a potentiostat and ions and molecules with the electrolyte, as illustrated in figure 3.1. The relevant thermodynamic variables are therefore the potential U and the chemical potentials $\{\mu_i\}$ of adsorbing ions and molecules.

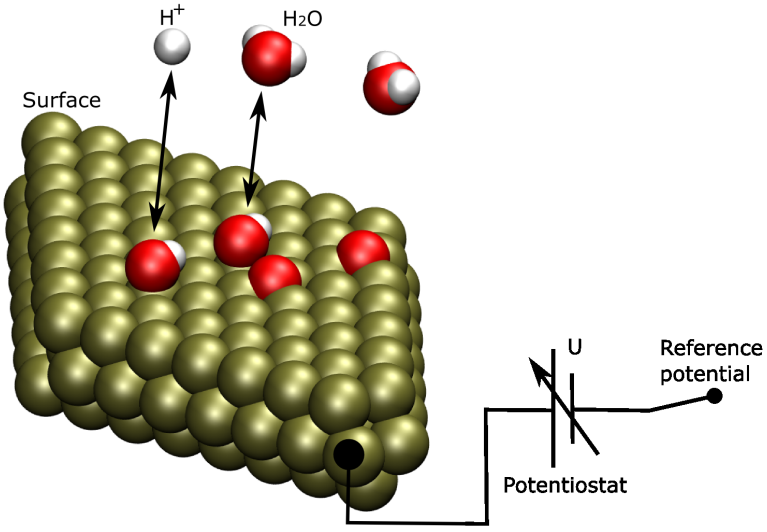

Figure 3.1: Sketch of a surface exchanging electrons with a potentiostat at potential U. Ions and molecules are exchanged with the electolyte.

Consider a hydrogen electrode at equilibrium,

$$\mathrm{H}_2(aq) + e^- \rightleftarrows \frac{1}{2}\mathrm{H}_2(g)\,. \tag{3.2}$$

Formally, the change in free energy by the forward reaction in Eq. (3.2) is

$$\Delta G = \mu^{\ominus}_{\mathrm{H}_2} + k_B T \ln a_{\mathrm{H}_2} - \mu^{\ominus}_{\mathrm{H}^+} - k_B T \ln a_{\mathrm{H}^+} - \mu_{e^-}\,, \tag{3.3}$$

where the k_B is the Boltzmann constant, T is the temperature and the chemical potentials μ_i and activities a_i have their usual meanings. In reaction (3.2) the electron is at a metallic electode at a potential U measured on some potential scale. The chemical potential of the electron at this electrode may therefore be written as

$$\mu_{e^-} = \mu^{\ominus}_{e^-,S} - e\,(U - U^{\ominus}_{\mathrm{S}})\,, \tag{3.4}$$

where $\mu^{\ominus}_{e^-,S}$ is a constant depending on the potential scale and $U^{\ominus}_{\mathrm{S}}$ is the zero of the potential scale. For an electrode in equilibrium $\Delta G = 0$, and

$$\mu^{\ominus}_{\mathrm{H}_2} - \mu^{\ominus}_{\mathrm{H}^+} - \mu^{\ominus}_{e^-,S} = k_B T \ln \frac{a_{\mathrm{H}^+}}{a_{\mathrm{H}_2}} - e\,(U - U^{\ominus}_{\mathrm{S}})\,. \tag{3.5}$$

In the special case, where H_2 and H^+ are at standard conditions, i.e. $p_{H_2} = 1$ bar and pH = 0,

$$\mu^{\ominus}_{H_2} - \mu^{\ominus}_{H^+} - \mu^{\ominus}_{e^-,S} = -e\,(U - U^{\ominus}_{S})\ . \tag{3.6}$$

If we choose to measure potentials relative to the hydrogen electrode at standard conditions, we have $U - U^{\ominus}_{SHE} = 0$ by definition [2], and

$$\boxed{\mu^{\ominus}_{H_2} = \mu^{\ominus}_{H^+} + \mu^{\ominus}_{e^-}} \tag{3.7}$$

We will refer to equation (3.7) as the standard hydrogen electrode (SHE) equation. It relates the chemical potentials of solvated protons and electrons with the chemical potential of H_2 in the gas phase. From a computational point of view μ_{H_2} is much easier to calculate than μ_{H^+}, because the latter involves the free energy of solvation of a proton.

For any hydrogen electrode in equilibrium, we then have from equation (3.3) and (3.7)

$$U - U^{\ominus}_{SHE} = \frac{k_B T}{e} \ln \frac{a_{H^+}}{_{H_2}} = -\frac{k_B T}{e} \ln 10\, pH - \frac{k_B T}{e} \ln a_{H_2}\ , \tag{3.8}$$

where we have used the notional definition of pH [57]

$$pH = -\frac{\ln a_{H^+}}{\ln 10}\ . \tag{3.9}$$

Equation (3.8) gives the potential of a reversible hydrogen electrode (RHE) relative to the standard hydrogen electrode (SHE). The importance of the RHE lies in the fact that most processes relevant for oxygen reduction and oxygen evolution are in equilibrium at a constant potential[3] *vs.* the RHE rather than the SHE. Assuming standard partial pressure of hydrogen, a potential on the RHE scale may be converted to the SHE scale by

$$U - U^{\ominus}_{SHE} = U - U^{\ominus}_{RHE} - \frac{k_B T}{e} \ln 10\, pH, \tag{3.10}$$

where $U - U^{\ominus}_{SHE}$ is the potential relative to the SHE and $U - U^{\ominus}_{RHE}$ is the potential relative to the RHE.

3.2 Water Oxidation

At positive potentials water may be oxidized to OH or O at a site $*$:

$$H_2O(l) + * \rightleftarrows OH* + H^+ + e^-, \tag{3.11}$$

$$H_2O(l) + * \rightleftarrows O* + 2H^+ + 2e^-, \tag{3.12}$$

The electrons are placed at the electrode with a potential U relative to the SHE. Using the SHE equation (3.7), the change in free energy for the forward reactions in (3.11) and (3.12) are

$$\Delta G_{OH*} = G_{OH*} - G_* - \mu_{H_2O(l)} + \frac{1}{2}\mu^{\ominus}_{H_2} + k_B T \ln a_{H^+} - eU, \tag{3.13}$$

and

$$\Delta G_{O*} = G_{O*} - G_* - \mu_{H_2O(l)} + \mu^{\ominus}_{H_2} + 2\,(k_B T \ln a_{H^+} - eU)\,, \tag{3.14}$$

[2] We have for notational simplicity dropped the super script S in $\mu^{\ominus}_{e^-,S}$ when the SHE defines zero potential.

[3] This is only approximately true for surface processes.

respectively, where $G_{\mathrm{OH}*}$ and $G_{\mathrm{O}*}$ are the free energy of the surface with OH or O adsorbed respectively and G_* is the free energy of the surface before the adsorption process. All free energies G_i should be calculated at the potential U. The exchange of charge between the electrolyte and the electrode is already included in the eU term. However, there may be an effect on the binding energy from the electric field at the interface due to interaction between the electric field and the dipole of the adsorbed molecule. $\mu_{\mathrm{H_2O(l)}}$ is the chemical potential for liquid water, which is calculated from the vapor pressure of water at the temperature of interest. At 298 K, the vapor pressure is 0.035 bars, so $\mu^{\ominus}_{\mathrm{H_2O(l)}} = \mu^{\ominus}_{\mathrm{H_2O(g)}} + k_B T \ln 0.035$.

3.3 The Electric Field

The energetic effect from the electric field may be included approximately, by assuming a constant width d of the Helmholtz layer at the solution side of the interface. We assume the electric field is constant within the Helmholtz layer and zero outside. If the width of the Helmholtz layer is d and the potential in the metal and in the solution is V_m and V_s respectively, then the component of the electric field in the direction away from the metal is $\epsilon = -\frac{V_s - V_m}{d}$.

For O formation we define

$$\Delta G^{\circ}_{\mathrm{O}*} = G^{\epsilon=0}_{\mathrm{O}*} - G^{\epsilon=0}_{*} - \mu_{\mathrm{H_2O(l)}} + \mu^{\ominus}_{\mathrm{H_2}} \tag{3.15}$$

and

$$\Delta\Delta G^{field}_{\mathrm{O}*}(U) = G^{\epsilon}_{\mathrm{O}*} - G^{\epsilon=0}_{\mathrm{O}*} - (G^{\epsilon}_{*} - G^{\epsilon=0}_{*}), \tag{3.16}$$

where G^{ϵ} is the free energy of a system with an external electric field of magnitude ϵ. We may then write eq. (3.14) as

$$\Delta G_{\mathrm{O}*} = \Delta G^{\circ}_{\mathrm{O}*} + 2\left(k_B T \ln a_{\mathrm{H^+}} - eU\right) + \Delta\Delta G^{field}_{\mathrm{O}*}(U)\ , \tag{3.17}$$

Note $\Delta G^{\circ}_{\mathrm{O}*}$ is the change in free energy from the chemical reaction witout external field.

$$\mathrm{H_2O}(l) + * \rightarrow \mathrm{O}* + \mathrm{H_2(g)}\,. \tag{3.18}$$

Similar arguments hold for OH formation from eq. (3.11), so in general we can write eq. (3.13) and eq. (3.14) on the form

$$\Delta G_{\mathrm{OH_{2-\nu}}} = \Delta G^{\circ}_{\mathrm{OH_{2-\nu}}} + \nu\left(k_B T \ln a_{\mathrm{H^+}} - eU\right) + \Delta\Delta G^{field}_{\mathrm{OH_{2-\nu}}}(U)\ . \tag{3.19}$$

where $\nu = 1$ for OH and $\nu = 0$ for $\mathrm{H_2O}$. $\Delta G^{\circ}_{\mathrm{OH_{2-\nu}}}$ is the change in free energy from the *chemical* reaction

$$\mathrm{H_2O}(l) + * \rightarrow \mathrm{OH_{2-\nu}}* + \frac{\nu}{2}\mathrm{H_2(g)}\,. \tag{3.20}$$

and $\Delta\Delta G^{field}_{\mathrm{OH_{2-\nu}}}(U)$ is the change in free energy due to the presence of the electric field at the solid-liquid interface, which is not included in $\Delta G^{\circ}_{\mathrm{OH_{2-\nu}}}$.

$\Delta\Delta G^{field}_{\mathrm{X}}(U)$ is then approximated as the change in adsorption energy of X due to a uniform electric field of magnitude $\epsilon = -U_h/d$.

$$\Delta\Delta G^{field}_{\mathrm{X}}(U) \approx E^{\epsilon}_{\mathrm{X}} - E^{0}_{\mathrm{X}} - (E^{\epsilon}_{*} - E^{0}_{*}), \tag{3.21}$$

where E^{ϵ} is the total energy of the system with a uniform external field ϵ and E^0 is the total energy without an external electric field. The correction may be expanded in powers of the electric field [54],

$$\Delta\Delta G^{field}_{\mathrm{X}}(U) = \alpha\epsilon - \frac{1}{2}\beta\epsilon^2 + \cdots\,. \tag{3.22}$$

where α is the dipole moment and β is the static polarizability of the adsorbate at the surface.

Several theoretical studies have investigated the effect of an electric field on the adsorption energies at metal surfaces. Cluster calculations by Koper and van Santen showed the electric field has a minor effect on the adsorption energy of H, OH and O[58]. Hyman and Medlin also found the effect of a homogeneous electric field on the O adsorption energy on a Pt slab to be small[59]. A similar conclusion was recently found by Fang and Liu [60]. So for adsorbates with a small dipole moment perpendicular to the surface, the variation in adsorption energy with field is in general small compared to the q term in (3.19).

3.4 Anion Adsorption

At positive potentials adsorption of anions from the electrolyte becomes thermodynamically favored. For the electrochemical production of chlorine, adsorbed chlorine is an obvious candidate for an intermediate in the overall reaction. Electrochemical evolution of chlorine is considered in chapter 8.

Consider the formation of adsorbed chlorine $\mathrm{Cl_{ads}}$ from chloride ions

$$\mathrm{Cl^-} + * \rightarrow \mathrm{Cl}* + e^- \,. \tag{3.23}$$

Formally, the change in free energy from this process is

$$\Delta G_{\mathrm{Cl}} = G_{\mathrm{Cl}*} + \mu_{e^-} - G_* - \mu_{\mathrm{Cl^-}} \,. \tag{3.24}$$

The apparent challenge is to calculate $\mu_{e^-} - \mu^-_{\mathrm{Cl}}$ without too much effort and without sacrificing accuracy. This is easily achieved through a series of thermodynamic arguments similar to those for the reversible hydrogen electrode in section 3.1, which are outlined in the following.

For a chlorine electrode at equilibrium

$$\mathrm{Cl^-(aq)} \rightleftarrows \frac{1}{2}\mathrm{Cl_2(g)} + e^- \,, \tag{3.25}$$

it holds, that

$$0 = \frac{1}{2}\left(\mu^{\ominus}_{\mathrm{Cl_2}} + k_B T \ln a^{\ominus}_{\mathrm{Cl_2}}\right) + \mu_{e^-} - \mu^{\ominus}_{\mathrm{Cl^-}} - k_B T \ln a_{\mathrm{Cl^-}}, \tag{3.26}$$

We may again formally write

$$\mu_{e^-} = \mu^{\ominus}_{e^-,S} - e\,(U - U^{\ominus}_S) \,. \tag{3.27}$$

For a reversible chlorine electrode at standard conditions (SClE) $a_{\mathrm{Cl_2}} = a_{\mathrm{Cl^-}}$ and $U = U^{SClE}$, so

$$0 = \frac{1}{2}\mu^{\ominus}_{\mathrm{Cl_2}} + \mu^{\ominus}_{e^-,S} - e\left(U^{SClE} - U^{\ominus}_S\right) - \mu^{\ominus}_{\mathrm{Cl^-}} \,. \tag{3.28}$$

In theory we may chose to measure potentials relative to the reversible "standard chlorine electrode" (SClE), for which we then obtain the relation

$$\frac{1}{2}\mu^{\ominus}_{\mathrm{Cl_2}} = \mu^{\ominus}_{\mathrm{Cl^-}} - \mu^{\ominus}_{e^-,SClE} \,. \tag{3.29}$$

While this definition is convenient for computational studies involving only Cl adsorption, it is in general advantageous to refer all adsorption processes to a single potential scale, as this allows the study of co-adsorption and competitive adsorption in e.g. mixed Cl*+O* phases. When the potential is measured at the SHE scale we obtain

$$\boxed{\frac{1}{2}\mu^{\ominus}_{\mathrm{Cl_2}} + e\,(U^{\ominus}_{SClE} - U^{\ominus}_{SHE}) = \mu^{\ominus}_{\mathrm{Cl^-}} - \mu_{e^-}.} \tag{3.30}$$

From standard tables over redox potentials it is known that $U^{\ominus}_{SClE} - U^{\ominus}_{SHE} = 1.36\text{V}$ at 298 K [61]. Inserting (3.30) into (3.24), we obtain for chlorine adsorption

$$\Delta G_{\text{Cl}*} = G_{\text{Cl}*} - G_* - \frac{1}{2}\mu^{\ominus}_{\text{Cl}_2} - k_B T \ln a_{\text{Cl}^-} - e\,(U - U^{\ominus}_{SClE})\,, \tag{3.31}$$

$$= \Delta G^{\circ}_{\text{Cl}*} - k_B T \ln a_{\text{Cl}^-} - e\,(U - U^{\ominus}_{SClE}) + \Delta\Delta G^{field}_{\text{Cl}}\,(U)\ , \tag{3.32}$$

where we have defined $\Delta G^{\circ}_{\text{Cl}*} = G_{\text{Cl}*} - G_* - \frac{1}{2}\mu^{\ominus}_{\text{Cl}_2}$, which corresponds to the dissociative free energy of adsorption for Cl_2

$$\frac{1}{2}\text{Cl}_2(\text{g}) + * \rightleftarrows \text{Cl}*\,, \tag{3.33}$$

and $\Delta\Delta G^{field}_{\text{Cl}}\,(U)$ is defined according to eq. (3.21).

3.5 Surface Phase Diagrams

Until now we have only considered the change in free energy from oxidation of water at a surface site ((3.11) and (3.12)) and adsorption of chlorine (3.23) as isolated processes. By combining the equations above it is possible to calculate the surface free energy of an arbitrary surface with N_{O} excess O, N_{OH} excess OH, and N_{Cl} excess Cl relative to some reference surface in equilibrium with water, protons and chloride ions at a specified potential U and activities a_{H^+} and a_{Cl^-}. Denoting the reference surface by $(0,0,0)_{\text{ads}}$ and the adsorbed phase by $(N_{\text{O}}, N_{\text{OH}}, N_{\text{Cl}})_{\text{ads}}$, the adsorbed phase may be formed from the reference surface by

$$\begin{aligned}(0,0,0)_{\text{ads}} + (N_{\text{O}} + N_{\text{OH}})\,\text{H}_2\text{O(l)} + N_{\text{Cl}}\text{Cl}^-(\text{aq}) \rightarrow \\ (N_{\text{O}}, N_{\text{OH}}, N_{\text{Cl}})_{\text{ads}} + (2N_{\text{O}} + N_{\text{OH}})\,\text{H}^+ + (2N_{\text{O}} + N_{\text{OH}} + N_{\text{Cl}})\,e^-\,.\end{aligned} \tag{3.34}$$

We now introduce the chemical reaction

$$\begin{aligned}(0,0,0)_{\text{ads}} + (N_{\text{O}} + N_{\text{OH}})\,\text{H}_2\text{O(l)} + \frac{N_{\text{Cl}}}{2}\text{Cl}_2(2) \rightarrow \\ (N_{\text{O}}, N_{\text{OH}}, N_{\text{Cl}})_{\text{ads}} + \frac{1}{2}\,(2N_{\text{O}} + N_{\text{OH}})\,\text{H}_2\,,\end{aligned} \tag{3.35}$$

with the corresponding change in free energy, $\Delta G^{\circ}_{N_{\text{O}},N_{\text{OH}},N_{\text{Cl}}}$, for the forward reaction defined in the usual way. The free energy of $(N_{\text{O}}, N_{\text{OH}}, N_{\text{Cl}})_{\text{ads}}$ relative to $(0,0,0)_{\text{ads}}$ in the electrochemical environment is simply

$$\begin{aligned}\Delta G_{N_{\text{O}},N_{\text{OH}},N_{\text{Cl}}} = G^{\circ}_{N_{\text{O}},N_{\text{OH}},N_{\text{Cl}}} \\ - (2N_{\text{O}} + N_{\text{OH}})\,(eU - k_B T \ln a_{\text{H}^+}) \\ - N_{\text{Cl}}\,(e\,(U - U^{\ominus}_{SClE}) + k_B T \ln a_{\text{Cl}^-}) \\ + \Delta\Delta G^{field}_{N_{\text{O}},N_{\text{OH}},N_{\text{Cl}}},\end{aligned} \tag{3.36}$$

clarify (3.19) and (3.32). Adsorbate-adsorbate interactions are included in the energy of $(N_{\text{O}}, N_{\text{OH}}, N_{\text{Cl}})_{\text{ads}}$ but configurational entropy is neglected. Since the correction due to the electric field is rather small, we may approximate it by

$$\Delta\Delta G^{field}_{N_{\text{O}},N_{\text{OH}},N_{\text{Cl}}} = \sum_{\text{X}\in\{\text{O,OH,Cl}\}} N_{\text{X}}\Delta\Delta G^{field}_{\text{X}}(U), \tag{3.37}$$

where it is implicitly assumed that adsorbate interactions have no effect on the field dependence of adsorption energies. N_{X} may even be negative if, for example, O vacancies are formed in an oxide surface. Hydrogen adsorption may easily be included as well.

When comparing the stability of extended adsorbate phases, the free surface energy per unit area determines the most stable adsorbate phase.

3.6 The OOH Intermediate

A frequently encountered intermediate in the oxygen reduction reaction (ORR) and the oxygen evolution reaction (OER) is OOH*, which may be formed during reduction of O_2

$$O_2 + * + H^+ + e^- \rightarrow OOH* \tag{3.38}$$

or oxidation of water

$$2H_2O + * \rightarrow OOH* + 3H^+ + 3e^- , \tag{3.39}$$

where the latter reaction suggests it may be treated as OH formation atop an already formed O*. According to equation (3.36), the free energy of OOH* is then

$$\Delta G_{OOH*} = \Delta G^{\circ}_{OOH*} - 3\left(eU - k_B T \ln a_{H^+}\right) + \Delta\Delta G^{field}_{OOH*} . \tag{3.40}$$

3.7 Entropy and Zero Point Energy

The free energy of surface structures is decomposed into contributions from changes in DFT energies ΔE_{DFT}, changes in zero point energies ΔZPE and changes in entropy ΔS, so that:

$$\Delta G^{\circ} = \Delta E_{\mathrm{DFT}} + \Delta ZPE - T\Delta S . \tag{3.41}$$

We have used the zero point energies calculated for the adsorbates on one representative metal or oxide. Variations in ΔZPE between different materials are believed to be small. We have neglected effects of surface coverage on ΔZPE. ΔS is approximated from the loss of entropy of the gas phase molecules upon binding them to the surface and taken from experimental tables [61, 62]. The used corrections are shown in appendix A.

3.8 Surface Dissolution

Electrodes may dissolve in acidic or alkaline solutions. The free energy of dissolution may be estimated from standard reduction potentials and thermochemical data, as uniform dissolution of a monolayer of metal atoms on the surface corresponds to dissolution of an equivalent amount of bulk material. When speaking of a process as spontaneous, it will be in the sense $\Delta G < 0$, which gives a conservative estimate of the stability *vs.* dissolution. An important example is dissolution of a metal M in acidic solution:

$$M(s) \rightarrow M^{z+}(aq) + ze^- . \tag{3.42}$$

The change in free energy from this process is

$$\Delta G_{diss} = \mu^{\ominus}_{M^{z+}} + k_B T \ln a_{M^{z+}} + z\left(\mu^{\ominus}_{e^-} - eU\right) - \mu^{\ominus}_{M(s)} , \tag{3.43}$$

where U is the potential of the electrode of material M on the SHE scale. From the standard reduction potential $U^{\ominus}_{M,z}$ of

$$M^{z+} + ze^- \rightleftarrows M(s), , \tag{3.44}$$

the equilibrium potential for (3.42) is known at standard conditions. Inserting standard conditions and the equilibrium condition $\Delta G_{diss} = 0$ at $U = U^{\ominus}_{M,z}$ into (3.43), we find

$$\mu^{\ominus}_{M(s)} - \mu^{\ominus}_{M^{z+}} - z\mu^{\ominus}_{e^-} = U^{\ominus}_{M,z} \tag{3.45}$$

Inserting this back into (3.43), we obtain the change in free energy for dissolution at arbitrary potential U

$$\Delta G_{diss} = k_B T \ln a_{M^{z+}} - ze\left(U - U^{\ominus}_{M,z}\right) . \tag{3.46}$$

Dissolution in alkaline solution may be treated similarly. Dissolution of alloys may also be calculated as described in Ref. [63].

3.9 Water at Metal Surfaces

Adsorbates formed at the surface may interact with solvent molecules in the liquid electrolyte. Especially OH* and OOH* intermediates may be stabilized by participating in hydrogen bonded adsorbate structures. Here we describe the experimentally observed structures of H_2O and OH on which the calculation of the formation energy of OH and OOH is based. We then present in detail the formulas for calculating the formation energies.

3.9.1 H_2O and OH on Pt(111)

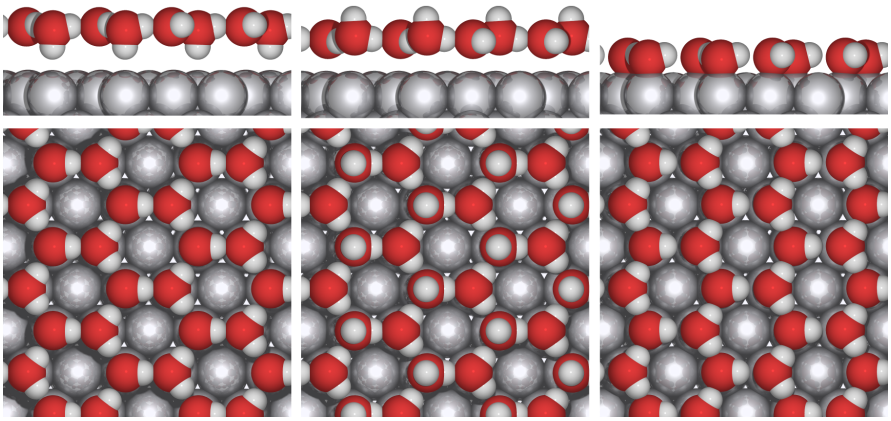

Figure 3.2: Hydrogen ordered $(\sqrt{3} \times \sqrt{3})R30°$ phases of H_2O(p)-H_2O(d) (left), H_2O(p)-H_2O(u) (middle) and H_2O(p)-OH (right) on Pt(111). Hydrogen is white, oxygen is red and platinum is gray.

Monolayers of H_2O

Water deposition on Pt(111) has been studied extensively at low temperatures in UHV[64]. Structures with $(\sqrt{37} \times \sqrt{37})R25.3°$ and $(\sqrt{39} \times \sqrt{39})R16°$ periodicity have been observed by He atom diffraction[65]. Three different hexagonal superstructures and a disordered liquid-like phase have been observed in STM experiments[66]. $(\sqrt{3} \times \sqrt{3})R30°$, $(\sqrt{37} \times \sqrt{37})R25.3°$ and $(\sqrt{39} \times \sqrt{39})R16°$ have been observed in LEED experiments [67, 68], with the water coverage saturating with the $(\sqrt{39} \times \sqrt{39})R16°$ structure [69]. XAS, XES and XPS suggest that water in bilayers forms a nearly flat layer with only 0.25 Å O-O corrugation. In UHV the hydrogen atoms of half of the water molecules are pointing out of the adsorbate plane towards the Pt surface [70].

Figure 3.2 shows the simplest $(\sqrt{3} \times \sqrt{3})R30°$ water structures and OH-H_2O structure. Adsorbed monolayers of water are often called bilayers because of the corrugation. In these structures water molecules adsorb in different geometries. Some water molecules lie in a plane that is nearly parallel to the plane of the surface. We denote this type of water molecules by H_2O(p) [71]. Other water molecules lie in a plane that is perpendicular to the plane of the surface. In this case, one hydrogen and the oxygen still lie in the plane of the bilayer, while the other hydrogen atom either points "down" towards the surface or "up" away from the surface. We denote these two types of water by H_2O(d) and H_2O(u) respectively. In chapter 6, we further distinguish between H_2O(p) at different distances from the surface. We denote H_2O(p) in the H_2O-OH structure by H_2O(p1) and denote H_2O(p) in the H_2O(p)-H_2O(v) structure by H_2O(p2).

Water Multilayers

Under multilayer growth of water bilayers, the $(\sqrt{39} \times \sqrt{39})R25.3°$ structure remains stable. After a thickness of 4-5 layers is reached, the water film transforms into a $(\sqrt{3} \times \sqrt{3})R30°$ structure[69]. The transition into the $(\sqrt{3} \times \sqrt{3})R30°$ structure is irreversible and water desorption does not revert the structure to a $(\sqrt{39} \times \sqrt{39})R25.3°$ periodicity. Presumably the $(\sqrt{3} \times \sqrt{3})R30°$ structure has a lattice constant similar to ice I_h and is incommensurate with the Pt lattice [64]. However, DFT calculations by Meng *et al.* showed that a commensurate $(\sqrt{3} \times \sqrt{3})R30°$ superstructure becomes more stable than the $(\sqrt{37} \times \sqrt{37})R25.3°$ and $(\sqrt{39} \times \sqrt{39})R16°$ superstructures as the film thickness is increased to 3 layers [72]. Single bilayers and multiple bilayers of water on Pt(111) formed in UHV desorb at temperatures ranging from 150 K to 170 K [69].

OH-H_2O Phases

In UHV the reaction between O and H_2O leads to the formation of $(\sqrt{3} \times \sqrt{3})R30°$ and (3x3) structures at temperatures between 155 K and 180 K [73, 74]. Based on DFT calculations, Michaelides and Hu proposed the existence of a mixed OH-H_2O overlayer, with OH and H_2O adsorbed at atop sites in a $(\sqrt{3} \times \sqrt{3})R30°$ superstructure [75, 76]. The structure is reproduced in Figure 3.2. Simulated STM images and the calculated vibrational frequencies of the H2O-OH (3x3) phase are in agreement with experiment [73, 40]. The H2O-OH phase is found to be nearly coplanar on Pt [77, 75, 74]. The oxygen atoms in the H2O-OH $(\sqrt{3} \times \sqrt{3})R30°$ phase are calculated to be 2.11 to 2.17 Å above the Pt surface[75]. This agrees well with IV-LEED experiments by Held *et al.*. They find that the O atoms in the H_2O-OH structure adsorb at Pt atop sites 2.14-2.17 Å above the surface [77]. H_2O desorption from the O precovered surface happens at 190 K.

Theoretical calculations indicate that the binding energy per water molecule is higher for the $(\sqrt{39} \times \sqrt{39})R25.3°$ bilayer than for the $(\sqrt{37} \times \sqrt{37})R25.3°$ and $(\sqrt{3} \times \sqrt{3})R30°$ bilayers[78, 72]. In the $(\sqrt{39} \times \sqrt{39})R25.3°$ bilayer 9 % of the water is partly dissociated into H_3O^+ and OH^-[78].

Ab-initio Molecular Dynamics

MD simulations of a single water bilayer by Meng [79] showed that OH^- is present on Pt top sites in the inner part of the bilayer 2.23 Å away from the Pt surface, whereas H_3O^+ is in the outer part of the bilayer. The oxygen density of the outer part of the bilayer peaks 3.27 Å away from the Pt surface. The inner part of the bilayer contains only 20 % of the water molecules.

MD simulations of a proton disordered waterlayer with a 6×6 superstructure were performed by Delle Site *et al.*. They observed no water dissociation, but 5 of the 24 water molecules were found to adsorb on Pt atop sites 2.33 Å above the Pt surface. The remaining water molecules were distributed 3.1-3.4 Å away from the surface.[80]

First principles MD simulations of liquid water at 353 K have been performed by Otani *et al.* using the effective screening method to model electrostatic screening by the solution. Employing a $(3 \times 2\sqrt{3})$ Pt(111) surface cell with an equivalent of 4 D_2O bilayers each with a 2/3 ML water coverage they found that at the potential of zero charge D_2O was adsorbed on the atop sites of about 1/6 of the Pt atoms at a distance 2.5 Å above the surface[81]. At potentials negative of the potential of zero charge, Otani *et al.* found that D_2O preferred to orient with the deuterium atoms pointed towards the Pt surface.

3.9.2 Energy of OH and OOH

The effect of solvation is included for OH and OOH by incorporating the adsorbate in an H_2O/OH superstructure with a 2/3 ML total coverage. The most stable structures

are generally found when H_2O, OH and OOH occupy sites with a $(\sqrt{3} \times \sqrt{3})R30°$ periodicity.
The $(\sqrt{3} \times \sqrt{3})R30°$ H_2O-OH structure has been found to be stable in UHV experiments as described above. $(\sqrt{3} \times \sqrt{3})R30°$ H_2O-H_2O structures are less stable than $(\sqrt{39} \times \sqrt{39})R16°$ structures for monolayer coverages. However, the DFT calculations by Meng *et al.* showed that the $(\sqrt{3} \times \sqrt{3})R30°$ water structure is more stable than the $(\sqrt{39} \times \sqrt{39})R16°$ structure when the water layer is 3 bilayers thick [72]. Since we are really trying to model liquid water, a $(\sqrt{3} \times \sqrt{3})R30°$ water structure should be a reasonable approximation.
The adsorption energy of OH in a particular OH/H_2O superstructure with N_{OH} OH adsorbates and N_{H_2O} H_2O adsorbates is calculated as

$$\begin{aligned}\Delta E_{OH*} = \big(E_{OH/H_2O} + {}^1\!/_2 N_{OH} E_{H_2} - (N_{OH} + N_{H_2O})\, E_{H_2O} \\ - E_{slab} - N_{H_2O} \Delta E_{H_2O}\big)\, / N_{OH},\end{aligned} \tag{3.47}$$

where E_{OH/H_2O} is the total energy of the OH/H_2O superstructure, E_{slab} is the total energy of the slab without adsorbates, E_{H_2} and E_{H_2O} are the total energies of H_2 and H_2O molecule in the gas phase respectively, and ΔE_{H_2O} is the average adsorption energy of H_2O in a H_2O(p)/H_2O(v) water bilayer structure on the surface,

$$\Delta E_{H_2O} = \left(E_{H_2O/H_2O} - E_{slab} - N'_{H_2O} E_{H_2O}\right) / N'_{H_2O}, \tag{3.48}$$

where E_{H_2O/H_2O} is the total energy of the H_2O(p)/H_2O(v) superstructure with N'_{H_2O} water molecules. The adsorption energy of OOH in an $OOH/H_2O/OH$ superstructure is calculated as

$$\begin{aligned}\Delta E_{OOH*} = \big(E_{OOH/H_2O/OH} + {}^1\!/_2 \left(N_{OOH} + N_{OH}\right) E_{H_2} \\ - (2N_{OOH} + N_{OH} + N_{H_2O})\, E_{H_2O} \\ - E_{slab} - N_{H_2O} \Delta E_{H_2O} - N_{OH} \Delta E_{OH*}\big)\, / N_{OOH}.\end{aligned} \tag{3.49}$$

3.10 Discussion

Instead of electrochemical water oxidation, described by (3.12), we may form O directly at a surface by O_2 dissociation

$$\frac{1}{2}O_2 + * \rightleftarrows O* \,. \tag{3.50}$$

The free energy of adsorption is

$$\Delta G_{O*} = G_O - G_* - \frac{1}{2} k_B T \ln a_{O_2} \,, \tag{3.51}$$

which should be compared to the electrochemical oxidation in (3.14). Figure 3.3 shows the stability diagram for Ag(111), which will be calculated in the following chapter. The left y-axis shows the potential required for the formation of a given adsorption phase, while the right y-axis shows the O_2 partial pressure[4] that would be required in order to form a similar oxygen covered phase from reaction (3.50) at pH=14. The figure shows that in experiments, only a narrow range of structures are thermodynamically accessible at 298 K by variation of the O_2 partial pressure alone, compared to the accessible phases that may be reached by adjusting the potential 1 V. The figure emphasizes the relative magnitude of the material and pressure gap when going from UHV experiments and simulations to an electrochemical setup, compared to the gap when going from UHV to industrial pressures. The behavior is simply a result of the thermodynamic driving force for O-adsorption being linear in potential and logarithmic in pressure. The result is not really surprising.

[4]For simplicity we have assumed O_2 is an ideal gas over the entire pressure range $a_{O_2} = p_{O_2}/p^{\ominus}$.

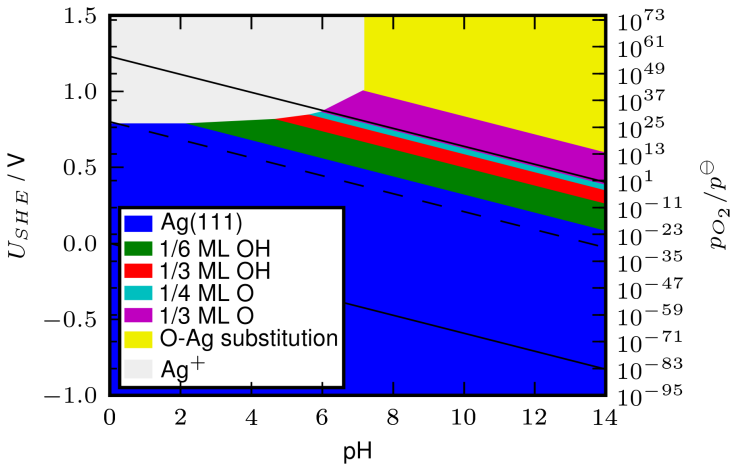

Figure 3.3: Surface Pourbaix diagram showing the most stable O and OH phases on Ag(111). The left y-axis shows the potential on the SHE scale required to form a given phase. The right y-axis shows the O_2 partial pressure required to form a similar O-covered phase according to eq. (3.51). The pressures have been aligned to the potential at pH=14.

The O_2 partial pressure at 0 V is the O_2 pressure in equilibrium with H_2O(l) and H_2 at 1 bar. So the comparison between the materials and pressure gaps for electrochemical and solid-gas interfases above may not be completely fair, as the effect of gas composition at industrial conditions also increases the material and pressure gap for a solid-gas interfase.

It may be argued that the structure of the catalyst surface itself, and not only the adsorbate structures formed over the surface, is determined by the non-equilibrium kinetics of the catalyzed reaction[38]. A dynamical description of the entire surface structure is beyond the scope of this thesis.

3.11 Summary

In this chapter we have derived equations that allow us to calculate the change in free energy for electrochemical water oxidation ((3.11) and (3.12)) and chlorine adsorption (3.23) from simple slab calculations. In general the methodology replaces the free energy of dissolved ions (Cl^- and H^+) and liquid water by the free energy of gas phase molecules in equilibrium with the dissolved ions or liquid water. In this process experimental thermodynamic data is used to adjust the chemical potentials of the gas phase species. The electric field at the electrode-electrolyte interface may be included assuming a constant field in the Helmholtz layer of constant width. The energetic effect of the field is small on an absolute scale. In the following chapters all potentials will be measured relative to the SHE ($U^{\ominus}_{SHE} = 0$, $\mu^{\ominus}_{e^-} = \mu^{\ominus}_{e^-,SHE}$) and all unless explicitly stated otherwise.

Chapter 4

Oxygen Reduction Reaction - on Ag(111) and Ni(111)

Proton exchange membrane (PEM) fuel cells have attracted considerable attention especially for transportation applications. It is recognized that many of the major drawbacks for the PEM fuel cell are related to the cathode reaction[4]. The oxygen reduction reaction (ORR) at the cathode is sluggish and introduces significant over potentials[82]. In addition only Pt and Pt alloy catalysts show a reasonable activity and stability in the acid environment. In alkaline fuel cells where the flexibility concerning the cathode catalyst is much larger, non-precious metals like Ni and Ag have been used.[83]

In this chapter we introduce the oxygen reduction reaction and a simple model for ORR by Nørskov and co-workers[11], in which the oxygen binding energy ΔE_{O*} is used as a descriptor for ORR activity. This model will form the basis of the theoretical studies in this and the following chapter. Here, we then consider the effect of on-surface O adsorption on the binding energies of O* and OH*. Finally we construct surface Pourbaix Diagrams for Ag(111) and Ni(111) and calculate the stability of ORR intermediates at the surfaces that are found to be stable at reasonably high potentials of 0.5-0.8 V *vs.* RHE.

4.1 ORR Intermediates

The overall reaction for oxygen reduction is

$$2H_2 + O_2 \rightleftarrows 2H_2O. \tag{4.1}$$

In an acidic environment the overall reaction consists of the anode reaction

$$2H_2 \rightarrow 4H^+ + 4e^-, \tag{4.2}$$

and the cathode reaction

$$O_2 + 4H^+ + 4e^- \rightarrow 2H_2O\,. \tag{4.3}$$

Several mechanisms have been proposed based on experiment[84, 85, 13] or theoretical calculations [86, 87, 84, 88, 89, 90, 91]. In this work we will focus on a simple model by Nørskov and co-workers, in which it is assumed that the oxygen reduction goes through the following series of intermediates[11]

$$O_2(g) + 4H^+ + 4e^- + * \rightarrow OOH* + 3H^+ + 3e^-, \tag{4.4a}$$

$$OOH* + 3H^+ + 3e^- \rightarrow O* + H_2O(l) + 2H^+ + 2e^-, \tag{4.4b}$$

$$O* + H_2O(l) + 2H^+ + 2e^- \rightarrow OH* + H_2O(l) + H^+ + e^-, \tag{4.4c}$$

$$OH* + H_2O(l) + H^+ + e^- \rightarrow * + 2H_2O(l). \tag{4.4d}$$

The free energy of O* and OH* relative to water may be calculated from equation (3.19) and the free energy of OOH* from (3.40). The free energy of the initial state in (4.4a) may be calculated from

$$\Delta G_{O_2} = 4U^{\ominus}_{H_2O/O2} - 4\left(eU - k_B T \ln a_{H^+}\right) , \tag{4.5}$$

where $U_{H_2O/O2}$ is the standard potential of the cathode reaction (4.3), and $U_{H_2O/O2} = 1.23V$ at 298.15 K. If we neglect the electric field, the change in free energy of each step will be of the form $\Delta G = \Delta G_i + eU$, where ΔG_i is independent of potential. This means that as the potential is decreased from the reversible potential of reaction (4.3) the thermodynamic driving force for the total reaction in (4.3) will increase. This is illustrated in Figure 4.1, where data from Karlberg *et al.* on Pt(111) has been reproduced. The need to decrease the operating potential for the electrochemical cell

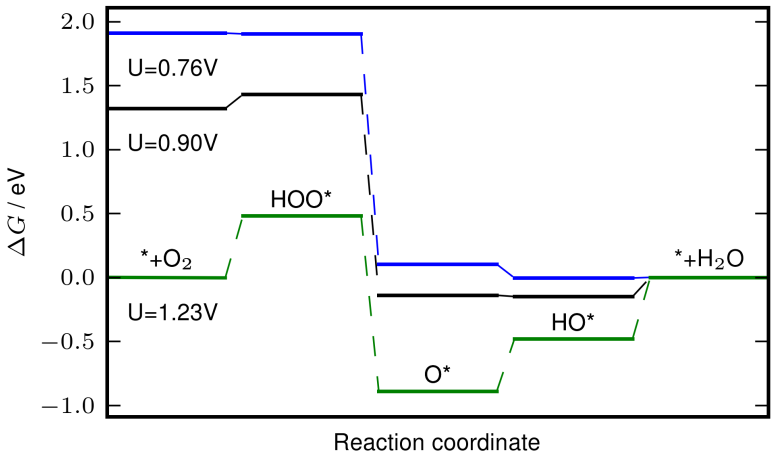

Figure 4.1: Potential energy diagram for Pt(111) involving the intermediates from (4.4). The figure is based on data calculated by Karlberg *et al.* [92], and includes contributions from the electric field. At $U = 1.23$V O_2 and H_2O are in equilibrium, however formation of OOH* and the reduction of O* and OH* to H_2O are all uphill in free energy. At $U = 0.90$V reduction of OH* to H_2O has the largest ΔG. At $U < 0.76$V all steps reduce the free energy.

to reach an appreciable current (reaction rate) results in the so-called over potential. The optimum catalyst would of course have $\Delta G = 0$ for all steps at the reversible potential $U_{H_2O/O2}$ at pH=0.

However, as the binding energy of the intermediates OH*, O* and OOH* are correlated, the binding energy of any of the intermediates may be expressed by the binding energy of a single intermediate. Usually the binding energies of the intermediates are expressed as a function of the oxygen binding energy, ΔE_{O*}, defined by the reaction

$$H_2O + * \rightarrow O* + H_2, \tag{4.6}$$

so that

$$\Delta E_{O*} = E_{O*} + E_{H_2} - E_* + E_{H_2O} . \tag{4.7}$$

A metal that binds intermediates too strongly requires very high overpotentials to remove O* or OH* from the surface. On the other hand a metal that binds O* too weakly also binds OOH* weakly and require high overpotentials to stabilize OOH*. From these correlations it is unlikely to find a metal with optimal OH*, O* and OOH* binding energies, and high overpotentials for ORR are to be expected[11]. The model in Ref. [11] qualitatively identifies Pt as the most active catalyst for ORR at low

temperatures. Another outcome of the model is that Pt binds intermediates stronger than the optimal catalyst based on the linear relations. This has been supported by subsequent calculations and experiments[93, 14].

It should be noted that additional barriers could be present between the intermediates (4.4). It could however be expected that these barriers would follow BEP relations [94]. This means that these barriers are also related to the binding energy of a single intermediate. In this a case, the general trends may be largely unaffected. From the previous studies it was unclear why cheaper metals such as silver or nickel may be used successfully in alkaline fuel cells but not in acidic PEM fuel cells.

4.1.1 ORR in an Alkaline Environment

In alkaline solution, H_2 rather than H_3O^+ may act as the proton donor. The overall anode reaction is then

$$4OH^- + 2H_2 \rightarrow 4H_2O + 4e^-, \tag{4.8}$$

and the overall cathode reaction is

$$O_2 + 2H_2O + 4e^- \rightarrow 4OH^-. \tag{4.9}$$

This may be split into the following elementary steps

$$O_2 + 2H_2O + 4e^- + * \rightarrow OOH* + H_2O + OH^- + 3e^-, \tag{4.10a}$$

$$OOH* + H_2O + OH^- + 3e^- \rightarrow O* + H_2O + 2OH^- + 2e^-, \tag{4.10b}$$

$$O* + H_2O + 2OH^- + 2e^- \rightarrow OH* + 3OH^- + 1e^-, \tag{4.10c}$$

$$OH* + 3OH^- + 1e^- \rightarrow * + 4OH^-, \tag{4.10d}$$

We will therefore consider the same intermediates at the surface in alkaline and acidic solution. The free energy of the intermediates relative to water may be calculated from (3.19), (3.40) and (4.5). Alternatively, another set of equations based on (4.10) and (4.8) could be derived by an approach similar to the one in chapter 3,. However we now assume water is in equilibrium with OH^- rather than H^+. Since this approach would also rely on $OH^- + H^+ \rightleftarrows H_2O$ being in equilibrium in order to relate a_{OH^-} to a_{H^+} and thereby introduce a pH scale, we may just as well use the equations already derived for acid solution. For example, if we consider removal of OH* from the surface (4.10d), the change in free energy of this step, from (3.19) is

$$\Delta G = -\Delta G_{OH*} = -\Delta G^\circ_{OH*} - k_B T \ln a_{H^+} + eU - \Delta\Delta G^{field}_{OH*}(U) \ . \tag{4.11}$$

The potential where removal of OH* becomes thermodynamically favored is determined by $\Delta G = 0$. If we neglect $\Delta\Delta G^{field}_{OH*}(U)$, (4.11) may be solved analytically for U_{OH*}, with

$$U_{OH*} = \frac{\Delta G^\circ_{OH*}}{e} + \frac{k_B T}{e} \ln a_{H^+} \ . \tag{4.12}$$

This potential is identical to the potential obtained from a Nernst equation written for (4.4d). The potential of the hydrogen anode in a solution with the same pH, is from equation (3.8) at 1 bar H_2 pressure

$$U_{RHE} = \frac{k_B T}{e} \ln a_{H^+} \ . \tag{4.13}$$

The potential of reversible OH* removal is therefore constant, if it is measured relative to a hydrogen electrode in a solution with the same pH as the solution at the cathode. This is also the relevant setup for measuring the cell potential in a fuel cell. Similar arguments hold for the change in free energy of the other reaction steps. Neglecting the electric field, there is no difference in the free energy of the ORR intermediates calculated in acidic and alkaline environment at fixed potential on the RHE scale. We note that the electric field in the double layer could very well be different from acid to alkaline solution. Besides, barriers which are not treated within this model may depend on whether the proton donor is H_2O or H_3O^+.

4.2 Surface Coverage

The linear correlations and the adsorption energies for the trend study of the ORR activity used in Ref. [11] were generally based on calculations in unit cells with low coverage ($\theta \leq 1/3ML$). However, it was also shown that Pt at low coverages had a slightly too strong ΔE_{O*} compared to the optimum oxygen binding energy. On the other hand, Pt with 1/2 ML oxygen adsorbs intermediates somewhat too weakly and behaves quite similar to Au(111) [11]. Weakened adsorption energy with increasing oxygen coverage could be expected because adsorbate-adsorbate repulsion increases at high coverages, and a similar effect would be anticipated for more reactive metals such as Rh or Ni. In fact, if a material bind O* and OH* strongly and removal of these species is difficult under certain ORR conditions, we would expect the coverage of O* or OH* to be high. For this reason it may be relevant to consider ORR at a surface with a high coverage of O* or OH*. For reactive metals it is generally found, that the mixed OH-H_2O phases with θ_{OH*} =1/3 are unstable relative to pure O-phases with coverage $\theta_{O*} \leq 1/3ML$ at potentials relevant for good ORR catalysts ($\approx$ 0.8V *vs.* RHE). This may be rationalized by the much larger charge transfer for pure O-phases than the mixed OH-H_2O phase. While OH phases with more than 1/3 ML OH are possible, we do not find them to be very stable. In the following we therefore focus on the change in O* and OH* adsorption energies with increasing O* coverage.

Figure 4.2 shows the weakening of OH* and O* binding energy with increasing O* coverage on close packed transition metal surfaces[1]. The calculations are performed in a (2x2) surface cell. The O adsorption energy at θ_O initial O coverage is defined as

$$\Delta E_{O*}(\theta_O) = E_{(1+4\cdot\theta_O)O*} + E_{H_2} - E_{4\cdot\theta_O O*} + E_{H_2O}\,, \tag{4.14}$$

where $E_{(1+4\cdot\theta_O)O*}$ is the total energy of the surface with $1+4\cdot\theta_O$ adsorbed O atoms. The OH adsorption energy at θ_O initial O coverage is defined as

$$\Delta E_{OH*}(\theta_O) = E_{4\cdot\theta_O O*+OH*} + \frac{1}{2}E_{H_2} - E_{4\cdot\theta_O O*} + E_{H_2O}\,. \tag{4.15}$$

For the surface without any adsorbates, OH may adsorb at hollow, bridge or atop sites depending on the metal. O is found to always adsorb most strongly to hollow sites. When OH is co-adsorbed with O, the strong preference for O to adsorb in hollow sites and the OH-O repulsion force OH to adsorb atop the surface metal atom that is not coordinated to O in the hollow site. ΔE_{O*} increases monotonously with O coverage while $\frac{\partial \Delta E_{O*}}{\partial \theta_O}$ is about the same for all the considered elements. However repulsions appear to be strongest on Ni, Cu, Ag and Au. Recently the coverage dependent oxygen adsorption energy was studied by Miller and Kitchin[95]. Figure 4.3 shows ΔE_{OH*} plotted *vs.* ΔE_{O*} for initial O coverages of 0, 1/4 and 1/2 ML O. The points are distributed along a single line, but quantitatively the correlation is not very good - especially in the interesting region of O adsorption energies, ΔE_{O*} between 1.5 eV and 2.5 eV. This is exemplified by the fact that clean Ag and Ni with 1/2 ML O, which both have a differential O adsorption energy near 2 eV, differ in their differential OH adsorption energies by about 1 eV. It appears that the adsorption energies for 0 and 1/4 ML O could be fitted by a single trend line. However, there are systematic deviations for the adsorption energies at 1/2 ML O.

[1] Computational Details: The adsorption energies have been calculated using the RPBE functional. Adsorbates were placed on one side of 3 layer slabs and the adsorbates and the topmost metal layer was allowed to relax until the largest force component was below 0.05 eV/Å. The KS eigenstates are expanded in a plane wave basis with a 340 eV cutoff. The first Brillouin zone is sampled using a $4 \times 4 \times 1$ Monkhorst Pack grid. The dipole interaction between periodic images of the slabs have been decoupled.

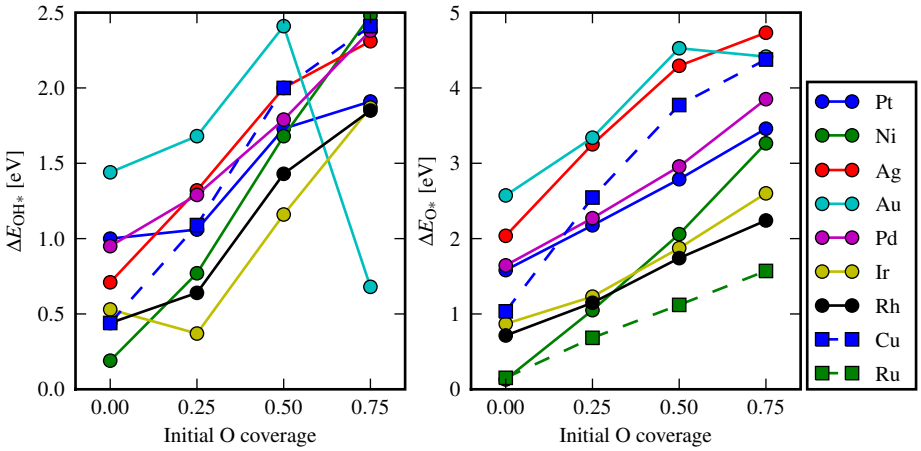

Figure 4.2: $\Delta E_{\mathrm{OH}*}$ and $\Delta E_{\mathrm{O}*}$ in eV *vs.* initial O coverage.

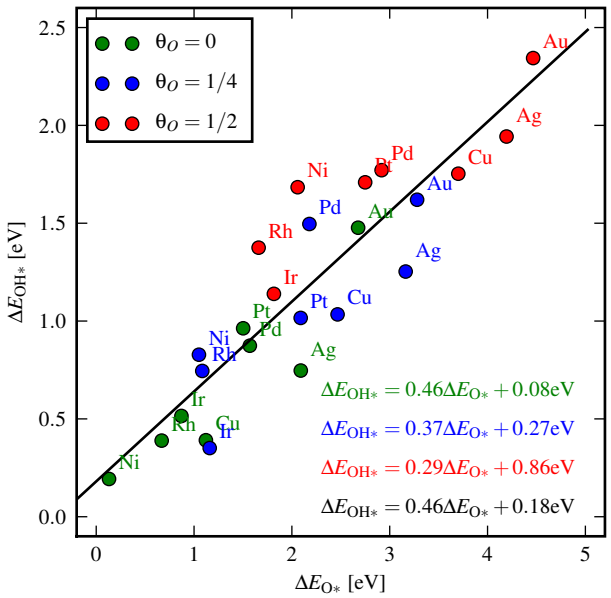

Figure 4.3: $\Delta E_{\mathrm{OH}*}$ *vs.* $\Delta E_{\mathrm{O}*}$ in eV for initial O coverages of 0, 1/4 and 1/2 ML O. The best linear fits are typed in the color corresponding to coverage in the legend. The black line $\Delta E_{\mathrm{OH}*} = 0.46\Delta E_{\mathrm{O}*} + 0.16eV$ is the best fit for all the data.

4.3 Surface Pourbaix Diagrams for Ag(111) and Ni(111)

Since a unified treatment of oxygen reduction at all O surface coverages is not possible using simple scaling relations between O and OH binding energies, c.f. Figure 4.3, we turn to detailed calculations of the surface structures at the Ag(111) and the Ni(111) surfaces. Our aim is first to identify the most stable phases as a function of potential and pH on Ag(111) and Ni(111). With the most stable phase as a starting point, we then calculate the stability of intermediates in the oxygen reduction reaction. This approach ensures that surface coverages correspond to the most stable surface under these conditions. We estimate their catalytic activity for ORR by determining the highest potential at which all ORR reaction steps reduce the free energy. We refer to this potential as the ORR-potential. We have considered different adsorbate-

adsorbate superstructures in (2x2) and ($\sqrt{3} \times 3$) surface unit cells[2]. The energies of the considered phases are shown in appendix B Table B.1. The electric field has been neglected in constructing the phase diagrams for Ag(111) and Ni(111), but included for the calculation of the potential energy surface for ORR using the corrections calculated by Karlberg *et al.* [92], assuming $\epsilon = -\frac{U}{d}$ with $d = 3.0$ Å.

4.3.1 Ag(111)

To investigate the Ag(111) surface, different structures of hydroxyl and oxygen on the surface have been considered. In acidic solution, dissolution of Ag is spontaneous at potentials above 0.80 V, according to

$$\mathrm{Ag(s)} \rightarrow + \mathrm{Ag^+} + e^- \text{ with } U^{\ominus} = 0.8\mathrm{V} \textit{ vs.} \text{ SHE}, \tag{4.16}$$

so that ORR on this surface is unlikely. In alkaline environments the dissolution process is

$$\mathrm{Ag(s)} + \mathrm{H_2O(l)} \rightarrow \mathrm{AgO^-(aq)} + 2\mathrm{H^+(aq)} + e^-, U^{\ominus} = 2.2\mathrm{V} \textit{ vs.} \text{ SHE}. \tag{4.17}$$

Surface Pourbaix Diagram for Ag(111)

In alkaline solution at low potentials, the most stable surface structure considered is the clean Ag(111) surface, showing that Ag is a noble metal. At pH = 14, the free energy of dissolution in (4.17) is negative for U > 0.5 V *vs.* SHE for the clean (111) surface. Dissolution is therefore not as critical as in acidic solution, see Figure 4.4. Water oxidation starts at 0.93 V *vs.* RHE forming a structure with 1/6 ML HO* and

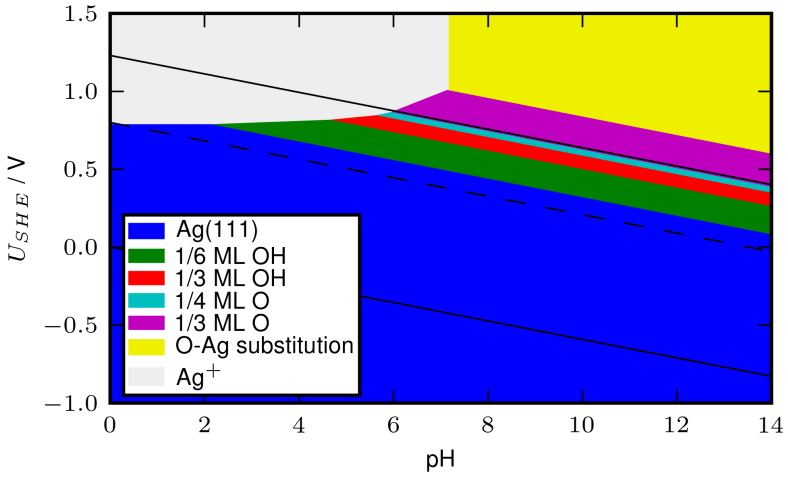

Figure 4.4: Surface Pourbaix diagram for Ag(111). The two solid lines mark 0 V *vs.* RHE and 1.23 V *vs.* RHE, c.f. (3.10). Water is thermodynamically stable between these lines. The dashed line at $U = 0.8$V *vs.* RHE marks the potential of a good ORR catalyst under steady state conditions. It is seen that dissolution is a much larger problem in acidic than in alkaline electrolytes, and that the coverage of the Ag surface is low at $U = 0.8$V *vs.* RHE.

[2]Computational Details: The adsorption energies have been calculated using the RPBE functional. Adsorbates were placed on one side of 3 layer slabs and the adsorbates and the topmost metal layer were allowed to relax until the largest force component was below 0.02 eV/Å. The KS eigenstates are expanded in a plane wave basis with a 350 eV cutoff and the density expanded in a plane wave basis with a 500 eV cutoff. The first Brillouin zone is sampled using an $8 \times 8 \times 1$ Monkhorst Pack grid for the (2x2) surface unit cell and a $10 \times 6 \times 1$ Monkhorst Pack grid for the ($\sqrt{3} \times 3$) surface unit cell. The dipole interaction between periodic images of the slabs have been decoupled. The calculations on Ni were performed spin polarized and unpolarized otherwise.

1/2 ML water. At 1.11 V *vs.* RHE the HO* coverage increases to 1/3 ML HO*. At potentials above 1.19 V *vs.* RHE hydroxyl is oxidized further to O*. At higher potentials we find that as more oxygen or hydroxyl is adsorbed on the surface, O atoms will spontaneously substitute Ag atoms on the surface when the surface is relaxed. This may be interpreted as an onset of dissolution or oxidation of the Ag(111) surface. We note that the substitution is favored by 0.25 V relative to the alkaline dissolution process at pH = 14. The pH and U range where the observed substitution mechanism is favorable instead of alkaline dissolution is shown in the Pourbaix diagram Figure 4.4. The substitution becomes spontaneous at potentials above 1.44 V *vs.* RHE. The potential of the onset of dissolution or oxidation is determined by the details of the substituted Ag surface, and it is very likely that surfaces with different atomic configurations turn out to be more stable than the ones we have considered. This may include, for example, a surface oxide[96, 97] or even formation of bulk Ag_2O which may form at potentials above 1.18 V *vs.* RHE.

We have added the potentials of the reversible hydrogen and oxygen electrodes to the Pourbaix diagram to mark the stability range of water at $U_{\mathrm{RHE}} = 0\mathrm{V}$ and $U_{\mathrm{RHE}} = 1.23\mathrm{V}$, respectively. We have also added a line at $U_{\mathrm{RHE}} = 0.80\mathrm{V}$, because it is a realistic potential for a good ORR catalyst. As eluded to earlier, the relative energies of surface structures formed by water oxidation (3.11) and (3.12) does not vary along the lines of constant U_{RHE}. This means that at $U_{\mathrm{RHE}} = 0.80\mathrm{V}$, the same surface structure will be relevant for ORR regardless of pH. For silver, the thermodynamics of corrosion however change going from acidic to alkaline environment.

CV experiments in alkaline electrolytes show a reversible peak around 0.3 V *vs.* RHE on Ag(111), and at lower potentials on Ag(100) and Ag(110)[98, 99]. This peak has been suggested to be caused by hydrogen adsorption, alkali metal deposition or oxidation of water to HO*[100]. Recent EC-STM experiments have shown that the Ag(111) surface is unmodified up to a potential near 0.7 V *vs.* RHE, after which protrusions begin to emerge, which are assigned to 2D Ag_2O nuclei[101]. Our calculations do not support the view that the CV peak at 0.3 V *vs.* RHE is due to HO* or H* on the flat Ag(111) surface, as we find water oxidation starts at 0.93 V *vs.* RHE. To adsorb HO* at 0.3 V *vs.* RHE requires a stabilization of HO* by 0.63 eV relative to our calculations. Such stabilization could, in principle, be caused by HO* adsorbing at steps or defects rather than on the Ag(111) terraces. This is however an unlikely explanation for the existence of a peak at 0.3 V *vs.* RHE, as the HO* coverage is reported to be 0.2-0.35 ML.[98, 99] We note that our theoretical HO* formation is in good agreement with the high potential adsorption peak starting at 0.9 V *vs.* RHE also observed in CV experiments.[99]

ORR on Ag(111)

We find the Ag(111) surface is free of adsorbates up to 0.93 V *vs.* RHE, where 1/6 ML hydroxyl is adsorbed, followed by additional HO* adsorption to form a structure with 1/3 ML hydroxyl at 1.11 V *vs.* RHE. At any reasonable overpotential we would therefore expect the total coverage on the surface to be very low. At 1/6 ML total coverage the rate limiting step is the formation of HOO*, which becomes exothermic at potentials below 0.73 V *vs.* RHE. This is in agreement with previous estimations based on DFT calculations of the oxygen binding energy on Ag(111)[11]. The adsorption of HOO* being rate limiting reflects the fact that Ag is a noble metal that binds the intermediates too weakly relative to the optimal ORR catalyst. Ag therefore seems like a good alternative to Pt, however the problem in acidic solution is dissolution rather than activity. Dissolution involves only electron transfer to Ag, which means that the relevant dissolution potential will not change vs. SHE. Since ORR in alkaline environments runs at lower potentials *vs.* SHE, Ag-dissolution becomes less of a problem. Assuming the effect of the electric field in the dipole layer is similar on Pt(111) and Ag(111), the electric field destabilizes O* by about 0.04 eV and stabilizes HO* by about 0.06 eV at the ORR potential. The adsorption energy

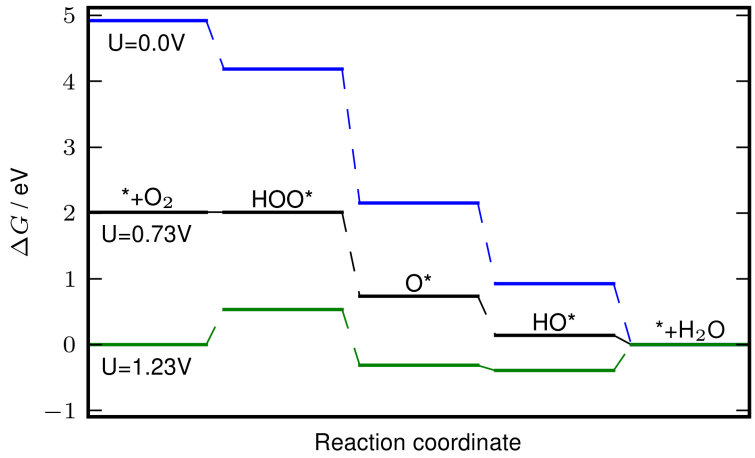

Figure 4.5: The free energy of ORR intermediates on Ag(111) at potentials 0 V *vs.* RHE, 0.73 V *vs.* RHE and 1.23 V *vs.* RHE.

of HOO*, which determines the overpotential in this model, is destabilized by about 0.01 eV by the electric field. The corrections due to the electric field are therefore too small to change the qualitative picture of ORR on Ag(111). The free energy of the intermediates is shown at different potentials in Figure 4.5 including the corrections due to the potential.

4.3.2 Ni(111)

The Ni(111) surface is quite reactive, and corrosion is a problem in acidic as well as alkaline solutions. We consider the acidic dissolution process[62]

$$\mathrm{Ni} \rightarrow \mathrm{Ni}^{2+}(\mathrm{aq}) + 2e^-, \text{ with } U^{\ominus} = -0.257\mathrm{V} \textit{ vs.} \text{ SHE}, \tag{4.18}$$

and the dominant alkaline corrosion process[62, 102, 103]

$$\mathrm{Ni} + 3\mathrm{H_2O(l)} \rightarrow \mathrm{Ni(OH)_3^-(aq)} + 2e^- + 3\mathrm{H^+(aq)}, \text{ with } U^{\ominus} = 0.63\mathrm{V} \textit{ vs.} \text{ SHE}. \tag{4.19}$$

Surface Pourbaix Diagram for Ni(111)

We find that at $U = 0$V *vs.* RHE, 1/4 ML H* is adsorbed at the surface up to 0.14 V *vs.* RHE. Oxygen starts to adsorb at $U > 0.20$V *vs.* RHE, with 1/3 ML O* stabilized by water being the most stable structure in the potential range from 0.34 V *vs.* RHE to 0.82 V *vs.* RHE. The highest resistance against corrosion is obtained at pH = 9.9, where $\Delta G < 0$ for $U > 0.38$V *vs.* RHE, as seen from Figure 4.6 and 4.7. The free energy of formation for O* is 0.39 eV/O at 1/4 ML O coverage, which is in reasonable agreement with the experimental value of 0.49 ± 0.10 eV/O*[104]. In contrast to Taylor *et al.* [51], we do not find HO* or coadsorbed O* and HO* to be stable on the Ni(111)-surface. However, we note that at 0.18 V the free energies of 1/4 ML H*, 1/4 ML O* and 1/6 ML HO* are equal within 0.1 eV. The difference could therefore be caused by different functionals and atomic structures of the adsorbates. In UHV experiments oxygen on Ni(111) may form an ordered p(2×2) structure with 0.25 ML coverage or a $(\sqrt{3}\times\sqrt{3})R30°$-O structure with 0.33 ML coverage[105]. Oxidation of the Ni(111) surface initiates at a coverage between 0.33 and 0.5 ML[104, 105], suggesting that ORR on the metallic Ni surface could occur on a surface with up to 1/2 ML O*. Thermodynamically $\beta - \mathrm{Ni(OH)_2}$ is however the most stable nickel phase at these conditions[102]. One might expect that the adsorption of O* would lead to increased thermodynamic stabilization of the Ni(111) surface against dissolution.

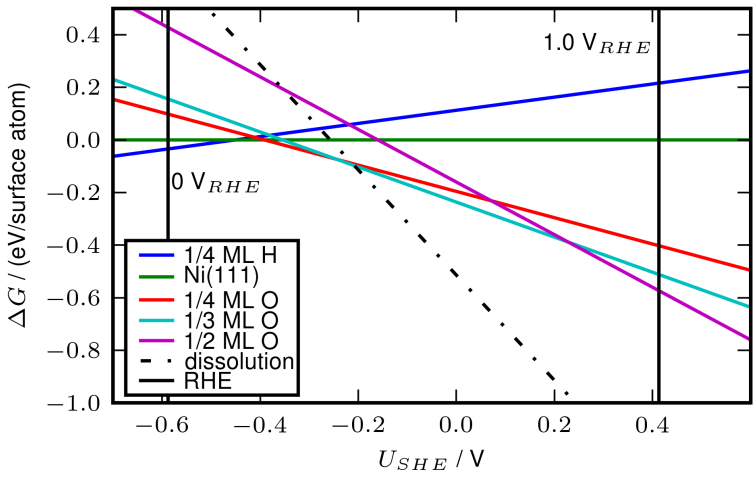

Figure 4.6: The most stable Ni(111) structures at pH = 9.9. The resistance against dissolution is at maximum at this pH because G of the acidic and alkaline dissolution are equal at this pH. Neglecting dissolution, the oxygen coverage then increases gradually with 1/3 ML O* having a broad stability range from 0.34 V *vs.* RHE to 0.82 V *vs.* RHE. Dissolution is however spontaneous for U > 0.38 V *vs.* RHE. The two vertical black lines mark 0 V *vs.* RHE and 1 V *vs.* RHE.

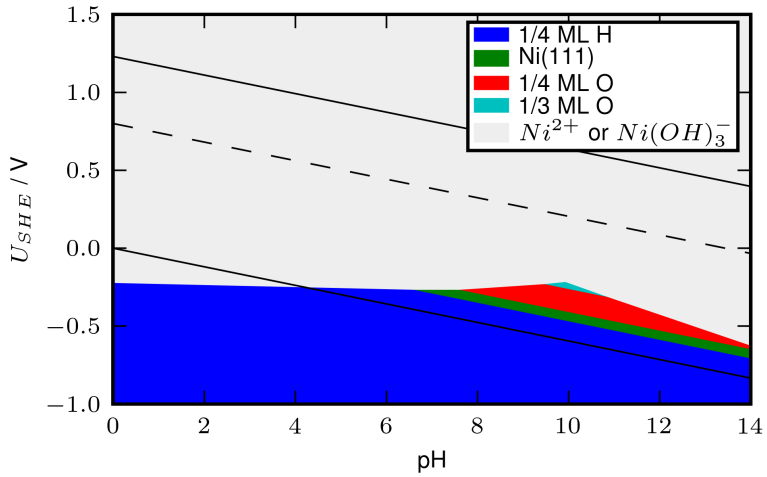

Figure 4.7: Surface Pourbaix diagram for Ni(111) including alkaline and acidic dissolution. The two solid lines mark 0 V *vs.* RHE and 1.23 V *vs.* RHE, c.f. (3.10). The dashed line at $U = 0.8$V *vs.* RHE marks the potential of a good ORR catalyst under steady state conditions. Dissolution is a problem in both acidic and alkaline electrolytes. The best resistance against dissolution is obtained at pH = 9.9, where dissolution becomes spontaneous for $U > 0.38$V *vs.* RHE. Oxygen is adsorbed for $U > 0.20$V *vs.* RHE, c.f. Figure 4.6.

However, from Figure 4.6 it is clear that the stabilization is insignificant. Other effects, such as stabilization of low-coordinated Ni atoms on the surface by O and OH are probably more important.

ORR on Ni(111)

On the clean Ni(111) surface O_2 dissociates easily, so the rate limiting step on Ni at very low coverage is reduction of O* to HO* or HO* to H_2O. With a water layer

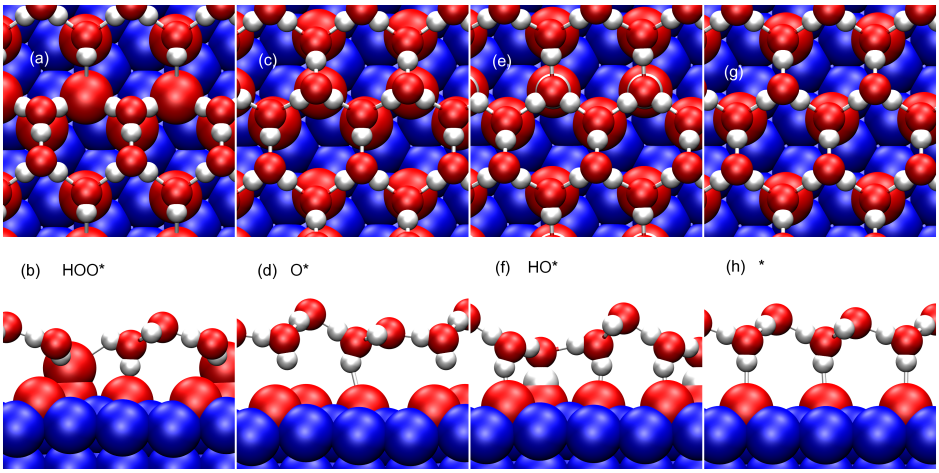

Figure 4.8: ORR intermediates forming at vacancies in the $(\sqrt{3} \times \sqrt{3})R30°$-O structure: (a) + (b): The HOO* intermediate dissociates into hydroxyl and oxygen. (c) + (d): Adsorbed oxygen completing the $(\sqrt{3} \times \sqrt{3})R30°$-O structure. (e) + (f): Adsorbed hydroxyl. (g) + (h): The vacancy. Ni atoms are blue, O atoms red and H atoms white.

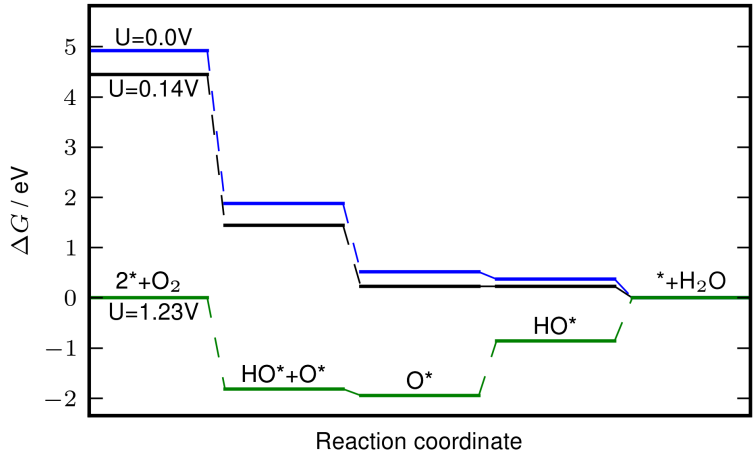

Figure 4.9: The free energy of the intermediates adsorbed at vacancies in $(\sqrt{3} \times \sqrt{3})R30°$-O. All steps decrease the free energy at potentials below 0.14 V *vs.* RHE. A water layer has been used to stabilize all intermediates as shown in figure 4.8. Without the water layer to stabilize O*, the self-consistent ORR potential is 0.26 V *vs.* RHE.

included to stabilize HO* on the surface, we find $\Delta G^{\circ}_{OH*} = 0.27$eV and $\Delta G^{\circ}_{OH} = 0.41$eV. All reduction steps are therefore exothermic at $U < 0.14$V *vs.* RHE, which shows that the clean Ni(111) surface is too reactive to be a good ORR catalyst. From the surface Pourbaix diagram we would however expect some oxygen at the surface at higher potentials. This changes the adsorption energies due to adsorbate interactions. To take adsorbate interactions into account we consider ORR involving $(\sqrt{3} \times \sqrt{3})R30°$-O on the surface, as it is the most stable structure in the potential range from 0.33 to 0.82 V *vs.* RHE, cf. Figure 4.6. The oxygen reduction reaction might occur by adsorption and subsequent reduction of O_2 at vacancies in the $(\sqrt{3} \times \sqrt{3})R30°$-O structure, as shown in Figure 4.8. The free energy of the intermediates is shown in Figure 4.9. We find that spectator O* makes the Ni(111) surface a bit

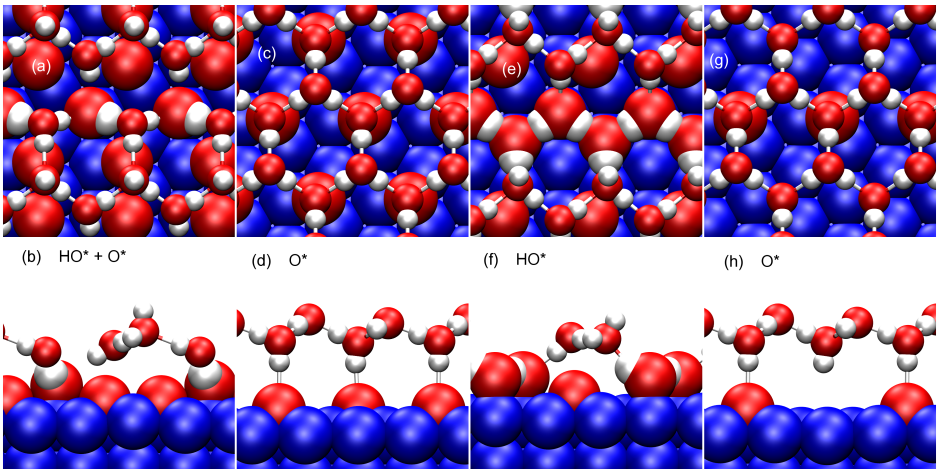

Figure 4.10: Intermediates adsorbed at free sites in the $(\sqrt{3} \times \sqrt{3})R30°$-O structure. (a) + (b): HOO*. (c) + (d): O*, (e) + (f): HO*, (g) + (f): The $(\sqrt{3} \times \sqrt{3})R30°$-O structure is completed by OH* desorbing.

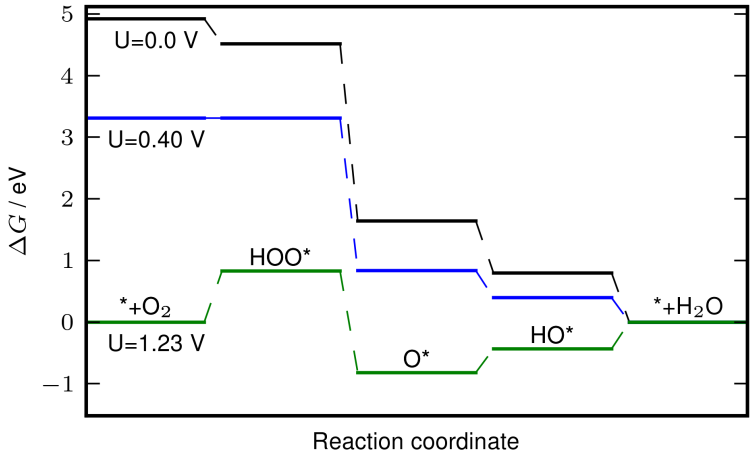

Figure 4.11: Free energy of the intermediates along the reaction path (4.4) or (4.10) adsorbed at the free sites in the $(\sqrt{3} \times \sqrt{3})R30°$-O structure. Because the formation of HOO* limits the ORR potential, the overpotential could be reduced if the binding energies could be increased. If O_2 dissociates easily on the $(\sqrt{3}\times\sqrt{3})R30°$-O structure, the overpotential is also decreased.

more noble because the binding energies of O* and HO* are decreased by about 0.1 eV. The HOO* intermediate dissociates on this surface. OOH* also dissociates when it is placed alone in the $3 \times \sqrt{3}$ cell. All steps are exothermic for $U < 0.14$V *vs.* RHE with the rate limiting step being a reduction of O* to HO*.

Another possible reaction mechanism on the $(\sqrt{3} \times \sqrt{3})R30°$-O surface is that O_2 adsorbs and is reduced at free sites on the surface as shown in Figure 4.10. Because of repulsion between adsorbed oxygen and H_2O adsorbed at the top sites, a H_2O-HO* bonding network directly on the surface is rather unstable. We find HO* to be most stable when a water layer is placed above the surface, with hydrogen bonding between the surface and the water layer. A similar structure is found to be the most stable for O* and HOO*, except that it has been possible to include HOO* in the water layer, as it protrudes from the surface. When HOO* is included in the water layer and allowed to relax, hydrogen moves from HOO* to a nearby water

molecule, forming a H_3O molecule. The H-O bond in H_3O is 1.05 Å and the H-OO* bond is 1.51 Å. The free energy of the intermediates is shown in Figure 4.10. The free energies of O* and HO* have increased significantly compared to the clean Ni(111) surface, making the surface much more noble. The significantly increased interaction between adsorbates may be rationalized by the fact that the adsorbates bind to the same Ni atoms on the surface. The rate limiting step is the formation of HOO*, which is exothermic at potentials below 0.40 V *vs.* RHE. The binding free energies for oxygen and hydroxyl are 1.64 and 0.80 eV respectively. The O* and HO* binding energy on Ni(111) with 1/3 ML O suggests that this surface is a good ORR catalyst comparable to Pt, but the binding energy of HOO* is weaker than that of Pt. Formation of HOO* therefore becomes the rate limiting step on Ni. An alternative to the OOH formation mechanism in (4.4) or (4.10) is that oxygen dissociates on the surface. An estimate of the O_2 dissociation barrier, based on the oxygen binding energy and the Brøndsted-Evans-Polany relationship between the adsorption energy and the activation energy[94], suggests that dissociation on the $(\sqrt{3} \times \sqrt{3})R30°$-O surface is non-activated. Taking the dissociation reaction path into consideration increases the ORR potential to a value close to that of Ag and Pt, because reduction of O* and HO* is efficient on the $(\sqrt{3} \times \sqrt{3})R30°$-O surface. However, metallic Ni will dissolve in alkaline solution at $U = 0.7 - 0.8$V *vs.* RHE, clarified in Figure 4.7.

4.4 Summary

In this chapter we have introduced the oxygen reduction reaction and the simple model by Nørskov and co-workers[11] for the reaction path. We have demonstrated that adsorbate-adsorbate repulsions will decrease adsorbate binding energies significantly at high O coverages.

We have constructed surface Pourbaix diagrams for Ag(111) and Ni(111) based on DFT calculations. These diagrams show the most stable surface structure as a function of pH and potential. The surface structure under reaction conditions is obviously important for the activity. The calculated formation potentials for HO* at 0.93 V *vs.* RHE on Ag(111) is in good agreement with experiment [99, 98]. Having identified the most stable surface structure present at 0.8V *vs.* RHE for a surface in equilibrium with water and H^+/OH^-, we investigated the stability of ORR intermediates formed at a surface with O* and OH* coverages close to the most stable surface in the absence of O_2. This means that one of the ORR intermediates corresponds to the most stable surface structure in the absence of O_2. We therefore obtain self-consistency in the sense that the surface is stable at the surface structure dependent ORR potential. The self-consistency changes the activity of the much too reactive catalyst Ni, because the increased (1/3 ML) O* coverage at the ORR potential has made Ni adsorb additional adsorbates weaker and makes Ni effectively more noble. The activity of the too noble catalyst Ag is, however, unaffected. We demonstrate that whereas there is no effect of the pH on the coverage of adsorbates at the ORR-potential[3], pH has a dramatic effect on the dissolution potential relative to the ORR potential. For Ni the ORR-potential line $U = 0.8$V *vs.* RHE in Figure 4.6 is still in the dissolution area at pH = 14, which means that for Ni the stability limits the ORR-potential. For Ag the line for $U = 0.8$V *vs.* RHE in the Pourbaix diagrams starts in the dissolution region in acid at pH=0 and as pH is increased the ORR potential line moves into the stability region of the clean Ag(111) surface, as shown in Figure 4.4. The stability thereby offers an explanation of why it is possible to use Ag in alkaline fuel cell cathodes.

[3]Within the approximation that the effect of the electric field through $\Delta\Delta G^{field}$ is small.

Chapter 5

Pt and Pd Alloys for Oxygen Reduction

To make Pt based low temperature polymer fuel cells viable for applications in vehicles, catalyst Pt loadings must be decreased. Gasteiger proposed that sufficiently reduced loadings could be achieved with Pt-based alloys with stable activity 2-4 times higher than pure Pt nanoparticles currently used in fuel cells [106]. Several Pt alloys, notably those including late 3d transition metals such as Cr, Fe, Co, Ni and Cu[107, 108, 106, 109, 93, 110, 111, 112], have been shown to be more active than Pt.

The model for the ORR described in chapter 4 is used in this chapter as a starting point for a computational screening for Pt and Pd alloys active for ORR. The model predicts that alloys binding O about 0.2 eV weaker than Pt should have optimal activity [11, 93]. The model was derived based on model calculations on fcc (111) surfaces. So for the screening to be relevant it must hold that (111) facets of nanoparticle catalysts contribute substantially to the total turnover for Pt alloy catalysts. For Pt this seems reasonable, as surfaces which are more open than (111) most likely bind O and OH too strong to be active [109]. The surface structure of Pt alloys depends on preparation conditions. When annealed in vacuum, some alloys *e.g.* Pt_3Ni form a Pt skin at the surface with an enrichment of the alloying element in the second layer and damped concentration oscillations into the bulk alloy [110]. This structure appears to be (meta)-stable under ORR conditions. If the surface is prepared in UHV by sputtering without annealing, non-Pt atoms in the surface may dissolve when the sample is brought into contact with an acid electrolyte. This has been reported to result in a roughend 'skeleton'-surface [110]. However, dissolution of Fe has been reported to lead to flat Pt(111)-(1x1) terraces and not roughened skeleton surfaces[113].

5.1 Computational Screening

We consider alloys terminated by a 1 monolayer thick skin of Pt atoms. The electronic properties of the surface layer will then be close to those of a regular Pt surface, but there will be some modifications arising from the underlying alloy. Figure 5.1 shows the output of the screening study performed by J. Greeley[1]. We have considered

[1]Computational Details: The Kohn-Sham valence states are expanded in a plane wave basis with kinetic energy below 340 eV. The cutoff for the charge density is 500 eV. Exchange and correlation effects are approximated by the RPBE exchange correlation functional. For the screening in Figure 5.1, the oxygen adsorption energies are calculated in a (2×2) surface unit cell on a 4 layer slab, where the two top most layers and adsorbates have been relaxed until a maximum force below 0.05 eV/Å is obtained. The first Brillouin zone is sampled by an $18(1\times1)$ Chadi-Cohen k point grid[114]. For the potential energy surfaces and Figures 5.8 and 5.10 we have used (8×8) and (4×4) Monkhorst Pack grids of special k points for calculations on (2×2) and $(\sqrt{12}\times\sqrt{12})R30^\circ$ surface unit cells respectively [115]. Adsorbates are in these cases relaxed until a maximum force below 0.02 eV/Å is

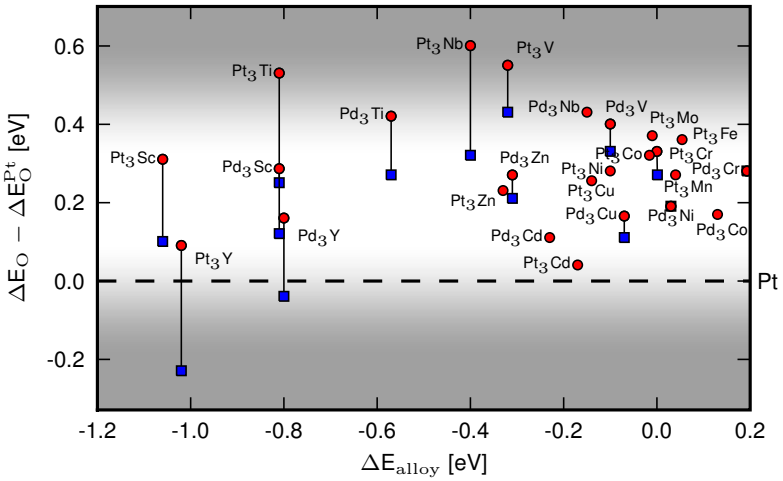

Figure 5.1: Output of a computational screening study, showing the oxygen binding energy relative to that of Pt as a function of the alloy formation energy. The most active catalyst have oxygen binding energies that are 0 to 0.4 eV weaker than on Pt. The window has been marked by a gray scaled gradient to recognize the limited accuracy of the DFT calculations. The circles (squares) show the oxygen binding energy calculated on surfaces with 50 % (25 %) concentration of the alloying element in the second layer.

alloys where the 2nd layer has been eniched by solute atoms, X, and contains 50 % X rather than 25 % X as in the bulk. An X enriched subsurface could be formed by exchange of X and Pt/Pd atoms between the first and the second layer of the alloy if the alloy is annealed in vacuum [110]. It is also possible that if the stoichiometric alloy surface is brought into contact with the acidic electrolyte, the solute X atoms in the first surface layer will dissolve. The remaining Pt/Pd atoms could then diffuse to heal the formed defects. In this case the solute concentration in the second layer is probably closer to 25 % than 50 %.

Figure 5.1 shows the oxygen binding energy relative to Pt on the y-axis. The x-axis shows the alloy formation energy obtained from a database of DFT calculated formation energies [116, 117]. For Pt alloys the alloy formation energy is defined by

$$\Delta E_{\text{alloy}} = \frac{1}{4}\left(E^{bulk}_{\text{Pt}_3\text{X}} - 3E^{bulk}_{\text{Pt}} - E^{bulk}_{\text{X}}\right), \tag{5.1}$$

where $E^{bulk}_{\text{Pt}_3\text{X}}$ is the total energy of the alloy per Pt_3X formula unit and E^{bulk}_{X} is the total energy per atom of the bulk element X.

The domain where the predicted activity is less than the activity of Pt is shaded with a gray gradient. Given the accuracy of DFT and the applied model, we consider materials within the white area of the figure to be candidates for having enhanced activity relative to Pt. Some of the well-known alloys with Fe, Co, Ni and Cu show up in Figure 5.1. However, it is more interesting that alloys with Sc and Y also are suggested to be active.

These alloys are also highly stable against phase separation into Pd/Pt and X. In fact Pt_3Sc and Pt_3Y are the most stable fcc alloys in a database with more than 60000 compounds[116, 117]. The good stability of scandium and yttrium alloys may be explained by the alloys having a d-band that is close to being half filled as Pt/Pd contributes 9 d-electrons each and Y/Sc 1 d-electron per atom. It could be hoped, that the high alloy stability also could stabilize the alloys kinetically against dissolution.

obtained.

5.2 Potential Energy Surfaces for ORR

In this section we calculate or estimate the free energy of the ORR intermediates, OOH, O and OH intermediates on $Pt_3Sc(111)$ and $Pt_3Y(111)$ at $U = 0.9$ V and pH = 0 and compare their stability in comparison to those on a Pt(111) surface. We consider Pt_3Y and Pt_3Sc and with 25 % or 50 % Y/Sc in the second layer at a moderately low coverage of OH. For Pt_3Y with 25 % Y in the second layer, O adsorption is quite strong, c.f. Figure 5.1 and we find that at 0.9 V V *vs.* RHE some sites at the (111) facet are most likely blocked. We therefore also estimate the stability of ORR intermediates at a surface where these sites have been blocked by spectator O adsorbates.

5.2.1 Calculational Method

The free energy of the intermediates on Pt(111) at 0.9 V including a uniform external field have been calculated previously[92]. To minimize variations in the absolute free energy due to slightly different calculational setups, the binding energy of adsorbates on Pt_3X is calculated relative the binding energy on Pt with identical calculational parameters. The absolute free energies are then obtained by adding the relative binding energy to the absolute free energy on Pt reported previously in Ref. [92]. We thus implicitly assume the zero-point energies of the intermediates do not vary with the surface composition.

For Pt_3Y and Pt_3Sc, the shift in work function relative to Pt results in an additional potential drop across the metal-solution interface, and the field in the dipole layer must increase accordingly. We assume a 3 Å thick dipole layer and use the field dependence of OOH, O and OH calculated by Karlberg *et al.* on Pt(111) [92]. The free energy of an adsorbate A on the surface X is then calculated from

$$\Delta G_{\mathrm{A}}^{\mathrm{X}} = \Delta G_{\mathrm{A}}^{\mathrm{Pt}} + \Delta E_{\mathrm{A}}^{\mathrm{X}} - \Delta E_{\mathrm{A}}^{\mathrm{Pt}} + \Delta\Delta E_{\mathrm{A}}^{\mathrm{X},field} \tag{5.2}$$

Where $\Delta E_{\mathrm{A}}^{\mathrm{X}}$ is the adsorption energy of A on X calculated in this work, $\Delta G_{\mathrm{A}}^{\mathrm{Pt}}$ is the free energy of X at 0.9 V reported previously and $\Delta E_{\mathrm{A}}^{\mathrm{X},field}$ is the shift in adsorption energy caused by the change in the electric field in the double layer region. $\Delta E_{\mathrm{A}}^{\mathrm{X},field}$ is shown in Table 5.1.

	$W_{\mathrm{Pt_3X}}$	$-\Delta W_{\mathrm{Pt_3X}}$	$\Delta G_{\mathrm{O}*}^{field}$	$\Delta G_{\mathrm{OH}*}^{field}$	$\Delta G_{\mathrm{OOH}*}^{field}$
Pt_3Y (50 % Y)	5.16	0.37	0.00	-0.03	-0.01
Pt_3Sc (50 % Sc)	5.10	0.43	0.00	-0.04	-0.01
Pt_3Y (25 % Y)	5.42	0.11	0.00	-0.01	0.00
Pt_3Sc (25 % Sc)	5.39	0.14	0.00	-0.01	0.00
Pt_3Y (0 % Y)	5.58	-0.05	0.00	0.00	0.00
Pt_3Sc (0 % Sc)	5.62	-0.09	0.00	0.01	0.00

Table 5.1: Work function on Pt_3Y and Pt_3Sc and the resulting corrections to adsorption energies at 0.9 V and pH=0 based on Ref. [92] assuming a uniform electric field across a 3 Å thick dipole layer. $\Delta W_{\mathrm{Pt_3X}} = W_{\mathrm{Pt_3X}} - W_{\mathrm{Pt}}$. The surfaces are terminated by a 1 ML thick Pt-skin and the concentration of X in the second layer is shown in parenthesis. The rest of the slab is stoichiometric in each layer. The work function on Pt(111) is calculated to be 5.53 eV. All numbers are in eV.

According to the scaling relations for the ORR intermediates, the OH and the OOH formation energies will ultimately limit the activity of the catalyst [11, 14]. Accurate evaluation of these free energies is therefore important and requires incorporation of the adsorbates into a water layer to stabilize these by forming hydrogen bonds with the water environment. We have used a $(\sqrt{12} \times \sqrt{12})R30°$ surface unit cell to calculate the stability of OH* and OOH* as the (2×2) symmetry of the underlying

ordered bulk alloy and the $(\sqrt{3}\times\sqrt{3})R30°$ symmetry of a water layer may be treated in this unit cell. The formation energy of OH and OOH is calculated according to (3.47) and (3.49) respectively. Water layers on Pt(111) with H_2O(d) and H_2O(u) have almost the same energy. We have modeled the water layer on Pt_3X and Pt with a H_2O(p)-H_2O(u) layer.

The considered structures are ultimately constructed based on "intelligent guess work". In general, the most stable OOH structures are formed by replacing OH or H_2O by OOH in a stable OH+H_2O structure. This ensures some "self-consistency" in the considered intermediates, c.f. chapter 3. This means that the OH coverage in the water layer is realistic compared to the potential. The free energy of OOH in the OOH/H_2O/OH overlayer is calculated using the average energy of OH in the most stable OH structure, c.f. equation (3.49). This is done to minimize the risk of erroneously finding a very "stable" OOH structure based on an unstable OH reference energy. It is naturally important that the OOH energy calculated by (3.49) reflects the OOH binding energy, including interactions with the surface and the nearby adsorbates.

5.2.2 Results

In the following paragraphs we present the structures identified as the most probable intermediates in the ORR. The free energies of the intermediates are summarized in Table 5.3. For notational simplicity we will refer to the changes in free energy going from O_2 to the OOH intermediate and from O or OH to H_2O as the reaction barriers, even though there may be additional barriers for the reaction as discussed above.

Pt(111)

The energy of OH is based on the calculation of OH/H_2O(p) and H_2O(u)/H_2O(p) $(\sqrt{3}\times\sqrt{3})R30°$ super structures. If we allow for symmetry breaking by proton disorder in a $(\sqrt{3}\times\sqrt{3})R30°$ cell we only find up to 0.017 eV stabilization per OH using the same H_2O(u)/H_2O(p) $(\sqrt{3}\times\sqrt{3})R30°$ reference for water. Symmetry breakings in other unit cells may give further stabilization of OH [74], and to conform with previous calculations, we use the OH formation energy calculated with the OH/H_2O(p)-$(\sqrt{3}\times\sqrt{3})R30°$ structure.

In Ref. [92] the energy of OOH was calculated in a $(\sqrt{3}\times\sqrt{3})R30°$ OOH/H2O superstructure. In this work we have included OOH in a $(\sqrt{12}\times\sqrt{12})R30°$ OH/H2O superstructure with 1/3 ML OH coverage. This is a more realistic environment for OOH, as we expect the OH coverage to be high and the OOH coverage to be low at 0.9 V *vs.* SHE. OOH is 0.10 eV more stable in the $(\sqrt{12}\times\sqrt{12})R30°$ OH/H_2O structure than in the $(\sqrt{3}\times\sqrt{3})R30°$ OOH/H2O structure, and this further stabilization has been included in the free energy of OOH. If the formation energy of OOH in a pure waterlayer is calculated in a $(\sqrt{12}\times\sqrt{12})R30°$ supercell, a similar stabilization of 0.08 eV relative to the $(\sqrt{3}\times\sqrt{3})R30°$ OOH/H_2O super structure is obtained. The discussed OOH structures are shown in appendix C along with a table of their formation energies. Since the free energy of OOH with co-adsorbed H_2O and OH is calculated in the $(\sqrt{12}\times\sqrt{12})R30°$ supercell for the Pt_3X alloys, it would be unreasonable to directly compare the free energy of OOH on Pt_3X with the free energy of OOH on Pt in a $(\sqrt{3}\times\sqrt{3})R30°$ cell.

It is found that the largest increase in free energy for ORR at this potential is 0.15 eV, due to the reduction of OH to water.

Pt_3Y with 50 % Y in the 2nd layer

The average energy of adsorbed OH* is found to have a minimum at $\theta_{OH} = 1/6$ ML OH*. At this coverage $\Delta G_{OH*} = 0.0$ eV at 0.9 V *vs.* RHE. The free energy of OOH is calculated by including OOH in an OH/H_2O layer with 1/6 ML OH*. The free energy of O* is calculated in a (2×2) surface unit cell. A schematic model of these

intermediates is shown on Figure 5.2. We find that for this surface, activating O_2 and forming OOH is uphill in free energy by 0.10 eV, whereas reducing O to water is uphill by 0.05 eV.

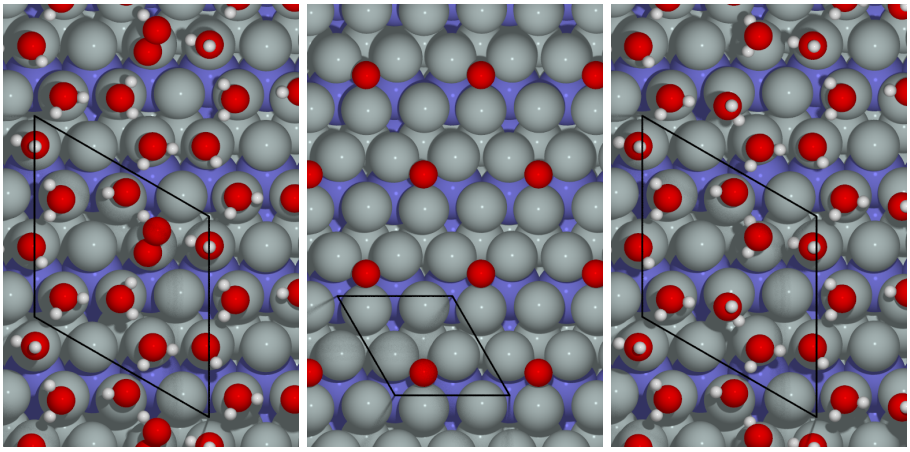

(a) (b) (c)

Figure 5.2: ORR intermediates on Pt_3Y with 50% Y in the 2nd layer. OH and OOH adsorb on Pt sites which have at least one Y atom as neighbor in the subsurface layer. Pt is gray, Y is blue, O is red and H is white.

Pt_3Sc with 50 % Sc in the 2nd layer

The average OH adsorption energy is strongest at 1/4 ML OH* coverage, but is only 0.01 eV weaker at 1/6 and 1/3 ML OH* coverage, see Table 5.2. At $\theta_{OH} = 1/4$ ML the average free energy of OH* is 0.00 eV. At 1/4 ML OH* coverage, OOH* appears to be rather unstable relative to on Pt, c.f. Table 5.2. This may be because the most stable OOH* structure has not been found for this OH* coverage. At 1/6 ML OH* coverage, which is also possible based on the energetics, OOH* formation is comparable to what has previously been found for Pt in Ref. [92] and for Pt_3Y with 50 % Y in the second layer. The way the OOH formation energy is calculated through equation (3.49) makes the formation energy somewhat uncertain as it is also sensitive to the OH formation energy.

For the purpose of comparing the potential energy surface for ORR on Pt_3Y and Pt_3Sc, the difference in OOH* formation energy may be better estimated by directly comparing formation energies without water and OH*. For the potential energy surface, we therefore calculate the free energy of OOH by shifting the free energy of OOH* on Pt_3Y, as calculated above in an $OOH/OH/H_2O$ layer with 1/6 ML OH, by the difference between the adsorption energies of OOH* on Pt_3Y and Pt_3Sc calculated in a (2×2) surface unit cell. In the (2×2) surface cell, OOH* is 0.02 eV more stable on Pt_3Y than on Pt_3Sc. however, from calculations including water and OH, OOH is 0.02 eV more stable on Pt_3Sc than on Pt_3Y with 50 % Y or Sc in the second layer.

Neglecting changes in the electric field due to changes in the work function (see Table 5.1), OH is about 0.18 eV less stable on Pt_3Y and Pt_3Sc with 50 % Y/Sc in the second layer than on Pt. The formation energy of OOH shows some fluctuations as a function of OH coverage. However, at least at some coverages it is possible to find OOH formation energies within 0.02 eV of what has previously been found on Pt(111)[92]. From this approximation, we find that forming OOH is uphill in free energy by 0.12 eV, while reducing O and OH to water is downhill in free energy.

θ_{OH}	0	1/12	1/6	1/4	1/3
$\delta E_{OH*}^{Pt_3Y}$	-	0.21	0.18	0.19	0.20
$\delta E_{OOH*}^{Pt_3Y}$	0.07	0.12	0.00	0.04	0.42
$\delta E_{OH*}^{Pt_3Sc}$	-	0.25	0.19	0.18	0.20
$\delta E_{OOH*}^{Pt_3Sc}$	0.10	0.06	-0.02	0.15	-

Table 5.2: OH and OOH formation energies in eV relative to Pt[92] as a function of OH coverage for Pt_3Y and Pt_3Sc with 50 % Y/Sc in the second layer. $\delta E_{ads}^{Pt_3X} = \Delta E_{ads}^{Pt_3X} - \Delta E_{ads}^{Pt}$, where ΔE_{ads}^{Pt} is obtained from $(\sqrt{3} \times \sqrt{3})R30°$ superstructures. $\Delta E_{OOH*}^{Pt_3X}$ is calculated using the most stable reference for ΔE_{OH*} in equation (3.49). The table is based on 25 OH/H_2O and 25 $OOH/OH/H_2O$ super structures for Pt_3Y and 20 OH/H_2O and 9 $OOH/OH/H_2O$ super structures for Pt_3Sc.

Pt_3X with 25 % X in the 2nd layer

The OH free energy is calculated from an OH/H2O layer with 1/3 ML OH* where the $(\sqrt{3} \times \sqrt{3})R30°$ symmetry of the adsorbate structure has been broken. The OOH* free energy is calculated from an OH/H_2O super structure with 1/3 ML OH. The free energy of O* is calculated in a (2×2) surface unit cell. A schematic model of these intermediates on Pt_3Y are shown in Figure 5.3. For Pt_3Sc, forming OOH* is uphill

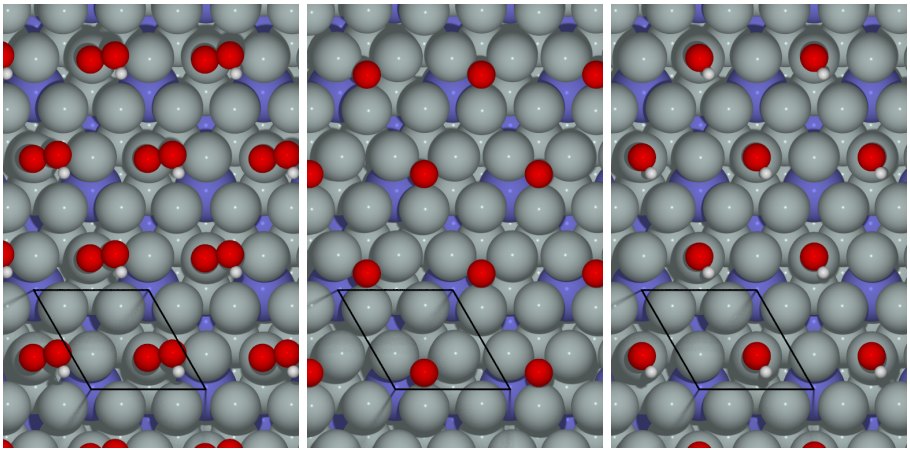

(a) (b) (c)

Figure 5.3: The most stable ORR intermediates on reduced Pt_3Y with 25 % Y in the 2nd layer. OH and OOH adsorb on Pt sites, which only have Pt neighbors in the 2nd layer. The free energy of OOH and OH has been calculated including water in a $(\sqrt{12} \times \sqrt{12})R30°$ unit cell, but is shown here without water in a (2×2) unit cell for clarity.

by 0.10 eV and has the highest barrier, as formation of water from OH* is uphill by 0.04 eV. From the free energy diagram for Pt_3Y with 25 % Y in the second layer it is seen that oxygen is bound by 0.34 eV at 0.9 V, so it is likely that many of these sites are blocked by O* at this potential. Oxygen reduction could then proceed on the remaining free sites, and we will estimate the free energy of OOR intermediates formed at a surface with 1/4 ML O* as a spectator species.

Pt_3Y with 25 % Y in the 2nd layer and 1/4 ML co-adsorbed O

The free energy of OOH is calculated from the shift in OOH binding energy on Pt_3Y due to 1/4 ML co-adsorbed O relative to OOH in an OOH/H_2O layer on Pt_3Y with 25 % Y in the second layer. The formation energy of O is calculated in a (2×2) surface

unit cell. The free energy of OH is calculated by shifting the binding energy relative to Pt in the (2×2) surface unit cell. This will most likely overestimate the free energy of OH, as the stabilization by hydrogen bonding could be over estimated. The OOH formation energy should be better estimated, as there is little interaction between a full water layer and the surface. Interestingly the estimated barrier for OOH formation is 0.06 eV, while the barrier for removal of OH is 0.09 eV. A schematic model of these intermediates adsorbed on Pt3Y is shown on Figure 5.4.

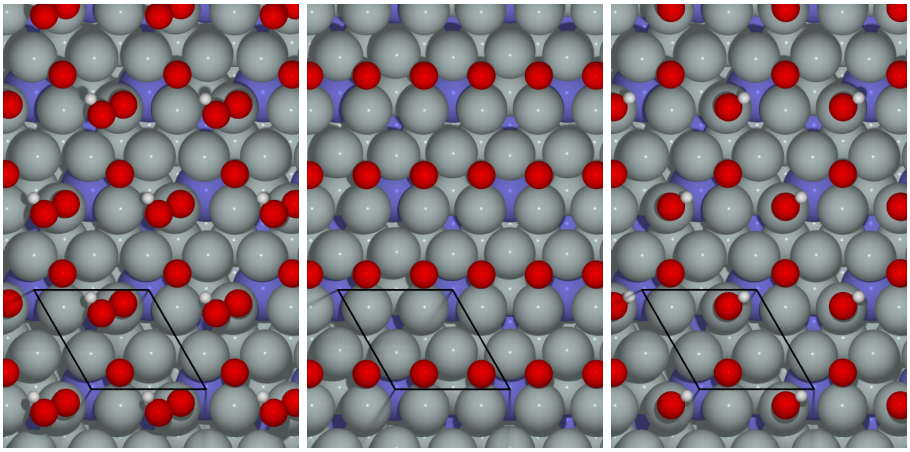

(a) (b) (c)

Figure 5.4: ORR intermediates on Pt3Y with 25 % Y in the 2nd layer, in the case where the most reactive sites on the surface have been blocked by oxygen. The OOH and the OH intermediates, which determine the ORR volcano, then adsorb on Pt sites with a Y neighbor in the 2nd layer.

5.2.3 Summary

We have calculated the free energy of the OER intermediates at 0.9 V including water and corrections due to the electric field. The free energies of the intermediates are summarized in Figure 5.3.

Adsorbate	ΔG_{O_2}	ΔG_{OOH*}	ΔG_{O*}	ΔG_{OH*}	ΔG_1	ΔG_2 (max)
Pt [92]	1.32	1.43	-0.14	-0.15	0.11	**0.15**
Pt, this work	1.32	1.33	-0.14	-0.15	0.01	**0.15**
Pt_3Y (50 % Y)	1.32	1.42	-0.05	0.00	**0.10**	0.05
Pt_3Sc (50 % Sc)	1.32	1.44	0.19	0.00	**0.12**	0.00
Pt_3Y (25 % Y)	1.32	1.30	-0.34	-0.14	-0.02	**0.34**
Pt_3Y, (25 % Y, 1/4 ML O)	1.32	1.38	0.03	-0.09	0.06	**0.09**
Pt_3Sc (25 % Sc)	1.32	1.42	-0.01	-0.04	**0.10**	0.04

Table 5.3: The free energy of ORR intermediates in eV calculated at 0.9 V as described in the text. The largest reaction barriers ΔG_1 and ΔG_2 for activating O_2 and reducing O or OH are also shown.

At 0.9 V the largest increase in free energy on Pt(111) is related to reduction of OH to H_2O. For Pt_3Y with 50 % Y in the second layer and Pt_3Sc with 25 % or 50 % Sc in the second layer, we find that activation of O_2 and the formation of OOH* leads to the largest increase in free energy, while removal of OH* is facile.

On Pt_3Y with 25 % Y in the second layer reduction of O to H_2O is uphill by 0.34 eV at 0.9 V. This means that most of these sites will be blocked at these conditions.

If the OER intermediates are formed at a surface where all these sites are blocked by oxygen, our calculations suggest that reduction of OH to H_2O has the largest ΔG. Figure 5.5 shows the free energy diagram constructed from the ORR intermediates

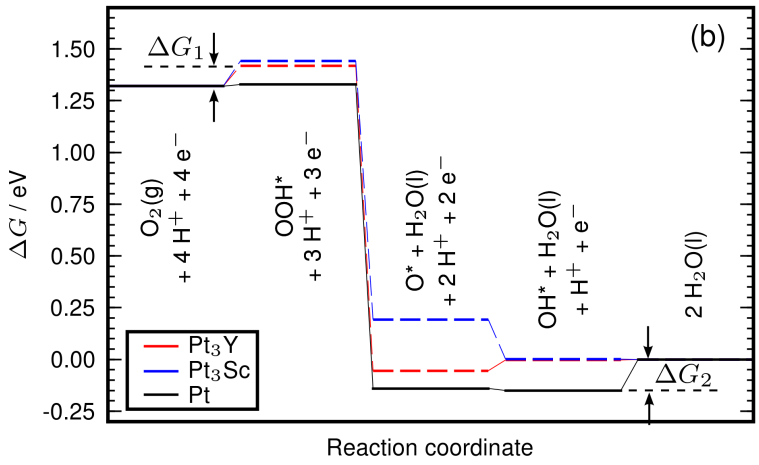

Figure 5.5: Free energy diagram for the Oxygen Reduction Reaction on Pt, Pt_3Sc and Pt_3Y. Calculated based on alloys with 50 % Sc or Y in the second layer.

on Pt, Pt_3Y with 50 % Y in the second layer and Pt3Sc with 50 % Sc in the second layer based on data from Table 5.3. It is seen from the figure that OER may proceed with lower barriers on these Pt_3Y and Pt_3Sc surfaces than on Pt. Whether formation of OOH* or formation of H_2O from O* of OH* has the largest ΔG depends on the subsurface concentration of Y and Sc. However, all the considered Pt_3Y and Pt_3Sc surfaces have sites that are more active than Pt(111).

5.3 Measured ORR Activity

To evaluate the activity of the suggested Pt_3Y and Pt_3Sc alloys polycrystalline Pt_3Sc, Pt_3Y and Pt was gently sputter cleaned by Ar in UHV before being transferred to an electrochemical cell for measurement of the activity for ORR.[2] Figure 5.6 (a) shows the anodic sweep of cyclic voltammograms for Pt_3Sc, Pt_3Y and Pt in a 0.1 M $HClO_4$ solution saturated by O_2 at room temperature. It is seen that the activity of polycrystalline Pt_3Y and Pt_3Sc is higher than the activity of polycrystalline Pt. At low overpotentials near 1 V *vs.* RHE the current increase exponentially with increasing overpotential, which indicate a kinetically controlled rate. At high overpotentials, e.g. at 0.6 V *vs.* RHE, the rate is diffusion limited. Inbetween there is a region of mixed diffusion and kinetic rate control. One measure of the activity is the so-called half wave potential, $U_{\frac{1}{2}}$, where the current reaches half of the diffusion limited current. For Pt_3Sc, $U_{\frac{1}{2}}$ is 20 meV larger than on Pt, while Pt_3Y has a half wave potential that is 60 meV larger than on Pt. Figure 5.6 (b) shows the activity enhancement of Pt_3Sc and Pt_3Y relative to Pt defined as j_k/j_k^{Pt}, where j_k is the kinetically limited current corrected for mass transport limitations. At 0.9, Pt_3Sc is 50 % more active than Pt, while Pt_3Y is 6 times more active than Pt. To the best of our knowledge Pt_3Y shows the best ORR activity at these conditions for any polycrystaline metal surface. The activity improvement over Pt is nearly as good as for single crystaline $Pt_3Ni(111)$[110], but better than the activity improvement for polycrystaline Pt_3Ni.[118]

Figure 5.7 shows the improvment in activity over Pt for a range of Pt based catalysts, including the newly discovered Pt_3Y and Pt_3Sc catalysts as a function of the oxygen binding energy relative to Pt. The dashed lines mark the volcano predicted by the model [11, 14] and describe the activity reasonably well given the accuracy of DFT and that the experimental values are obtained from both polycrystaline and single crystal experiments.

5.4 Alloy Subsurface Structure

It is interesting that the Pt_3Sc and Pt_3Y alloys show higher activity than Pt despite having a larger lattice constant than Pt. Alloys formed from Pt and a late 3d transition metal have smaller lattice constant than Pt, and this has been used as an explanation for their increased activity [107]. The compressed lattice means that these alloys can rely on strain to weaken the adsorption energy of oxygen species relative to Pt[121], which is probably the case for dealloyed catalysts. In this section, we discuss effects of subsurface concentration of the alloying element X.

Figure 5.8 shows the oxygen binding energy at the most stable adsorption site for a number of Pt_3X alloys as a function of the concentration of the alloying element X in the second layer. The oxygen binding energy for Pt, 2.3 % compressed Pt and 3.5 % expanded Pt is also shown. The latter two correspond to the lattice constants calculated for bulk Pt_3Ni and Pt_3Y alloys respectively and may be used as models for thick Pt skins formed on these surfaces if we neglect lateral surface relaxations. In general, oxygen binding weakens as the concentration of X in the second layer increases. Evidently, Pt that is under 2.3% compressive strain has an O binding energy in the right domain. Moreover, the oxygen binding energy on alloys of Co, Fe and Ni do not depend substantially on the concentration of X in the second layer to achieve weaker binding. On the other hand, O adsorption on alloys of Sc, Y and Ti appears to depend strongly on the concentration of X in the second layer to achieve weaker binding. The 3.5 % expanded Pt slab binds oxygen too strongly. Consequently, the subsurface concentration of the alloying element should be more important for Pt_3Y and Pt_3Sc than for Pt alloys of the late 3d metals. Therefore, elucidation of the subsurface structure could improve our understanding of the origin of the catalytic

[2] All experiments have been performed by I. E. L. Stephens, A. S. Bondarenko, T. P. Johansson and I. Chorkendorff. Refer to paper P2 for further details.

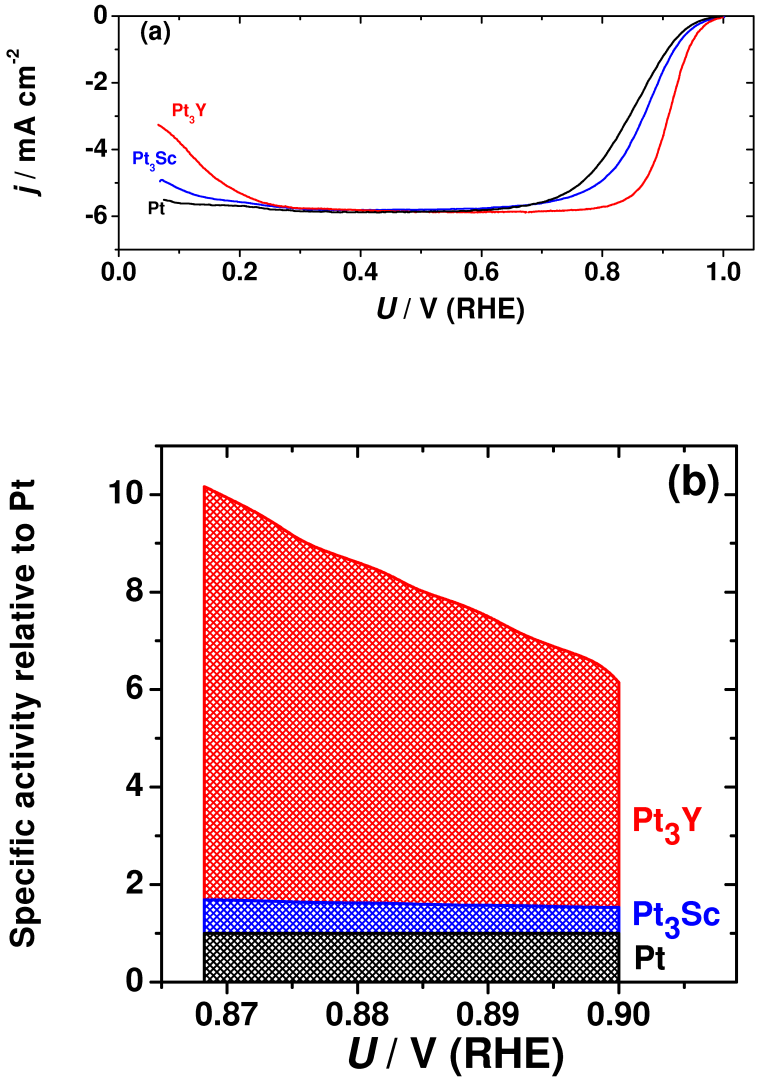

Figure 5.6: (a) Anodic sweeps of cyclic voltammograms of Pt, Pt_3Sc and Pt_3Y in 0.1 M $HClO_4$ saturated by O_2. (b) Activity enhancement relative to Pt, (j_k/j_k^{Pt}). See text or Paper P2 for details on the experiments. Figures made by A. S. Bondarenko and I. E. L. Stephens.

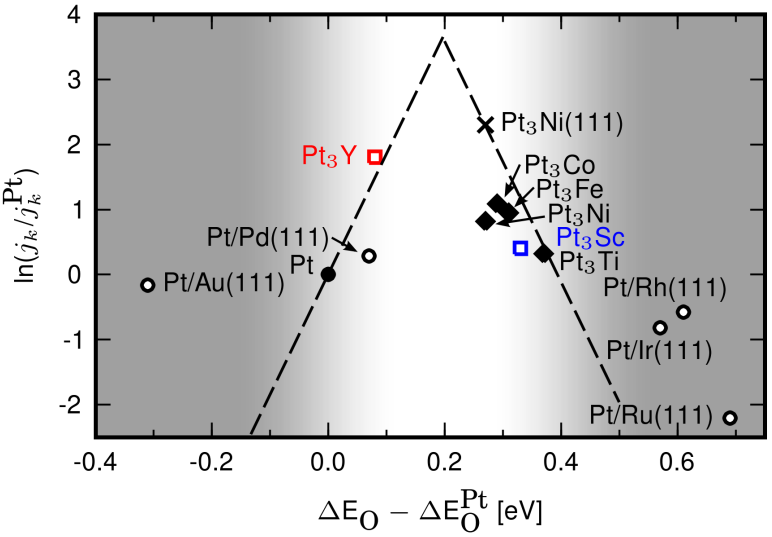

Figure 5.7: Volcano plot of the activity for the Oxygen Reduction Reaction based on calculations on Pt_3Sc and Pt_3Y with 50 % Sc/Y in the second layer. The circles mark experimental data based on Pt monolayers on single crystals [119]. The diamonds mark polycrystaline alloys annealed in UHV before immersion in the electrochemical cell[93]. The cross is single crystal $Pt_3Ni(111)$ annealed in UHV before immersion [110]. The squares are data points for Pt_3Y and Pt_3Sc based on experiments by I. Chorkendorff and co-workers. All data points except those for Pt_3Y and Pt_3Sc are adapted from Ref. [120].

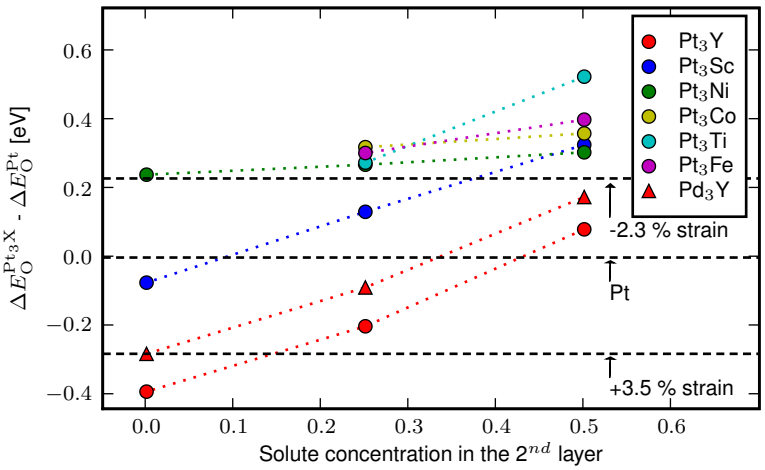

Figure 5.8: Oxygen binding energy relative to Pt on Pt_3X and Pd_3X alloys with a Pt or Pd skin as a function of the subsurface concentration of X in the second layer. The horizontal dashed lines mark the oxygen binding energy for 2.3 % compressed Pt, Pt, and 3.5 % expanded Pt. The O binding energy depends considereably on the subsurface X concentration for alloys of Sc, Y and Ti.

activity of Pt and Pd alloys with early transition metals.

However, not only is it difficult to determine the subsurface structure experimentally, but also theoretically. At operating conditions dissolution of the base metal or oxide formation is thermodynamically favored, so the catalyst is only kinetically stabilized by the Pt skin formed at the surface. The subsurface structure may be determined by the steady state kinetics of dealloying. Both the long term stability

Conc.	Pt_3Y	Pt_3Sc	Pt_3Ni	Pt_3Ti
50 %	-2.27	-1.24	0.36	-0.74
25 %	0.41	0.90	0.75	1.16

Table 5.4: The energy in eV required to move 1 X atom from the second layer to the first layer of a Pt_3X alloy with a 1 ML thick Pt skin for initial X concentrations of 50 % and 25 % in the second layer. For the early transition metals a 50 % concentration in the second layer is energetically unfavorable compared to having 25 % in the two topmost layers. The calculations are done in a (2×2) surface unit cell.

and activity are influenced by the thickness of the Pt skin required to stabilize the alloy against dissolution.

Stable long term activity of the Pt_3Y alloy seems to require that a 1 ML Pt skin be sufficient to kinetically stabilize the alloy [3]. Table 5.8 shows the change in energy when one X atom in the second layer is exchanged by 1 Pt atom in the first layer for some selected alloys in vacuum.[4]

In all cases, exchange from a surface with 25 % X is exothermic. However, there are most likely additional barriers for the exchange process. On the other hand, the final state and the transition state could be stabilized in the electrochemical environment. Alloys with 50 % X in the second layer are not stable relative to the formation of a bulk terminated alloy for Pt_3Y, Pt_3Sc and Pt_3Ti. This means that a surface structure with 25 % Y in the second layer is more likely than 50 % Y in the second layer. The increased activity relative to Pt could then be explained by the oxygen reduction taking place at the more active Pt sites with Y neighbors in the second layer as described above. The more reactive sites at the Pt_3Y surface could be blocked by oxygen. This interpretation agrees with the cyclic voltammogram for polycrystalline Pt_3Y in a N_2 saturated electrolyte. Here, water oxidation appears to start at a lower potential than on polycrystalline Pt, see Figure 5.9. It is of course also possible that

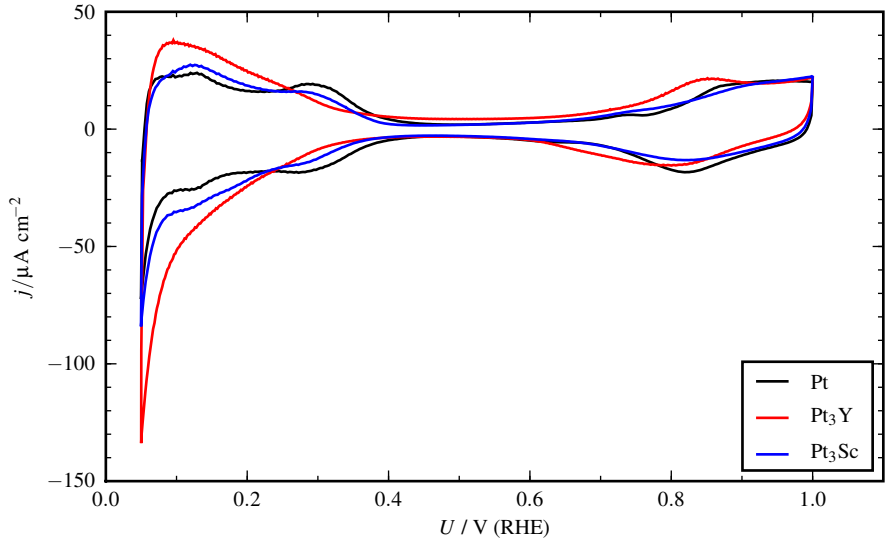

Figure 5.9: Cyclic voltammograms of Pt, Pt_3Y and Pt_3Sc in a N_2 saturated 0.1 M $HClO_4$ electrolyte. The scan rate is 20 mV/s and the temperature is 296 K ± 2 K. Measurements by A. S. Bondarenko and I. E. L. Stephens.

[3] Unless, of course, the high activity also is a property of a thick expanded Pt skin.
[4] Exchange energies at 50 % concentration has been calculated by Jeff Greeley.

the early water oxidation peak at Pt_3Y originates from processes at other facets than (111). To clarify this more experimental results would be needed, preferably on single crystals.

5.4.1 Trends in Adsorption Energies on Pt_3X Alloys

Figure 5.10 shows the correlations between the formation energy of (a) O and OH and (b) OH and OOH for adsorption on the most stable sites calculated in a (2×2) surface unit cell. In general, the OH adsorption energy increases with increasing O adsorption energy with a slope of 0.35 for the best fit. The mean absolute error from the fit is only 0.03 eV. This is rather small compared to the absolute value of the O and OH formation energies on Pt. Partly due to the fact that alloying only introduce minor shifts in the adsorption energies, the scattering around the fit looks quite large.

Part of the scattering is, however, related to the subsurface atomic structure of the alloy. Oxygen binds to hollow sites, whereas OH and OOH are found to adsorb on atop sites for the Pt terminated surfaces considered here. First, if we assume the adsorbate binding energy is controlled by the interaction with the local density of states projected onto the Pt atoms that bind to the adsorbates in a Newns-Anderson picture[122]. It is then clear that variations in the local density of states across the alloy surface may result in violations of the linear relations between O and OH adsorption energies on homogeneous surfaces[7]. This is because different Pt atoms bind oxygen constaining species with different strengths. In fact, O, OH and OOH adsorption energies varies appreciably across the surface.

The correlation between OH and OOH at the most stable sites in Figure 5.10b is excellent, with a slope of 0.97 close to the ideal 1 from scaling [7]. The mean absolute error from the fit is 0.02 eV. The good correlation may be explained by the fact that OH and OOH most often adsorb at the same Pt site, thus interacting with the same density of states. However, there are, still outliers, such as Pt_3Sc with 50 % Sc in the second layer where OH and OOH do not adsorb at the same site. This is also the case for Pt_3Y with 50 % Y in the second layer, where the adsorption energy of OH only varies 0.01 eV between sites while OOH varies 0.08 eV between top sites.

In Figure 5.10 we have marked the point corresponding to the most stable adsorption site for OH and OOH on Pt_3Y with 25 % Y in the second layer by Pt_3Y-25%Y. The adsorption energy on the other sites at this surface[5] is marked by Pt_3Y-25%Y*. We have marked the adsorption energy on this site when there is 25 % O coadsorbed on the surface by Pt_3Y-25%-Y(2×2)O. The OH and OOH adsorption energy on Pt_3Y with 25 % Y in the second layer and a (2×2)-O adsorbate structure is closer to the adsorption energies on Pt_3Y with 50 % in the second layer than to Pt_3Y without any O. This may be explained by the fact that for Pt_3Y-25%-Y(2×2)O and Pt_3Y-50%-Y the active site is atop a Pt atom with at least one Y neighbor in the second layer.

If we assume that effects of water are identical on all the considered surfaces and that the activity of a single site is uncorrelated to the activity of neighboring sites, the binding energies of OH and OOH shown in Figure 5.10, describe the activity of the most *reactive* site on Pt alloy surfaces for the majority of cases where OH and OOH are most stable on the same site. The activity of a site following the scaling relation of OH and OOH binding energies would have a ΔE around 0.1 eV positive for Pt. Surfaces that preferentially bind OOH stronger than OH relative to the linear relations are of course also of interest. We see that several Pt_3X surfaces such as Pt_3Y, Pt_3Co, Pt_3Ni, and 2.3 % compressed Pt[6] show OH and OOH binding energies around 0.1 eV weaker than Pt.

[5] They are all equivalent due to symmetry.

[6] This is the calculated compression in Pt_3Ni relative to Pt.

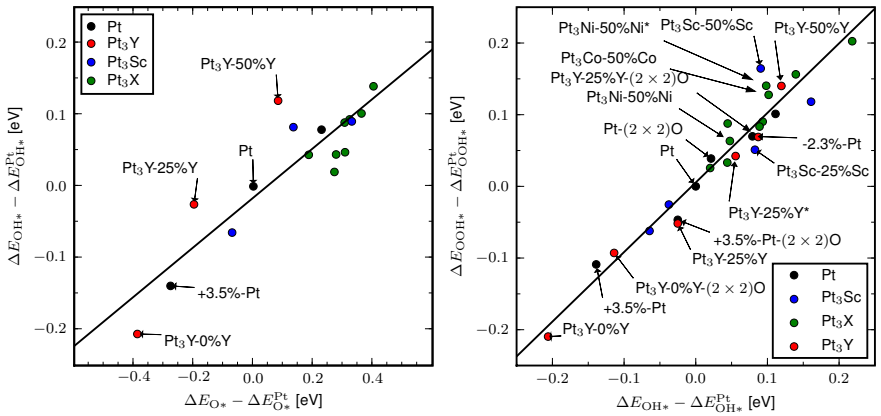

(a) (b)

Figure 5.10: Left: Correlation between the most stable O and OH binding energies for Pt_3X alloys and Pt surfaces. A least squares fit gives $\Delta E_{OH*} - \Delta E^{Pt}_{OH*} = 0.35(\Delta E_{O*} - \Delta E^{Pt}_{O*}) - 0.02$eV with a mean absolute error of 0.031 eV. Right: Correlation between the most stable OH and OOH binding energies on Pt_3X alloys. A few formation energies for OH and OOH at sites that are not the most stable ones have also been included. These have been marked by a *. A least squares fit gives $\Delta E_{OOH*} - \Delta E^{Pt}_{OOH*} = 0.97(\Delta E_{OH*} - \Delta E^{Pt}_{OH*})$ and the mean absolute error is 0.019 eV. Pt_3X refers Pt_3Co, Pt_3Fe, Pt_3Ni, and Pt_3Ti.

5.5 Summary

In this chapter we have presented the results of a computational screening study for active ORR catalyst based on the theoretical model developed in Ref. [11], c.f. chapter 4. The study focused on Pt_3X and Pd_3Y alloys which are known experimentally to form a passivating Pt or Pd skin. The activity of the previously known allous could be explained using our model [93]. More significantly, a new class of alloys from the group with Sc and Y was also presented as candidates with high activity.

The screening study focuses on the adsorption energy of oxygen, whereas the process with the highest increase in free energy at high potentials is the formation of OOH or the removal of OH, for catalysts that are close to Pt. Additional calculations involving solvated OH and OOH were therefore performed on Pt_3Sc and Pt_3Y in order to establish possible potential energy surfaces on these catalysts. Depending on the concentration of X in the second layer, different potential energy surfaces are possible.

Subsequent experiments on polycrystalline electrodes have shown that Pt_3Sc and Pt_3Y are indeed more active than Pt. Pt_3Y was even found to be 6-10 times more active than Pt in the range 0.9-0.87 V. The ability to predict the outcome of new experiments, here the activity of the new Pt_3X alloys, is also very strong evidence supporting the underlying model.

The effects of subsurface concentration of the alloying element on O, OH and OOH adsorption energies in a (2×2) surface unit cell without water have also been discussed.

Chapter 6

Monte Carlo Simulations of OH and O adsorption

Oxygen co-adsorbed with water has been studied on numerous materials [123, 124] and is of obvious interest, for the corrosion of metals[42]. In combination with H_2 adsorption, O_2 and H_2O on transition metal surfaces are also of interest for the hydrogen oxidation reaction and the oxygen reduction reaction in fuel cells. Complex spatio-temporal dynamics with propagating reaction fronts have been reported for the hydrogen oxidation on Pt(111) in UHV at low temperature[125, 126]. In spite of this, kinetic mean field equations have had success in describing the oxygen reduction reaction on platinum and Pt_3Ni [13, 14] at room temperature. The microscopic picture provided by a mean field model need, however, not be correct even though it fits with experiment. It is desireable to check the predictions of mean field models against predictions from Monte Carlo simulations[3].

Previously, cyclic voltammetry of Pt(111) in the hydrogen adsorption region has been treated by mean field and Monte Carlo simulations using adsorption energies and interaction energies based on DFT calculations.[127] No significant difference was observed between the mean field approximation and the Monte Carlo simulations, presumably because of a very weak nearest neighbor repulsion [3]. Mean field simulations of the OH adsorption region have also been performed based on DFT calculated adsorption energies [14].

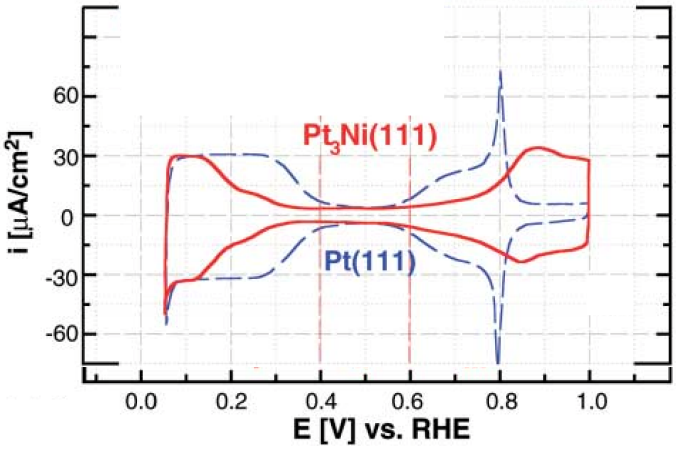

Figure 6.1: Experimental CV on Pt(111) and $Pt_3Ni(111)$ in N_2 saturated 0.1 M $HClO_4$, adapted from Stamenkovic *et al.* [110].

Monte Carlo simulations of CV experiments, where the adsorption energies and interaction parameters are taken as parameters, have been performed in a series of

papers by Koper *et al.* [128, 129, 130, 131, 132]. Of special relevance to the OH adsorption region is the general observation, that the current spike around 0.8 V *vs.* RHE, c.f. Figure 6.1, may be caused by an order disorder transition in the adsorbate layer.[128] Such a transition cannot be correctly captured by a mean field model. Another desirable feature of Monte Carlo models is that they offer a more accurate description of reactions on heterogeneous surfaces with interacting adsorbates.

In this chapter, we take initial steps towards Monte Carlo simulations of OH and O adsorption based on first principles calculations. The adsorption isotherms show reasonable agreement with integrated CV currents.

6.1 Lattice-Gas Model of the Metal-Liquid Interface

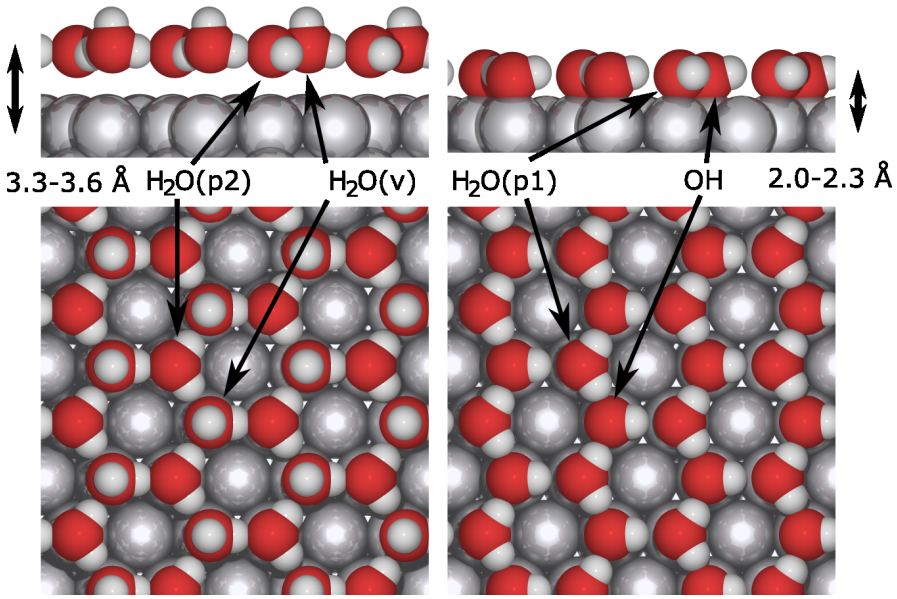

Figure 6.2: Hydrogen ordered $(\sqrt{3}\times\sqrt{3})R30°$ phases of H_2O-H_2O (left) and H_2O-OH (right) on Pt(111). The different types of water and OH have been labeled.

The water uptake and the kinetics of H_2O desorption from an O precovered Pt(111) surface habe been modeled by Karlberg *et al.* using a lattice gas Hamiltonian with angular dependent interaction energies [133, 134]. Inspired by their work, we use the different kinds of water and OH present in the water bilayer and the OH-H_2O $(\sqrt{3}\times\sqrt{3})R30°$ layer in the lattice gas Hamiltonian. We therefore have the the adsorbate states shown in Figure 6.2: OH adsorbed at a top site anf H_2O lying flat on the surface in the OH-H_2O layer. We denote the latter by H_2O(p1). H_2O lying parallel to the surface in the water bilayer is denoted by H_2O(p2). Water in the water bilayer with a hydrogen atom pointing away from the bilayer plane is denoted by H_2O(v). The focus of our study is on the cathode of the fuel cells. Thus at positive potentials we expect the electric field to favor water with the hydrogen pointing away from the electrode surface [54]. In addition, we also consider O adsorbed in fcc hollow sites. The main difference between the two water molecules lying parallel to the surface is that H_2O(p1) has a bond distance to Pt comparable to the H_2O monomer, whereas H_2O(p2) is further away from the surface, and hardly adsorbed at the surface. We note that the distances reported here are similar to those observed in MD simulations described previously [79, 80, 81].

6.2 Method

6.2.1 Hamiltonian

Interactions are included through a lattice Hamiltonian where water and OH are adsorbed on atop sites and O in fcc hollow sites on a hexagonal lattice

$$H = \sum_i (E^X_{ads} + E^X_{ato}) c^X_i + \frac{1}{2} \sum_{\langle i,j \rangle} V^{XY}_{ij}(\theta_1, \theta_2) c^X_i(\theta_1) c^Y_j(\theta_2) + \frac{1}{2} \sum_{(i,j)} V^{OX} c^O_i c^X_j \, . \tag{6.1}$$

Here E^X_{ads} and E^X_{ato} are the adsorption energy and the atomization energy of the species X respectively, and c^X_i is the occupation number of X at site i. This is 1 if an adsorbate X is at site i and 0 otherwise. $V^{XY}(\theta_1, \theta_2)$ is the interaction energy between adsorbates X and Y at sites i and j with adsorbate angles θ_1 and θ_2 as defined in (6.7). The sum $\langle i, j \rangle$ runs over all pairs of nearest neighbor top sites. Interactions with O adsorbates are included in the last sum, where (i, j) includes up to next nearest neighbor sites.

Karlberg *et al.* showed that second nearest neighbor interactions between OH-H_2O and OH-OH are less than 2 % of the nearest neighor interactions on Pt(111)[71]. The zero-point energy depends weakly on the configuration of water and OH[133] and has not been included in the interaction energies.

6.2.2 Surface Processes

We will only attempt to model the potential dependent equilibrium coverage of adsorbates. Technically, however, the surface processes are simulated using a combination of Kinetic Monte Carlo (KMC) and Metropolis Monte Carlo (MMC) methodologies. [1] We treat the electron transfer steps of the water discharge reaction kinetically

$$\mathrm{H_2O}* \underset{k_1^-}{\overset{k_1^+}{\rightleftharpoons}} \mathrm{OH}* + \mathrm{H^+(aq)} + e^-, \tag{6.2}$$

$$\mathrm{OH}* \underset{k_2^-}{\overset{k_2^+}{\rightleftharpoons}} \mathrm{O}* + \mathrm{H^+(aq)} + e^-. \tag{6.3}$$

At each potential of interest we find the dynamical equilibrium at the surface set up by (6.2) and (6.3). Between each kinetic step the surface is equilibrated by MMC. The MMC calculations use an annealing procedure starting from 50000 K and decrease the temperature in steps of 500 K until the final temperature of 300 K is reached. The simulations are done on a 50×50 hexagonal lattice with non-periodic boundary conditions. It has been checked that the results are converged with respect to the lattice size. The simulations are started from an equilibrated H_2O(p2)-H_2O(v) strcuture with a total coverage of 0.3 ML. The potential is then increased in steps of 0.05 V, where the adsorbate coverages are converged at each potential in a cycle of KMC steps and MMC runs. We treat the following processes in equilibrium

- Proton transfer of adsorbed species

$$\mathrm{H_2O(p1)}* + \mathrm{OH}* \rightarrow \mathrm{OH}* + \mathrm{H_2O(p1)}* \tag{6.4a}$$

$$\mathrm{H_2O(p1)}* + \mathrm{O}* \rightarrow 2\mathrm{OH}* \tag{6.4b}$$

- Diffusion and rotation of H_2O(p1), H_2O(p2)and OH
- O diffusion between adjacent hollow sites

[1] All Monte Carlo Simulations have been done by V. Viswanathan based on DFT calculated interaction energies and reversible potentials calculated by the author.

- Inter-conversion of H_2O(p2) and H_2O(p1)

Water diffusion is, in general, fast even at very low temperatures ($T \approx 25$K) [123]. Water is believed to diffuse easily along the close packed directions [75]. Michaelides *et al.* calculated the barrier for OH diffusion along the closepacked rows of Pt(111) is 0.1 eV and that H diffusion in the H_2O-OH phase is very fast ($E_a < 0.01$ eV) [75]. He also found that the barrier for the rotation of a water monomer on Ru(0001) is 0.02 eV[135]. We could expect a similar barrier on Pt(111).

The separation in kinetic and equilibrium steps is motivated by the fact that the chemical equilibrium steps typically are much faster than the electrochemical charge transfer reactions. In the present case, the kinetic code is "abused" to establish dynamical equilibrium at the surface at each potential of interest. However, if the separation into equilibrium processes and kinetic processes is accurate, real time propagation may be performed. We have used this methodology to simulate H_2O or D_2O desorption from O-precovered Ru(0001) and Au(111). The results are shown in appendix E. The desorption peaks show reasonable agreement with experiments.

Reversible Potentials

The rates in (6.4a) and (6.4b) are calculated using the CICV method and taken from Rai *et al.* [136]. The activation energy varies linearly with potential in the potential range of interest. As we are only interested in the surface coverage at dynamical equilibrium, we do not expect the results to depend appreciably on the specific method used for calculating the potential dependence of the rates. The ratios of the rates calculated from CICV are shifted to give the same equilibrium potentials as the thermodynamic method described in chapters 3 and 5 for the following phase transitions between ordered phases:

$$(\sqrt{3}\times\sqrt{3}) - H_2O(v)/H_2O(p2) \rightleftarrows (\sqrt{3}\times\sqrt{3}) - OH*/H_2O(p1) + H^+(aq) + e^-, \tag{6.5}$$

$$(\sqrt{3}\times\sqrt{3}) - OH*/H_2O(p1) \rightleftarrows (2\times 2) - O* + H_2O(l) + H^+(aq) + e^-, \tag{6.6}$$

The reversible potentials from the thermodynamic method is calculated relative to the adsorption energies on Pt(111) by Karlberg *et al.* [92]. The correction is similar to that used by Rai *et al.* [136], and is done because CICV does not properly include the stabilization of the final state and initial state due to water. It therefore gives reversible potentials that are much higher than the ones obtained from DFT calculations of the stability.

The formation of OH and O at the surface is primarily determined by the reversible potentials. However, the interaction data in the Monte Carlo simulations accounts for defect formation in the ordered (2×2)-O and$(\sqrt{3}\times\sqrt{3})R30°$-$OH*/H_2O$(p1) adsorbate phase. Further, the interaction potentials could, in principle, allow the formation of other structures than the mentioned ordered structures.

6.2.3 Interaction Parameters

We define the interaction potential $V_{X,Y}(\theta_1, \theta_2)$ as:

$$V(\theta_1, \theta_2) = E_{X+Y}(\theta_1, \theta_2) + E_{slab} - E_X - E_Y\,, \tag{6.7}$$

where $E_{X+Y}(\theta_1, \theta_2)$ is the total energy of the slab with the adsorbates X and Y at angles θ_1 and θ_2 respectively, E_{slab} is the total energy of the slab without adsorbates, whereas E_X and E_Y are the total energies of the slab with a X and Y adsorbate respectively. The isolated adsorbate is allowed to relax for O, OH and H_2O(p1) but is fixed for H_2O(p2) and H_2O(v), when calculating E_X and E_Y as discussed below.

The angular dependent potentials are constructed through the following steps. First an initial geometry is constructed. The angle dependent pair potentials is then

constructed by a rigid rotation of the adsorbates around an axis parallel to the z-axis through the O atom of the adsorbate. The interaction potentials are resolved at 6 discrete angles for each adsorbate. The adsorbate rotation angles are defined as in Figure 6.3. Finally, the interaction potentials are symmetrized by enforcing the symmetry $V(\theta_1, \theta_2) = V(-\theta_1, -\theta_2)$ and the additional symmetries $V(\theta_1, \theta_2) = V(\theta_2+180°, \theta_1+180°)$ and $V(\theta_1, \theta_2) = V(180°-\theta_2, 180°-\theta_1)$ when the two adsorbates are identical. The average interaction parameter is chosen for symmetry-equivalent interaction parameters. For oxygen, the most attractive interactions with the other adsorbates have been chosen.

When constructing the initial geometry for OH, H_2O(p1) and O are allowed to relax with the O atom in the adsorbate constrained to a high symmetry site. The geometry is relaxed from an initial structure close to the most attractive configuration of the dimer. This optimizes the geometry to the configuration we expect to be most frequent at the surface. For the H_2O(p1)-H_2O(p1) interaction, this procedure results in the water molecule accepting the hydrogen bond to move to a distance 3.09 Å away from the surface with the hydrogen atoms pointing towards the surface at an angle near 45 %. A similar dimer structure has been reported by other groups[137, 72]. We do, however, not expect these dimers to be very abundant at the surface at 298 K and have not considered this kind of water further. The initial geometry for the H_2O(p1)-H_2O(p1) interaction potential is therefore constructed with H_2O(p1) fixed in the geometry adopted by H_2O(p1) in the extended H_2O(p1)-OH structure. H_2O(v) and H_2O(p2) are unstable in dimer configurations and relax to H_2O(p1). The H_2O(v) and H_2O(p2) molecules are consequently constrained to the geometry adapted in the $(\sqrt{3} \times \sqrt{3})R30°$-$H_2O$(v)-$H_2O$(p) structure.

6.2.4 Calculational Details

The angular dependent nearest neighbor interactions between adsorbates is calculated in a (3×3) surface unit cell with 3 layers. The metal atoms in the slab are frozen to the positions they have when the first atomic layer of the slab is relaxed without any adsorbates. For the interaction energies, the PBE functional has been used, [25] with a 350 eV plane wave cutoff for the KS eigenstates and 500 eV for the density. The first Brillouin zone is sampled with a $(4 \times 4 \times 1)$ Monkhorst-Pack grid of **k**-points [115]. When the adsorbates are relaxed, this is done until the largest force component is below 0.02 eV/Å.

For the formation energies and the equilibrium potentials of (6.5) and (6.6), the Kohn-Sham valence states are expanded in a plane wave basis with kinetic energy below 340 eV. The cutoff for the charge density is 500 eV. Exchange and correlation effects are approximated by the RPBE exchange correlation functional [26]. All calculations are done on 4 layer slabs of closepacked atoms, where the two top most layers and the adsorbates have been relaxed until the maximum force is below 0.02 eV/Å. The O and OH adsorption energies are calculated in a (2×2) surface unit cell and a (8×8) Monkhorst-Pack grid of special k-points has been used. The reversible potential for OH formation on Pt_3Ni is calculated using a $(\sqrt{12} \times \sqrt{12})R30°$ supercell with proton ordered $(\sqrt{3} \times \sqrt{3})R30°$ H_2O(u)/H_2O(p) and OH/H_2O(p) structures. The free energies of O and OH covered surfaces are calculated by normalizing the formation energy relative to Pt calculated by Karlberg *et al.* [92] similar to equation (5.2). To find the reversible potentials, we then use use their calculated field dependent adsorption energy linearized around 0.9 V to find solve for the equilibrium potentials of (6.5) and (6.6).

6.3 Results

6.3.1 Interaction Potentials

The interaction potentials are shown in Figure 6.3 and in Table E.1. Key features of the adsorbate structures are determined by the relative magnitude of interaction parameters, and will be discussed in the following.

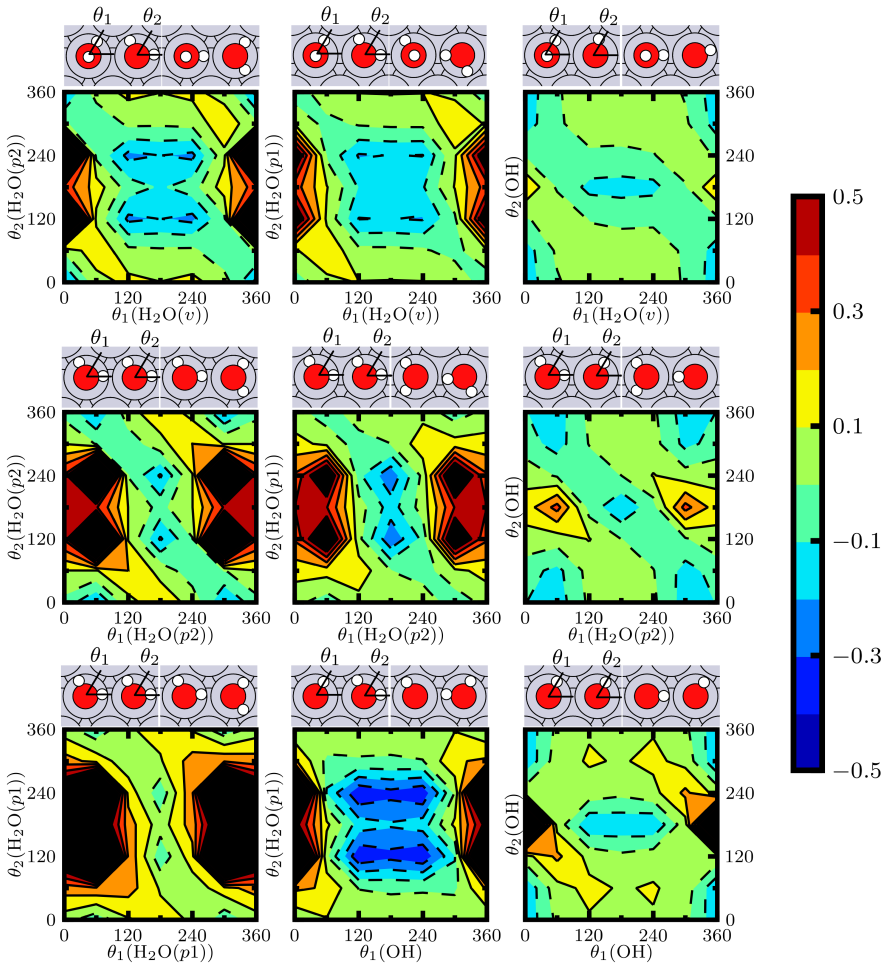

Figure 6.3: Interaction potentials on Pt(111). From the upper left to lower right corner: H_2O(v)-H_2O(p2), H_2O(v)-H_2O(p1),H_2O(v)-OH, H_2O(p2)-H_2O(p2), H_2O(p2)-H_2O(p1),H_2O(p2)-OH, H_2O(p1)-H_2O(p1), H_2O(p1)-OH, OH-OH. The insets above the contour plots show the angle definitions with the (60°,60°) configuration as an example (left) and the most attractive pair interaction (right). Interaction parameters with O are shown in Table D.1.

A key feature determining the structure of the adsorbate layer is the highly attractive H_2O(p1)-OH interaction when H_2O(p1) is the hydrogen bond donor. Configurations where hydrogen atoms at the adsorbates are directed towards each other are repulsive by more than 0.5 eV.

From the interaction potentials, formation of an extended H_2O(v)-H_2O(p1) RT3 phase from an extended $(\sqrt{3} \times \sqrt{3})R30°$ H_2O(v)-H_2O(p2) phase costs 49 meV / H_2O(p), so some H_2O(p1) will be present at the surface at all potentials. Formation of $(\sqrt{3} \times \sqrt{3})R30°$ OH-H_2O(p2) from $(\sqrt{3} \times \sqrt{3})R30°$ OH-H_2O(p1) costs 1.02 eV / H_2O(p1), meaning the adsorption of OH will be accompanied by H_2O adsorption. Further, because OH-H_2O(p1) interactions are more attractive than OH-OH

interactions, domains of $(\sqrt{3} \times \sqrt{3})R30°$ OH-H_2O(p1) tend to be formed.

H_2O(p1) with one OH neighbor and two H_2O(v) neighbors is stable relative to H_2O(p2) in the same environment by 0.46 eV when OH is the hydrogen bond acceptor. On the other hand it is only 4 meV more stable, when OH is the hydrogen bond donor. Therefore some of the edges of the OH-H_2O(p1) islands may be decorated by H_2O(p1).

The calculated adsorbate-adsorbate interaction potentials show reasonable agreement with the similar potentials calculated by Karlberg *et al.*[134]. However, they used only a single H_2O(p) adsorbate. Our calculated potentials are slightly less attractive than those found by Karlberg *et al.*[134].

Convergence of the interaction potentials with slab thickness is checked by increasing the thickness. If the H_2O(p)-OH interaction potential is calculated on a 4 layer slab, the interaction parameters differ by less than 27 meV from when the 3 layer slab is used. The average deviation between the interaction parameters calculated on the 3 layer and the 4 layer slab is 12 meV.

6.3.2 OH and O Adsorption on Pt(111)

Bulk 2^{nd} layer Ni conc.	Pt_3Ni 50 %	Pt_3Ni 25 %	Pt_3Ni 0 %	Pt 2.3 % 0 %	Pt 0 %
ΔE_{OH}^{A}	1.18	1.22	1.15	1.16	1.08
ΔE_{OH}^{B}	1.13	1.10	1.12	1.16	1.08
ΔE_{OH}^{C}	1.30	1.22	1.15	1.16	1.08
ΔE_{OH}^{D}	1.30	1.22	1.15	1.16	1.08
ΔE_{O}^{E}	1.91	1.87	1.84	1.83	1.60
ΔE_{O}^{F}	1.91	1.87	1.84	1.83	1.60
ΔE_{O}^{G}	2.17	2.14	1.78	1.83	1.60
ΔE_{O}^{H}	2.19	1.87	1.84	1.83	1.60
Average ΔE_{OH}	1.22	1.19	1.14	1.16	1.08
Average ΔE_{O}	2.04	1.94	1.83	1.83	1.60
$U_{OH}^{rev.}$	0.91	0.88	0.84	-	0.76
$U_{O}^{rev.}$	1.11	1.12	1.09	-	0.95

Table 6.1: Formation energies of O and OH in eV and reversible potentials in V *vs.* RHE on Pt_3Ni with a Pt skin and different Ni concentrations in the second layer and on compressed Pt and uncompressed Pt. The adsorption sites on Pt_3Ni are shown in Figure 6.6.

The simulated potential dependent coverage on Pt(111) is shown in Figure 6.4, and compared to the charge transfer from OH adsorption in the butterfly region between 0.6 V *vs.* RHE and 0.95 V *vs.* RHE in the CV measured by Stamenkovic *et al.* [110]. According to the model OH, adsorbs between 0.65 V *vs.* RHE and 0.85 V *vs.* RHE. At 0.85 V *vs.* RHE OH starts to get oxidized to O and a $(\sqrt{3} \times \sqrt{3})R30°$-O structure is completed at 1.05 V *vs.* RHE. The OH-H_2O(p1) adsorbate structure, the mixed O-OH structure and the O adsorbate structure that develop during the anodic scan are shown in Figure 6.5. Ex-situ electrochemical XPS experiments by Watanabe and co-workers find that oxygen formation starts between 0.85 V *vs.* RHE and 0.9 V *vs.* RHE in 0.1 M HF (hydrofluoric acid), which is in reasonable agreement with our simulations[138].

It should be noted that CV does not measure the charge transfer from adsorption directly, but also contains contributions from variations in double layer capacitance with potential. The double layer capacitance has been assumed to be constant in the integration of the experimental CV. However, both electrochemical impedance spectroscopy and Frumkins Thermodynamic method show that the double layer capacitance changes in the region of OH adsorption [139, 140]. The integration also assumes an adsorption valency of 1. That is, however, barely different from our ap-

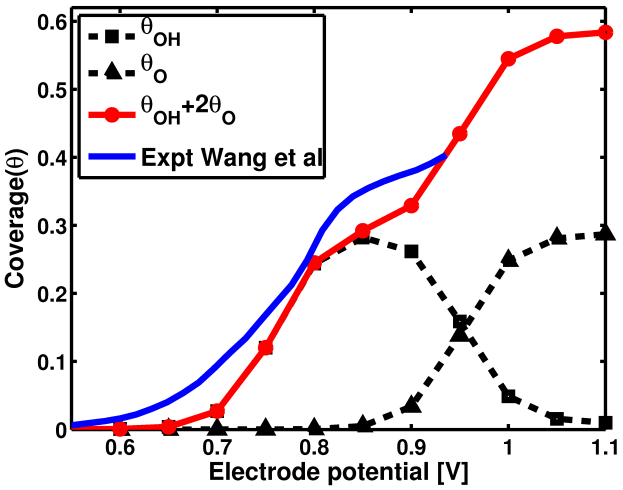

Figure 6.4: Simulated integrated cyclic voltammogram for Pt(111). The electrode potential is measured *vs.* RHE. MC simulation and figure by V. Viswanathan *et al.* and experiment from Stamenkovic *et al.* [110].

proach, as we have not included any direct field dependence besides that used for calculating the reversible potentials.

The simulated curve follows the integrated CV quite well. The charge transfer at 0.6-0.75 V and at 0.8-0.9 V is also too low compared to the CV. The gradual increase in charge in the latter region is however captured, and is described by the oxidation of OH to O within our model. A similar effect was observed by Rai *et al.* [136]. The current appears to increase again at 0.9 V, which our model attributes to increased oxidation of OH to O. It may be that this oxidation in our model actually happens too fast. However in this region, irreversible processes, *e.g.* Pt-O place exchange could begin to occur.[141] That was, however, not observed in *ex situ* EC-XPS experiments in 0.1 M HF by Wakisaka *et al.* [138].

The sharp peak in the CV at 0.8 V *vs.* RHE shown in Figure 6.4, corresponds in our calculations to when about 1/3 ML OH has been adsorbed on the surface. The current spike has been suggested to be caused by an order-disorder transition [128] or by OH formed from water interacting with perchlorate [142]. However, since the peak is present in HF as well, the peak at 0.8 V is most likely due to an order-disorder transition. It would require simulations at more densely spaced potentials to resolve this delicate feature in our simulations. At 0.8 V the charge from the integrated CV is about 0.05 electrons per Pt atom larger than in our simulations.

Higher OH coverages than those found in our model could be caused by the formation of phase-antiphase domains with a higher local OH coverage at the domain boundaries or by coexistence of $(\sqrt{3}\times\sqrt{3})R30^\circ$ domains and (1×1) OH domains. Because the OH adsorption feature ends with a very sharp peak indicative of attractive interactions or an order-disorder phase transition, we consider the former explanation to be the most likely of the two. Periodic structures with higher OH coverage than 1/3 ML OH could in principle also be formed[2], but our interaction potentials appear not to favor this.

6.3.3 OH and O on $Pt_3Ni(111)$

Theoretical calculations have indicated that the effect of solute concentration in the subsurface layers affect the binding energy of ORR intermediates by 0.05 eV or less for Pt_3X alloys with X=Fe,Ni,Co [93, 143]. For the new class of Pt and Pd alloys studied

[2]For example a (2×1) OH-H_2O structure with 0.5 ML OH.

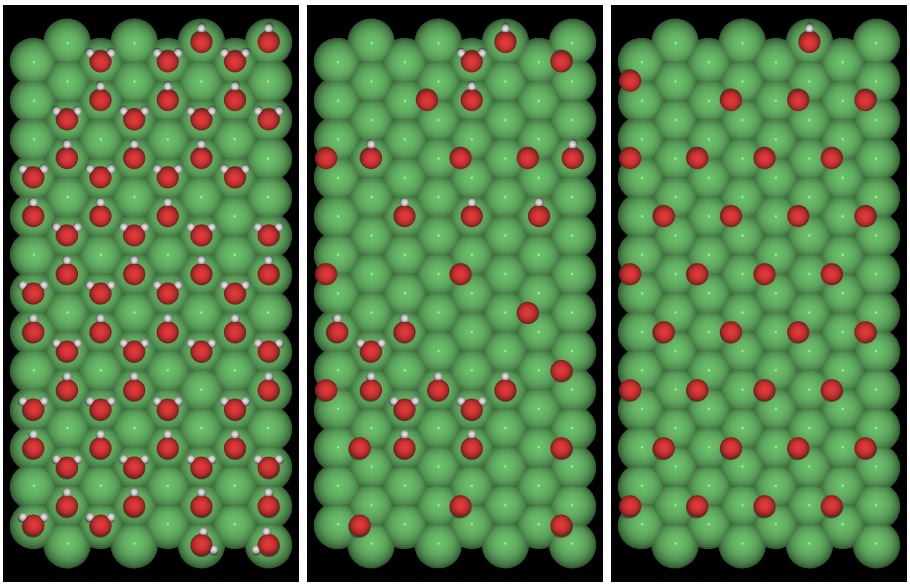

(a) (b) (c)

Figure 6.5: Snapshot of adsorbate structures on Pt(111) formed during the simulated CV at (a) 0.85 V *vs.* RHE, (b) 0.90 V *vs.* RHE and (c) 1.10 V *vs.* RHE. The Pt atoms are green, O red and H white. H_2O(p2) and H_2O(v) are not plotted. Figure produced by V. Viswanathan.

in chapter 5, subsurface concentration may have a large effect on the binding energy of ORR intermediates. This is because these alloys cannot rely on a compressed Pt skin to obtain weaker binding of intermediates relative to Pt. Further, the variation in oxygen adsorption energy depends more on subsurface X concentration in the 2nd layer for early transition metals than for the late 3d transition metals, c.f. Figures 5.1 and 5.8. To fully comprehend the ligand effects of subsurface solute concentration on ORR activity, a micro dynamical model capable of incorporating site heterogeneity is required.

Site Heterogeneity

To study the effect of site heterogeneity on the CV of a Pt surface alloy, we have calculated the formation energy of OH at atop sites and O at fcc hollow sites on Pt_3Ni alloys. These are terminated with a 1 ML Pt skin with 0, 25 % or 50 % Ni in the second layer and bulk composition in the third and fourth layers. The Pt_3Ni alloy surface is shown in 6.6, for a surface with 50 % and 25 % Ni in the second layer. The adsorption sites have been marked by letters A-H, and the corresponding formation energies are shown in Table 6.1.

In general, O and OH binding energies are weaker on Pt_3Ni than on pure Pt and become even weaker as the Ni content in the second layer increases. For Pt_3Ni depleted of Ni in the second layer there is still a weakening of the binding energies relative to Pt and some dependence of the alloy structure below the second layer. Here the adsorption energies change by 0.05 eV for O and 0.02 eV for OH depending on the adsorption site. The formation energy of O and OH is also shown for a 2.3 % compressed Pt slab in Table 6.1. This corresponds to Pt with the lattice constant used in the DFT calculations for the Pt_3Ni alloy. It is seen that part of the destabilization of adsorbates relative to Pt comes from the compression of the Pt overlayer on Pt_3Ni and that Ni in the third and fourth subsurface layers appears to result in slightly stronger binding energies.

The unit cell considered is too small for a complete analysis of the effect of sub-

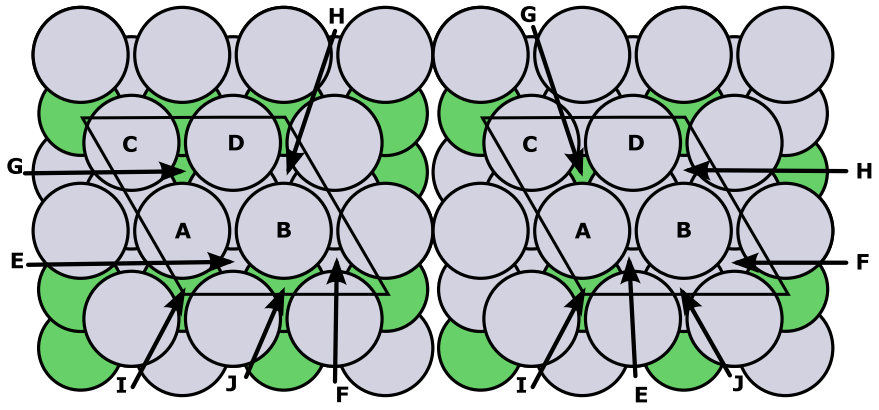

Figure 6.6: Heterogeneous adsorption sites at a Pt skin on Pt_3Ni with 50 % Ni (left) and Pt_3Ni with 25 % Ni (right) in the 2nd layer.

surface Ni on the binding energies at specific sites. For the Monte Carlo simulations, we therefore model the surface by a (50×50) lattice with heterogeneous sites with (2x2) periodicity.

Adsorption

To estimate the effect of the lattice compression when going from Pt(111) to a Pt skin on Pt_3Ni, we calculate the H_2O(p)-OH interaction potential and the H_2O(p1)-H_2O interaction potential on a 4 layer Pt slab compressed by 2.3 %. This corresponds to the calculated contraction of the lattic constant in Pt_3Ni compared to Pt. Compression weakens the most attractive OH-H_2O interactions at $(\theta_1 \in \{120°, 180°, 240°\}, \theta_2 = 120°)$ by up to 9 meV. On the other hand, the most attractive H_2O(p1)-H_2O(p1) interaction at $(\theta_1 = 60°, \theta_2 = 0°)$ is strengthend by 15 meV. Because the interaction potentials are not strongly affected by lattice compression, the Monte Carlo simulations are done using the same interaction potentials V as on Pt.

Variations in the adsorption energy of H_2O(p1) on Pt_3Ni with 50 % Ni in the second layer were below 9 meV, and have been neglected here. The change in the electric field due to changes in the workfunction is not included for the Pt_3Ni alloys, as the change in workfunction is 0.11 eV or less. This affects binding energies by less than 11 meV.

From calculations of OH in the OH/H_2O(p)-$(2\sqrt{3} \times 2\sqrt{3})R30°$ structure, we find a 0.15 V shift in the reversible potential for OH formation relative to Pt. This agrees well with the 0.13 V shift used in Ref. [14] and with the 0.31 eV decrease in O binding energy at the most stable adsorption site. For the extended OH/H_2O structure, OH is adsorbed on all possible top sites. Accordingly, we find a 0.14 eV shift in the average OH formation energy on Pt_3Ni relative to Pt. This means that the reversible potential for OH adsorption shifts primarily due to weaker OH binding on Pt_3Ni. For Pt_3Ni with 25 % or 0 % Ni in the second layer, we therefore approximate the reversible potential from the shift in the reversible potential relative to Pt_3Ni with 50 % Ni in the second layer.

Figure 6.7 shows the simulated OH and H_2O adsorption on Pt_3Ni with 50 % Ni in the second layer. With 50 % Ni in the second layer the onset of OH adsorption is offset by $\sim$ 50 mV compared to the experiment by Stamenkovic *et al.* [110], but roughly similar to the CV by Rossmeisl *et al.* [14] for the reasons discussed above. Oxygen adsorption does not become important before 1.0 V, where the OH coverage has nearly reached 1/3 ML.

With 25 % Ni in the second layer, OH adsorption shifts $\sim$ 30 mV towards negative potential and comes closer to the experimental curve. With 0 % Ni in the second layer, OH adsorption moves even closer to the experimental curve (see Figure F.1 in

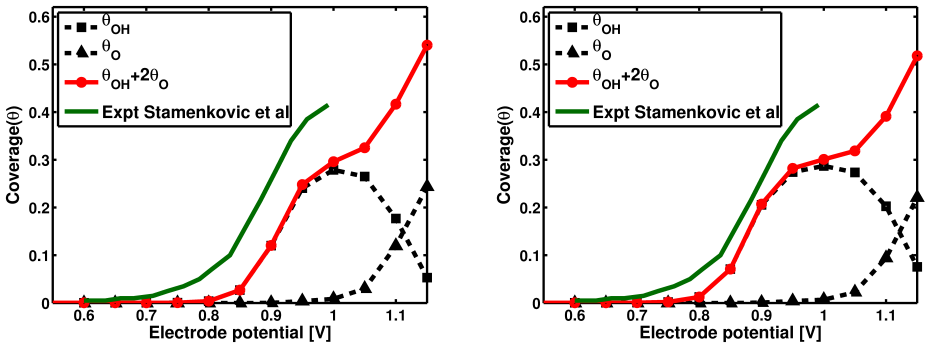

Figure 6.7: Simulated integrated cyclic voltammogram for Pt_3Ni with 50 % (left) and 25 % Ni (right) in the second layer. The electrode potential is measured *vs.* RHE. MC simulation by V. Viswanathan *et al.* and experiment by Stamenkovic *et al.* [110].

appendix F). The negative shift of the OH adsorption isotherm agrees qualitatively with the stonger oxygen binding energy on surfaces with low Ni concentration in the second layer, c.f. Table 6.1.

6.4 Summary

In this chapter we have simulated the potential dependent OH and O adsorption on Pt(111) and Pt_3Ni in the limit of an infinitely slow scan rate. The simulations are performed employing DFT calculated interaction and formation energies as input to Monte Carlo simulations. For Pt(111) we find a reasonable agreement with integrated CV and electrochemical XPS experiments. We then simulated OH and O adsorption on $Pt_3Ni(111)$ surfaces terminated by a 1 ML Pt skin and an ordered (2×2) subsurface alloy structure with 50 %, 25 % or 0 % Ni in the second layer. We observed that OH adsorption shifts to more negative potentials as the subsurface Ni concentration is decreased.

Chapter 7

Stability of Rutile Oxides

The discovery of the Dimensionally Stable Anodes (DSA) was one of the most important technological discoveries in electrochemistry in the 20th century[144]. The DSAs consist of a mixture of catalytically active transition metal oxides and additives to enhance stability. [145] Oxides used as DSA's include spinels, dioxides and perovskites. Among the dioxides RuO_2 stabilized by TiO_2 and possibly other additives such as IrO_2 and SnO_2, have been widely studied. They are used for the electrochemical production of oxygen and chlorine. Before the discovery of DSA, graphite anodes were used in industry. Because of severe corrosion the anodes had to be replaced often, and the corrosion of the anodes had to be taken into account in the design of the electrolyzers [146]. Stability is thus a major challenge for anodes. For example, at

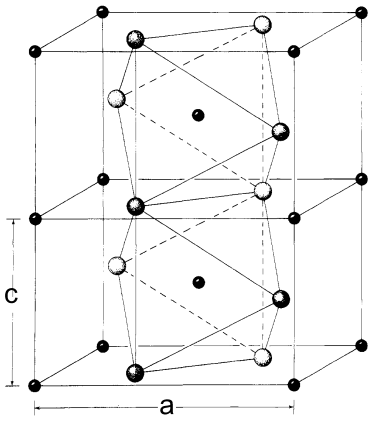

Figure 7.1: The rutile crystal structure. The metal atoms are small black spheres and the oxygen atoms are large spheres. Reproduced from Ref. [147].

high potential RuO_2 is oxidized to RuO_4 which is a volatile compound[55]. MnO_2, which could be interesting for oxygen evolution and reduction[148], forms Mn^{2+} ions in acid solution [55].

Formation energies and atomization energies have been used to evaluate the accuracy of exchange correlation functionals on solids [149, 150]. Paier *et al.* found that formation energies for PBE, PBE0 and HSE03[149], were in better agreement with experiment than the atomization energies. They attributed this to larger errors in the total energy on the isolated atoms than in the bulk crystals. Wang *et al.* found that PBE was unable to describe the reaction energies for the progressive oxidation of a series of metal oxides[150]. However, if they applied a constant shift of 1.36 eV partially attributed to the error on the O_2 molecule, it was possible to describe the reaction energies within GGA+U [151, 152] by fitting a single U for each metal to the reaction energies. In their study, Wang *et al.* generally focused on the monoxides,

sesquioxides and dioxides of the 3d transition metal oxides.

7.1 Computational Details

The Kohn-Sham valence states are expanded in a plane wave basis with kinetic energy below 350 eV. The cutoff for the charge density is 500 eV. The atoms are relaxed until a maximum force below 0.05 eV/Å is obtained. The Brillouin zone is sampled with an $(8 \times 8 \times 8)$ Monkhorst-Pack grid. Spin polarization effects are included for the metals and oxides in which the metals are magnetic. The metals are treated in their most stable crystal structure except for Mn, which has been calculated in the bcc structure.

7.2 The Rutile Crystal Structure

The rutile crystal structure may be constructed from a hexagonal closepacked array of oxygen anions by placing M^{4+} cations in half of the octahedral interstices such that no occupied octahedrons share common faces [153]. Electrostatic repulsion between the metal cations twists the octahedrons, making the actual structure tetragonal. The rutile structure is shown in Figure 7.1. The octahedrons, corresponding to the occupied octahedral sites, share edges forming rows along the c-direction. The apices at the top of the square bi-pyramids in one row of octahedrons are linked to the edges of neighboring rows.

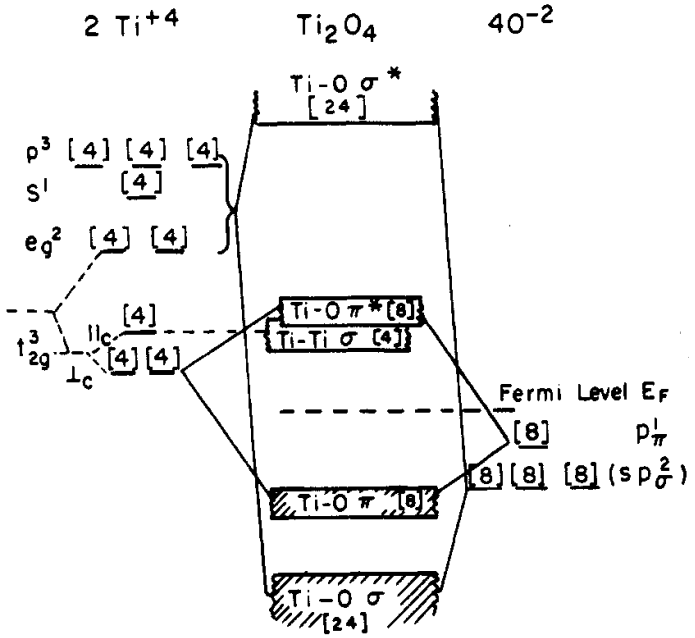

Figure 7.2: A schematic diagram of the bandstructure of two formula units of rutile TiO_2. See the text for details. The numbers in parenthesis shows the number of electrons that can be accommodated in the bands per two formula units of the metal dioxide. The bond symmetry is also shown. Figure reproduced from Ref. [147].

7.3 Bandstructure

The band structure of rutile and related oxides have been descried theoretically in a model proposed by Goodenough[153] and extended by Rogers et al. [147]. The model is reproduced in figure 7.2. We note that some oxides form metal-metal bonds [147], but that this effect has not been considered in the following analysis. Oxygen is 3-fold coordinated in a planar geometry and is assumed to be sp^2 hybridized. The metal atoms are 6-fold coordinated and the d-orbitals split into 3 t_{2g} orbitals and 2 e_g orbitals in the octahedral crystal field.

With the particular choice of unit cell shown in Figure 7.3, the d_{z^2} and $d_{x^2-y^2}$ orbitals on the labelled metal atom have e_g symmetry. The d_{xy}, d_{yz} and d_{zx} orbitals have t_{2g} symmetry. The e_g orbitals are directed towards the oxygen atoms. Together with the metal valence s and p orbitals the e_g orbitals hybridize with O sp^2 states to form bonding and anti-bonding states with σ character. The d_{yz} and d_{zx} form π bonds with the non-hybridized O $2p_z$ orbitals. The d_{xy} orbital that lie in a plane containing the c-direction is essentially non-bonding, but may broaden due to the overlap with similar orbitals on neighboring metal cations along the rows of octahedrons.

7.3.1 RuO_2

The projected density of states for RuO_2 calculated with DACAPO using the RPBE functional is shown in figure 7.3. Because the octahedrons are distorted, the the d-orbitals does not have the exact symmetry of the crystal structure and some mixing of the bands should be expected. The calculated density of states agrees quite well with the model described above. O 2p states have high weight between -8 to -1 eV and little weight for $\epsilon - \epsilon_F >$ -1 eV. The Ru 4d states all have some weight at low energy ($\epsilon - \epsilon_F <$ -1 eV) from the hybridization with the O 2p orbitals. This shows that the bonding in RuO_2 is partly covalent rather than purely ionic. Ru 4d states with e_g symmetry have a larger splitting than the states with t_{2g} symmetry. The antibonding $\sigma*$ band formed from e_g states is higher in energy than the $\pi*$ band formed from t_{2g} states. The d_{xy} orbital is largely non-hybridized but is broardened by about 1 eV.

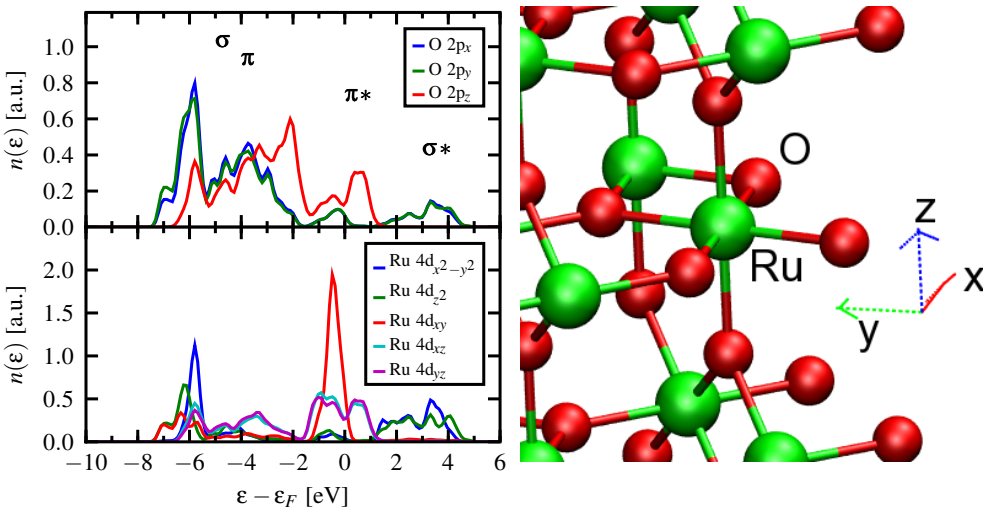

Figure 7.3: Left: Density of states projected onto the O 2p states and the Ru 4d states in RuO_2. Right: RuO_2 in the rutile crystal structure. The density of states to the left have have been projected onto the atomic orbitals of the atoms labelled on the figure to the right. The symmetry of the bands is shown in the figure to the left. The bonding states (-8 to -1 eV) have primarily O 2p character, whereas the anti-bonding states have high metal t_{2g} (d_{xy}, d_{yz}, d_{zx}) or e_g (d_{z^2}, $d_{x^2-y^2}$) character.

7.4 Formation Energy

In this section we focus on the formation of rutile metal dioxides from the reaction of the metal with water:

$$M(s) + 2H_2O(l) \rightarrow MO_2(s) + 2H_2(g)\,. \tag{7.1}$$

The free energy of formation is defined as

$$\Delta G_{form} = G(MO_2(s)) + 2G(H_2(g)) - G(M(s)) - 2G(H_2O(l)) \tag{7.2}$$

The free energy of $H_2(g)$ and $H_2O(l)$ are calculated as done as described in chapter 3 including zero point energies within the harmonic approximation and entropy from thermodynamic tables. We neglect ZPE and entropy for the bulk crystal phases. From a harmonic vibrational analysis it is estimated that the error from this is below 0.10 eV and 0.02 eV for RuO_2 and IrO_2 respectively[1]. Experimental values for (7.1) may be obtained from the electrochemical series [154, 55, 155]. If the half cell reduction reaction

$$MO_2(s) + 4H^+ + 4e^- \leftrightarrow M(s) + 2H_2O(l)\,, \tag{7.3}$$

has the standard potential U *vs.* the standard hydrogen electrode, then (7.1) has the experimental free energy of formation

$$\Delta G^{exp}_{form} = 4eU\,. \tag{7.4}$$

In some cases (7.3) may be obtained directly from the electrochemical series. In other cases it may be necessary to combine the standard potentials for

$$M^{n+} + ne^- \leftrightarrow M(s) \tag{7.5}$$

and

$$MO_2(s) + 4H^+ + (4-n)e^- \leftrightarrow M^{n+} + 2H_2O(l)\,. \tag{7.6}$$

7.5 Calculated Formation Energies

Figure 7.4 shows the calculated ΔG_{Form} as a function of the experimental free energies. We have compared the calculated formation free energies to two sets of experimental formation energies. The first set is based on data from Ref. [55] and Ref. [155]. We will refer to this set as A. The second set is a bit smaller and based solely on the experimental data collected by Bratsch[154]. We refer to this set as B. For RPBE, the mean error (ME) is 0.00 eV are -0.11 eV, whereas the mean absolute error (MAE) is 0.30 eV and 0.31 eV, for datasets A and B respectively as shown in table 7.1. Here, the error is defined as

$$\Delta\Delta G^{error}_i = \Delta G^{experiment}_i - \Delta G^{DFT}_i\,. \tag{7.7}$$

For comparison, the formation free energy calculated non-selfconsistently with PBE is also shown in table 7.1. The ME is 0.68 eV and 0.79 eV and the MAE is 0.73 eV and 0.81 eV for datasets A and B respectively. This reflects that PBE systematically overestimates the formation free energy by 0.7 eV to 0.8 eV. The two sets of experimental data have also been compared. The mean absolute deviation is 0.25 eV. Some data points are significantly different in the two sets. We find the mean absolute difference between the two sets is comparable to the error between RPBE and the experimental values.

[1] Calculations by J. I. Martinez.

Oxide	ΔG^{A}_{form}[55, 155]	ΔG^{B}_{form} [154]	ΔG^{PBE}_{form}	ΔG^{RPBE}_{form}
TiO_2	-4.26	-4.30	-4.83	-3.97
NbO_2	-2.72	-2.76	-3.36	-2.55
VO_2	-2.08	-	-2.76	-1.97
GeO_2	-0.98	-0.42	-0.87	-0.03
CrO_2	-0.68	-	-1.44	-0.60
WO_2	-0.48	-0.62	-1.45	-0.64
MoO_2	-0.29	-0.61	-0.29	0.13
SnO_2	-0.03	-0.47	-0.75	0.05
MnO_2	0.10	0.10	-0.87	-0.16
ReO_2	1.06	1.10	0.05	0.93
PbO_2	2.49	2.66	1.78	2.65
OsO_2	2.75	2.60	1.40	2.26
RuO_2	3.15	-	2.36	3.10
IrO_2	3.70	2.92	1.68	2.53
PtO_2	4.05	3.68	3.26	4.05
ME(A)	0.00	0.13	0.79	0.00
MAE(A)	0.00	0.25	0.81	0.30
MA(B)	-0.13	0.00	0.68	-0.11
MAE(B)	0.25	0.00	0.73	0.31

Table 7.1: Formation free energies of rutile oxides. From left to right: ΔG^{A}_{form} is the experimental free energy obtained from Refs. [55, 155], ΔG^{B}_{form} is the experimental free energy obtained from Ref. [154], ΔG^{PBE}_{form} is the free energy calculated non-selfconsistent with the PBE functional on the basis of a RPBE self-consistent calculation. ΔG^{RPBE}_{form} is the formation energy calculated self-consistently with the RPBE functional. ME(A) and MAE(A) are the mean error and the mean absolute error relative to the experimental data in Refs. [55, 155]. ME(B) and MAE(B) are the mean error and the mean absolute error relative to the experimental data in Refs. [154]. All energies are in eV.

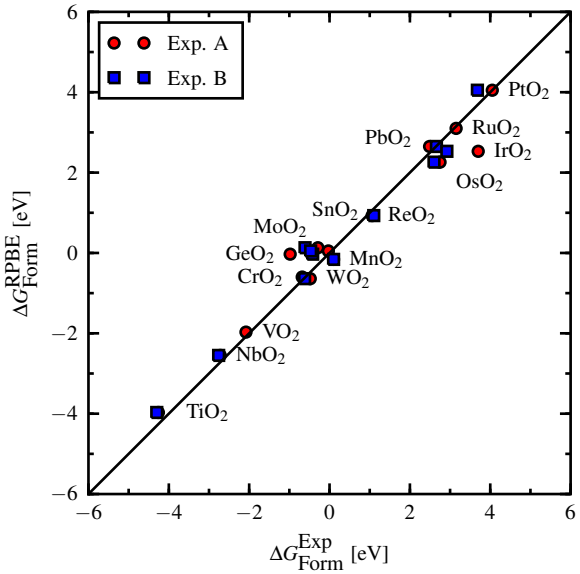

Figure 7.4: The calculated formation free energies ΔG_{Form} plotted as a function of the experimental formation free energies. Set A is obtained from Refs [55, 155] and set B is obtained from [154]. There is nearly a *one-to-one* correspondence between the calculated and the experimental formation energies at this energy scale. The mean absolute error (MAE) is around 0.3 eV.

The formation energies of the rutile oxides are reproduced surprisingly well with RPBE, considering the known shortcomings of standard GGA's. Part of the error usually encountered when calculating the formation energies of oxides is related to a poor description of the O_2 molecule [150]. The large overbinding in the O_2 molecule is well known. The DFT error[2] on the reaction energy of

$$O_2 \rightarrow 2O \tag{7.8}$$

is $\Delta\Delta E_{PBE} = -1.01$ eV and $\Delta\Delta E_{RPBE} = -0.60$ eV for PBE and RPBE respectively.[156] It is reasonable to assume that a large part of the error in formation energies is due to difficulties in describing the O_2 triplet spin state [11].

If equation (7.8) is viewed as a way to form atomic oxygen before the formation of the oxide, we could replace (7.8) by the reaction

$$H_2O \rightarrow H_2 + O\,, \tag{7.9}$$

which is equivalent to the electrochemical source of oxygen used extensively in this work. The error on the reaction energy of (7.9) is $\Delta\Delta E_{PBE} = -0.56$ eV and $\Delta\Delta E_{RPBE} = 0.14$ eV for PBE and RPBE respectively.[156] The error in describing a free O atom is therefore significantly reduced if it described using H_2O dissociation rather than O_2 dissociation. This justifies both our choice of the electrochemical H_2O/H_2 reference and our choice of xc-functional.

Another reason for the good agreement with experiment is probably that the data set only contains rutile oxides. For these structures correlation is not as strong as in monoxides and sesquioxides. Correlation is particularly strong for 3d oxides and only a few 3d oxides have been included. Lastly, the large range of formation energies from -4 to 4 eV makes the agreement look very good.

[2]The error is here defined according to (7.7) but with energy rather than free energy.

7.6 Trends in Oxide Formation Energies

Gelatt *et al.* proposed a model to understand trends in the formation energies of transition metal compounds in the rocksalt structure [157]. The formation of these transition metal compounds is split into two steps. First, the metal is expanded from the bulk equilibrium structure to the structure the metal atoms have in the compound. The deformation of the metal costs some energy, ΔE_{Deform}, defined as

$$\Delta E_{Deform} = E^{bulk}_{expanded} - E^{bulk}_{equilibrium}, \tag{7.10}$$

where $E^{bulk}_{expanded}$ and $E^{bulk}_{equilibrium}$ is the total energy of the deformed metal and the metal in the equilibrium geometry respectively[3]. We approximate $\Delta E_{Deform} \approx \Delta G_{Deform}$. ΔE_{Deform} can be expected to be some fraction of the cohesive energy. Second, the oxygen atoms are accommodated into the expanded metal, which yields the bond energy ΔE_{Bond}. We define the bond free energy as

$$\Delta G_{Bond} = E^{M,bulk}_{expanded} + 2G(H_2O(l)) - E(MO_2) - 2G(H_2(g))\,, \tag{7.11}$$

where we have approximated the free energy of the metal and the oxide by the DFT energy. With this definition[4],

$$\Delta G_{Form} = \Delta G_{Deform} - \Delta G_{Bond}\,. \tag{7.12}$$

The trends in ΔG_{Form}, ΔG_{Deform} and ΔG_{Bond} are shown in figure 7.5 for a series of rutile 4d metal oxides. Only NbO_2, MoO_2 and RuO_2 were included in the comparison to the experimental formation free energies in figure 7.4, as we could not find experimental support for the existence of the rutile structures of PdO_2, RhO_2 and ZrO_2. They are included here for the purpose of studying the trends in the formation energy of rutile oxides. Variations in ΔG_{Deform} are expected to follow a parabolic dependence on the number of d-electrons similar to the cohesive energy of the transition metals[158, 159]. Figure 7.5 shows this is indeed the case. The deformation energy is between 1.3 eV and 3.7 eV, being largest for MoO_2 and RuO_2. Variations in bond energy can be predicted from the bandstructure, if the valence bands are being rigidly shifted as they are filled when moving through the transition metal series [157]. For the rutile like oxides, changing the number of electrons may induce electronic and structural instabilities resulting in symmetry breaking. This can, for example, lead to formation of metal-metal pairs in the structure[147]. However, we expect the energy scale for these instabilities are significantly smaller than the variation in formation energies observed here. If bonding states are being filled, we expect the compound to become more stable and ΔG_{Bond} to increase. If non-bonding states are being filled we expect little change in the bonding energy, whereas ΔG_{Bond} is expected to increase when anti bonding states are being filled. The bond energy varies monotonically between -6.5 eV and 3.3 eV in an almost linear fashion with increased filling of the t_{2g} states. The linear decrease in ΔG_{Form} from ZrO_2 to RuO_2 suggests a single antibonding band is being filled. Going from RuO_2 to RhO_2 it is possible that a nonbonding orbital is being filled. PdO_2 lies on the same trend line as ZrO_2, NbO_2, MoO_2 and RuO_2. Looking at the model of the bandstructure in figure 7.2, it is seen that starting with ZrO_2, then the bonding σ and π band are already filled. Additional electrons are therefore placed in the nonbonding σ band or the antibonding $\pi*$ band. The observed decrease in ΔG_{Bond} is therefore explained by the filling of antibonding states.

The variation in ΔG_{Form} is dominated by the variation in ΔG_{Bond}. ΔG_{Form} therefore shows little structure as a single antibonding state is being filled. The most stable rutile oxides (relative to the bulk metals) are obtained for the early transition metal oxides, where only bonding and possibly non-bonding states are filled.

[3]Non-magnetic and Ferro-magnetic spin structures were tested. The most stable electronic structure has been used, although it has only minor effect on the total energy.

[4]This definition is chosen do make an increase in ΔG_{Bond} correspond to a stronger metal-Oxygen bond.

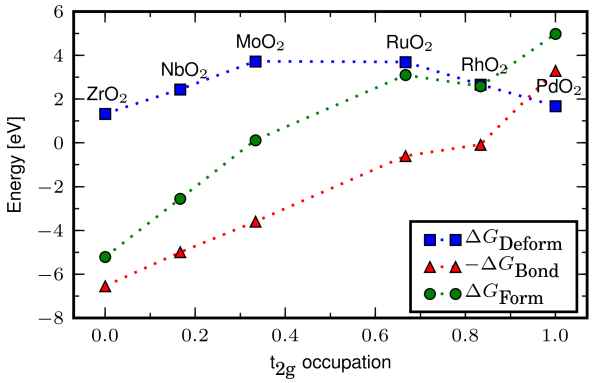

Figure 7.5: The formation energy ΔG_{Form} is decomposed into the energy cost of deforming the metal lattice ΔG_{Deform} and the energy yield by chemisobing oxygen into the lattice ΔG_{Bond}; $\Delta G_{Form} = \Delta G_{Deform} - \Delta G_{Bond}$.

7.7 Summary

In this chapter we have shown that the trends in the formation energy of a wide range of rutile oxides are described surprisingly well by GGA functionals. We believe this is because DFT errors from the self-interaction and correlation in the GGA functional are small for the majority of the rutile oxides considered in this study. For the transition metals, the formation of rutile oxides becomes less exothermic for the more noble transition metals. Using 4d transition metals as an example it is shown that the formation energy, ΔG_{Form}, increases almost linearly with the number of d-electrons in the metal. This trend may be understood based on a simple model, where the metal first is deformed into the structure adapted by the metal ions in the rutile lattice, and second the oxygen is introduced into the lattice. It is found that the binding of oxygen in the deformed metal lattice dominates the trends in formation energies and the variations in the energy required to deform the lattice are small. The increase in formation energy with the number of d-electrons may then be explained by an increasing number of electrons being filled into anti-bonding orbitals going towards the noble metals.

Chapter 8

Chlorine Evolution on Rutile (110) Surfaces

Chlorine is very important in the chemical industry, where 50 % of the total turnover depends on chlorine and caustic soda [160]. The electrochemical production of chlorine is currently one of the most important applications of electrochemisty in industry[161]. 1 % of the electricity produced in Japan and 2 % in the US is used to produce chlorine.[162, 163] The most commonly used electrocatalysts are the Dimensionally Stable Anodes [144, 164].

However, chlorine production by the Deacon process have recently been seen as an alternative to the energy intensive electrochemical chlorine production [165, 166, 167, 168, P6].

The overall Chlorine Evolution Reaction (ClER) at the anode is

$$2\mathrm{Cl}^-(\mathrm{aq}) \rightarrow \mathrm{Cl}_2(\mathrm{g}) + 2e^-, U^{\ominus}_{\mathrm{SClE}} = 1.36\,\mathrm{V}\ \textit{vs.}\ \mathrm{SHE}. \tag{8.1}$$

Not much is known about the reaction at the atomic scale, and single crystal measurements of activity have only recently become available [169, 170]. Different reaction mechanisms have been proposed over the last 30 years, despite the simplicity of the overall reaction. Among the basic proposed reaction steps, some are similar to those suggested for the hydrogen evolution reaction, with the initial Volmer step

$$* + \mathrm{Cl}^- \rightleftarrows \mathrm{Cl}* + e^-, \tag{8.2}$$

followed by recombination through a Tafel step

$$2\mathrm{Cl}* \rightarrow 2* + \mathrm{Cl}_2(\mathrm{g}), \tag{8.3}$$

or the Heyrovsky step

$$\mathrm{Cl}* + \mathrm{Cl}^- \rightarrow * + \mathrm{Cl}_2(\mathrm{g}) + e^-, \tag{8.4}$$

where $*$ denotes an active site. Within our approach, we calculate the free energy of the final state in (8.2) but as we refrain from calculating the barriers of (8.2) and (8.4), the relative rates of the two latter steps cannot be predicted. However, easy formation of Cl* is a necessary condition for both mechanisms.

On RuO_2 electrodes, the Krishtalik mechanism [171, 172, 173] has been suggested. In this mechanism, the Volmer step (8.2) is followed by further oxidation of the Cl$*$ complex

$$\mathrm{Cl}* \rightarrow (\mathrm{Cl}*)^+ + e^-. \tag{8.5}$$

This step is rate determining, and possibly followed by

$$(\mathrm{Cl}*)^+ + \mathrm{Cl}^- \rightarrow * + \mathrm{Cl}_2(\mathrm{g}). \tag{8.6}$$

The atomic details of the active site * and the $(Cl*)^+$ intermediate is unknown [170]. However it has been suggested to be an oxygen site [169, 170] or a metal site [170].

Chlorine evolution has been reported to be inhibited by high proton concentrations for some catalysts. These include TiO_2/RuO_2[174], Ti/RuO_2 electrodes[175] and electrochemically oxidized Ru[176]. The most simple interpretation is based on the "acid-base equilibrium"

$$H* \rightleftarrows * + e^- + H^+(aq), \tag{8.7}$$

determining the availability of the active sites $*$, possibly with separated electron and proton transfer processes [175, 177, 178].

Cl_2 evolution is considered a facile reaction and may proceed at low overpotentials on many surfaces[145]. It has been observed that electrocatalysts that are good for oxygen evolution also are good for chlorine evolution[161]. However, the reasons for this are not well understood.

In this chapter we present surface stability diagrams for IrO_2 and RuO_2 in equilibrium with liquid water, protons and chloride ions as a function of pH and potential. Based on the stable surfaces at conditions near chlorine evolution, we show the most likely active site, $*$, is related to cus-adsorbed species and propose reaction paths for the ClER on IrO_2 and RuO_2. We then show that the binding energies of Cl, OCl and OCl scale with the binding energy of O on the cus site. This enables a simple unified model for the oxygen evolution reaction (OER) and ClER at the cus sites of rutile (110) surfaces, since the free energy of all intermediates in the two reactions now are linearly correlated to a single parameter, or descriptor. We again take this to be the oxygen binding energy at the cus site, ΔE_{O^c}.

8.1 Computational Details

The calculations in this chapter are done on periodically repeated 4 layer slabs of rutile (110). We have used a (2×1) surface unit cell and $(4 \times 4 \times 1)$ Monkhorst-Pack type k-point sampling for the slab calculations, aplane wave basis of 350 eV for the Kohn-Sham eigenstates and 500 eV for the density. A Fermi smearing of 0.1 eV is used. The two bottom layers of the slab are fixed in their bulk structure, while the two top layers as well as possible adsorbates on it are relaxed until the sum of the absolute forces is less than 0.05 eV/Å.

8.1.1 Phase Diagrams

Phase diagrams are constructed according to (3.36) based on the DFT calculated formation energies. Adsorbate interactions are in principle included in the surface phase diagram. When considering both free sites $^{b/c}$, $OH^{b/c}$, $O^{b/c}$, and $Cl^{b/c}$ which may form at the bridge sites and the cus sites, the number of possible configuration grows fast with the size of the super cell. In constructing the surface phase diagram, we concentrate on phases where each type of site is dominated by a single type of adsorbate. Mixed phases may exist near the phase boundaries and the extent of the mixed phases is affected by adsorbate-adsorbate interactions. In the cases where we have considered mixed phases, the areas of the mixed phases are smaller than the areas of the separate unmixed phases. In general, adsorbates bind stronger at bridge sites than cus sites, so free metal cation sites are most likely found at the cus sites. Oxygen binds stronger than X = OH, Cl, OCl, so O^b+X^c is generally more stable than X^b+O^c. We have systematically considered the structures 2 X^b + 2 Y^c with X = *, O, OH, Cl and Y = *, O, OH, Cl, OCl in the (2×1) unit cell. However, we did not consider the unlikely 2 $*^b$ + 2 Y^c structures.

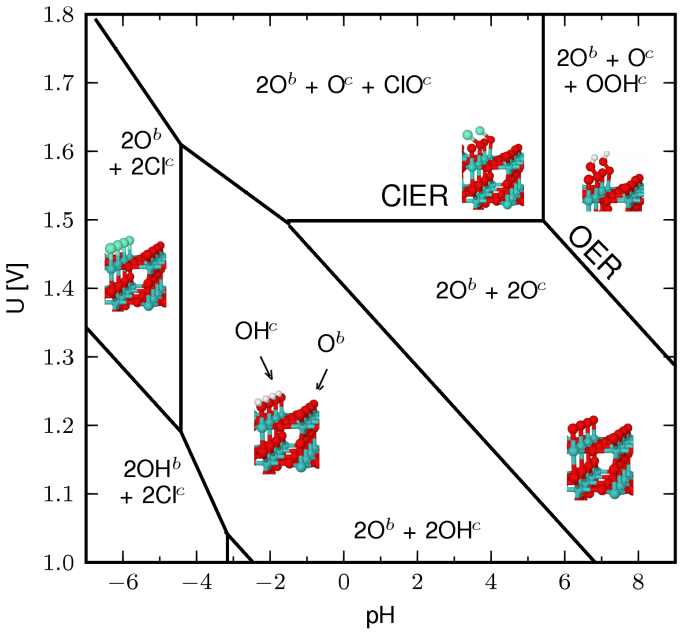

Figure 8.1: Surface phase diagram for $IrO_2(110)$ in equilibrium with Cl^-, H^+ and H_2O at 298.15 K and $a_{Cl^-} = -1$. The regions where we expect chlorine or oxygen evolution to become significant have been marked. Adsorbates adsorbed at a cus site are marked by a superscript ^{c} and adsorbates at bridge sites are marked with superscript ^{b}.

8.2 Surface Phase Diagram for IrO_2

Figure 8.1 shows the interesting part of the phase diagram of IrO_2. At pH=7 the surface sites are covered by OH and O at most potentials. At low potential, the surface is covered by OH groups (not shown). Increasing the potential oxidizes OH to O first at the bridge sites and then at the cus sites. Eventually formation of OOH becomes thermodynamically favored. When this happens, we expect oxygen evolution to become appreciable and the surface structure is determined by the kinetics of the steady state evolution of oxygen. The formation of chlorine adsorbates directly at the cus sites requires pH < -3. Formation of Cl at the bridge sites requires an even lower pH.

We would expect that for a good catalyst the formation of the Cl intermediate has $\Delta G \approx 0$ eV near 1.36 V, and that there are free sites available for the formation of this intermediate. A mechanism involving Cl adsorbed directly on an Ir cation does not fulfill any of these requirements. Instead, we see from the phase diagram that a ClO^c intermediate is thermodynamically favored for U > 1.5 V in the pH range from 0 to 3. This suggests the following sequence of intermediates on IrO_2

$$O^c + 2Cl^-(aq) \rightarrow OCl^c + Cl^-(aq) + e^- \rightarrow O^c + Cl_2(g) + 2e^-. \tag{8.8}$$

Both steps have $|\Delta G| = 0.14$ eV at $U = 1.36$ V, and a significant amount of O^c sites exist at U > 1.36 V.

8.3 Surface Phase Diagram for RuO_2

The phase diagram for RuO_2 (110), shown in Figure 8.2, turns out to be a bit more complicated. At pH = 7, the surface is dominated by species formed by the oxidation

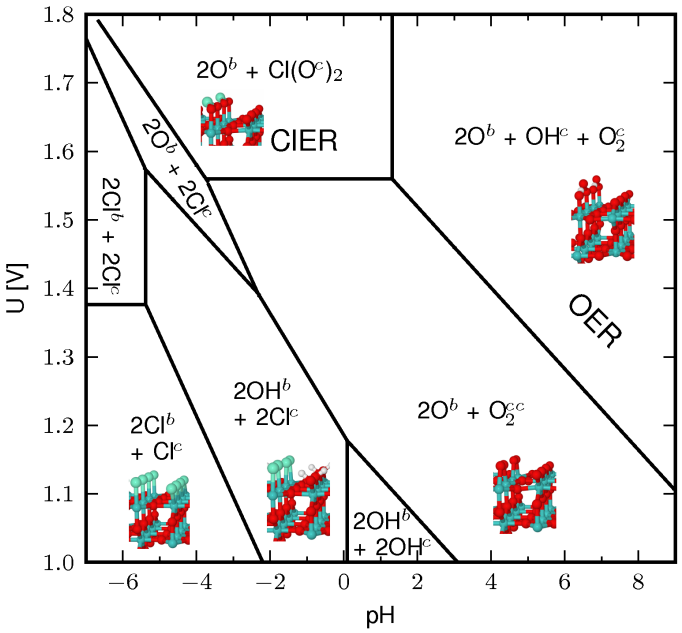

Figure 8.2: Surface phase diagram for $RuO_2(110)$ in equilibrium with Cl^-, H^+ and H_2O at 298.15 K and $a_{Cl^-} = -1$. The regions where we expect chlorine or oxygen evolution to become significant have been marked. Adsorbates adsorbed at a cus site are marked by a superscript ^{c} and adsorbates at bridge sites are marked with superscript ^{b}.

of water. At low potential, only the bridge sites are covered by OH. When the potential is increased, OH is formed at the cus sites, before OH is oxidized to O. We find that oxygen association at the cus sites

$$2O^c \rightarrow O_2^{cc} \tag{8.9}$$

is exothermic by 0.71 eV for the fully O covered surface. The association barrier is only 0.18 eV while desorption of O_2^{cc} is endothermic by 1.16 eV. O_2^{cc} will therefore most likely be present at the surface rather than O_c. Oxygen evolution could happen by further oxidation of the surface

$$H_2O + O_2^{cc} \rightarrow O_2^c + *^c + H_2O \rightarrow O_2^c + OH^c + H^+ + e^-. \tag{8.10}$$

Desorption of O_2 from this surface has $\Delta G = 0.1$ eV. When O_{2c} + OH_c starts to form, we expect oxygen evolution to become important. Additional barriers could be involved, although we will not go further into the details of oxygen evolution. On RuO_2 chlorine species are formed at pH < 1.3. However, near 1.36 V, oxygen is still the most stable adsorbate. We find that the 2 O^b + O^c + OCl^c intermediate is meta stable relative to a 2 O^b + $Cl(O^c)_2$ structure. The latter structure forms at U > 1.5 V, and we expect this to be the intermediate on $RuO_2(110)$. This gives the following intermediates

$$O_2^{cc} + 2Cl^-(aq) \rightarrow Cl(O^c)_2 + Cl^-(aq) + e^- \rightarrow O^c + Cl_2(g) + 2e^-. \tag{8.11}$$

We note in passing that the formation of O_2^{cc} and $Cl(O^c)_2$ depend on the presence of pairs of Ru cus sites at the surface, and it may not be relevant for alloys of for example TiO_2 and RuO_2. Neglecting the formation of O_2^{cc} and $Cl(O^c)_2$ and considering (8.8) we find that at 1.36 V each step has $|\Delta G| = 0.05$-0.12 eV. This depends on whether there is O^c or OCl^c adsorbed at the other cus site in the (2x1) unit cell.

8.4 Scaling Relations

To generalize our results for $IrO_2(110)$ and $RuO_2(110)$, we derive scaling relations for the formation energy of Cl^c, OH^c and O^c at a cation cus site ^{c}, as well as the formation of O_2^{cc} and $Cl(O^c)_2$ adsorbed at two cus sites. We here define the adsorption energy of chlorine relative to Cl_2(g)

$$\Delta E_{Cl^c} = E_{Cl^c} - E_{*^c} - \frac{1}{2}E_{Cl_2} \tag{8.12}$$

For oxygen the energy is calculated relative to water

$$\Delta E_{O^c} = E_{O^c} - E_{*^c} - E_{H_2O} + E_{H_2}, \tag{8.13}$$

and for ClO^c we apply the combined reference energy states from above,

$$\Delta E_{ClO^c} = E_{ClO^c} - E_{*^c} - \frac{1}{2}E_{Cl_2} - E_{H_2O} + E_{H_2}. \tag{8.14}$$

The adsorption energy of O_2^{cc} is defined with reference to water and hydrogen,

$$\Delta E_{O_2^{cc}} = E_{O_2^{cc}} - E_{2*^c} - 2E_{H_2O} + 2E_{H_2}, \tag{8.15}$$

and the adsorption energy of $Cl(O^c)_2$ is defined by

$$\Delta E_{Cl(O^c)_2} = E_{Cl(O^c)_2} - E_{2*^c} - 2E_{H_2O} + 2E_{H_2} - \frac{1}{2}E_{Cl_2} \tag{8.16}$$

The scaling relations are calculated in a (2×1) surface cell, so the total coverage at the cus-sites varies between 50% and 100%. In Figure 8.3 the adsorption energies

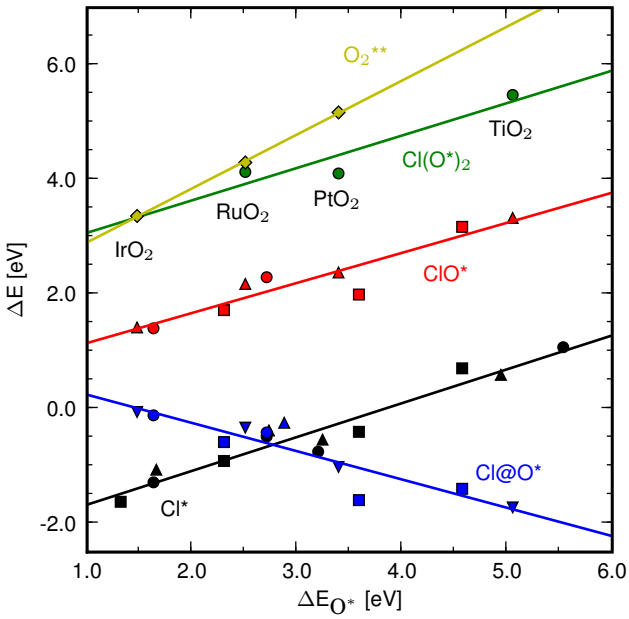

Figure 8.3: Linear relations for adsorbates formed at the cus site of rutile (110) surfaces. $\Delta E_{Cl^c} = 0.59\Delta E_{O^c} - 2.26$, MAE = 0.17 eV, $R^2 = 0.93$; $\Delta E_{ClO^c} = 0.52\Delta E_{O^c} + 0.62$, MAE = 0.16 eV, $R^2 = 0.89$; $\Delta E_{Cl(O^c)_2} = 0.56\Delta E_{O^c} + 2.51$, MAE = 0.21 eV, $R^2 = 0.87$; $\Delta E_{O_2^{cc}} = 0.94\Delta E_{O^c} + 1.96$, MAE = 0.02 eV, $R^2 = 1.00$; The linear relation for Cl adsoption on O^c is based on the linear relation for ClO^c.

of Cl^c and ClO^c as defined above are plotted against the O binding at the cus-site

with the same environment at the surface. The plot clearly shows that the Cl and O adsorption energies are linearly correlated.

Similar linear energy relations between adsorption energies of hydrogenated species (CH_x, OH, SH, and NH_x) and the adsorption of the corresponding dehydrogenated atoms: (C, O, S, and N) have previously been shown for transition metals [7] and transition metal compounds including oxides [179, P4]. The scaling of Cl with respect to O is close to the scaling of OH with respect to O, with a slope near 1/2. This reflects the fact that Cl has a valency of one, the same as the oxygen atom in OH.[7] Consequently, ClO^c also scales as OH^c and similar to HOO^c. These results suggest that the oxygen adsorption energy is a general descriptor for the reactivity of oxides. This has also been suggested for cations in oxides by Pankratiev for some other adsorbates [180].

Adsorption of Cl atop O^c may also be determined by

$$\Delta E_{\mathrm{Cl@O^c}} = E_{\mathrm{ClO^c}} - E_{\mathrm{O^c}} - \frac{1}{2}E_{\mathrm{Cl_2}} = \Delta E_{\mathrm{ClO^c}} - \Delta E_{\mathrm{O^c}}. \tag{8.17}$$

The linear scaling relations make it possible to analyze the most stable surface structures and the stability of intermediates in the chlorine evolution reaction as a continuous *function* of the descriptor for reactivity - the oxygen binding energy. The specific oxides correspond to points with a specific oxygen binding energy. The descriptor approach does not directly identify more active catalysts, but may eventually be combined with a screening study similar to that in chapter 5 to identify candidates with a good activity. It should however be kept in mind that catalyst stability is a huge issue in chlorine evolution that must also be considered.

8.5 Trends in Stable Surface Phases

To obtain an understanding of how the activity varies with the catalyst, we employ the linear relations established earlier and the linear relation between OH* and O* established[1] in Ref. [179]. We focus on intermediates formed at the cus sites. Since the binding energy of all intermediates at the cus sites scales directly with $\Delta E_{\mathrm{O^c}}$, it is possible to construct a generalized phase diagram showing the most stable phase at a potential U as a function of the descriptor, $\Delta E_{\mathrm{O^c}}$. This is shown for $a_{\mathrm{Cl^-}}$=1 and pH=0 in Figure 8.4. In the limit of weak binding, oxygen association becomes exothermic and barrierless, so phases like ClO^c and $Cl(O^c)_2$ may not form. From the linear relations we find that

$$\mathrm{O_2^{cc}} \rightarrow \mathrm{O_2(g)} + 2\,\mathrm{^c}, \tag{8.18}$$

has $|\Delta G| < 0$ for $\Delta E_{\mathrm{O^c}} > 2.97$eV. We therefore chose to consider only OH^c and Cl^c for $\Delta E_{\mathrm{O^c}} > 2.97$eV. The free energies of OH^c and Cl^c phases are within 0.01-0.27 eV depending on the oxide. We thus expect some coexistence in these regions of phase space. For IrO_2 the oxygen binding energy is in the range from 1.32 to 1.63 eV. For RuO_2 the oxygen binding energy is in the range from 2.30 to 2.71 eV. For PtO_2 in the rutile crystal structure the oxygen binding energy is in the range from 3.20 to 3.59 eV. For unreactive rutile oxides such as TiO_2 or SnO_2 the oxygen binding energy is near 5 eV. The variation in adsorption energy with coverage may be seen as an uncertainty arising from neglecting adsorbate-adsorbate interactions. For the considered oxides, $\Delta E_{\mathrm{O^c}}$ is more affected by changing the oxide than changing the O coverage. The change of the most stable adsorbate when the potential is increased is qualitatively reproduced for RuO_2 and IrO_2. Decreasing $\Delta E_{\mathrm{O^c}}$ favors the formation of first OH^c/Cl^c, then $Cl(O^c)_2$, and O_2^{cc}, ClO^c, and finally O^c. Formation of O_2^{cc} and $Cl(O_2^c)$ reflects the intermediate O^c binding energy compared to IrO_2 and TiO_2. Increasing the potential favors transfer of electrons to the surface making OH^c and Cl^c, then O^c, and finally ClO^c more stable at the surface.

[1] $\Delta E_{\mathrm{OH*}} = 0.61\Delta E_{\mathrm{O*}} - 0.90$eV

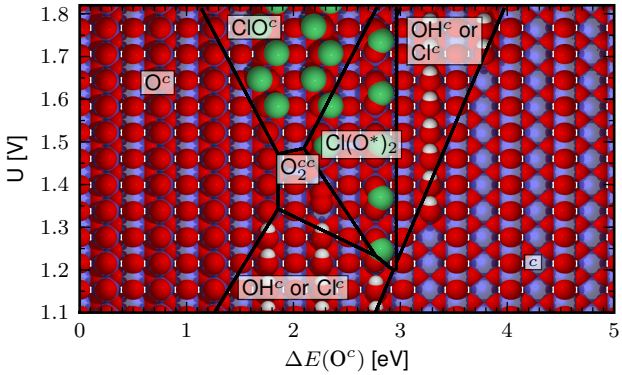

Figure 8.4: The most stable surface at pH=0 and a_{Cl^-}=1 as a function of potential, U, and the surface reactivity descriptor, $\Delta E_{\mathrm{O}*}$. Metal ions are blue, oxygen atoms red, hydrogen atoms white, and chlorine atoms are green.

8.6 Trends in Activity

Firstly, we investigate the mechanism involving $\mathrm{ClO}^{\mathrm{c}}$

$$\mathrm{O}^{\mathrm{c}} + 2\mathrm{Cl}^-(\mathrm{aq}) \rightarrow \mathrm{OCl}^{\mathrm{c}} + \mathrm{Cl}^-(\mathrm{aq}) + e^- \rightarrow \mathrm{O}^{\mathrm{c}} + \mathrm{Cl}_2(\mathrm{g}) + 2e^-. \tag{8.19}$$

The potential at which all steps are neutral or downhill is:

$$U = U^{\ominus}_{SClE} + \frac{|\Delta G_{\mathrm{ClO}^{\mathrm{c}}} - \Delta G_{\mathrm{O}^{\mathrm{c}}}|}{e} \tag{8.20}$$

where $U^{\ominus}_{SClE}$ is the equilibrium potential for the chlorine evolution reaction at standard conditions on the SHE scale (*i.e.* 1.36 V). Secondly, we investigate the mechanism involving $\mathrm{Cl}(\mathrm{O}^{\mathrm{c}})_2$:

$$\mathrm{O}_2^{\mathrm{cc}} + 2\mathrm{Cl}^-(\mathrm{aq}) \rightarrow \mathrm{ClO}^{\mathrm{c}}{}_2 + \mathrm{Cl}^-(\mathrm{aq}) + e^- \rightarrow \mathrm{O}^{\mathrm{c}} + \mathrm{Cl}_2(\mathrm{g}) + 2e^-. \tag{8.21}$$

The potential at which all steps are neutral or downhill is:

$$U = U^{\ominus}_{SClE} + \frac{\left|\Delta G_{\mathrm{Cl}(\mathrm{O}^{\mathrm{c}})_2} - \Delta G_{\mathrm{O}_2^{\mathrm{cc}}}\right|}{e}. \tag{8.22}$$

Thirdly, we consider a mechanism involving Cl* adsorbed directly at the metal cus site,

$$2\mathrm{Cl}^-(\mathrm{aq}) + *^{\mathrm{c}} \rightarrow \mathrm{Cl}^-(\mathrm{aq}) + \mathrm{Cl}^{\mathrm{c}} + e^- \rightarrow \mathrm{Cl}_2(\mathrm{g}) + *^{\mathrm{c}} + 2e^-. \tag{8.23}$$

This mechanism may be relevant for oxides with weaker adsorption energy at the cus site relative to RuO_2. However, our calculations suggest that this mechanism will be somewhat poisoned by OH^{c} formation at the cus sites. The potential where all steps are neutral or down hill is:

$$U = U^{\ominus}_{SClE} + \frac{|\Delta G_{\mathrm{Cl}^{\mathrm{c}}}|}{e}. \tag{8.24}$$

RuO_2 and PtO_2 have $|\Delta G_{\mathrm{Cl}^{\mathrm{c}}}| < 0.05$eV for high and low coverage of Cl^{c} respectively. These could in principle work as good catalysts following this path. However for RuO_2, we find the cus sites are blocked by O_2^{cc}.

Since the different chlorine evolution potentials are all functions of $\Delta E_{\mathrm{O}^{\mathrm{c}}}$ the potentials may be plotted directly in the phase diagram as shown in Figure 8.5. This is similar to the Sabatier activity volcano curves known from heterogeneous catalysis [9]. Having the surface phase diagram in the same plot as the potential volcano directly assures that the activity volcano and the stable surface configuration agrees.

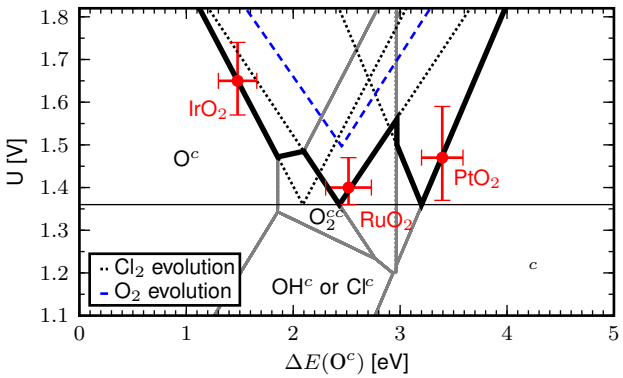

Figure 8.5: Sabatier volcanoes (black dotted) for the considered reaction paths involving ClO^c, $Cl(O^c)_2$ and Cl^c (from left to right). The domains of the most stable surface structure as function of potential and oxygen binding energy is marked with gray borderlines. To be truly active, the intermediate should form at sites that are stable as this makes the active site abundant. The full black line shows the combined Sabatier volcano taking into account the stability of the active sites for a given mechanism. The Sabatier volcano for oxygen evolution from Ref. [179] (dashed blue) shows OER always requires a higher potential than ClER at these conditions. The activity of IrO_2 and RuO_2 are indicated with error bars derived from the variation of the O^c adsorption energy with varying O^c coverage.

In other words, the different mechanisms are relevant in different areas of the phase diagram, which are easily obtained by looking at Figure 8.5. The thick black line marks the volcanoes, where the mechanism involves one of the most stable surfaces as an intermediate at the potential where all steps are neutral or downhill in free energy. We note that the surface composition during oxygen and chlorine evolution is not determined by equilibrium, but rather by steady state. However, it seems plausible that the surface composition determined by equilibrium is one of the intermediates during the reaction.

Figure 8.5 also shows the activity of IrO_2 and RuO_2 based on O^c adsorption energy, with the error bars corresponding to the variation of the O^c adsorption energy when going from low to high O^c coverage. If the accuracy of the linear relations are taken into account, the three investigated mechanisms form a single volcano with a broad plateau for ΔE_{O^c} between 1.5 eV and 3.5 eV. Deviations from the linear relations may be important in this region. The agreement between the detailed analysis for IrO_2 and RuO_2 and the linear relations is therefore surprisingly good. We find RuO_2 to be at the top of the volcano, whereas IrO_2 binds Cl on top O^c too weakly. TiO_2 does not appear on this activity scale. To our knowledge, only a few studies of the relative activity of rutile oxides have been carried out. Kuhn and Mortimer found IrO_2 and RuO_2 to have similar activities and to be more active than TiO_2. Mixtures of TiO_2 with Ir and Ru are more active than mixtures of TiO_2 with Cr, Co, or Pt[181]. Arikado *et al.* found the over-potential increases in the order RuO_2 <Ti/PtO_2 <IrO_2[182]. Kelly *et al.* found the specific activity of Ru sites at $Ru_xTi_{1-x}O_2$ to be 45 % more active than the Ir sites at $Ir_xTi_{1-x}O_2$.[183, 184] We note the discrepancy between the relative activity of RuO_2, IrO_2, and PtO_2 could be because different preparation methods may lead to different surface roughness factors and different concentrations of residual chlorine in thermally prepared oxides.[183] The high activity of RuO_2 and IrO_2 relative to TiO_2 is in agreement with experiments.

The rutile crystal structure of PtO_2 is not the most stable structure for PtO_2[185, 186, 187]. However, it is possible that some PtO_2 may be found in the rutile crystal phase if PtO_2 is mixed with oxides that do form the rutile crystal phase.

For comparison, the potential for oxygen evolution is shown in the same plot. It

is seen that the potential for chlorine evolution is lower than the potential for oxygen evolution in spite of the lower equilibrium potential for oxygen evolution. This is the reason why electrochemical chlorine evolution is possible. It is also seen that a good oxygen evolution catalyst is also a good chlorine evolution catalyst. A comparison of the experimental potentials for OER and ClER has suggested that the selectivity of oxides does not depend appreciably on the catalyst material.[161] The potential of chlorine evolution changes with the potential of oxygen evolution with a slope of 1.

Interestingly, one of the biggest outliers in the comparison was a Pt/MnO_2 catalyst in acid where the potential for oxygen evolution was 0.3 eV higher than the potential of chlorine evolution. MnO_2 has an oxygen binding energy around 3.3 eV at high O coverage. Based on Figure 8.5, we would therefore expect the potential for chlorine evolution to be 0.4 V lower than the potential for oxygen evolution.

Single crystal experiments on RuO_2 find the (110) surface to be less active for Cl_2 evolution than the (101) and the (320) surfaces [169, 170]. On polycrystalline RuO_2,[175, (P5)] mixed RuO_2+TiO_2,[174] and RuO2 (320)[170] the activity depends on pH, whereas the activity of RuO_2 (110) is independent on pH. The variation of activity with pH has been explained by the reaction

$$OH^c \rightarrow O^c + H^+(aq) + e^-, \tag{8.25}$$

determining the availability of active O^c sites.[188, 170, 175, 174] This clearly requires O^c and OH^c to be near equilibrium at the reaction conditions for Cl_2 evolution. Since the bridge sites and cus-sites on the (110) surface of rutile oxides fulfill the same scaling relations between O and OH adsorption as perovskites,[8] it is reasonable to assume the scaling relations are identical for all rutile oxide surfaces. In this case, Figure 8.5 applies for any rutile oxide surface, but with the oxygen adsorption energy depending on the specific surface facet.

It has been argued that the binding energy on the stepped (320) surface is stronger than on the (110) surface.[170] If it is assumed the O_2^{cc} and $Cl(O^c)^2$ intermediates form at the (320) surface as well, Figure 8.5 shows that as ΔE_{O^c} is decreased from ca. 2.6 eV, the $OH^c/{O_2}^{cc}$ equilibrium shifts to higher potential. This leads to an increased blocking of the active sites by OH^c at a fixed overpotential. The over-potential at constant current is found to be 80 meV lower on the (320) surface than on the (110) surface,[170] and thus within the vertical error bars indicated in Figure ΔE_{O^c}.

8.7 Summary

In this chapter we have, based on DFT calculations and the thermodynamic equations from Chapter 3, constructed surface stability diagrams for the (110) facets of IrO_2 and RuO_2 in equilibrium with water, protons and chloride ions as a function of pH and potential. At conditions where we would expect electrochemical evolution of chlorine to commence, we identify OCl^c and $Cl(O^c)_2$ as the most stable surface terminations on IrO_2 and RuO_2. This strongly suggests that the evolution of chlorine at these surfaces involves the formation of these intermediates. The formation of these intermediates does not require a large overpotential.

We then show that the stability of all intermediates, in the suggested mechanisms on IrO_2, RuO_2 and the intermediate Cl_c formed directly at the cation cus site, scales with the oxygen binding energy at the cus site. Based on these scaling relations we construct a generalized phase diagram, showing the most stable phases as a function of potential and the oxygen binding energy of the cus site. The diagram shows what surface structure will tend to dominate as as the catalyst material is varied.

The same scaling relations are then used to construct Sabatier volcanoes for each of the three reaction mechanisms. We then impose the additional constraint that either the active site or the chlorine intermediate should be present at the most stable surface at potentials just below the Sabatier volcano. If this is not the case, we could expect that the active site would not be present at the surface to a great extent. This would

decrease the overall turnover. The oxidation of water at the active sites thus controls the nature of the accessible active sites at the surface. The result is a flexibility in mechanism that changes with the overall binding energy of the intermediates. The combined Sabatier volcano has a broad peak with a low overpotential required to form the chlorine containing intermediates. Further, the overpotential for ClER is found to be higher than the overpotential previously reported for OER in [179] using a similar analysis. The qualitative picture of ClER on IrO_2 and RuO_2 agrees with our more detailed calculations.

Chapter 9

Summary and Outlook

In this thesis we have addressed the surface structure and catalytic activity of several model surfaces using density functional theory and a thermodynamic approach to calculate the free energy of adsorbate phases and reaction intermediates.

We have presented the details of the thermodynamic approach. Barriers for electrochemical reactions are not calculated. Instead, the free energy of the reaction intermediates are taken as sampling points of the free energy surface.

Electrochemical systems are open systems and at the positive potentials in oxygen reduction and chlorine evolution, O* or OH* may form adsorbate structures that affect the catalytic activity of the surface. We have constructed surface phase diagrams for Ni(111) and Ag(111) in equilibrium with water, electrons and protons as a function of pH and potential. Based on the phase diagrams we considered the oxygen reduction reaction on surfaces that are stable under oxygen free conditions. The reactive metal Ni is effectively made more noble by adsorbate-adsorbate repulsions. This makes Ni(111) work as a better catalyst, when there is some oxygen at the surface. OH and O adsorbate structures are only formed on Ag(111) at high potentials. The free energy of the reaction intermediates on Ag(111) suggests it should be comparable to Pt. Silver is, however, unstable in acidic solution, so its use is restricted to alkaline fuel cells. This draws attention to one of the key challenges in electrochemistry, which is to find catalysts that are not only active but also stable.

Under reaction conditions, the surface adsorbate structure is ultimately determined by the steady state of the reaction rather than equilibrium. We have introduced a model that uses DFT calculated formation energies and interaction potentials as input to a combination of equilibrium and dynamical Monte Carlo simulations. The method has been applied to the potential dependent adsorption of O and OH on Pt and Pt_3Ni and shows a reasonable agreement with integrated CVs and electrochemical XPS. The model may be extended to treat kinetically limited processes.

Apart from metal surfaces, rutile oxides also exhibit high electrocatalytic activity for a number of reactions. In order to design new catalysts based on these structures, theoretical methods are required to predict their stability. We have calculated the formation energies of a wide range of rutile oxides. On this broad scale the formation energies are surprisingly well described for these oxides. In addition we have explained the trends in oxide formation energy using a simple model. However, a more wide ranging study of different corrosion mechanisms would be necessary in order to accurately predict the electrochemical stability of these catalysts.

We have considered chlorine evolution from rutile 110 surfaces. The oxidation of water at the surface modifies the available catalytic sites. The free energy analysis indicates that this introduce a large degree of flexibility in the mechanism. The top of the Sabatier volcano constructed from the combined mechanisms becomes surprisingly broad. Due to scaling relations between Cl adsorption energy and O adsorption energy chlorine evolution will always occur at a lower potential than oxygen evolution.

Finally, we have also presented the results of a computational screening study for

Pt and Pd alloys active for ORR based on a thermodynamic model, where the oxygen binding energy is used as a descriptor for the ORR activity. The study identifies alloys consisting of Pt or Pd and an early transition metal as promising catalyst candidates. Detailed calculations of the free energy of the intermediates on Pt_3Y and Pt_3Sc confirmed that these alloys most likely have higher activity than Pt. Experiments have confirmed that these alloys indeed have higher activity than Pt. The ability to predict a new catalyst is strong evidence in support of the underlying model and the use of the thermodynamic approach for this reaction.
Even though the newly discovered catalyst have better activity than Pt, there is still room for improvement, since the overpotential is still high and the catalysts are still based on 75 % Pt or Pd. The discovery, however, lends hope that the same methodology can be applied to similar systems in the future. Another key point of interest that has arisen from the discovery of these catalysts is they have a larger lattice constant than Pt. On the contrary, other catalysts based on Pt overlayers or alloys with late 3d elements have a smaller lattice constant than Pt. Hopefully, experiments and computations will be able to shed more light on the nature of the active site on these new, interesting materials.

References

[1] A. M . Bond. *Broardening Electrochemical Horizons.* Oxford University Press, 2002.

[2] R. A. Marcus. Electron-transfer reactions in chemistry - theory and experiment (nobel lecture). *Angew. Chem. Int. Ed.*, 32(8):1111–1121, August 1993.

[3] M. T. M. Koper. Introductory lecture electrocatalysis: theory and experiment at the interface. *Faraday Discuss.*, 140:11–24, 2009.

[4] G. M. Whitesides and G. W. Crabtree. Don't forget long-term fundamental research in energy. *Science*, 315(5813):796–798, February 2007.

[5] J. Sehested, K. E. Larsen, A. L. Kustov, A. M. Frey, T. Johannessen, T. Bligaard, M. P. Andersson, J. K. Nørskov, and C. H. Christensen. Discovery of technical methanation catalysts based on computational screening. *Top. Catal.*, 45(1-4):9–13, August 2007.

[6] F. Studt, F. Abild-Pedersen, T. Bligaard, R. Z. Sorensen, C. H. Christensen, and J. K. Nørskov. Identification of non-precious metal alloy catalysts for selective hydrogenation of acetylene. *Science*, 320(5881):1320–1322, June 2008.

[7] F. Abild-Pedersen, J. Greeley, F. Studt, J. Rossmeisl, T. R. Munter, P. G. Moses, E. Skulason, T. Bligaard, and J. K. Nørskov. Scaling properties of adsorption energies for hydrogen-containing molecules on transition-metal surfaces. *Phys. Rev. Lett.*, 99(1):016105, 2007.

[8] E. M. Fernandez, P. G. Moses, A. Toftelund, H. A. Hansen, J. I. Martinez, F. Abild-Pedersen, J. Kleis, B. Hinnemann, J. Rossmeisl, T. Bligaard, and J. K. Nørskov. Scaling relationships for adsorption energies on transition metal oxide, sulfide, and nitride surfaces. *Angew. Chem. Int. Ed.*, 47(25):4683–4686, 2008.

[9] T. Bligaard, J. K. Nørskov, S. Dahl, J. Matthiesen, C. H. Christensen, and J. Sehested. The bronsted-evans-polanyi relation and the volcano curve in heterogeneous catalysis. *J. Catal.*, 224(1):206–217, 2004.

[10] E. Skulason, G. S. Karlberg, J. Rossmeisl, T. Bligaard, J. Greeley, H. Jonsson, and J. K. Nørskov. Density functional theory calculations for the hydrogen evolution reaction in an electrochemical double layer on the pt(111) electrode. *Phys.Chem.Chem. Phys.*, 9(25):3241–3250, 2007.

[11] J. K. Nørskov, J. Rossmeisl, A. Logadottir, L. Lindqvist, J. R. Kitchin, T. Bligaard, and H. Jonsson. Origin of the overpotential for oxygen reduction at a fuel-cell cathode. *J. Phys. Chem. B*, 108(46):17886–17892, November 2004.

[12] W. Kohn. Nobel lecture: Electronic structure of mater-wave functions and density functionals. *Rev. Mod. Phys.*, 71(5):1253, 1999.

[13] J. X. Wang, F. A. Uribe, T. E. Springer, J. Zhang, and R. R. Adzic. Intrinsic kinetic equation for oxygen reduction reaction in acidic media: the double tafel slope and fuel cell applications. *Faraday Discuss.*, 140:347–362, 2008.

[14] J. Rossmeisl, G. S. Karlberg, T. Jaramillo, and J. K. Nørskov. Steady state oxygen reduction and cyclic voltammetry. *Faraday Discuss.*, 140:337–346, 2008.

[15] L.E. Ballentine. *Quantum Mechanics a Modern Development*. World Scientific, corrected printing edition, 1998.

[16] P. Hohenberg and W. Kohn. Inhomogenous electron gas. *Phys. Rev.*, 136:B864–B871, 1964.

[17] E. H. Lieb. Density functionals for coulomb-systems. *Int. J. Quant. Chem.*, 24(3):243–277, 1983.

[18] M. Levy. Electron-densities in search of hamiltonians. *Phys. Rev. A*, 26(3):1200–1208, 1982.

[19] W. Kohn and L.J. Sham. Self-consistent equations including exchange and correlation effects. *Phys. Rev.*, 140:A1133–A1138, 1965.

[20] D. M. Ceperly and B. J. Alder. Ground state of the electron gas by a stochastic method. *J. Chem. Phys.*, 45:566–569, 1980.

[21] L. Wilk, S.J. Vosko, and M. Nusair. Accurate spin-dependent electron liquid correlation energies for local spin density calculations: a critical analysis. *Can. J. Phys*, 58:1200, 1980.

[22] J.P. Perdew and A. Zunger. Self-interaction correction to density-functional approximations for many-electron systems. *Phys. Rev. B*, 23:5048, 1981.

[23] Y. Wang and J.P. Perdew. Correlation hole of the spin-polarized electron-gas, with exact small-wave-vector and high-density scaling. *Phys. Rev. B*, 44(24):13298–13307, 1991.

[24] M. Ernzerhof and G.E. Scuseria. Assesment of perdew burke ernzerhof exchange-correlation functional. *J. Chem. Phys.*, 110(11):5029, 1999.

[25] J.P. Perdew, K. Burke, and M. Ernzerhof. Generalized gradient approximation made simple. *Phys. Rev. Lett.*, 77(18):3865, 1996.

[26] B. Hammer, L.B. Hansen, and J.K. Nørskov. Improved adsorption energetics within density-functional theory using revised perdew-burke-ernzerhof functionals. *Phys. Rev. B*, 59(11):7413–7421, 1999.

[27] T. Van Voorhis and G.E. Scuseria. A never form for the exchange-correlation energy functional. *J. Chem. Phys.*, 109(2):400–410, 1998.

[28] V.N. Staroverov, G.E. Scuseria, J.M. Tao, and Perdew JP. Comparative assessment of a new nonempirical density functional: Molecules and hydrogen-bonded complexes. *J. Chem. Phys.*, 119(23):12129–12137, 2003.

[29] *Open Source DFT code, see: wiki.fysik.dtu.dk/dacapo.*

[30] S. R. Bahn and K. W. Jacobsen. An object-oriented scripting interface to a legacy electronic structure code. *Comput. Sci. Eng.*, 4(3):56–66, MAY-JUN 2002.

[31] *Atomic Simulation Environment (ASE): see https://wiki.fysik.dtu.dk/ase2/.*

[32] D. Vanderbilt. Soft self-consistent pseudopotentials in a generalized eigenvalue formalism. *Phys. Rev. B*, 41(11):7892–7895, Apr 1990.

[33] G. Kresse and J. Furthmuller. Efficiency of ab-initio total energy calculations for metals and semiconductors using a plane-wave basis set. *Comput. Mater. Sci.*, 6(1):15–50, July 1996.

[34] J. Neugebauer and M. Scheffler. Adsorbate-substrate and adsorbate-adsorbate interactions of na and k adlayers on al(111). *Phys. Rev. B*, 46(24):16067–16080, December 1992.

[35] L. Bengtsson. Dipole correction for surface supercell calculations. *Phys. Rev. B*, 59(19):12301–12304, May 1999.

[36] I Chorkendorff and J. W. Niemantsverdriet. *Concepts of Modern Catalysis And Kinetics*. Wiley-VCH, 2003.

[37] R. A. Santen and M. Neurock. *Molecular heterogeneous catalysis*. Wiley-VCH, Weinheim, 2006.

[38] R. Imbihl, R. J. Behm, and R. Schlögl. Bridging the pressure and material gap in heterogeneous catalysis. *Phys. Chem. Chem. Phys.*, 9(27):3459–3459, 2007.

[39] M. Rieger, J. Rogal, and K. Reuter. Effect of surface nanostructure on temperature programmed reaction spectroscopy: First-principles kinetic monte carlo simulations of co oxidation at ruo_2(110). *Phys. Rev. Lett.*, 100(1):016105–4, January 2008.

[40] G. S. Karlberg, F. E. Olsson, M. Persson, and G. Wahnstrom. Energetics, vibrational spectrum, and scanning tunneling microscopy images for the intermediate in water production reaction on pt(111) from density functional calculations. *J. Chem. Phys.*, 119(9):4865–4872, September 2003.

[41] J. K. Nørskov, T. Bligaard, J. Rossmeisl, and C. H. Christensen. Towards the computational design of solid catalysts. *Nat. Chem.*, 1(1):37–46, April 2009.

[42] C. Stampfl, M. Veronica Ganduglia-Pirovano, K. Reuter, and M. Scheffler. Catalysis and corrosion: the theoretical surface-science context. *Surf. Sci.*, 500(1-3):368–394, March 2002.

[43] C. Stampfl, A. Soon, S. Piccinin, H. Q. Shi, and H. Zhang. Bridging the temperature and pressure gaps: close-packed transition metal surfaces in an oxygen environment. *Journal of Physics-condensed Matter*, 20(18):1–19, 2008.

[44] K. Reuter, D. Frenkel, and M. Scheffler. The steady state of heterogeneous catalysis, studied by first-principles statistical mechanics. *Phys. Rev. Lett.*, 93(11):116105–, September 2004.

[45] K. Reuter and M. Scheffler. First-principles kinetic monte carlo simulations for heterogeneous catalysis: Application to the co oxidation at ruo_2(110)ruba. *Phys. Rev. B*, 73(4):045433–17, January 2006.

[46] X. G. Wang, W. Weiss, S. K. Shaikhutdinov, M. Ritter, M. Petersen, F. Wagner, R. Schlogl, and M. Scheffler. The hematite (alpha-fe2o3) (0001) surface: Evidence for domains of distinct chemistry. *Phys. Rev. Lett.*, 81(5):1038–1041, 1998.

[47] X. G. Wang, A. Chaka, and M. Scheffler. Effect of the environment on alpha-al2o3 (0001) surface structures. *Phys. Rev. Lett.*, 84(16):3650–3653, 2000.

[48] E. Protopopoff and P. Marcus. Potential-ph diagrams for hydroxyl and hydrogen adsorbed on a copper surface. *Electrochim. Acta.*, 51(3):408–417, October 2005.

[49] P. Marcus and E. Protopopoff. Potential-ph diagrams for adsorbed species - application to sulfur adsorbed on iron in water at 25-degrees-c and 300-degrees-c. *J. Electrochem. Soc.*, 137(9):2709–2712, September 1990.

[50] J.-S. Filhol and M. Neurock. Elucidation of the electrochemical activation of water over pd by first principles. *Angew. Chem. Int. Ed.*, 45(3):402–406, 2006.

[51] C. Taylor, R. G. Kelly, and M. Neurock. First-principles calculations of the electrochemical reactions of water at an immersed ni(111)/h2o interface. *J. Electrochem. Soc.*, 153(12):E207–E214, 2006.

[52] Christopher D. Taylor, Robert G. Kelly, and Matthew Neurock. First-principles prediction of equilibrium potentials for water activation by a series of metals. *J. Electrochem. Soc.*, 154(12):F217–F221, December 2007.

[53] T. Jacob. Theoretical investigations on the potential-induced formation of pt-oxide surfaces. *J. Electroanal. Chem.*, 607(1-2):158–166, September 2007.

[54] J. Rossmeisl, J. K. Nørskov, C. D. Taylor, M. J. Janik, and M. Neurock. Calculated phase diagrams for the electrochemical oxidation and reduction of water over pt(111). *J. Phys. Chem. B*, 110(43):21833–21839, November 2006.

[55] M. Pourbaix. *Atlas of Electrochemical Equilibria*. Pergamon Press, 1966.

[56] C. Taylor, R. G. Kelly, and M. Neurock. Theoretical analysis of the nature of hydrogen at the electrochemical interface between water and a ni(111) single-crystal electrode. *J. Electrochem. Soc.*, 154(3):F55–F64, March 2007.

[57] A. D. McNaught and A. Wilkinson. *IUPAC. Compendium of Chemical Terminology, 2nd ed.* Blackwell Scientific Publications, Oxford, 1997.

[58] M. T. M. Koper and R. A. van Santen. Interaction of h, o and oh with metal surfaces. *J. Electroanal. Chem.*, 472(2):126–136, August 1999.

[59] M. P. Hyman and J. W. Medlin. Theoretical study of the adsorption and dissociation of oxygen on pt(111) in the presence of homogeneous electric fields. *J. Phys. Chem. B*, 109(13):6304–6310, 2005.

[60] Y. H. Fang and Z. P. Liu. Surface phase diagram and oxygen coupling kinetics on flat and stepped pt surfaces under electrochemical potentials. *J. Phys. Chem. C*, 113(22):9765–9772, 2009.

[61] P.W. Atkins. *Physical Chemistry, 6th ed.,*. Oxford University Press: Oxford U.K., 1998.

[62] R.C. Weast. *CRC Hanbook of Chemistry and Physics*. The Chemical Rubber Company: Cleveland , OH, 1968-1969.

[63] J. Greeley and J.K. Nørskov. Electrochemical dissolution of surface alloys in acids: Thermodynamic trends from first-principles calculations. *Electrochim. Acta.*, 52(19):5829–5836, May 2007.

[64] A. Verdaguer, G. M. Sacha, H. Bluhm, and M. Salmeron. Molecular structure of water at interfaces: Wetting at the nanometer scale. *Chem. Rev.*, 106(4):1478–1510, April 2006.

[65] A. Glebov, A. P. Graham, A. Menzel, and J. P. Toennies. Orientational ordering of two-dimensional ice on pt(111). *J. Chem. Phys.*, 106(22):9382–9385, June 1997.

[66] M. Morgenstern, J. Muller, T. Michely, and G. Comsa. The ice bilayer on pt(111): Nucleation, structure and melting. *Z. Phys. Chem.*, 198:43–72, 1997.

[67] L. E. Firment and G. A. Somorjai. Low-energy electron-diffraction studies of the surfaces of molecular-crystals (ice, ammonia, naphthalene, benzene). *Surf. Sci.*, 84(2):275–294, 1979.

[68] G. Zimbitas, S. Haq, and A. Hodgson. The structure and crystallization of thin water films on pt(111). *J. Chem. Phys.*, 123(17):174701–9, November 2005.

[69] S. Haq, J. Harnett, and A. Hodgson. Growth of thin crystalline ice films on pt(1 1 1). *Surf. Sci.*, 505:171–182, May 2002.

[70] H. Ogasawara, B. Brena, D. Nordlund, M. Nyberg, A. Pelmenschikov, L. G. M. Pettersson, and A. Nilsson. Structure and bonding of water on pt(111). *Phys. Rev. Lett.*, 89(27):276102, Dec 2002.

[71] G. S. Karlberg and G. Wahnstrom. Density-functional based modeling of the intermediate in the water production reaction on pt(111). *Phys. Rev. Lett.*, 92(13):136103, April 2004.

[72] Sheng Meng, E. G. Wang, and Shiwu Gao. Water adsorption on metal surfaces: A general picture from density functional theory studies. *Phys. Rev. B*, 69(19):195404–, May 2004.

[73] K. Bedurftig, S. Volkening, Y. Wang, J. Wintterlin, K. Jacobi, and G. Ertl. Vibrational and structural properties of oh adsorbed on pt(111). *The Journal of Chemical Physics*, 111(24):11147–11154, 1999.

[74] T. Schiros, L.-A. Naslund, K. Andersson, J. Gyllenpalm, G. S. Karlberg, M. Odelius, H. Ogasawara, L. G. M. Pettersson, and A. Nilsson. Structure and bonding of the water-hydroxyl mixed phase on pt(111). *J. Phys. Chem. C*, 111(41):15003–15012, OCT 18 2007.

[75] A. Michaelides and P. Hu. A density functional theory study of hydroxyl and the intermediate in the water formation reaction on pt. *J. Chem. Phys.*, 114(1):513–519, January 2001.

[76] A. Michaelides and P. Hu. Catalytic water formation on platinum: A first-principles study. *J. Am. Chem. Soc.*, 123(18):4235–4242, May 2001.

[77] G. Held, C. Clay, S. D. Barrett, S. Haq, and A. Hodgson. The structure of the mixed oh+h2o overlayer on pt111. *J. Chem. Phys.*, 123(6):064711, August 2005.

[78] P. J. Feibelman. Comment on "vibrational recognition of hydrogen-bonded water networks on a metal surface". *Phys. Rev. Lett.*, 91(5):059601–, July 2003.

[79] S. Meng. Dynamical properties and the proton transfer mechanism in the wetting water layer on pt(111). *Surf. Sci.*, 575(3):300–306, February 2005.

[80] L. Delle Site, L. M. Ghiringhelli, O. Andreussi, D. Donadio, and M. Parrinello. The interplay between surface-water and hydrogen bonding in a water adlayer on pt(111) and ag(111). *Journal of Physics-condensed Matter*, 19(24):1–7, 2007.

[81] M. Otani, I. Hamada, O. Sugino, Y. Morikawa, Y. Okamoto, and T. Ikeshoji. Structure of the water/platinum interface–a first principles simulation under bias potential. *Phys. Chem. Chem. Phys.*, 10(25):3609–3612, 2008.

[82] N.M. Markovic and P. N. Ross. -. *CATTECH.*, 4:110, 2000.

[83] J. Larmine and A. Dicks. *Fuel Cell Systems Explained*. J. Wiley, Chichester, West Sussex, 2003.

[84] Y. X. Wang and P. B. Balbuena. Design of oxygen reduction bimetallic catalysts: Ab-initio-derived thermodynamic guidelines. *J. Phys. Chem. B*, 109(40):18902–18906, October 2005.

[85] A. B. Anderson, J. Roques, S. Mukerjee, V. S. Murthi, N. M. Markovic, and V. Stamenkovic. Activation energies for oxygen reduction on platinum alloys: Theory and experiment. *J. Phys. Chem. B*, 109(3):1198–1203, January 2005.

[86] A. B. Anderson and T. V. Albu. Catalytic effect of platinum on oxygen reduction - an ab initio model including electrode potential dependence. *J. Electrochem. Soc.*, 147(11):4229–4238, November 2000.

[87] A. B. Anderson. O-2 reduction and co oxidation at the pt-electrolyte interface. the role of h2o and oh adsorption bond strengths. *Electrochim. Acta.*, 47(22-23):3759–3763, August 2002.

[88] M. P. Hyman and J. W. Medlin. Mechanistic study of the electrochemical oxygen reduction reaction on pt(111) using density functional theory. *J. Phys. Chem. B*, 110(31):15338–15344, 2006.

[89] T. Jacob. The mechanism of forming h2o from h-2 and o-2 over a pt catalyst via direct oxygen reduction. *Fuel Cell.*, 6(3-4):159–181, 2006.

[90] P. Vassilev, R. A. van Santen, and M. T. M. Koper. Ab initio studies of a water layer at transition metal surfaces. *J. Chem. Phys.*, 122(5):054701, February 2005.

[91] A. U. Nilekar and M. Mavrikakis. Improved oxygen reduction reactivity of platinum monolayers on transition metal surfaces. *Surf. Sci.*, 602(14):L89–L94, July 2008.

[92] G. S. Karlberg, J. Rossmeisl, and J. K. Nørskov. Estimations of electric field effects on the oxygen reduction reaction based on the density functional theory. *Phys. Chem. Chem. Phys.*, 9:5158–5161, 2007.

[93] V. Stamenkovic, B. S. Mun, K. J. J. Mayrhofer, P. N. Ross, N. M. Markovic, J. Rossmeisl, J. Greeley, and J. K. Nørskov. Changing the activity of electrocatalysts for oxygen reduction by tuning the surface electronic structure. *Angew. Chem. Int. Ed.*, 45(18):2897–2901, 2006.

[94] J. K. Nørskov, T. Bligaard, A. Logadottir, S. Bahn, L. B. Hansen, M. Bollinger, H. Bengaard, B. Hammer, Z. Sljivancanin, M. Mavrikakis, Y. Xu, S. Dahl, and C. J. H. Jacobsen. Universality in heterogeneous catalysis. *J. Catal.*, 209(2):275–278, July 2002.

[95] S. D. Miller and J. R. Kitchin. Relating the coverage dependence of oxygen adsorption on au and pt fcc(111) surfaces through adsorbate-induced surface electronic structure effects. *Surf. Sci.*, 603(5):794–801, 2009.

[96] G. Rovida, F. Pratesi, M. Magliett, and E. Ferroni. Effects of oxygen on silver surface-structure. *Journal of Vacuum Science & Technology*, 9(2):796–&, 1972.

[97] J. Schnadt, A. Michaelides, J. Knudsen, R. T. Vang, K. Reuter, E. Laegsgaard, M. Scheffler, and F. Besenbacher. Revisiting the structure of the p(4x4) surface oxide on ag(111). *Phys. Rev. Lett.*, 96(14):146101, 2006.

[98] S.L. Horswell, A.L.N. Pinheiro, E.R. Savinova, M. Danckwerts, B. Pettinger, M.-S. Zei, and G. Ertl. A comparative study of hydroxide adsorption on the (111), (110), and (100) faces of silver with cyclic voltammetry, ex situ electron diffraction, and in situ second harmonic generation. *Langmuir*, 20(25):10970–10981, 2004.

[99] B. B. Blizanac, P. N. Ross, and N. M. Markovic. Oxygen reduction on silver low-index single-crystal surfaces in alkaline solution: Rotating ring disk(ag(hkl)) studies. *J. Phys. Chem. B*, 110(10):4735–4741, March 2006.

[100] E. R. Savinova, A. Scheybal, M. Danckwerts, U. Wild, B. Pettinger, K. Doblhofer, R. Schlogl, and G. Ertl. Structure and dynamics of the interface between a ag single crystal electrode and an aqueous electrolyte. *Faraday Discuss.*, 121:181–198, 2002.

[101] V. Maurice, L. H. Klein, H. H. Strehblow, and P. Marcus. In situ stm study of the surface structure, dissolution, and early stages of electrochemical oxidation of the ag(111) electrode. *J. Phys. Chem. C*, 111:16351–16361, 2007.

[102] B. Beverskog and I. Puigdomenech. Revised pourbaix diagrams for nickel at 25-300 degrees c. *Corrosion. Sci.*, 39(5):969–980, 1997.

[103] C.F Baes and R.E. Mesmer. *The Hydrolysis of Cations*. Krieger Publishing Company, Malabar, FL, 1976.

[104] J. T. Stuckless, C. E. Wartnaby, N. Al-Sarraf, St. J. B. Dixon-Warren, M. Kovar, and D. A. King. Oxygen chemisorption and oxide film growth on ni100, 110, and 111: Sticking probabilities and microcalorimetric adsorption heats. *J. Chem. Phys.*, 106(5):2012–2030, 1997.

[105] A. R. Kortan and R. L. Park. Phase-diagram of oxygen chemisorbed on nickel(111). *Phys. Rev. B*, 23(12):6340–6347, 1981.

[106] H. A. Gasteiger, S. S. Kocha, B. Sompalli, and F. T. Wagner. Activity benchmarks and requirements for pt, pt-alloy, and non-pt oxygen reduction catalysts for pemfcs. *Appl. Catal. B Environ.*, 56(1-2):9–35, March 2005.

[107] S. Mukerjee and S. Srinivasan. Enhanced electrocatalysis of oxygen reduction on platinum alloys in proton-exchange membrane fuel-cells. *J. Electroanal. Chem.*, 357(1-2):201–224, October 1993.

[108] T. Toda, H. Igarashi, H. Uchida, and M. Watanabe. Enhancement of the electroreduction of oxygen on pt alloys with fe, ni, and co. *J. Electrochem. Soc.*, 146(10):3750–3756, October 1999.

[109] V. R. Stamenkovic, B. S. Mun, M. Arenz, K. J. J. Mayrhofer, C. A. Lucas, G. F. Wang, P. N. Ross, and N. M. Markovic. Trends in electrocatalysis on extended and nanoscale pt-bimetallic alloy surfaces. *Nat. Mater.*, 6(3):241–247, March 2007.

[110] V. R. Stamenkovic, B. Fowler, B. S. Mun, G. F. Wang, P. N. Ross, C. A. Lucas, and N. M. Markovic. Improved oxygen reduction activity on pt3ni(111) via increased surface site availability. *Science*, 315(5811):493–497, January 2007.

[111] R. Srivastava, P. Mani, N. Hahn, and P. Strasser. Efficient oxygen reduction fuel cell electrocatalysis on voltammetrically dealloyed pt-cu-co nanoparticles. *Angew. Chem. Int. Ed.*, 46(47):8988–8991, 2007.

[112] M. Wakisaka, H. Suzuki, S. Mitsui, H. Uchida, and M. Watanabe. Increased oxygen coverage at pt-fe alloy cathode for the enhanced oxygen reduction reaction studied by ec-xps. *J. Phys. Chem. C*, 112(7):2750–2755, February 2008.

[113] L. J. Wan, T. Moriyama, M. Ito, H. Uchida, and M. Watanabe. In situ stm imaging of surface dissolution and rearrangement of a pt-fe alloy electrocatalyst in electrolyte solution. *Chem. Comm.*, -(1):58–59, 2002.

[114] D. J. Chadi and Marvin L. Cohen. Special points in the brillouin zone. *Phys. Rev. B*, 8(12):5747–5753, Dec 1973.

[115] H. J. Monkhorst and J. D. Pack. Special points for brillouin-zone integrations. *Phys. Rev. B*, 13(12):5188–5192, Jun 1976.

[116] G. H. Johannesson, T. Bligaard, A. V. Ruban, H. L. Skriver, K. W. Jacobsen, and J. K. Nørskov. Combined electronic structure and evolutionary search approach to materials design. *Phys. Rev. Lett.*, 88(25):255506, June 2002.

[117] T. Bligaard, G. H. Johannesson, A. V. Ruban, H. L. Skriver, K. W. Jacobsen, and J. K. Nørskov. Pareto-optimal alloys. *Appl. Phys. Lett.*, 83(22):4527–4529, December 2003.

[118] U. A. Paulus, A. Wokaun, G. G. Scherer, T. J. Schmidt, V. Stamenkovic, N. M. Markovic, and P. N. Ross. Oxygen reduction on high surface area pt-based alloy catalysts in comparison to well defined smooth bulk alloy electrodes. *Electrochim. Acta.*, 47(22-23):3787–3798, August 2002.

[119] J. L. Zhang, M. B. Vukmirovic, Y. Xu, M. Mavrikakis, and R. R. Adzic. Controlling the catalytic activity of platinum-monolayer electrocatalysts for oxygen reduction with different substrates. *Angew. Chem. Int. Ed.*, 44(14):2132–2135, 2005.

[120] J. Rossmeisl and J. K. Nørskov. Electrochemistry on the computer: Understanding how to tailor the metal overlayers for the oxygen reduction reaction (a perspective on the article, "improved oxygen reduction reactivity of platinum monolayers on transition metal surfaces", by au nilekar and m. mavrikakis). *Surf. Sci.*, 602(14):2337–2338, July 2008.

[121] Y. Xu, A. V. Ruban, and M. Mavrikakis. Adsorption and dissociation of o_2 on pt-co and pt-fe alloys. *J. Am. Chem. Soc.*, 126(14):4717–4725, April 2004.

[122] B. Hammer and J. K. Nørskov. Theoretical surface science and catalysis–calculations and concepts. In Bruce C. Gates and Helmut Knozinger, editors, *Impact of Surface Science on Catalysis*, volume Volume 45, pages 71–129. Academic Press, 2000.

[123] P. A. Thiel and T. E. Madey. The interaction of water with solid-surfacesfundamental-aspects. *Surf. Sci. Rep.*, 7(6-8):211–385, 1987.

[124] Michael A. Henderson. The interaction of water with solid surfaces: fundamental aspects revisited. *Surf. Sci. Rep.*, 46(1-8):1–308, May 2002.

[125] C. Sachs, M. Hildebrand, S. Volkening, J. Wintterlin, and G. Ertl. Spatiotemporal self-organization in a surface reaction: From the atomic to the mesoscopic scale. *Science*, 293(5535):1635–1638, August 2001.

[126] C. Sachs, M. Hildebrand, S. Volkening, J. Wintterlin, and G. Ertl. Reaction fronts in the oxidation of hydrogen on pt(111): Scanning tunneling microscopy experiments and reaction-diffusion modeling. *J. Chem. Phys.*, 116(13):5759–5773, April 2002.

[127] G. S. Karlberg, T. F. Jaramillo, E. Skulason, J. Rossmeisl, T. Bligaard, and J. K. Nørskov. Cyclic voltammograms for h on pt(111) and pt(100) from first principles. *Phys. Rev. Lett.*, 99:126101, 2007.

[128] M. T. M. Koper and J. J. Lukkien. Modeling the butterfly: the voltammetry of (root 3 x root 3)r30 degrees and p(2x2) overlayers on (111) electrodes. *J. Electroanal. Chem.*, 485(2):161–165, May 2000.

[129] M. T. M. Koper, J. J. Lukkien, N. P. Lebedeva, J. M. Feliu, and R. A. van Santen. Adsorbate interactions and phase transitions at the stepped platinum/electrolyte interface: experiment compared with monte carlo simulations. *Surf. Sci.*, 478(1-2):L339–L344, 2001.

[130] M. T. M. Koper and J. J. Lukkien. Modeling the butterfly: influence of lateral interactions and adsorption geometry on the voltammetry at (111) and (100) electrodes. *Surf. Sci.*, 498(1-2):105–115, 2002.

[131] C. Saravanan, M. T. M. Koper, N. M. Markovic, M. Head-Gordon, and P. N. Ross. Modeling base voltammetry and co electrooxidation at the pt(111)-electrolyte interface: Monte carlo simulations including anion adsorption. *Phys. Chem. Chem. Phys.*, 4(12):2660–2666, 2002.

[132] C. G. M. Hermse, A. P. van Bavel, M. T. M. Koper, J. J. Lukkien, R. A. van Santen, and A. P. J. Jansen. Modelling the butterfly: (root 3 x root 7) ordering on fcc(111) surfaces. *Surf. Sci.*, 572(2-3):247–260, 2004.

[133] G. S. Karlberg and G. Wahnstrom. An interaction model for oh+h2o-mixed and pure h2o overlayers adsorbed on pt(111). *J. Chem. Phys.*, 122(19):194705, 2005.

[134] G. S. Karlberg, G. Wahnstrom, C. Clay, G. Zimbitas, and A. Hodgson. Water desorption from an oxygen covered pt(111) surface: Multichannel desorption. *J. Chem. Phys.*, 124(20):204712, 2006.

[135] A. Michaelides, A. Alavi, and D. A. King. Different surface chemistries of water on ru0001: From monomer adsorption to partially dissociated bilayers. *J. Am. Chem. Soc.*, 125(9):2746–2755, March 2003.

[136] V. Rai, M. Aryanpour, and H. Pitsch. First-principles analysis of oxygen-containing adsorbates formed from the electrochemical discharge of water on pt(111). *J. Phys. Chem. C*, 112(26):9760–9768, July 2008.

[137] V. A. Ranea, A. Michaelides, R. Ramrez, P. L. de Andres, J. A. Vergs, and D. A. King. Water dimer diffusion on pd111 assisted by an h-bond donor-acceptor tunneling exchange. *Phys. Rev. Lett.*, 92(13):136104–, April 2004.

[138] M. Wakisaka, H. Suzuki, S. Mitsui, H. Uchida, and M. Watanabe. Identification and quantification of oxygen species adsorbed on pt(111) single-crystal and poly-crystalline pt electrodes by photoelectron spectroscopy. *Langmuir*, 25(4):1897–1900, February 2009.

[139] E. Sibert, R. Faure, and R. Durand. High frequency impedance measurements on pt(111) in sulphuric and perchloric acids. *J. Electroanal. Chem.*, 515(1-2):71–81, November 2001.

[140] N. Garcia-Araez, V. Climent, E. Herrero, J. M. Feliu, and J. Lipkowski. Thermodynamic approach to the double layer capacity of a pt(111) electrode in perchloric acid solutions. *Electrochim. Acta.*, 51(18):3787–3793, May 2006.

[141] B. E. Conway. Electrochemical oxide film formation at noble-metals as a surface-chemical process. *Progr. Surf. Sci.*, 49(4):331–452, 1995.

[142] A. Berna, V. Climent, and J. M. Feliu. New understanding of the nature of oh adsorption on pt(111) electrodes. *Electrochem. Comm.*, 9(12):2789–2794, December 2007.

[143] M. P. Hyman and J. W. Medlin. Effects of electronic structure modifications on the adsorption of oxygen reduction reaction intermediates on model pt(111)-alloy surfaces. *J. Phys. Chem. C*, 111(45):17052–17060, November 2007.

[144] S. Trasatti. Electrocatalysis: understanding the success of dsa (r). *Electrochim. Acta.*, 45(15-16):2377–2385, 2000.

[145] S Trasatti. *Interfacial Electrochemistry: Theory, Experiment, and Applications*, chapter 43, pages 769–792. Marcel Dekker, New York, 1999.

[146] H. B. Beer. The invention and industrial-development of metal anodes. *J. Electrochem. Soc.*, 127(8):C303–C307, 1980.

[147] D. B. Rogers, R. D. Shannon, A. W. Sleight, and J. L. Gillson. Crystal chemistry of metal dioxides with rutile-related structures. *Inorg. Chem.*, 8(4):841, 1969.

[148] J. Rossmeisl, K. Dimitrievski, P. Siegbahn, and J. K. Nørskov. Comparing electrochemical and biological water splitting. *J. Phys. Chem. C*, 111(51):18821–18823, 2007.

[149] J. Paier, M. Marsman, K. Hummer, G. Kresse, I. C. Gerber, and J. G. Angyan. Screened hybrid density functionals applied to solids. *J. Chem. Phys.*, 124(15):154709, 2006.

[150] L. Wang, T. Maxisch, and G. Ceder. Oxidation energies of transition metal oxides within the gga+u framework. *Phys. Rev. B*, 73(19):195107, May 2006.

[151] V. I. Anisimov, J. Zaanen, and O. K. Andersen. Band theory and mott insulators: Hubbard u instead of stoner i. *Phys. Rev. B*, 44(3):943, July 1991.

[152] S. L. Dudarev, G. A. Botton, S. Y. Savrasov, C. J. Humphreys, and A. P. Sutton. Electron-energy-loss spectra and the structural stability of nickel oxide: An lsda+u study. *Phys. Rev. B*, 57(3):1505–, January 1998.

[153] J. B. Goodenough. Metallic oxides. *Prog. Solid State Chem.*, 5:145, 1971.

[154] S. G. Bratsch. Standard electrode-potentials and temperature coefficients in water at 298.15-k. *J. Phys. Chem. Ref. Data*, 18(1):1–21, 1989.

[155] D. R. Lide, editor. *CRC Handbook of Chemistry and Physics*. CRC, New York, 1996.

[156] S. Kurth, J. P. Perdew, and P. Blaha. Molecular and solid-state tests of density functional approximations: Lsd, ggas, and meta-ggas. *Int. J. Quant. Chem.*, 75(4-5):889–909, 1999.

[157] C. D. Gelatt, A. R. Williams, and V. L. Moruzzi. Theory of bonding of transition-metals to non-transition metals. *Phys. Rev. B*, 27(4):2005–2013, 1983.

[158] J. Friedel and C. M. Sayers. Role of d-d electron correlations in cohesion and ferromagnetism of transition-metals. *Journal De Physique*, 38(6):697–705, 1977.

[159] M. S. S. Brooks and B. Johansson. Exchange integral matrices and cohesive energies of transition-metal atoms. *Journal of Physics F-metal Physics*, 13(10):L197–L202, 1983.

[160] Euro chlor (representing the chloro-alkali industry, chlorine industry review 2007- 2008).

[161] S. Trasatti. Electrocatalysis in the anodic evolution of oxygen and chlorine. *Electrochim. Acta.*, 29(11):1503–1512, 1984.

[162] N. Furuya and H. Aikawa. Comparative study of oxygen cathodes loaded with ag and pt catalysts in chlor-alkali membrane cells. *Electrochim. Acta.*, 45(25-26):4251–4256, 2000.

[163] Los Alamos National Laboratory. Chlor-alkali cells. http://www.lanl.gov/orgs/mpa/mpa11/chlor.htm, August 2009.

[164] A. M. Couper, D. Pletcher, and F. C. Walsh. Electrode materials for electrosynthesis. *Chem. Rev.*, 90(5):837–865, July 1990.

[165] *U.S. Patent, 165.802, 1875*, 1875.

[166] D. Crihan, M. Knapp, S. Zweidingey, E. Lundgren, C. J. Weststrate, J. N. Andersen, A. P. Seitsonen, and H. Over. Stable deacon process for hcl oxidation over ruo2. *Angew. Chem. Int. Ed.*, 47(11):2131–2134, 2008.

[167] S. Zweidinger, D. Crihan, M. Knapp, J. P. Hofmann, A. P. Seitsonen, C. J. Weststrate, E. Lundgren, J. N. Andersen, and H. Over. Reaction mechanism of the oxidation of hcl over ruo2(110). *J. Phys. Chem. C*, 112(27):9966–9969, July 2008.

[168] N. Lopez, J. Gomez-Segura, R. P. Marin, and J. Perez-Ramirez. Mechanism of hcl oxidation (deacon process) over ruo2. *J. Catal.*, 255(1):29–39, April 2008.

[169] T. Hepel, F. H. Pollak, and W. E. Ogrady. Chlorine evolution and reduction processes at oriented single-crystal ruo2 electrodes. *J. Electrochem. Soc.*, 133(1):69–75, 1986.

[170] E. Guerrini, V. Consonni, and S. Trasatti. Surface and electrocatalytic properties of well-defined and vicinal ruo2 single crystal faces. *J. Solid State Electrochem.*, 9(5):320–329, 2005.

[171] R.G. Erenburg, L.I. Krishtalik, and I.P. Yaroshevskaya. -. *Elektrokhimiya*, 11:1068, 1975.

[172] R.G. Erenburg, L.I. Krishtalik, and I.P. Yaroshevskaya. -. *Elektrokhimiya*, 11:1072, 1975.

[173] R.G. Erenburg, L.I. Krishtalik, and I.P. Yaroshevskaya. -. *Elektrokhimiya*, 11:1236, 1975.

[174] R.G. Erenburg. -. *Elektrokhimiya*, 20:1602, 1984.

[175] J. L. Fernandez, M. R. G. de Chialvo, and A. C. Chialvo. Kinetic study of the chlorine electrode reaction on ti/ruo2 through the polarisation resistance part 1: experimental results and analysis of the ph effects. *Electrochim. Acta.*, 47(7):1129–1136, January 2002.

[176] M. Thomassen, C. Karlsen, B. Borresen, and R. Tunold. Kinetic investigation of the chlorine reduction reaction on electrochemically oxidised ruthenium. *Electrochim. Acta.*, 51(14):2909–2918, 2006.

[177] J. L. Fernandez, M. R. G. de Chialvo, and A. C. Chialvo. Kinetic study of the chlorine electrode reaction on ti/ruo2 through the polarisation resistance part ii: mechanistic analysis. *Electrochim. Acta.*, 47(7):1137–1144, January 2002.

[178] J. L. Fernandez, M. R. G. de Chialvo, and A. C. Chialvo. Kinetic study of the chlorine electrode reaction on ti/ruo2 through the polarisation resistance part iii: proposal of a reaction mechanism. *Electrochim. Acta.*, 47(7):1145–1152, January 2002.

[179] J. Rossmeisl, Z.-W. Qu, H. Zhu, G. J. Kroes, and J. K. Nørskov. Electrolysis of water on oxide surfaces. *J. Electroanal. Chem.*, 607(1-2):83–89, September 2007.

[180] Y. D. Pankratiev. Correlation between oxygen binding energy and catalytic activity of oxides. *React. Kinet. Catal. Lett.*, 20(3):255–259, September 1982.

[181] A. T. Kuhn and C. J. Mortimer. Kinetics of chlorine evolution and reduction on titanium-supported metal-oxides especially ruo2 and iro2. *J. Electrochem. Soc.*, 120(2):231–234, 1973.

[182] T. Arikado, C. Iwakura, and H. Tamura. Some oxide catalysts for anodic evolution of chlorine - reaction-mechanism and catalytic activity. *Electrochim. Acta.*, 23(1):9–15, 1978.

[183] E. J. Kelly, D. E. Heatherly, C. E. Vallet, and C. W. White. Application of ion-implantation to the study of electrocatalysis .1. chlorine evolution at ru-implanted titanium electrodes. *J. Electrochem. Soc.*, 134(7):1667–1675, July 1987.

[184] E. J. Kelly, C. E. Vallet, and C. W. White. Application of ion-implantation rbs to the study of electrocatalysis - comparison of chlorine evolution at ir-implanted and ru-implanted titanium electrodes. *J. Electrochem. Soc.*, 137(8):2482–2491, August 1990.

[185] O. Muller and R. Roy. Formation and stability of platinum and rhodium oxides at high oxygen pressures and structures of pt304, beta-pto2 and rho2. *J. Less Common Met.*, 16(2):129–&, 1968.

[186] K. B. Schwartz and C. T. Prewitt. Structural and electronic properties of binary and ternary platinum oxides. *J. Phys. Chem. Solids*, 45(1):1–21, 1984.

[187] S. P. Zhuo and K. Sohlberg. Platinum dioxide phases: Relative thermodynamic stability and kinetics of inter-conversion from first-principles. *Phys. B Condens. Matter*, 381(1-2):12–19, May 2006.

[188] L. I. Krishtalik. Kinetics and mechanism of anodic chlorine and oxygen evolution reactions on transition-metal oxide electrodes. *Electrochim. Acta.*, 26(3):329–337, 1981.

[189] A. Shavorskiy, M. J. Gladys, and G. Held. Chemical composition and reactivity of water on hexagonal pt-group metal surfaces. *Phys. Chem. Chem. Phys.*, 10(40):6150–6159, 2008.

[190] V. Rai. *Molecular Modeling of PEM Fuel Cell Electrochemistry.* PhD thesis, Stanford University, 2009.

[191] A. P. J. Jansen. Monte-carlo simulations of chemical-reactions on a surface with time-dependent reaction-rate constants. *Comput. Phys. Comm.*, 86(1-2):1–12, 1995.

[192] P. J. Feibelman. Partial dissociation of water on ru(0001). *Science*, 295(5552):99–102, January 2002.

[193] G. Held and D. Menzel. The structure of the $(\sqrt{} \times \sqrt{3})r30°$ bilayer of d2o on ru(001). *Surf. Sci.*, 316(1-2):92–102, September 1994.

[194] K. Andersson, A. Nikitin, L. G. M. Pettersson, A. Nilsson, and H. Ogasawara. Water dissociation on ru(001): An activated process. *Phys. Rev. Lett.*, 93(19):196101, November 2004.

[195] N. S. Faradzhev, K. L. Kostov, P. Feulner, T. E. Madey, and D. Menzel. Stability of water monolayers on ru(0001): Thermal and electronically induced dissociation. *Chem. Phys. Lett.*, 415(1-3):165–171, 2005.

[196] S. Meng, E. G. Wang, C. Frischkorn, M. Wolf, and S. W. Gao. Consistent picture for the wetting structure of water/ru(0001). *Chemical Physics Letters*, 402(4-6):384–388, 2005.

[197] M. Tatarkhanov, E. Fomin, M. Salmeron, K. Andersson, H. Ogasawara, L. G. M. Pettersson, A. Nilsson, and J. I. Cerda. The structure of mixed h2o-oh monolayer films on ru(0001). *J. Chem. Phys.*, 129(15):154109, October 2008.

[198] G. Held and D. Menzel. Isotope effects in structure and kinetics of water adsorbates on ru(001). *Surf. Sci.*, 327(3):301–320, April 1995.

[199] C. Clay, S. Haq, and A. Hodgson. Intact and dissociative adsorption of water on ru(0001). *Chemical Physics Letters*, 388(1-3):89–93, April 2004.

[200] M. J. Gladys, A. A. El-Zein, A. Mikkelsen, J. N. Anderson, and G. Held. Modifying the adsorption characteristics of water on ru0001 with preadsorbed oxygen. *Phys. Rev. B*, 78(3):035409–11, July 2008.

[201] C. Clay, S. Haq, and A. Hodgson. Hydrogen bonding in mixed oh+h_2o overlayers on pt(111). *Phys. Rev. Lett.*, 92(4):046102, January 2004.

[202] P. Cabrera-Sanfelix, D. Sanchez-Portal, A. Mugarza, T. K. Shimizu, M. Salmeron, and A. Arnau. Water adsorption on o(2 x 2)/ru(0001): Stm experiments and first-principles calculations. *Phys. Rev. B*, 76(20):205438, 2007.

[203] P. Cabrera-Sanfelix, A. Arnau, A. Mugarza, T. K. Shimizu, M. Salmeron, and D. Sanchez-Portal. Decisive role of the energetics of dissociation products in the adsorption of water on o/ru(0001). *Phys. Rev. B*, 78(15):155438, October 2008.

[204] M. Haruta, T. Kobayashi, H. Sano, and N Yamada. Novel gold catalysts for the oxidation of carbon-monoxide at a temperature far below 0-degrees-c. *Chem. Lett.*, 2:405–408, 1987.

[205] P. Vassilev and M. T. M. Koper. Electrochemical reduction of oxygen on gold surfaces: A density functional theory study of intermediates and reaction paths. *J. Phys. Chem. C*, 111(6):2607–2613, February 2007.

[206] B. K. Min, X. Deng, D. Pinnaduwage, R. Schalek, and C. M. Friend. Oxygen-induced restructuring with release of gold atoms from au(111). *Phys. Rev. B*, 72(12):121410, September 2005.

[207] M. M. Biener, J. Biener, and C. M. Friend. Revisiting the s-au(111) interaction: Static or dynamic? *Langmuir*, 21(5):1668–1671, March 2005.

[208] S. M. Driver, T. F. Zhang, and D. A. King. Massively cooperative adsorbate-induced surface restructuring and nanocluster formation. *Angew. Chem. Int. Ed.*, 46(5):700–703, 2007.

[209] A. E. Baber, S. C. Jensen, E. V. Iski, and E. C. H. Sykes. Extraordinary atomic mobility of au111 at 80 kelvin: Effect of styrene adsorption. *J. Am. Chem. Soc.*, 128(48):15384–15385, December 2006.

[210] N. Saliba, D. H. Parker, and B. E. Koel. Adsorption of oxygen on au(111) by exposure to ozone. *Surf. Sci.*, 410(2-3):270–282, August 1998.

[211] K. A. Davis and D. W. Goodman. Propene adsorption on clean and oxygen-covered au(111) and au(100) surfaces. *J. Phys. Chem. B*, 104(35):8557–8562, September 2000.

[212] K. D. Gibson and S. J. Sibener. O atom induced gradual deconstruction of the 23 x root 13 au(111) surface. *J. Phys. Chem. A*, 111(49):12398–12401, 2007.

[213] J. J. Pireaux, M. Liehr, P. A. Thiry, J. P. Delrue, and R. Caudano. Electron spectroscopic characterization of oxygen-adsorption on gold surfaces .2. production of gold oxide in oxygen dc reactive sputtering. *Surf. Sci.*, 141(1):221–232, 1984.

[214] J. M. Gottfried, N. Elghobashi, S. L. M. Schroeder, and K. Christmann. Oxidation of gold by oxygen-ion sputtering. *Surf. Sci.*, 523(1-2):89–102, January 2003.

[215] N. D. S. Canning, D. Outka, and R. J. Madix. The adsorption of oxygen on gold. *Surf. Sci.*, 141(1):240–254, 1984.

[216] M. Todorova, W. X. Li, M. V. Ganduglia-Pirovano, C. Stampfl, K. Reuter, and M. Scheffler. Role of subsurface oxygen in oxide formation at transition metal surfaces. *Phys. Rev. Lett.*, 89(9):096103, August 2002.

[217] B. K. Min, A. R. Alemozafar, D. Pinnaduwage, X. Deng, and C. M. Friend. Efficient co oxidation at low temperature on au(111). *J. Phys. Chem. B*, 110(40):19833–19838, October 2006.

[218] R. A. Ojifinni, J. L. Gong, D. W. Flaherty, T. S. Kim, and C. B. Mullins. Annealing effect on reactivity of oxygen-covered au(111). *J. Phys. Chem. C*, 113(22):9820–9825, 2009.

[219] H. Shi and C. Stampfl. First-principles investigations of the structure and stability of oxygen adsorption and surface oxide formation at au(111). *Phys. Rev. B*, 76(7):075327, August 2007.

[220] T. A. Baker, C. M. Friend, and E. Kaxiras. Atomic oxygen adsorption on au(111) surfaces with defects. *J. Phys. Chem. C*, 113(8):3232–3238, 2009.

[221] T. A. Baker, C. M. Friend, and E. Kaxiras. Effects of chlorine and oxygen coverage on the structure of the au(111) surface. *J. Chem. Phys.*, 130(8):084701, 2009.

[222] R. A. Ojifinni, N. S. Froemming, J. Gong, M. Pan, T. S. Kim, J. M. White, G. Henkelman, and C. B. Mullins. Water-enhanced low-temperature co oxidation and isotope effects on atomic oxygen-covered au(111). *J. Am. Chem. Soc.*, 130(21):6801–6812, 2008.

[223] G. S. Karlberg. Adsorption trends for water, hydroxyl, oxygen, and hydrogen on transition-metal and platinum-skin surfaces. *Phys. Rev. B*, 74(15):153414, 2006.

[224] R. G. Quiller, T. A. Baker, X. Deng, M. E. Colling, B. K. Min, and C. M. Friend. Transient hydroxyl formation from water on oxygen-covered au(111). *J. Chem. Phys.*, 129(6):064702, 2008.

Appendix A

Entropy and ZPE Corrections

	TS	$T\Delta S$	ZPE	ΔZPE	$\Delta ZPE - T\Delta S$
H_2O(l)	0.67	0	0.56	0	0
OH* + $^1/_2$ H_2	0.2	-0.47	0.44	-0.12	0.35
O* + H_2	0.41	-0.27	0.34	-0.22	0.05
$^1/_2$O +H_2	0.73	0.05	0.32	-0.24	-0.29
H_2	0.41		0.27		
$^1/_2$ O_2	0.32		0.05		
O*	0		0.07		
OH*	0		0.3		
H*	0		0.17		

Table A.1: Zero Point Energies (ZPE) and entropic corrections at 300 K. ZPE are obtained from vibrational calculations within the harmonic approximation. Adapted from Ref. [11]

	TS	$T\Delta S$	ZPE	ΔZPE	$\Delta ZPE - T\Delta S$
H_2O(l)	0.67	0	0.56	0	0
$H_2O \rightarrow OH^c + {}^1/_2H_2$	0.2	-0.47	0.5	-0.06	0.41
$H_2O \rightarrow O^c + H_2$	0.41	-0.27	0.34	-0.22	0.05
$H_2O \rightarrow {}^1/_2O_2 + H_2$	0.73	0.05	0.32	-0.24	-0.29
$^1/_2Cl_2 \rightarrow Cl^c$	-	-0.34	-	0.02	0.37
Cl_2	0.69	-	0.06	-	-
H_2	0.41	-	0.27	-	-
$^1/_2$ O_2	0.32	-	0.95	-	-
Cl^c	0	-	0.05	-	-
O^c	0	-	0.07	-	-
OH^c	0	-	0.36	-	-
H^c	0	-	0.17	-	-

Table A.2: Zero Point Energies (ZPE) and entropic corrections at 298 K. ZPE are obtained from vibrational calculations within the harmonic approximation. ZPE for adsorbed species have been calculated for an adsorbate at the cus site of RuO_2. Taken from paper P5.

Appendix B

Energies for Surface Pourbaix Diagrams

	ΔE° / eV			ΔG° / eV			
Metal	Pt	Ag	Ni	Pt	Ag	Ni	Area
Clean surface	0.00	0.00	0.00	0.00	0.00	0.00	4 or 6
1/4 ML O*	1.50	2.10	0.32	1.55	2.15	0.37	4
1/3 ML O*	3.21	4.36	0.89	3.31	4.46	0.99	6
1/2 ML O*	3.59	5.29	1.58	3.69	5.39	1.68	4
2/3 ML O*	7.89	4.36	4.48	8.09	4.46	4.68	6
1/4 ML HO*	0.96	0.75	0.20	1.31	1.10	0.55	4
1/6 ML HO* in water	0.55	0.58	-0.08	0.90	0.93	0.27	6
1/3 ML HO* in water	1.02	1.33	0.16	1.72	2.03	0.86	6
ML HO* in water	2.08	2.23	2.65	3.13	3.28	0.44	6
2/3 ML HO* with water	3.31	3.58	3.22	4.71	4.98	4.62	6
1/6 ML HOO* in water	3.75	3.79	0.37	4.15	4.19	0.77	6
1/6 HOO* + 1/6 HO* in water	4.31	4.53	2.82	5.06	5.28	3.57	6
1/3 ML HOO* with water	7.53	7.76	4.45	8.33	8.56	5.25	6
Water Layer	-1.39	-1.32	-1.26	-1.39	-1.32	-1.26	6

Table B.1: Formation energies, ΔE°, and free energies of formation, ΔG°, for surface structures on Ag(111), Ni(111) and Pt(111). In addition the surface area in units of (1×1) surface cells is shown.

Appendix C

Pt_3X Alloys

C.1 OOH on Pt(111)

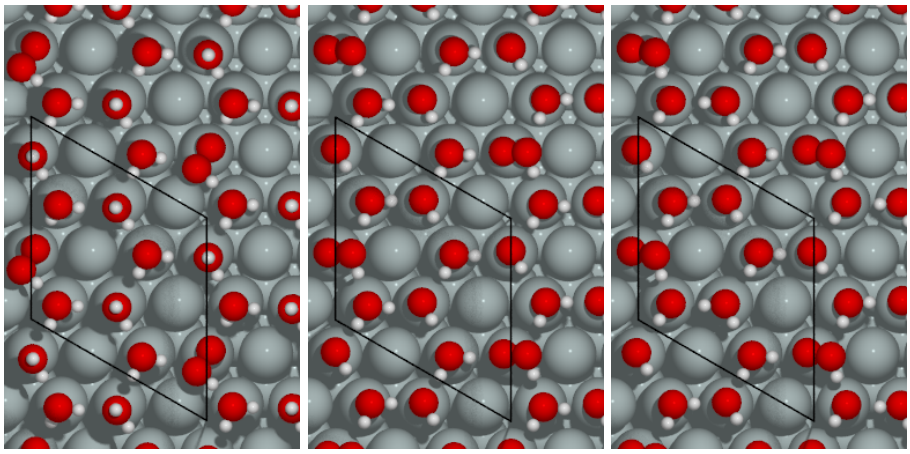

Figure C.1: OOH in a water layer and in mixed H_2O/OH layers. From left to right: 7 H_2O, 4 H_2O + 3 OH (A) and 4 H_2O + 3 OH (B). 4 H_2O + 3 OH (B) is created from 4 H_2O + 3 OH (A) by proton transfer from the H_2O, that accepts the hydrogen bond from OOH, to a neighboring OH.

$\Delta\Delta E_{OOH*}$	7 H_2O	4 H_2O + 3 OH (A)	4 H_2O + 3 OH (B)
Pt	-0.08	-0.03	-0.10
Pt_3Y (25 % Y)	-0.11	-0.05	-0.13
Pt_3Y (50 % Y)	0.07	0.09	-0.02
Pt_3Sc (25 % Sc)	-0.03	0.07	-0.01
Pt_3Sc (50 % Sc)	0.10	0.15	0.08

Table C.1: Formation energy of OOH in a water layer and in mixed H_2O/OH layers relative to the OOH formation energy in the OOH/H_2O $(\sqrt{3}\times\sqrt{3})R30^\circ$ superstructure, $\Delta\Delta E_{OOH*} = \Delta E_{OOH*} - \Delta E_{OOH*}^{Pt-(\sqrt{3}\times\sqrt{3})R30^\circ}$. The structures are shown in figure C.1 for Pt. The formation energies of OOH in similar structures on Pt_3Sc and Pt_3Y have been included for comparison. It does not mean they correspond to the most stable OOH intermediates on these surfaces. All energies are in eV.

Surface	$\Delta\Delta E_{OH*}$	$\Delta\Delta E_{O*}$	$\Delta\Delta E_{OOH*}$
Pt	0.00	0.00	0.00
Pt_3Sc-0%Sc$-(2\times2)O$	-0.04	0.41	-0.03
Pt_3Ni-0%Ni	0.04	0.19	0.03
Pt_3Co-25%Co	0.09	0.32	0.09
Pt_3Fe-25%Fe	0.09	0.31	0.08
Pt_3Fe-50%Fe	0.14	0.40	0.16
Pt_3Ni-50%Ni	0.05	0.31	0.06
Pt_3Y-0%Y$-(2\times2)O$	-0.11	0.01	-0.09
Pt_3Sc-25%Sc	0.08	0.13	0.05
Pt_3Ti-25%Ti	0.04	0.28	0.09
+3.5%-Pt	-0.14	-0.28	-0.11
Pt_3Y-50%Y	0.12	0.08	0.14
Pt_3Sc-50%Sc	0.09	0.33	0.16
Pt_3Sc-0%Sc	-0.06	-0.07	-0.06
+3.5%-Pt$-(2\times2)O$	-0.03	0.15	-0.05
-2.3%-Pt	0.08	0.23	0.07
Pt_3Y-25%Y$-(2\times2)O$	0.09	0.17	0.07
Pt_3Co-50%Co	0.10	0.36	0.13
Pt$-(2\times2)O$	0.02	0.49	0.04
Pt_3Y-0%Y	-0.21	-0.39	-0.21
Pt_3Ni-25%Ni	0.02	0.27	0.03
-2.3%-Pt$-(2\times2)O$	0.11	0.94	0.10
Pt_3Y-25%Y	-0.03	-0.20	-0.05
Pt_3Y-25%Y*	0.06	0.31	0.04
Pt_3Sc-25%Sc$-(2\times2)O$	0.16	0.57	0.12

Table C.2: Binding energies of OH, O and OOH relative to Pt(111) calculated in a (2×2) cell. The adsorption energy is calculated on the most stable site. In most cases, this is the same site for OH and OOH. However for Pt_3Y-25%Y* the adsorption energy is calculated on the second most stable site.

C.2 Binding energies on Pt_3X surfaces

Appendix D

Pair Potentials

D.1 Pt(111)

	H_2O(v)	H_2O(p2)	H_2O(p2)	OH	O
ΔE_{ads}	-0.01	-0.08	-0.24	-2.09	-3.73
$V_{NN}^{O,X}$	-0.02	0.12	1.09	1.77	0.28
$V_{NNN}^{O,X}$	-0.02	-0.01	-0.04	-0.03	0.000

Table D.1: Adsorption energy ΔE_{X} of the adsobate X, nearest neighbor (NN) and next nearest neighbor (NNN) interaction energies V^{OX} between X and O on Pt(111). All energies are in eV.

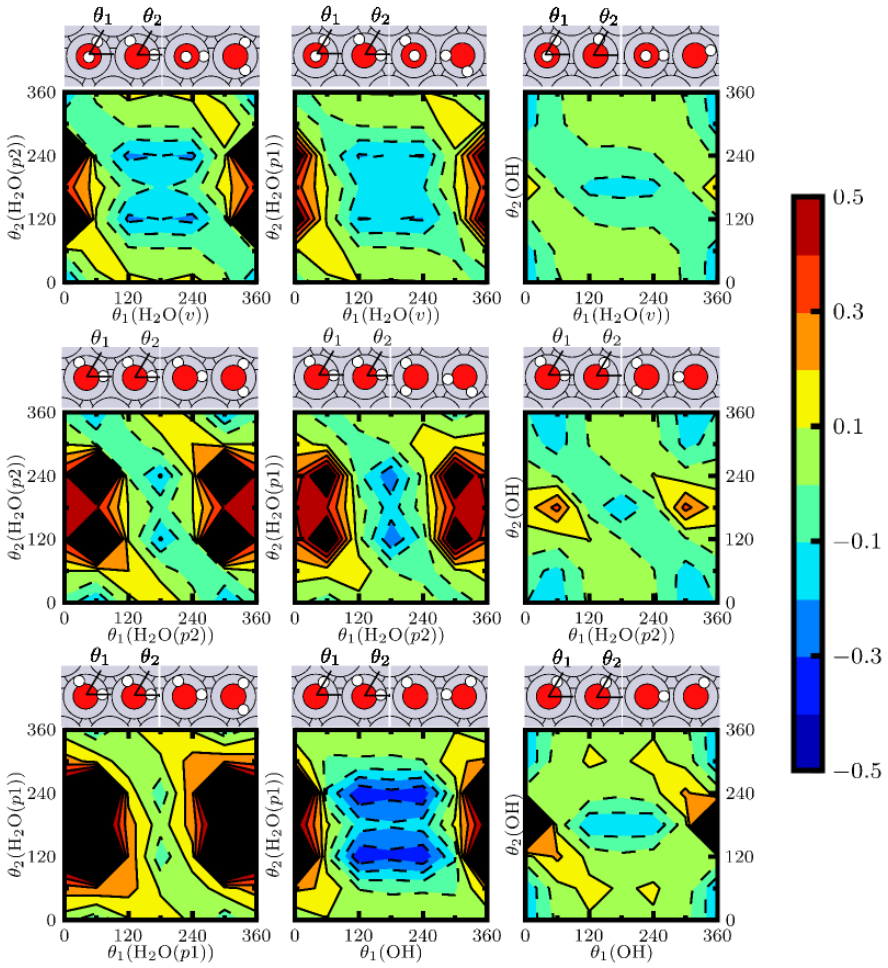

Figure D.1: Interaction potentials on Pt(111). From the upper left to lower right corner: H_2O(v)-H_2O(p2), H_2O(v)-H_2O(p1),H_2O(v)-OH, H_2O(p2)-H_2O(p2), H_2O(p2)-H_2O(p1),H_2O(p2)-OH, H_2O(p1)-H_2O(p1), H_2O(p1)-OH, OH-OH. The insets above the contour plots show the angle definitions with the (60°,60°) configuration as an example (left) and the most attractive pair interaction (right). Interaction parameters with O are shown in Table D.1.

Appendix E

Temperature Programmed Desorption of Water from Oxygen Precovered Surfaces

In Temperature Programmed Desorption (TPD) experiments the temperature of a sample placed in UHV is increased linearly with time, and the mass to charge ratio of the desorbing species is measured with a mass spectrometer. This gives information about desorption barriers and possible interactions between the adsorbed species at the surface. For more complex desorption spectra it is, however, difficult to infer anything about the atomic structure of adsorbates at the surface from TPD alone. Like any other UHV technique, it is best used in combinations with other techniques.

As described previously, $(\sqrt{3}\times\sqrt{3})R30^\circ$ OH/H_2O structures are formed on Pt(111) at surfaces dosed with O and H_2O in UHV. A recent XPS study of Ru(0001), Rh(111), Pd(111), Ir(111) and Pt(111) by Held and co-workers showed that H_2O dissociates when the surface is precovered with less than 0.2 ML oxygen, whereas dissociation does not happen at coverages above 0.25 ML [189]. Water dissociation leads to multiple desorption peaks.

In order to evaluate the applicability of the model described in the previous chapter, we employ the Hamiltonian (6.1) in simulating TPD of water from O precovered surfaces of Ru(0001) and Au(111). This gives a hint to the accuracy of the interaction potentials of OH and H_2O for the late transition and noble metals.

In this chapter we briefly describe the employed method. For Ru(0001) and Au(111) we then discuss some experimental and theoretical results from literature relevant for our simulations, and show the results of our simulations and compare them to experiments.

E.1 Method

We treat interactions with the lattice gas Hamiltonian (6.1). We focus on structures formed by H_2O(p1) and OH and have not included H_2O(v) and H_2O(p2). This allows us to simulate TPD from surfaces where H_2O dissociates and there is not a large excess of water outside OH-H_2O(p1) domains. Desorption of water from multilayer structures and pure water domains, however, occurs at a lower temperature than desorption from OH-H_2O(p1) domains, so the processes can be separated in the TPD spectra.

The interaction potentials are calculated as described in Section 6.2.1. We have, however, used a $(3\times\sqrt{3})$ surface unit cell for the interaction potentials involving H_2O and OH. This is consistent with only including nearest neighbor interactions for these species. The O-O interactions on Au(111) are however calculated in a (4×4) surface

unit cell, because of long range repulsion between O atoms at this surface. Second nearest neighbor interactions between O on Ru(0001) was found to be ~ 0.001eV.[1]

The interaction potentials are shown in appendix D. Qualitatively the potentials are similar to those on Pt(111). We find that the potential energy surface is more flat on Au(111) than on Ru(0001). This is consistent with the findings by Karlberg *et al.*, that the main contribution to the interaction on Pt(111) is described by the interaction in the absence of the substrate[133]. Because the lattice constant is larger on Au(111) than on Pt(111) and Ru(0001), repulsion and attraction is weaker on Au(111). We treat H_2O and OH at atop sites and O adsorption at the most stable hollow site.

The hydrogen transfer reactions (6.4a) and (6.4b) as well as diffusion and rotation of H_2O and OH are treated in equilibrium. The desorption step

$$H_2O* \rightarrow * + H_2O \tag{E.1}$$

is treated kinetically. The desorption rate is

$$k_{des} = \nu \exp\left(-\frac{E_a}{k_B T}\right), \tag{E.2}$$

where E_a is the activation energy and calculated from the interaction potentials using a Bronsted-Hammond factor of 1/2[190], which describes how much the activation energy is affected by interactions. For the prefactor we use $\nu = 10^{-14}\text{s}^{-1}$. Karlberg *et al.* derived a value of $4 \cdot 10^{-14}\text{s}^{-1}$ on Pt(111)[134]. The master equation is solved using the first reaction method (FRM)[191]. We always choose a total initial coverage of $\theta_O + \theta_{H_2O} = 0.33$ ML and perform TPD simulations for varying H_2O:O doses. We use a 50×50 close packed lattice. The simulated heating rate is 1 K/s. [2]

E.2 Ru(0001)

E.2.1 Water Dissociation on Clean Ru(0001)

Water has been studied quite extensively on Ruthenium since the 1970's. Renewed interest was created, when DFT calculations by Feibelman showed that half dissociated D_2O-OD $(\sqrt{3} \times \sqrt{3})R30°$ water layers were more stable than undissociated water layers[192][3]. The vertical O-O distance projected onto the normal to the surface in the half dissociated water layers was 0.04 Å to 0.06 Å, whereas the vertical distance in undissociated water layers was above 0.50 Å. Half dissociated D_2O-OD layers therefore agrees better with IV-LEED experiments by Held and Menzel[193].

The dissociated water layer, however, disagrees with the change in workfunction upon adsorption of water. The disagreement may be explained by water dissociation on clean ruthenium being activated at low temperatures. In fact experiments show that short beam exposure may lead to significant amounts of OH by dissociation of H_2O on clean Ru(0001)[194, 195]. The dissociation barrier has been calculated to be 0.50 eV[135] to 0.62 eV[196], and larger than the average adsorption energy in the water bilayer structure on Ru(0001). XPS and XAS show that when the water layer dissociates, hydroxyl groups are formed with the O-H bond parallel to the surface[197].

H_2O multi-layers on clean Ru(0001) have also been reported to dissociate when heated above 175 K[197]. STM images reveal that heating results in the formation of H_2O-OH domains with a honeycomb structure. The domains form stripes that are 2.5-6 Ru lattice constants wide.[197] Hydrogen was reported to adsorb in a $(\sqrt{3}\times\sqrt{3})R30°$

[1] Because the metal atoms are frozen during the calculation of the interaction energies, long range interactions mediated by elastic deformations of the surface are not included.

[2] All Monte Carlo simulations have been done by V. Viswanathan based on DFT calculated interaction energies and reversible potentials calculated by the author.

[3] Hydrogen may either adsorb at the top sites within the D_2O-OD domains or diffuse to hollow sites in areas not covered by water. The latter possibility results in the most stable structure.

structure between the H_2O-OH domains. The formation of H_2O-OH domains that are narrow in one direction agrees with LEED experiments by Held and Menzel[198].

Isotope effects have been observed for water on Ru(0001). Whereas D_2O desorbs intact near 175 K, H_2O desorbs in two peaks at 165 K and 205 K [199] which leaves traces of H and O at the surface. This has been attributed to a kinetic isotope effect, where H_2O dissociation competes with H_2O desorption.[199] The branched desorption peaks for H_2O on Ru(0001) are sensitive to water coverage and trace amounts of O and H at the surface.[199]. A TPD of Ru(0001) is shown in Figure E.1. DFT finds that dissociation of water monomers has a barrier of 0.85 eV [135].

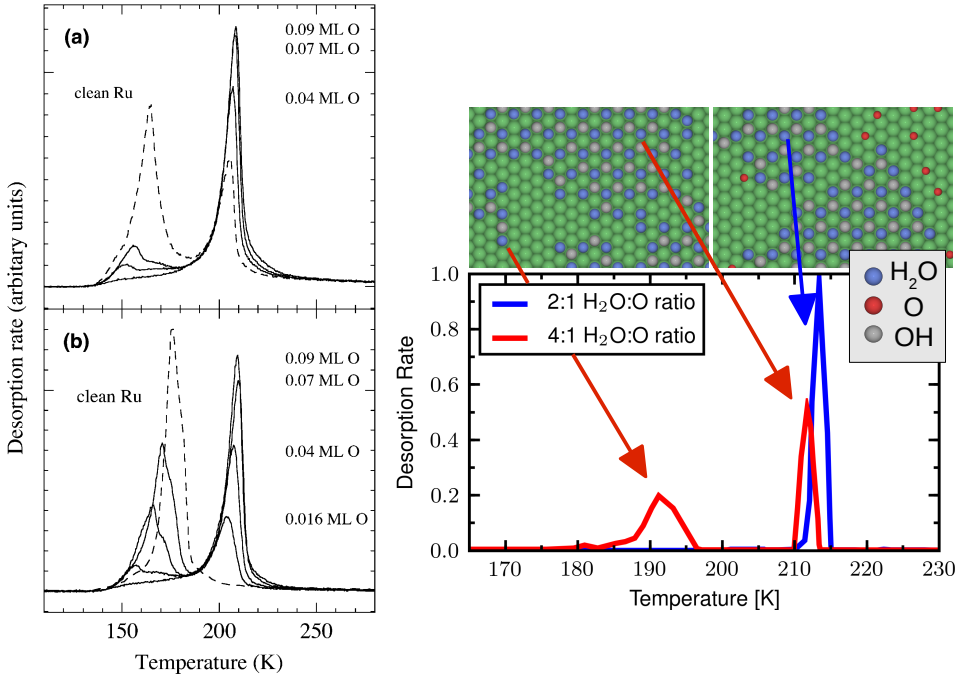

Figure E.1: TPD of water from clean and O dosed Ru(0001). Left: Experimental TPD by Clay *et al.* [199]. Top left: H_2O desorption. Bottom left: D_2O desorption. On clean Ru(0001) H_2O dissociates partially resulting in two desorption peaks. D_2O does not dissociate on clean Ru(0001) but dissociates at Oxygen precovered Ru(0001). Right: Simulated TPD at 2:1 and 4:1 H_2O:O coverage corresponding to 0.125 ML O and 0.067 ML O respectively. The peak at 190 K is caused by desorption of low coordinated water at the edges of D_2O-OD domains. The peak at 212 K comes from desorption at the interior of D_2O-OD domains.

E.2.2 Water Dissociation on Oxygen Pre-covered Ru(0001)

Gladys *et al.* have studied the change from dissociative H_2O adsorption at low oxygen coverage to molecular adsorption at $\theta_O \leq 0.18$ ML.[200] Water dissociation is reported to happen at 140 K with 0.11 ML precovered oxygen and at 150 K on the clean surface. At 0.11 ML O pre-coverage dosed with 0.57 ML H_2O, a small "multilayer peak" desorbs at 140 K and a peak assigned to H_2O-OH appears at higher temperature. Integrated XPS peak intensities indicate that at least 60 % of the adsorbed O reacts to form OH. At 0.18 ML O pre-coverage the TPD and Temperature Programmed XPS (TPXPS) spectra depend on sample annealing. Dosing O2 at 400 K results in OH formation upon H_2O adsorption, whereas annealing to 1100 K before dosing H2O, does not induce dissociation. Only 45 % of the preadsorbed O reacts with water. It has been suggested that the annealing leads to (2x2)O islands that are

unreactive towards water, whereas O in the as dosed layer at 400K forms a reactive disordered structure. Another suggestion is that oxygen blocks the active sites for water dissociation when the surface is annealed.

The vibrational frequencies of the H_2O-OH overlayer on Pt(111) and Ru(0001) are quite similar[199, 201]. The H_2O bilayer on the clean Ru(0001) surface has a broad OH stretching band of H_2O around 3390 cm^{-1} from hydrogen bonded OH, a sharp non bonded OH stretch at 3683 cm^{-1}, a scissor mode at 1630 cm^{-1} and low frequency peaks at 988 and 904 cm^{-1} assigned to bending modes. In the mixed H_2O-OH layer, the free and the bound stretch modes and the H_2O scission mode are absent, while the bending modes are shifted[199]. This is consistent with the mixed OH-H_2O layer having OH stretch modes and H_2O scission modes in a plane parallel to the surface plane. The reaction $3H_2O + O \rightarrow 2\ OH + 2\ H_2O$ is not stoichiometric on Ru(0001) and the overlayer is less ordered than on Pt(111), which has been suggested to be caused by co-adsorbed hydrogen at the surface [199].

Cabrera-Sanfelix *et al.* studied O and H_2O on Ru(0001) by STM experiments and DFT calculations for $\theta_O \leq 0.25$ ML and low coverage of water[202, 203]. The H_2O binding energy at (2×2)-O surface depends only weakly on water coverage, with a minimum at 0.125 ML H_2O coverage[202]. H_2O(p) at the (2x2)O/Ru(0001) surface is stabilized by 0.22 eV by hydrogen bonds to the oxygen atoms[202]. O and OH adsorption energies are found to have a weak dependence on O pre-coverage for $\theta_O \leq 0.25$ ML, with the O adsorption energy increasing less than 0.1 eV and the OH adsorption energy increasing about 0.2 eV when going from low coverage toward 0.25 ML. At these coverages O and OH are found to adsorb preferentially at hollow sites. For 0.25 ML Oxygen pre-coverage, the OH adsorption energy, however, drops significantly because at this coverage there exist no hollow sites, where the Ru atoms do not bind to at least one O atom in the (2×2)-O structure[203]. Cabrera-Sanfelix *et al.* only considered low coverage of water and no water stabilized OH phases were explicitly considered.

E.2.3 Simulated TPD

In our simulations we focus on water desorption from surfaces with less than 0.18 ML O, where water is expected to dissociate from the reaction with oxygen[200]. We do not consider any kinetic isotope effects and zero point energies are not included in the energies. We do also not consider the possibility of water dissociation besides (6.4). Our simulations therefore model D_2O desorption rather than H_2O desorption.

Our simulated peak at low temperature (190 K) arises from desorption of low-coordinated D_2O present at the surface at 2:1 D_2O:O ratio. The peak at high temperature (212 K) arises from desorption of D_2O surrounded by OD in the interior of D_2O-OD domains, see Figure E.1. As the D_2O:O ratio is decreased, increasing amounts of OD will decorate the edges of the D_2O-OD domains. This means the low temperature desorption vanishes for low D_2O:O ratios because all D_2O desorbs from the interior of the D_2O-OD domains.

The onset of the experimental peak at low temperature is most likely from desorption of water from the edges of water domains and the shoulder at slightly higher temperature is from desorption at edges of D_2O/OD domains. Because we do not have a large excess of water to form pure water domains, our simulated desorption peak at 190 K most likely corresponds to the broad shoulder at higher temperature of the low temperature peak in experiments.

We have not encountered formation of D_2O-OD stripes in our TPD simulations. It is possible that the formation of these structures depends on the isotope of water used in the experiment and the initial coverage of water and O. It is on the other hand possible that the finite extent of the D_2O-OD in one direction results from a structural relaxation due to a mismatch in the preferred D_2O-O structure on Ru, which is difficult to include in a lattice gas Hamiltonian of the type (6.1). It is, however, also possible that the water-OH stripes could be reproduced if more water

motifs are included in the simulations.

E.3 Au(111)

Gold is fairly well studied in catalysis, surface science and electrochemistry. The catalytic properties of gold nanoparticles and clusters have received considerable interest since Haruta *et al.* discovered high activity for CO oxidation on gold nanoparticles[204]. Au(100) also has extremely good activity for oxygen reduction in alkaline solution [205].

Reconstruction

In UHV Au(111) exhibits a $\left(\sqrt{3} \times 22\right)$ reconstruction with a secondary herringbone structure [206]. The $\left(\sqrt{3} \times 22\right)$ reconstruction results in a 4.4 % lateral compression in one of the [110] directions and consequently only every 23rd surface atom is in registry with the underlying bulk lattice. The secondary herringbone structure results from stress relief. The reconstruction is changed by adsorption of e.g. sulfur [207], oxygen [206], NO_2 [208] or styrene [209]. Less than 0.1 ML O is required to lift the $\left(\sqrt{3} \times 22\right)$. This is accompanied by a release of Au atoms from the reconstructed surface [206, 210, 211]. Helium diffraction experiments show that RF produced O atoms adsorbed on Au revert the $\left(\sqrt{3} \times 22\right)$ reconstruction partially to the (111) structure at 200 K for oxygen coverages less than 0.1 ML [212]. At 300 K, however, the reconstruction reappears [212].

In this work we only consider the unreconstructed surface. We do not expect the adsorption energies at the terrace to be severely affected by the reconstruction. It is likely that the reconstruction is at least partially lifted during the TPD experiment from the oxygen precovered surface due to the presence of oxygen or OH. Gold ad-atoms on the (111) terrace which may be produced when the reconstruction is lifted, could however stabilize O or OH adsorbates at the surface. This has not been considered in the current study.

Oxygen on Au(111)

Due to its noble nature, gold shows great stability in the electrochemical environment at a wide range of potentials and pH values [55]. Besides this, Au is known to interact very weakly with oxygen. In UHV O_2 does not adsorb dissociatively on Au(111) at low temperature [210]. Desorption of O_2 from Au(111) happens at $T = 520$-550 K.

Experimentally, atomic O has been formed on Au by ozone dozing [210], oxygen ion sputtering [213, 214], electron induced NO_2 dissociation [206] or by passing O_2 across a glowing filament near the dosing tube [211, 215].

It was shown by Scheffler and co-workers that for oxygen on the close-packed 4d late transition metal surfaces, the critical coverage at which subsurface oxygen becomes favored over on-surface oxygen decreases as one moves towards the more noble metals [216]. For the TPD of H_2O from surfaces with precovered oxygen it is therefore important to know what kind of oxygen is present under experimental conditions.

Using STM, Min *et al.* identify 3 different oxygen states on Au(111): chemisorbed O*, surface oxide and bulk oxide [217]. The activity for CO oxidation decreases in the order O* > surface oxide > bulk oxide. These findings are in agreement with result by Ojifinni *et al.* . They showed that annealing of an oxygen dosed Au(111) surface reduce reactivity - measured in terms of H_2O/O isotope scrambling, CO oxidation and carbonate formation and decomposition [218]. Further, they found that increasing O dosage above 0.18 ML decreases isotope scrambling of water [218].

Theoretical calculations of the O/Au(111) system have been performed by Shi and Stampfl. They found that a (4×4) surface oxide with 0.3125 ML O is more stable than atomic oxygen adsorbed on the surface at any temperature and pressure [219].

Baker *et al.* performed related calculations employing a $\left(\sqrt{3}\times\sqrt{3}\right)R30°$ surface cell and found that incorporation of Au into the adsorbate layer becomes thermodynamically favored for oxygen coverages above 2/3 ML. This may be formed at the oxygen chemical potential in ozone [220, 221].

These results suggest that on-surface O is metastable relative to a more strongly bound species of oxygen, *e.g* subsurface O or a surface oxide. However, that the strongly chemisorbed O cannot be formed at an appreciable rate at 200 K, whereas it is possible at 400 K. We therefore expect that oxygen under experimental conditions ($T < 200$K) of the water TPD is present as metastable oxygen on the gold surface.

Oxygen isotope scrambling experiments by Ojifinni *et al.* between H_2O and O clearly show reaction (6.4b) is taking place at an oxygen precovered Au(111) surface dosed with water [222]. From DFT calculations, they found a barrier of only 0.11 eV without incorporating the adsorbates into a water layer. However, the reaction was found to be endothermic by 0.05 eV. This suggests that OH would not be stable at the surface but only present transiently. However, they did not consider the stabilization of OH from hydrogen bonding to neighboring water molecules.[4] In contrast, Karlberg found it was energetically favorable to dissociate water in the presence of oxygen

$$H_2O* + O* \rightarrow 2OH* \tag{E.3}$$

at high water coverage on Ru, Rh, Ir, Pd, Pt, Ag and Au by forming extended $(\sqrt{3}\times\sqrt{3})R30°$ OH/H_2O structures [223].

Water desorption experiments from oxygen predosed Au(111) have been performed recently by Quiller *et al.* and by Ojifinni *et al.* [224, 222]. Figure E.2 shows the TPD results obtained by Ojifinni *et al.* . They dosed water and atomic oxygen produced from an RF source at 77 K. The heating rate was 1 K/s and coverages were determined from the mass balance of CO oxidation [222]. The figure shows mass spectrometer signals for clean Au(111) and Au(111) precovered by 0.18 ML ^{16}O or ^{18}O. Desorption peaks are at 155 K and 175 K respectively. Quiller *et al.* produced oxygen at Au(111) by ozone dozing at 200 K, and dosed water at 145 K. Using a heating rate of 2.4 K/s they observed water desorption peaks at 175 K and 195 K. Analysis of water TPD from Au(111) is complicated by the fact that there is no discernable difference between water desorbing from multilayers of water or a (sub-) monolayer of water on clean Au(111) [224]. The H_2O desorption peak at high temperature has a maximum area at 0.15 to 0.25 ML O precoverage [224].

E.3.1 Simulated TPD

The simulated TPD spectrum is shown in Figure E.2. Similar to what we observed on Ru, the low temperature peak disappears as the H_2O:O ratio is decreased. This has also been observed by Quiller *et al.* . They found that for Au(111) predosed with 0.2 ML O, the low temperature peak vanishes around 0.6 L water doseage [224]. The simulated desorption peaks at 130 K and 155 K are at a slightly lower temperature than in the experiments by Ojifinni *et al.* , who identified peaks at 155 K and 175 K. The relative areas of the peaks cannot readily be compared due to different initial coverages of O and H_2O in experiment and simulation.

E.4 Discussion and Summary

In this chapter we have simulated desorption of water from oxygen precovered Ru(0001) and Au(111) for initial structures with 0.0625 to 0.125 ML O and a total initial coverage of $\theta_O + \theta_{H_2O} = 0.33$ ML The redistribution of peak area with O coverage is qualitatively reproduced. We attribute the desorption peak at low temperature to water desorbing from the edges of H_2O-OH $(\sqrt{3}\times\sqrt{3})R30°$ domains and the high

[4] As a side note they calculated a 0.19 eV barrier for OH diffusion.

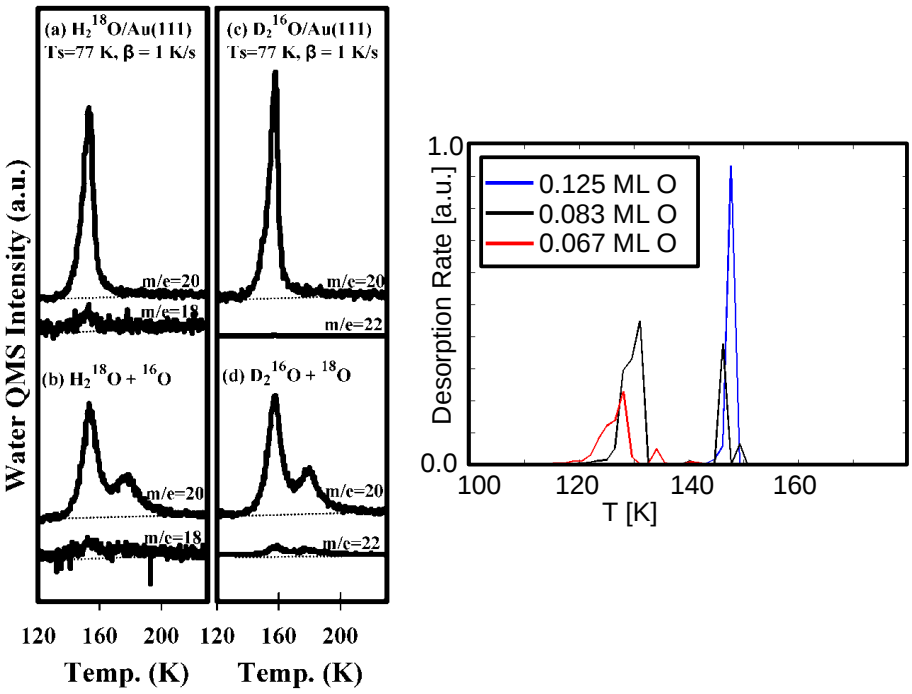

Figure E.2: Water desorption from Au(111). Left: Experimental TPD of H_2O and D_2O from clean Au(111) (top left) and Au(111) precovered with 0.18 ML O (bottom left). The water desorption peak on clean Au(111) is at 155 K. When oxygen is predosed on the surface, a desorption peak appears at 175 K. The figure also shows isotope scrambling between O and H_2O, demonstrating that OH forms at least transiently. Right: Simulated TPD at O coverages from 0.067 ML O to 0.125 ML O. Experimental TPD adapted from Ojifinni *et al.* [222].

temperature peak to desorption of water from the interior of the H_2O-OH domains.[5] As the H_2O:O ratio decreases, OH rather than H_2O will decorate the domain edges. In this way the area of the high temperature peak increases with a decreasing initial H_2O:O ratio. This is qualitatively reproduced in the Monte Carlo simulations by Karlberg *et al.* on O covered Pt(111) [134].

The simulated and the experimental peak positions agree within 25 K. However, the absolute desorption temperature depends on the Bronsted Hammond factor, which we have assumed to be 1/2. As expected, we find water desorbs from Au(111) at a lower temperature than from Ru(0001) for both clean and oxygen precovered surfaces. Both the adsorption energy of the water monomer and the attractive interactions between water and OH are stronger on Ru(0001) than on Au(111).

The good agreement between the simulated TPD peaks and the experimental peaks suggests the energy of H_2O in the OH environment is well described by the interaction potentials and the adsorption data. This lends credibility to the model for simulating CV described in chapter 6, which could be extended to other closepacked transition metal surfaces.

[5] The $(\sqrt{3} \times \sqrt{3})R30°$ superstructure should only be taken as a description of the oxygen atoms in H_2O and OH, as hydrogen disorder is present.

Adsorbate (X)	H_2O(v)	H_2O(p)	OH	O
ΔE_X	0.00	-0.11	-1.47	-2.65
V^{OX} (NN)	-0.10	0.12	1.04	0.38
V^{OX} (NNN)	-0.08	-0.14	-0.05	0.09

Table E.1: Adsorption energy ΔE_X of the adsobate X, nearest neighbor (NN) and next nearest neighbor (NNN) interaction energies V^{OX} between X and O on Au(111). All energies are in eV.

Adsorbate	H_2O(v)	H_2O(p3)	H_2O(p1)	OH	O
ΔE_X	-0.12	-0.22	-0.48	-2.64	-5.13
V^{OX} (NN)	0.01	0.58	1.58	1.94	0.18
V^{OX} (NNN)	-0.06	-0.03	-0.15	-0.07	0.00

Table E.2: Adsorption energy ΔE_X of the adsobate X, nearest neighbor (NN) and next nearest neighbor (NNN) interaction energies V^{OX} between X and O on Ru(0001). All energies are in eV.

E.5 Interaction Potentials

E.5.1 Au(111)

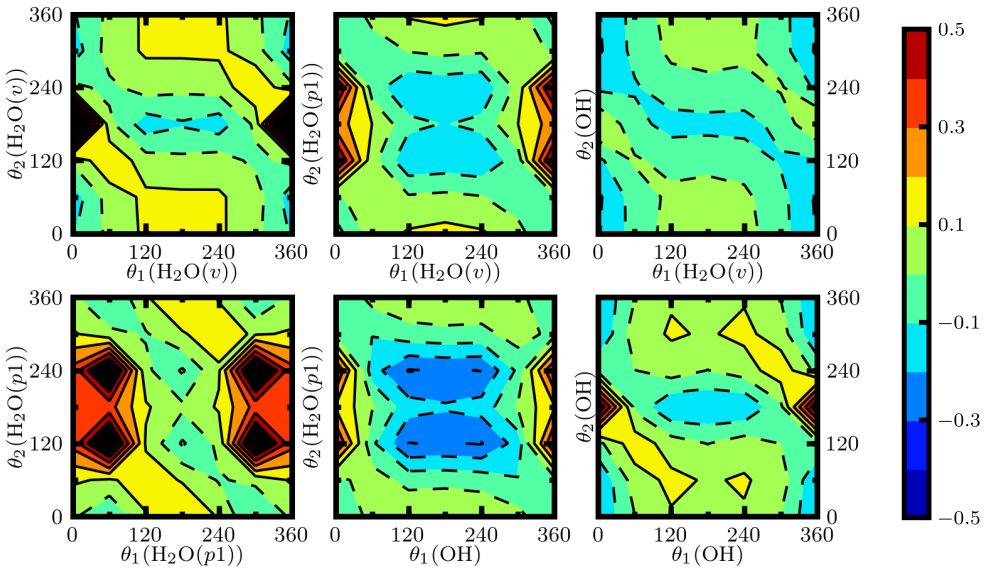

Figure E.3: Interaction potentials on Au(111). Interaction energies are in eV.

E.5.2 Ru(0001)

On Ru(0001) we have included a third type of water parallel, H_2O(p3). The structure is adapted from H_2O in a H_2O dimer configuration shown in Figure E.4. The structure is similar to the dimer structure found in calculations on Pd(111) by Michealides and co-workers [137]. These dimers are believed to diffuse faster than monomers.

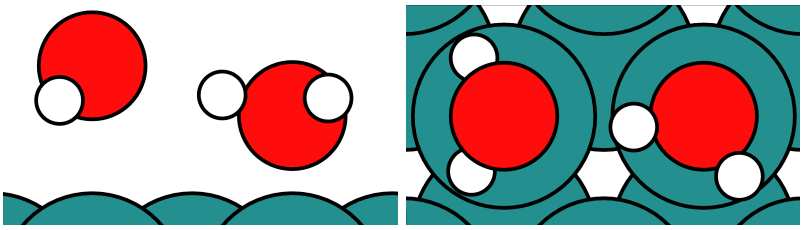

(a) (b)

Figure E.4: The structure of a H_2O(p3)-H_2O(p1) dimer on Ru(0001) seen from the side and the top.

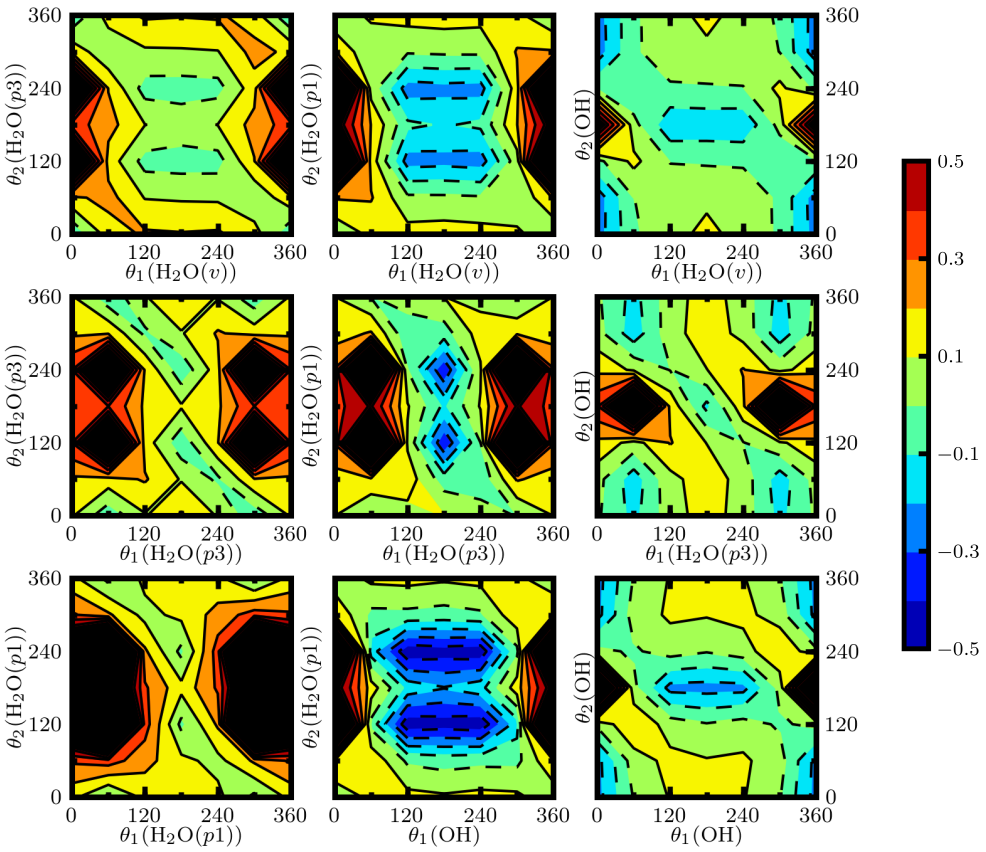

Figure E.5: Interaction potentials on Ru(0001). Interaction energies are in eV.

Appendix F

CV for Pt_3Ni with 0 % Ni in the Second Layer

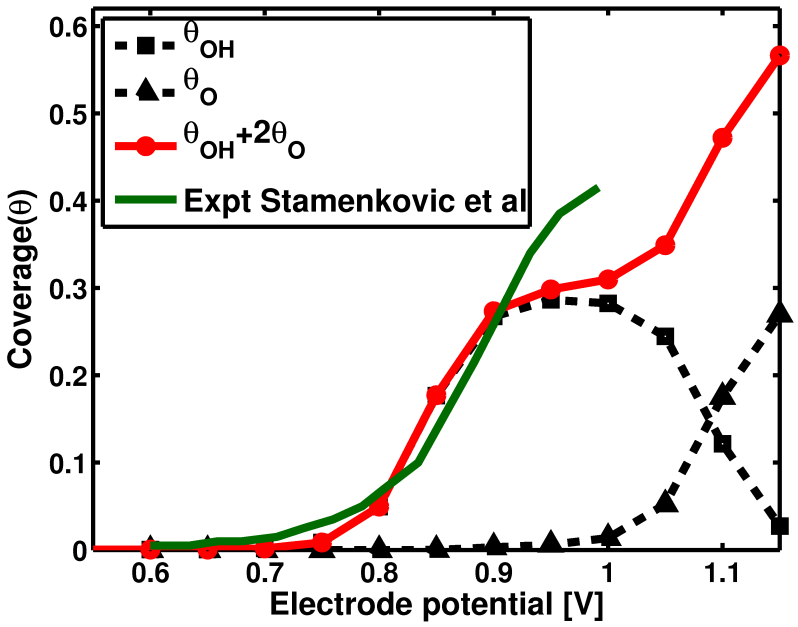

Figure F.1: CV for Pt_3Ni with 0 % Ni in the Second Layer. MC simulation by V. Viswanathan and experiment by Stamenkovic *et al.* [110].

P1

Surface Pourbaix Diagrams and Oxygen Reduction Activity of Pt, Ag and Ni(111) Surfaces Studied by DFT

H. A. Hansen, J. Rossmeisl and J. K. Nørskov

Phys. Chem. Chem. Phys., **10**, 3722-3730 (2008)

Surface Pourbaix diagrams and oxygen reduction activity of Pt, Ag and Ni(111) surfaces studied by DFT†

Heine A. Hansen, Jan Rossmeisl* and Jens K. Nørskov

Received 6th March 2008, Accepted 22nd April 2008
First published as an Advance Article on the web 27th May 2008
DOI: 10.1039/b803956a

Based on density functional theory calculations we investigate the electrochemically most stable surface structures as a function of pH and electrostatic potential for Pt(111), Ag(111) and Ni(111), and we construct surface Pourbaix diagrams. We study the oxygen reduction reaction (ORR) on the different surface structures and calculate the free energy of the intermediates. We estimate their catalytic activity for ORR by determining the highest potential at which all ORR reaction steps reduce the free energy. We obtain self-consistency in the sense that the surface is stable under the potential at which that particular surface can perform ORR. Using the self consistent surfaces, the activity of the very reactive Ni surface changes dramatically, whereas the activity of the more noble catalysts Pt and Ag remains unchanged. The reason for this difference is the oxidation of the reactive surface. Oxygen absorbed on the surface shifts the reactivity towards the weak binding region, which in turn increases the activity. The oxidation state of the surface and the ORR potential are constant *versus* the reversible hydrogen electrode (RHE). The dissolution potential in acidic solution, on the other hand, is constant *vs.* the standard hydrogen electrode (SHE). For Ag, this means that where the potential for dissolution and ORR are about the same at pH = 0, Ag becomes more stable relative to RHE as pH is increased. Hence the pH dependent stability offers an explanation for the possible use of Ag in alkaline fuel cell cathodes.

1. Introduction

Proton exchange membrane fuel cells are attracting considerable attention especially for transport applications. It is recognized that many of the major drawbacks for the PEM fuel cell are related to the cathode reaction. The oxygen reduction reaction (ORR) at the cathode is irreversible and introduces a significant potential drop.[1,2] Furthermore, only Pt and Pt alloy catalysts have a reasonable activity and stability in the acid environment. In alkaline fuel cells where the flexibility concerning the cathode catalyst is much larger, non-precious metals like Ni and Ag can be used.[3] From an atomistic point of view less is known about alkaline oxygen reduction. Water splitting potentials in acid and alkaline electrolytes are known from cyclic voltammetry.[4] However, the molecular structure of the surface is not known. It is obvious that the molecular structures on the surface is dependent on the metal, potential and pH of the electrolyte. To understand ORR catalysis at the atomic level it is important to determine the molecular structure of the surface in play.

The acidic cathode reaction has previously been studied applying a model based on density functional theory (DFT) calculations. The theoretic model provides understanding on why platinum is the most efficient elemental catalyst for oxygen reduction[5] and how it is possible to improve the ORR activity by alloying with other metals, *e.g.* Ni.[6,7] Previous theoretical studies have focused on the relevant surface structure for Pt and other good ORR catalysts. But from such a study it is not clear why metals such as silver or nickel may be used successfully in alkaline fuel cells but not in acidic PEM fuel cells.

In heterogeneous catalysis the atomic structure of the catalyst surface is important because it determines the activity of sites on the surface. A Pourbaix diagram shows the most stable bulk phase of an element in an aqueous environment as function of pH and potential. In the present work we identify the most stable surface structures relevant for oxygen reduction on the (111) surfaces of Ag, Ni and Pt. We refer to the corresponding phase diagrams for the surfaces as surface Pourbaix diagrams. Furthermore, for the three different metals we determine the potential where surface catalysis starts playing a limiting role for ORR. This introduces a self-consistency problem, since the ORR potential will depend on the surface structure and the surface structure depends on the potential. Fortunately only a few surfaces are relevant for ORR. In the context of steady state ORR the cathode surface structure is independent of pH. In other words: the ORR potentials *versus* the reversible hydrogen electrode (RHE) are the same in alkaline and acidic solution. Hence, we find that the reason for the activity of Ag and Ni in alkaline solution compared to acidic solution, is not related to a different surface structure, but rather related to higher dissolution potential (*vs.* RHE) and better stability in alkaline solution than in acidic solution.

Center for Atomic-scale Materials Design, Department of Physics, Technical University of Denmark, DK-2800 Lyngby, Denmark
† Electronic supplementary information (ESI) available: Energies and surface structures of the studies compounds. See DOI: 10.1039/b803956a

2. Methods

2.1 Surface Pourbaix diagrams

We determine the most stable surfaces without molecular oxygen present, as these are the relevant surfaces for the surface Pourbaix diagrams and normal cyclic voltammograms (CV). To calculate the stability of a surface we use the concept of the theoretical standard hydrogen electrode (SHE),[5] which has previously been shown to give reliable results for theoretical cyclic voltammograms for hydrogen on Pt surfaces[8] and for predicted ORR activity for Pt alloys.[6] The method is summarized here. It is assumed the surface is in equilibrium with protons and liquid water at 298 K, so that oxygen and hydroxyl may be exchanged between the surface and a reference electrolyte through the following steps

$$H_2O(l) + * \leftrightarrow HO* + H^+(aq) + e^- \quad (1)$$

and

$$HO* \leftrightarrow O* + H^+(aq) + e^-, \quad (2)$$

where * denotes a site on the catalyst surface and O* and HO* denote oxygen and hydroxide adsorbed on a site.

The oxidation of water to O* and HO* depends on the potential U and pH through the chemical potentials of H^+ and e^-. The reaction:

$$H^+(aq) + e^- \leftrightarrow 1/2H_2(g) \quad (3)$$

has $\Delta G^\circ = 0$ at standard conditions (pH = 0, $p(H_2)$ = 1 bar) defining $U = 0\ V_{SHE}$. This allows us to calculate the free energy of adsorbed O* and HO* at $U = 0$ V and pH = 0 directly from the free energy of the reactions

$$H_2O(l) + * \leftrightarrow HO* + 1/2H_2(g) \quad (4)$$

$$HO* \leftrightarrow O* + 1/2H_2(g). \quad (5)$$

This has the advantage that $H_2(g)$ is much easier to handle computationally than solvated protons. Reactions (4) and (5) define the free energy, ΔG_0, of HO* and O* at zero pH and zero potential *vs.* SHE.

At finite pH and potential, the free energy of reaction (3) is ($p(H_2)$ = 1 bar)

$$\Delta G = e\,U_{SHE} + k_B\,T \ln 10\ \mathrm{pH}, \quad (6)$$

Since (4) and (5) are independent of pH and potential, we may calculate the free energy of (1) and (2) at any pH and potential from

$$G(HO*) = \Delta G_0(HO*) - e\,U_{SHE} - k_B\,T \ln 10\ \mathrm{pH} + \Delta G_{field}, \quad (7)$$

where ΔG_{field} is the change in the adsorption energy due to the electric field in the electrochemical double layer at the cathode. To first order in the electric field $\Delta G_{field} = -\boldsymbol{\mu}\cdot\boldsymbol{E}$, where $\boldsymbol{\mu}$ is the dipole moment of the adsorbate and $\boldsymbol{E}$ is the electric field at the position of the dipole. ΔG_{field} has been studied in detail for Pt(111),[9,10] and the relative change in stability of O* and HO* is less than 0.11 eV when the potential is increased from 0 to 1 V *vs.* SHE. Since the first term in eqn (6) changes the relative stability of O* and HO* by 1 eV when the potential is increased by 1 V, the trends in adsorption energies are well described by neglecting ΔG_{field} in the construction of the surface Pourbaix diagram.[10]

We calculate ΔG_0 by correcting the DFT energies for zero point energies and entropy *via*

$$\Delta G_0 = \Delta E + \Delta ZPE - T\Delta S, \quad (8)$$

where ΔE is the DFT energy and ΔZPE is the change in zero-point energy of the adsorbates. We have used the zero point energy of the adsorbates on Cu(111) obtained within the harmonic approximation using the PW91 functional.[11,12] ΔS is approximated from the loss of entropy of the gas phase molecules upon binding them to the surface.[13,14] We note that the method described above could equally well have been formulated in terms of OH^- instead of H^+, without changing the results.

The free energy of a given molecular surface structure can be calculated as a function of potential U_{SHE} and pH from eqn (7). The structure with the lowest free energy at a given set of conditions determines the surface structure. An example is shown in Fig. 1, where the stability of different Ag(111) surfaces is plotted against potential at pH = 0. The lowest line determines the surface with the lowest free energy at a given potential. The surface Pourbaix diagram in Fig. 2 is then constructed by plotting the most stable surface as function of pH and U_{SHE}.

For HO* and HOO* we have included the possible stabilization by forming hydrogen bonds to water by incorporating the adsorbates in a hexagonal hydrogen bonded network with water. On Pt(111) this hexagonal water layer is known to be stable and has been observed in UHV experiments.[15,16] This approach for including water has previously been used in calculations.[5,9] We adjust the water layer found on Pt to fit Ni and Ag. The considered structures are shown in the ESI.†

The theoretical reversible hydrogen electrode (RHE) can be defined by demanding that the equilibrium in reaction (3) defines $U_{RHE} = 0$ at all conditions. The potential *versus* the reversible hydrogen electrode becomes

$$U_{RHE} = U_{SHE} + k_B\,T \ln 10\ \mathrm{pH}/e. \quad (9)$$

Clearly, at pH = 0, $U_{SHE} = U_{RHE}$ and any fixed potential *vs.* RHE, *e.g.* the potential for reversible water oxidation will

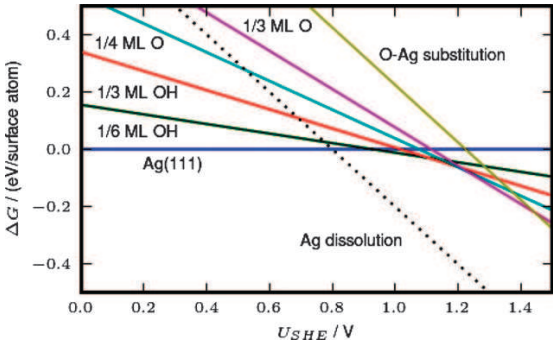

Fig. 1 Stability of O* and HO* on Ag(111) at pH = 0. Dissolution is spontaneous at $U_{RHE} > 0.80$ V. Neglecting dissolution, a structure with 1/6 ML HO stabilized by water forms at 0.93 V. The hydroxyl coverage increases to 1/3 ML at 1.11 V.

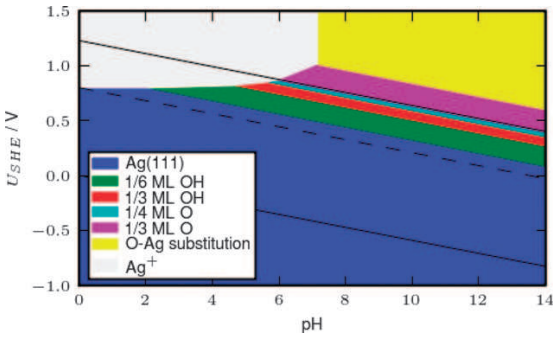

Fig. 2 Surface Pourbaix diagram for Ag(111). The dashed line at U_{RHE} 0.8 V marks the potential of a good ORR catalyst under steady state conditions. It is seen that dissolution is a much larger problem in acidic than in alkaline electrolytes, and that the coverage of the Ag surface is low at U_{RHE} 0.8 V.

show up as lines with a slope of $-k_{\mathrm{B}}T/e$ ln10 (−59 mV/pH at 298 K) in the Pourbaix diagrams. A special case of this is the formation of HO*, because by rewriting eqn (7) in terms of U_{RHE} and neglecting the effect of the electric field,

$$G(\mathrm{HO}^*) = \Delta G_0(\mathrm{HO}^*) - e\,U_{\mathrm{RHE}}, \tag{10}$$

we can see that hydroxyl adsorbs at a fixed potential *vs.* the RHE. A similar argument holds for the adsorption of O* formed from water, which means that the coverage and structure of adsorbed O* and HO* at a given U_{RHE} are independent of pH within this model. As the potential of the cathode relative to the hydrogen electrode determines the fuel cell potential, the coverage and structure of adsorbates at the cathode depend only on the fuel cell potential under steady state conditions and not on pH, provided we disregard dissolution and adsorption of the electrolyte ions.

The metals may dissolve in acidic or alkaline solution. The free energy of dissolution has been estimated from standard reduction potentials and thermochemical data, as uniform dissolution of a monolayer of metal atoms on the surface corresponds to dissolution of the bulk. When speaking of a process as spontaneous, it will be in the sense $\Delta G^{\circ}(U) < 0$, which gives a conservative estimate of the stability *vs.* dissolution. An example is dissolution of silver in acidic solution:

$$\mathrm{Ag(s)} \leftrightarrow \mathrm{Ag^+(aq)} + e^-. \tag{11}$$

Since this process involves electrons but not protons, the free energy of dissolution of the metal surface depends on the potential *vs.* SHE but not on pH. Hence the boundary between Ag and Ag^+-ions is horizontal in a Pourbaix diagram. Formation of 1/2 ML O on Ag(111) from H_2O requires transfer of one electron per Ag atom. The formation of Ag^+ ions also involves one electron. The difference in free energy of 1/2 ML O on Ag and Ag^+ ions therefore do not depend on the potential, so the boundary becomes vertical in a Pourbaix diagram.

Adsorption of spectator ions from the solvent, *e.g.* anions, usually involves only electrons.

$$^* + \mathrm{Cl^-(aq)} \leftrightarrow \mathrm{Cl}^* + e^- \tag{12}$$

The free energy of anion adsorption therefore depends on the potential *vs.* SHE, rather than the potential *vs.* RHE. If HO* and O* compete with spectator species for the free sites, then this might change the surface coverage of HO* and O* as function of potential *versus* the reversible hydrogen electrode for different pH. This effect has not been considered in this work.

2.2 Calculation details

All calculations have been done within density functional theory (DFT),[17,18] with the RPBE functional[19] for exchange and correlation. The RPBE functional has been shown to provide better[19] adsorption energies than the closely related PBE[20] functional. The Kohn–Sham equations[18] have been solved using a plane wave basis with a cutoff of 350 eV for the eigenstates and the densities have been described using a cutoff corresponding to 1000 eV. The ionic cores are described using Vanderbilt ultrasoft pseudo potentials,[21] which give faster convergence with respect to the plane wave basis set than norm conserving pseudo potentials.

The adsorption energies on Ag, Pt and Ni(111) have been calculated using (2×2) and (2×3) supercells consisting of 3 close packed layers of metal atoms. The top metal layer is allowed to relax and the two bottom layers are fixed in their bulk positions. The adsorbates are allowed to relax freely on the surface, until the maximum component of the Cartesian forces is below 0.02 eV $\mathrm{Å}^{-1}$. The periodically repeated slabs have been separated by at least 12.4 Å of vacuum and the dipoles of the images have been decoupled. The Brillouin zone has been sampled using an [8×8×1] and a [10×6×1] Monkhorst-Pack special grid of *k*-points[22] for the (2×2) and the (2×3) cells, respectively. The DFT calculations have been performed using Dacapo with the ASE interface on our local Linux cluster supercomputer.[23]

3. Results

3.1 Ag(111)

To investigate the Ag(111) surface, different structures of hydroxyl and oxygen on the surface have been considered. In acidic solution, dissolution of Ag is spontaneous at potentials above 0.80 V, see Fig. 1, so ORR on this surface is not likely. In alkaline environment the dissolution process is[24]

$$\mathrm{Ag(s)} + \mathrm{H_2O(l)} \leftrightarrow \mathrm{AgO^-(aq)} + 2\mathrm{H^+(aq)} + e^-,\ U^{\circ} = 2.2\ \mathrm{V}. \tag{13}$$

In alkaline solution at low potentials, the most stable surface considered is the clean Ag(111) surface, showing that Ag is a noble metal. At pH = 14, the free energy of dissolution in (13) is negative for $U_{\mathrm{SHE}} > 0.5$ V for the clean (111) surface. Dissolution is therefore not as critical as in acidic solution, see Fig. 2. Water oxidation starts at 0.93 V (RHE) forming a structure with 1/6 ML HO* and 1/2 ML water. At 1.11 V (RHE) the HO* coverage increases to 1/3 ML HO*. At potentials above 1.19 V (RHE) hydroxyl is oxidized further to O*. At higher potentials we find that as more oxygen or hydroxyl is adsorbed on the surface, O atoms will spontaneously substitute Ag atoms on the surface when the surface is

relaxed. This may be interpreted as an onset of dissolution or oxidation of the Ag(111) surface. We note that the substitution is favored by 0.25 V relative to the alkaline dissolution process at pH = 14. The pH and U range where the observed substitution mechanism is favorable instead of alkaline dissolution is shown in the Pourbaix diagram Fig. 2. The substitution becomes spontaneous at potentials above 1.44 V (RHE).

The potential of the onset of dissolution or oxidation is determined by the details of the substituted Ag surface, and it is very likely that surfaces with different atomic configurations turn out to be more stable than the ones we have considered—for example, a surface oxide[25,26] or even formation of bulk Ag_2O which may form at potentials above 1.18 V (RHE). The kinetics of the oxidation and dissolution mechanisms of the Ag(111) surface is without the scope of the present paper.

We have added the potentials of the reversible hydrogen and oxygen electrodes to the Pourbaix diagram to mark the stability range of water at U_{RHE} = 0 V and U_{RHE} = 1.23 V, respectively. We have also added a line at U_{RHE} = 0.80 V, because it is a realistic potential for a good ORR catalyst. We emphasize that the surface structure does not vary along the lines of constant U_{RHE}, if the surface does not dissolve. This means that at U_{RHE} = 0.80 V, the same surface structure will be relevant for ORR regardless of pH.

CV experiments in alkaline electrolytes show a reversible peak around 0.3 V (RHE) on Ag(111), and at lower potentials on Ag(100) and Ag(110).[4,27] This peak has been suggested to be caused by hydrogen adsorption, alkali metal deposition or oxidation of water to HO*.[28] Recent EC-STM experiments have shown that the Ag(111) surface is unmodified up to a potential near 0.7 V (RHE), after which protrusions, which are assigned to 2D Ag_2O nuclei, begin to emerge.[29]

Our calculations do not support the view that the CV peak at 0.3 V (RHE) is due to HO* or H* on the flat Ag(111) surface, as we find water oxidation to start at 0.93 V (RHE). To get HO* at 0.3 V therefore requires a stabilization of HO* by 0.63 eV relative to our calculations. Such stabilization could, in principle, be caused by HO* adsorbing at steps or defects rather than on the Ag(111) terraces. This is however an unlikely explanation for the existence of a peak at 0.3 V (RHE), as the HO* coverage is reported to be 0.2–0.35 ML.[4,27] We note that our theoretical HO* formation is in good agreement with the high potential adsorption peak starting at 0.9 V (RHE) also observed in CV experiments.[4]

3.2 Pt(111)

For Pt the surface structures have been investigated previously.[9,10] Here we have redone the calculations with the same setup as for Ag and Ni. At potentials below 0.78 V (RHE) the pure Pt surface without adsorbates is the most stable. Water is oxidized to O* at potentials above 0.78 V (RHE). From 0.78 V (RHE) to 1.0 V (RHE) the O coverage is 1/4 ML. At higher potentials the coverage increases gradually to 1/3 ML O, then 1/2 ML O *etc.*, see the Pourbaix diagram Fig. 3. Potentials near 1.5 V are required before standard dissolution becomes thermodynamically favored.

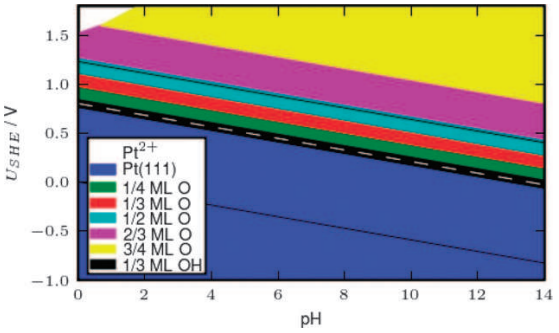

Fig. 3 Surface Pourbaix diagram for Pt(111). If ΔG_{field} is neglected, the oxygen coverage increases gradually starting at 0.78 V (RHE). If ΔG_{field} is included as found by Karlberg *et al.*,[9] 1/3 ML OH is less than 0.05 eV more unstable than O* in the potential range 0.78 VRHE–0.84 VRHE (black area). We consider O* and HO* to be equally stable in this potential range within the accuracy of the calculations.

Recent DFT calculations including the electric field in the double layer show that 1/3 ML hydroxyl in a hexagonal layer of water is stable from 0.75 V (RHE) to 0.9 V (RHE), as a result of the electric field stabilizing HO* relative to O*.[9,10] This surface has also previously been found to be stable in UHV.[15,16]

Including the effect of the electric field from ref. 9, we find that hydroxyl in the water layer is unstable by less than 0.05 eV relative to 1/4–1/3 ML O, in the potential range from 0.78 to 0.84 V (RHE). We therefore consider the stability of 1/3 ML hydroxyl and 1/3 ML O to be the same near 0.80 V (RHE) within the accuracy of the calculations.

3.3 Ni(111)

The Ni(111) surface is quite reactive, and corrosion is a problem in acidic as well as alkaline solutions. We consider the acidic dissolution[13] process

$$Ni(s) \leftrightarrow Ni^{2+}(aq) + 2e^-,\ U^\circ = -0.257\ V. \qquad (14)$$

and the dominant alkaline corrosion process[13,30,31]

$$Ni(s) + 3H_2O(l) \leftrightarrow 2e^- + 3H^+(aq) + Ni(OH)_3^-(aq),\quad U^\circ = 0.63\ V. \qquad (15)$$

We find that at U_{RHE} = 0 V, 1/4 ML H is adsorbed at the surface up to 0.14 V (RHE). Oxygen starts to adsorb at U_{RHE} > 0.20 V, with 1/3 ML O* stabilized by water being the most stable structure in the potential range from 0.34 V (RHE) to 0.82 V (RHE). The highest resistance against corrosion is obtained at pH = 9.9, where $\Delta G^\circ < 0$ for $U_{RHE} > 0.38$ V, as seen from Fig. 4 and 5. The free energy of formation for O* is 0.39 eV/O at 1/4 ML O coverage as calculated from (4) and (5), which is in reasonable agreement with the experimental value of 0.49 ± 0.10 eV/O*.[32]

In contrast to Taylor *et al.*,[33] we do not find HO* or co adsorbed O* and HO* to be stable on the Ni(111)-surface. However we note that at 0.18 V the free energies of 1/4 ML H*, 1/4 ML O* and 1/6 ML HO* are equal within 0.1 eV. The difference could therefore be caused by different functionals and atomic structures of the adsorbates.

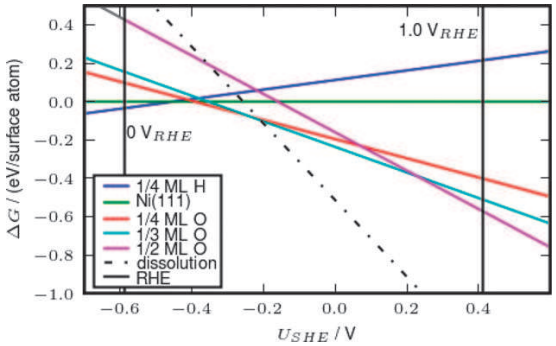

Fig. 4 The most stable Ni(111) surfaces at pH = 9.9. The resistance against dissolution is at maximum at this potential because ΔG of the acidic and alkaline dissolution are equal at this potential. Neglecting dissolution, the oxygen coverage then increases gradually with 1/3 ML O having a broad stability range from 0.34 V (RHE) to 0.82 V (RHE). Dissolution is spontaneous for $U > 0.38$ V (RHE).

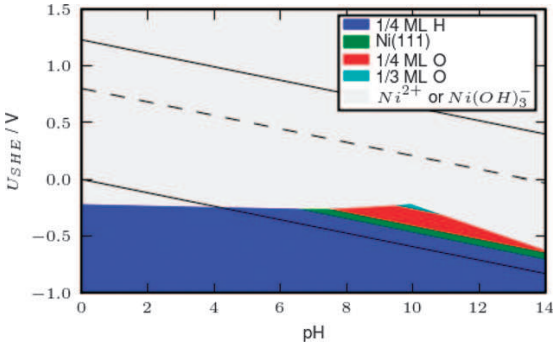

Fig. 5 Surface Pourbaix diagram for Ni(111) including alkaline and acidic dissolution. Dissolution is a problem in both acidic and alkaline electrolytes. The best resistance against dissolution is obtained at pH = 10, where dissolution becomes spontaneous for $U_{RHE} > 0.38$ V. Oxygen is adsorbed for $U_{RHE} > 0.20$ V.

In UHV experiments oxygen on Ni(111) may form an ordered $p(2\times2)$ structure with 0.25 ML coverage or a $(\sqrt{3}\times\sqrt{3})$R30°-structure with 0.33 ML coverage.[34] Oxidation of the Ni(111) surface initiates at a coverage between 0.33 and 0.5 ML,[32,34] suggesting that ORR on the metallic Ni surface could occur on a surface with up to 1/2 ML O. Thermodynamically β-$Ni(OH)_2$ is however the most stable nickel phase at these conditions.[30]

3.4 Oxygen reduction reaction

We now consider the situation in the presence of molecular oxygen. The aim is to determine the intermediates of the oxygen reduction reaction at the relevant surface for the different metals. In an acidic solution we write the electrode reactions as:

Anode:

$$H_2 \rightarrow 2H^* \rightarrow 2H^+ + 2e^- \quad (16)$$

Cathode:

$$\begin{aligned} O_2 + 4H^+ + 4e^- &\rightarrow HOO^* + 3H^+ + 3e^- \\ &\rightarrow H_2O + O^* + 2H^+ + 2e^- \\ &\rightarrow H_2O + HO^* + H^+ + e^- \rightarrow 2H_2O \end{aligned} \quad (17)$$

In an alkaline solution the same reactions can be expressed with OH^- instead:

Anode:

$$2OH^- + H_2 \rightarrow 2H^* + 2OH^- \rightarrow 2H_2O + 2e^- \quad (18)$$

Cathode:

$$\begin{aligned} O_2 + 2H_2O + 4e^- &\rightarrow HOO^* + H_2O + OH^- + 3e^- \\ &\rightarrow O^* + H_2O + 2OH^- + 2e^- \\ &\rightarrow HO^* + 3OH^- + e^- \rightarrow 4OH^- \end{aligned} \quad (19)$$

It is interesting to note that the adsorbed intermediates along the reaction coordinate are independent of the concentration of protons. The only change is the chemical potential of the protons, and that the proton donor changes from being H^+ or hydronium ion in acid electrolytes to being H_2O in alkaline electrolytes.

We now calculate the free energy of the intermediates in eqn (17) or (19). We will consider ORR feasible as long as all reaction steps along the reaction decrease the free energy. We determine the highest potential where this still holds, and refer to this as the ORR potential. The ORR potential depends on the metal and surface structure, which means we have to find the surface structure with the highest ORR potential that is consistent with the stability of the surface structure. We use the fact that the most stable surface at a given potential found above will be one of the intermediates during the ORR. Free energy diagrams of the intermediates on Pt, Ag and Ni are shown in Fig. 6, 7 and 11 at the ORR potential and at 0 V (RHE) and 1.23 V (RHE). The higher the ORR potential, the better the ORR catalyst.

It has previously been shown for Pt and Pt-alloys that the ORR potential is determined by either reduction of HO* (the last step in reaction 17) or the formation of OOH* (the first step in reaction 17).[9] For reactive surfaces the first of the two is rate determining and for noble surfaces the latter is rate

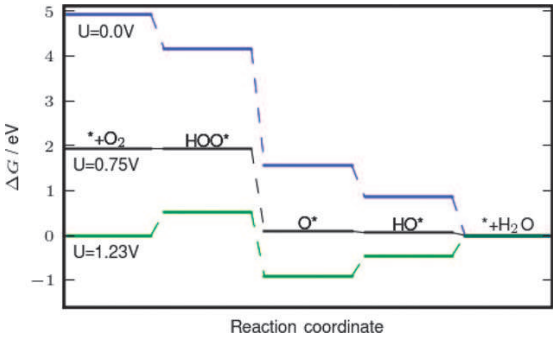

Fig. 6 Stability of the intermediates for the oxygen reduction reaction on Pt(111). The stability of the intermediates has been corrected for the effect of the electric field using the results of Karlberg *et al.*[9] The formation of HOO* and desorption of HO* become exothermic at nearly the same potential, in agreement with previous findings that Pt is close to the optimal catalyst for ORR.

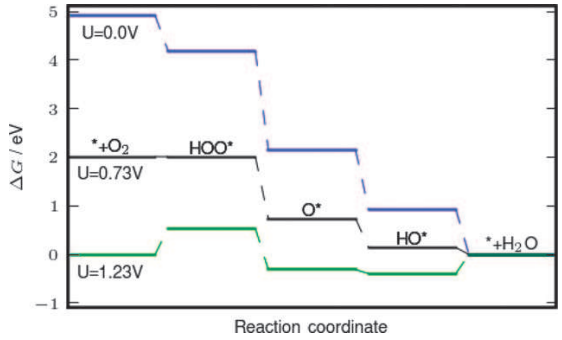

Fig. 7 Stability of intermediates for the oxygen reduction reaction on Ag(111). The formation of HOO* determines the overpotential, in agreement with previous trend studies showing that Ag binds adsorbates too weakly. The stability of the intermediates has been corrected for the effect of the electric field using the results of Karlberg *et al.*[9]

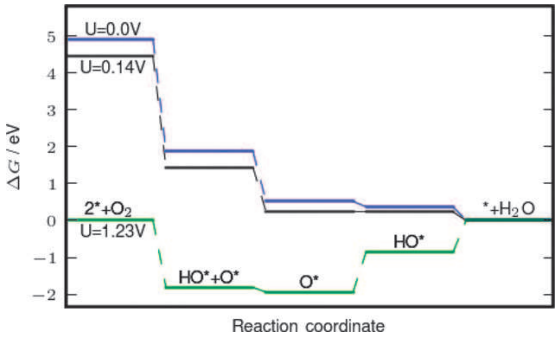

Fig. 9 The free energy of the intermediates adsorbed at vacancies in Ni – $\sqrt{3} \times \sqrt{3}$R30°– O. All steps decrease the free energy at potentials below 0.14 V. A water layer has been used to stabilize all intermediates as shown in Fig. 8. Without the water layer to stabilize O*, the self-consistent ORR potential is 0.26 V.

determining. Both reaction energies scale linearly with the oxygen binding energy, which determines a Sabatier volcano where the lowest overpotential is found for a material with the optimal trade-off between strong and weak binding of oxygen. Pt is close to this optimum, Ni binds too strongly and Ag binds just too weakly. However, previous analysis has been done for the surface relevant for Pt. As seen above, the most stable surface of Ni at a given potential will be different from the most stable Pt surface which, again, is different from the Ag surface.

3.4.1 ORR on Pt(111). We have previously studied ORR on Pt in details. The results are summarized here for comparison with Ag and Ni. The most stable surface in the relevant potential region is O* and the mixed HO*-water layer as discussed in details above. We therefore use these two surfaces to represent the two last ORR intermediates in eqn (17). We construct the OOH* intermediate from the HO*-water layer by inserting an oxygen atom between HO* and the surface.

The stability of the intermediates is shown in Fig. 6 at potentials 0.0, 0.75 and 1.23 V *vs.* RHE. The two potential determining steps are $O_2(g) + H^+ + e^- + * \rightarrow OOH*$ and $HO* + H^+ + e^- \rightarrow * + H_2O(l)$.[5] That these two steps determine the same ORR potential reflects that Pt has a reactivity close to optimal, as increasing ΔG_0 for one of the steps will decrease ΔG_0 for the other step due to the linear relations between the adsorption energies. Dissolution of Pt is not a big problem since it requires $U_{SHE} > 1.2$ V.

3.4.2 ORR on Ag(111). We find the Ag(111) surface to be free of adsorbates up to 0.93 V (RHE), where 1/6 ML hydroxyl is adsorbed, followed by additional HO* formation to form a structure with 1/3 ML hydroxyl at 1.11 V. At any reasonable overpotential we would therefore expect the total coverage on the surface to be very low. At 1/6 ML total coverage the rate limiting step is the formation of HOO*, which becomes exothermic at potentials below 0.73 V. This is in agreement with previous estimations based on DFT calculations of the oxygen binding energy on Ag(111).[5] The adsorption of HOO* being rate limiting reflects the fact that Ag is a

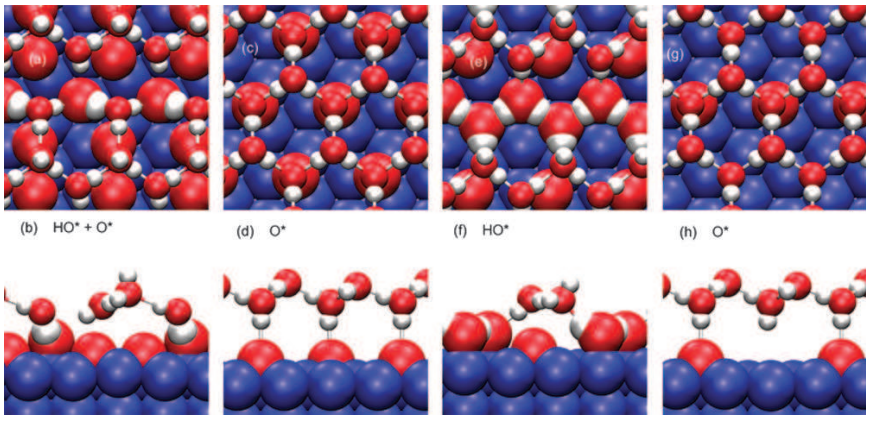

Fig. 8 Intermediates forming at vacancies on Ni – $\sqrt{3} \times \sqrt{3}$R30°– O. (a) + (b): The HOO* intermediates dissociates into hydroxyl and oxygen. (c) + (d): Adsorbed oxygen completing the $\sqrt{3} \times \sqrt{3}$R30°– O structure. (e) + (f): Adsorbed hydroxyl. (g) + (h): The vacancy. The Ni atoms and the molecules adsorbed directly at the surface are represented by spacefill whereas the surrounding water molecules, which are not in direct contact with the Ni surface, are represented by enlarged CPK spheres. Ni atoms are blue, O atoms red and H atoms white.

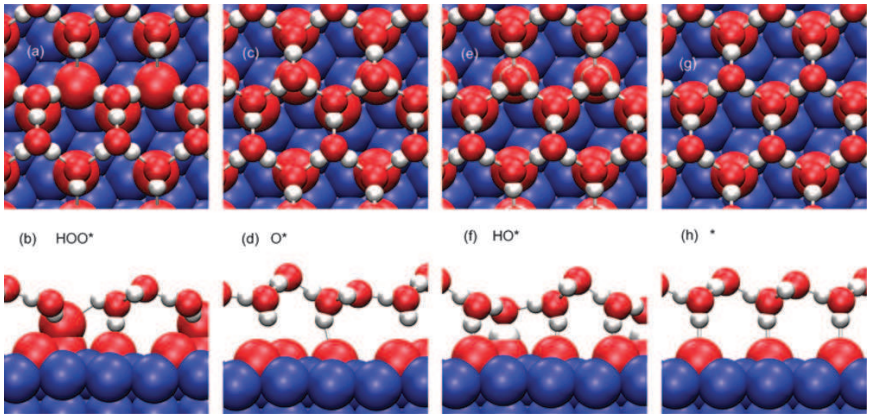

Fig. 10 Intermediates adsorbed at free sites on Ni – $\sqrt{3} \times \sqrt{3}$R30°– O. (a) + (b): HOO*. (c) + (d): O*, (e) + (f): HO*, (g) + (f): The Ni – $\sqrt{3} \times \sqrt{3}$R30°– O surface.

noble metal that binds the intermediates too weakly relative to the optimal ORR catalyst. Ag therefore seems like a good alternative to Pt, however the problem in acidic solution is dissolution and not activity. Dissolution involves only electron transfer to Ag, which means that the relevant dissolution potential will not change *vs.* SHE. Since ORR in alkaline environment runs at lower potentials *vs.* SHE, Ag-dissolution becomes less of a problem.

Assuming the effect of the electric field in the dipole layer is similar on Pt(111) and Ag(111), the electric field destabilizes O* by *ca.* 0.04 eV and stabilizes HO* by *ca.* 0.06 eV at the ORR potential. The adsorption energy of HOO*, which determines the overpotential in this model, is destabilized by *ca.* 0.01 eV by the electric field. The corrections due to the electric field are therefore too small to change the qualitative picture of ORR on Ag(111). The free energy of the intermediates is shown at different potentials in Fig. 7 including the corrections due to the potential.

3.4.3 ORR on Ni(111). On the clean Ni(111) surface O_2 dissociates easily, so the rate limiting step on Ni at very low coverage is reduction of O* to HO* or HO* to H_2O. With a water layer included to stabilize HO* on the surface, we find ΔG_0(HO*) = 0.27 eV and ΔG_0(O*) = 0.41 eV. All reduction steps are therefore exothermic at $U_{RHE} < 0.14$ V, which shows that the clean Ni(111) surface is too reactive to be a good ORR catalyst. From the surface Pourbaix diagram we would however expect some oxygen at the surface at higher potentials. This changes the adsorption energies due to adsorbate interactions.

To take adsorbate interactions into account we consider ORR involving the $\sqrt{3} \times \sqrt{3}$R30°– O surface, as it is the most stable in the potential range from 0.33 to 0.82 V (RHE). The oxygen reduction reaction might occur by adsorption and subsequent reduction of O_2 at vacancies in the $\sqrt{3} \times \sqrt{3}$R30° – O structure, as shown in Fig. 8. The free energy of the intermediates is shown in Fig. 9.

We find that spectator O* makes the Ni(111) surface a bit more noble because the binding energies of O* and HO* are decreased by *ca.* 0.1 eV. The HOO* intermediate dissociates on this surface. All steps are exothermic for $U_{RHE} < 0.14$ V with the rate limiting step being a reduction of O* to HO*.

Another possible reaction mechanism on the $\sqrt{3} \times \sqrt{3}$R30°– O surface is that O_2 adsorbs and is reduced at free sites on the surface as shown in Fig. 10. Because of repulsion between adsorbed oxygen and H_2O adsorbed at the top sites, a H_2O–HO* bonding network directly on the surface is rather unstable. We find HO* to be the most stable with the water layer placed above the surface, with hydrogen bonds between the surface and the water layer. A similar structure is found to be the most stable for O* and HOO*, except that it has been possible to include HOO* into the water layer, as it protrudes from the surface. When HOO* is included in the water layer and allowed to relax, hydrogen moves from HOO* to a nearby water molecule, forming a H_3O molecule. The H–O bond in H_3O is 1.05 Å and the H–OO* bond is 1.51 Å. The free energy of the intermediates is shown in Fig. 11. The free energies of O* and HO* have increased significantly compared to the clean Ni(111) surface, making the surface much more noble. The significantly increased interaction between adsorbates may be rationalized by the fact that the

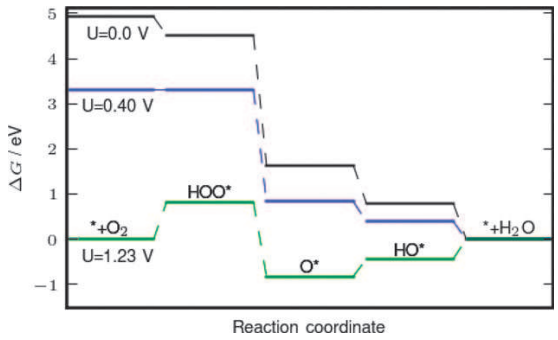

Fig. 11 Free energy of the intermediates along the reaction path (17) or (19) adsorbed at the free sites on Ni – $\sqrt{3} \times \sqrt{3}$R30°– O. Because the formation of HOO* limits the ORR potential, the overpotential could be reduced if the binding energies could be increased. If O_2 dissociates easily on the $\sqrt{3} \times \sqrt{3}$R30°– O surface, the overpotential is also decreased.

adsorbates bind to the same Ni atoms on the surface. The rate limiting step is the formation of HOO*, which is exothermic at potentials below 0.40 V (RHE). The binding free energies for oxygen and hydroxyl are 1.64 and 0.80 eV respectively. The O* and HO* binding energy on Ni(111) with 1/3 ML O suggests that this surface is a good ORR catalyst comparable to Pt, but the binding energy of HOO* is weaker than that of Pt. Formation of HOO* therefore becomes the rate limiting step on Ni.

An alternative to the OOH formation mechanism in eqn (17) or (19) is that oxygen dissociates on the surface. An estimate of the O_2 dissociation barrier, based on the oxygen binding energy and the Brøndsted–Evans–Polany relationship between the adsorption energy and the activation energy,[35] suggests that dissociation on the Ni – $\sqrt{3} \times \sqrt{3}$R30°– O surface is non-activated. Taking the dissociation reaction path into consideration increases the ORR potential to a value close to that of Ag and Pt, because reduction of O* and HO* is efficient on the Ni – $\sqrt{3} \times \sqrt{3}$R30°– O surface. However, metallic Ni will dissolve in alkaline solution at U_{RHE} = 0.7–0.8 V, clarified in Fig. 5.

4. Conclusion

We have, based on DFT calculations, constructed surface Pourbaix diagrams for Ag, Ni and Pt(111) surfaces at potentials relevant for oxygen reduction. These diagrams show the most stable surface structure as function of pH and potential. The surface structure is obviously important for the catalytic activity. The calculated values for the HO* formation potential is 0.86 V (RHE) for Pt and 0.93 V (RHE) for Ag, both in good agreement with experimental CV diagrams.[4,7] It is important to note that the coverage of O* and HO* is independent of pH at a given potential *vs.* RHE whereas the potential of dissolution is not.

We investigate oxygen reduction reaction on the different surface structures and calculate the free energy of the intermediates along the ORR. We estimate their catalytic activity for ORR by determining the highest potential at which all ORR reaction steps reduce the free energy. We refer to this potential as the ORR-potential. By demanding that one of the intermediates in ORR belongs to the most stable surface in the absence of molecular oxygen, it is possible to obtain self-consistency in the sense that the surface is stable at the surface structure dependent ORR potential. The self-consistency changes the activity of too reactive catalyst surfaces (Ni), whereas the activity for a close to optimal catalyst (Pt) and the too noble catalyst (Ag) is unchanged. The reason for this change is that as the reactive surface is oxidized, the absorbed oxygen shifts the reactivity towards the noble region, which in turn increases the activity. This explains why Ni has catalytic ORR activity but cannot be used in acidic PEM fuel cells. We find that whereas there is no effect of the pH on the coverage of adsorbates at the relevant ORR-potential, pH has a dramatic effect on the dissolution potential relative to the ORR potential. In the case of Ni the ORR-potential line (U = 0.8 V (RHE) in Fig. 5) is still in the dissolution area at pH = 14, which means that for Ni the stability limits the ORR-potential. For Ag the line of 0.8 V (RHE) in the Pourbaix starts for pH = 0 in the dissolution region and as pH is increased the ORR potential line moves further and further away from dissolution, as shown in Fig. 2. The stability thereby offers an explanation of the possible use of Ag in alkaline fuel cell cathodes.

Acknowledgements

CAMD is funded by the Lundbeck foundation. This work was supported by the Danish Center for Scientific Computing through grant no. HDW-1103-06. The work is also supported by EU and NABIT grant no. 2106-04-0039 through the Specific Target Project Apollon-B grant no. MMP3-CT-2006-033228.

References

1. N. M. Markovic and P. N. Ross, *CATTECH*, 2000, **4**, 110.
2. G. Hoogers and D. Thompsett, *CATTECH*, 1999, **3**, 106.
3. J. Larminie and A. Dicks, *Fuel cell systems explained*, J. Wiley, Chichester, West Sussex, 2003.
4. B. B. Blizanac, P. N. Ross and N. M. Markovic, *J. Phys. Chem. B*, 2006, **110**, 4735–4741.
5. J. K. Nørskov, J. Rossmeisl, A. Logadottir, L. Lindqvist, J. R. Kitchin, T. Bligaard and H. Jonsson, *J. Phys. Chem. B*, 2004, **108**, 17886–17892.
6. V. Stamenkovic, B. S. Mun, K. J. J. Mayrhofer, P. N. Ross, N. M. Markovic, J. Rossmeisl, J. Greeley and J. K. Nørskov, *Angew. Chem., Int. Ed.*, 2006, **45**, 2897–2901.
7. V. R. Stamenkovic, B. Fowler, B. S. Mun, G. F. Wang, P. N. Ross, C. A. Lucas and N. M. Markovic, *Science*, 2007, **315**, 493–497.
8. G. S. Karlberg, T. F. Jaramillo, E. Skulason, J. Rossmeisl, T. Bligaard and J. K. Nørskov, *Phys. Rev. Lett.*, 2007, **99**, 126101.
9. G. S. Karlberg, J. Rossmeisl and J. K. Nørskov, *Phys. Chem. Chem. Phys.*, 2007, **9**, 5158–5161.
10. J. Rossmeisl, J. K. Nørskov, C. D. Taylor, M. J. Janik and M. Neurock, *J. Phys. Chem. B*, 2006, **110**, 21833–21839.
11. S. Kandoi, A. A. Gokhale, L. C. Grabow, J. A. Dumesic and M. Mavrikakis, *Catal. Lett.*, 2004, **93**, 93–100.
12. M. Mavrikakis, personal communication.
13. R. C. Weast, *CRC Hanbook of Chemistry and Physics*, The Chemical Rubber Company, Cleveland, OH, 49th edn, 1968–1969.
14. P. W. Atkins, *Physical Chemistry*, Oxford University Press, Oxford, UK, 1998.
15. H. Ogasawara, B. Brena, D. Nordlund, M. Nyberg, A. Pelmenschikov, L. G. M. Petterson and A. Nilsson, *Phys. Rev. Lett.*, 2002, **89**, 276102.
16. C. Clay, S. Haq and A. Hodgson, *Phys. Rev. Lett.*, 2004, **92**, 046102.
17. P. Hohenberg and W. Kohn, *Phys. Rev.*, 1964, **136**, B864–B871.
18. W. Kohn and L. J. Sham, *Phys. Rev.*, 1965, **140**, A1133–A1138.
19. B. Hammer, L. B. Hansen and J. K. Nørskov, *Phys. Rev. B: Condens. Matter Mater. Phys.*, 1999, **59**, 7413–7421.
20. J. P. Perdew, K. Burke and M. Ernzerhof, *Phys. Rev. Lett.*, 1996, **77**, 3865–3868.
21. D. Vanderbilt, *Phys. Rev. B: Condens. Matter Mater. Phys.*, 1990, **41**, 7892–7895.
22. H. J. Monkhorst and J. D. Pack, *Phys. Rev. B: Solid State*, 1976, **13**, 5188–5192.
23. Dacapo is available from https://wiki.fysik.dtu.dk/dacapo, and ASE from https://wiki.fysik.dtu.dk/ase. The cluster consists of Intel Pentium-4 PC's and AMD Opteron servers: https://wiki.fysik.dtu.dk/niflheim/Hardware.
24. M. Pourbaix, *Atlas of Electrochemical Equilibria*, Oxford, New York, Pergamon Press, 1966.
25. G. Rovida, F. Pratesi, M. Magliett and E. Ferroni, *J. Vac. Sci. Technol.*, 1972, **9**, 796.

26. J. Schnadt, A. Michaelides, J. Knudsen, R. T. Vang, K. Reuter, E. Lægsgaard, M. Scheffler and F. Besenbacher, *Phys. Rev. Lett.*, 2006, **96**, 146101.
27. S. L. Horswell, A. L. N. Pinheiro, E. R. Savinova, M. Danckwerts, B. Pettinger, M.-S. Zei and G. Ertl, *Langmuir*, 2004, **20**, 10970–10981.
28. E. R. Savinova, A. Scheybal, M. Danckwerts, U. Wild, B. Pettinger, K. Doblhofer, R. Schlögl and G. Ertl, *Faraday Discuss.*, 2002, **121**, 181–198.
29. V. Maurice, L. H. Klein, H. H. Strehblow and P. Marcus, *J. Phys. Chem. C*, 2007, **111**, 16351–16361.
30. B. Beverskog and I. Puigdomenech, *Corros. Sci.*, 1997, **39**, 969–980.
31. C. F. Baes and R. E. Mesmer, *The Hydrolysis of Cations*, Krieger Publishing Company, Malabar, FL, 1986.
32. J. T. Stuckless, C. E. Wartnaby, N. Al-Sarraf, St. J. B. Dixon-Warren, M. Kovar and D. A. King, *J. Chem. Phys.*, 1997, **106**, 2012–2030.
33. C. Taylor, R. G. Kelly and M. Neurock, *J. Electrochem. Soc.*, 2006, **153**, E207–E214.
34. A. R. Kortan and R. L. Park, *Phys. Rev. B: Condens. Matter Mater. Phys.*, 1981, **23**, 6340–6347.
35. J. K. Nørskov, T. Bligaard, A. Logadottir, S. Bahn, L. B. Hansen, M. Bollinger, H. Bengaard, B. Hammer, Z. Sljivancanin, M. Mavrikakis, Y. Xu, S. Dahl and C. J. H. Jacobsen, *J. Catal.*, 2002, **209**, 275–278.

P2

Alloys of Platinum and Early Transition Metals as Oxygen Reduction Electrocatalysts

J. Greeley, I. E. L. Stephens, A. S. Bondarenko, T. P. Johansson, H. A. Hansen, T. F. Jaramillo, J. Rossmeisl, I. Chorkendorff and J. K. Nørskov

Accepted for publication in Nature Chemistry

nature chemistry

ARTICLES

PUBLISHED ONLINE: XX XX 2009 | DOI: 10.1038/NCHEM.367

Alloys of platinum and early transition metals as oxygen reduction electrocatalysts

J. Greeley[1†], I. E. L. Stephens[2], A. S. Bondarenko[2], T. P. Johansson[2], H. A. Hansen[1], T. F. Jaramillo[2†], J. Rossmeisl[1], I. Chorkendorff[2] and J. K. Nørskov[1]*

The widespread use of low-temperature polymer electrolyte membrane fuel cells for mobile applications will require significant reductions in the amount of expensive Pt contained within their oxygen reduction reaction (ORR) electrodes. Although progress has been made in this respect, further reductions through the development of more active and stable electrocatalysts are still necessary. Here we describe a new set of ORR electrocatalysts consisting of Pd or Pt alloyed with early transition metals such as Sc or Y. They were identified using density functional theory calculations as being the most stable Pt- and Pd-based binary alloys with ORR activity likely to be better than Pt. Electrochemical measurements show that the activity of polycrystalline Pt_3Sc and Pt_3Y electrodes is enhanced relative to pure Pt by a factor of 1.5–1.8 and 6–10, respectively, in the range 0.9–0.87 V.

The development of low-temperature polymer electrolyte membrane fuel cells (PEMFCs) is severely hampered by the fact that the oxygen reduction reaction (ORR) is slow, even when using platinum as a catalyst. Platinum is expensive and scarce, and it has been suggested that for PEMFCs to become viable using Pt-based catalysts, these catalysts would need to show a stable catalytic activity of at least two to four times that of Pt[1]. Several Pt alloys, including late transition metals such as Ni, Co, Cr, Fe and Cu, are considerably more active than Pt and have been studied intensively[1–11]. In the present paper, we introduce a new set of Pt intermetallic compounds with promising properties for the ORR.

The ORR is a 'difficult' catalytic reaction in the sense that the catalyst must be stable under the extremely corrosive conditions at a fuel cell cathode yet chemically active enough to be able to activate O_2 and noble enough to be able to release the oxygen from the surface to form H_2O. O_2 activation typically involves a proton and electron transfer to form adsorbed OOH before the O–O bond is broken[12], hence the catalyst must be able to stabilize OOH. After dissociation, adsorbed O and OH are formed on the catalyst surface, and the catalyst must not bind these species too strongly in order for desorption to be fast.

We concentrate on metallic ORR catalysts made from alloys or intermetallic compounds (referred to hereafter as alloys). We will limit ourselves to systems that form Pt or Pd overlayers (or 'skins') at the surface. These are the only metallic elements that are stable under the high potentials and acidic conditions of a PEMFC and, at the same time, exhibit surface chemical properties close to optimum for the ORR[12]. The overall goal is to find alloys of the composition Pt_3X or Pd_3X using the following criteria: (1) they should form Pt or Pd overlayers with ORR activity larger than that of Pt, and (2) they should be as stable as possible. Our approach is to first use density functional theory (DFT) calculations to identify interesting candidates and to then test them experimentally[13,14]. Computationally based electrocatalyst discovery is the principal aim of this approach, but more generally and, perhaps, more importantly, this study probes our present understanding of the ORR. In the field of catalysis, there is no stronger evidence for the robustness and accuracy of a theoretical framework than the ability to use that framework to identify new active materials.

Results

Computational screening. Our understanding of ORR activity trends on different metal surfaces is summarized in Fig. 1. Plotting measured activities for a series of different catalysts from a number of different experimental groups as a function of the calculated oxygen adsorption energy results in a simple 'volcano' relationship[6,12]. Fig. 1a shows such a volcano for different Pt overlayers and demonstrates that the oxygen adsorption energy is a good descriptor for the catalytic activity.

The origin of this picture is the following. Density functional calculations of the free energy changes during the ORR (see Fig. 1b) show that on close-packed Pt surfaces two reaction steps can be sluggish, that is, involve a positive change in free energy (ΔG): the first electron and proton transfer to form adsorbed OOH, and the last such transfer to remove OH (or O) from the surface to form water. We will use the values of ΔG for these steps (defined as ΔG_1 and ΔG_2, respectively) as a measure of the rate; the smaller the ΔG, the faster the corresponding reaction step is. The implicit assumption in this analysis is that any additional activation barriers are the same for all metals or that they scale with ΔG in a Brønsted–Evans–Polanyi-type relationship[15]; indeed, there is good evidence that this is a valid assumption[16]. By restricting our calculations to closely packed surfaces, another implicit assumption is that these dominate the activity of polycrystalline Pt and Pt_3X, as well as the surfaces of Pt nanoparticles in fuel cell catalysts. This also appears to be a reasonable conjecture, given that more open surfaces tend to bind O and OH considerably stronger and hence become blocked[17]. Moreover, experimental evidence suggests that the activity enhancement over Pt observed on extended surfaces of Pt_3X alloys is reproduced qualitatively on nanoparticulate Pt_3X alloy surfaces[4,7,18].

[1]Center for Atomic-scale Materials Design, Department of Physics, Building 311, Technical University of Denmark, DK-2800 Lyngby, Denmark, [2]Center for Individual Nano-Particle Functionality, Department of Physics, Building 312, Technical University of Denmark, DK-2800 Lyngby, Denmark; †Present address: Center for Nanoscale Materials, Argonne National Laboratory, Argonne, Illinois 60439 (J.G.), Department of Chemical Engineering, Stanford University, Stanford, California 94305-5025 (T.F.J.). *e-mail: norskov@fysik.dtu.dk

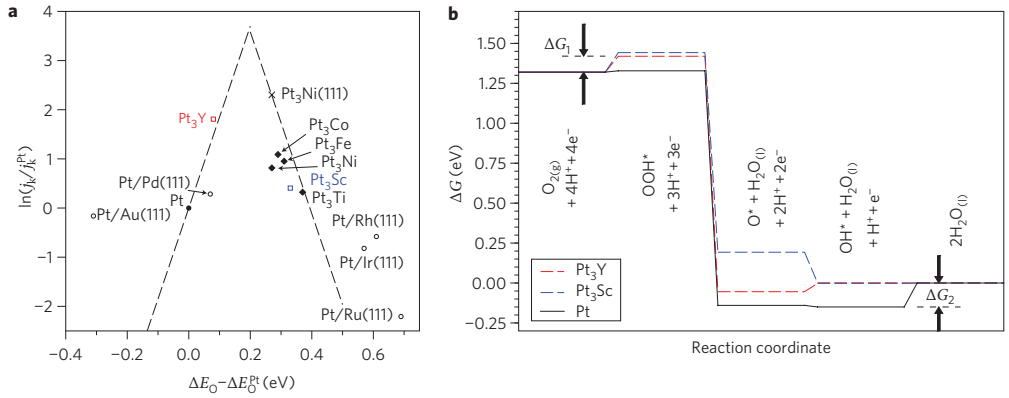

Figure 1 | Volcano plots and free energy diagrams for the oxygen reduction reaction on Pt-based transition metal alloys. a, Measured kinetic current density as reported in the literature for a range of alloy electrocatalysts with Pt 'skins' plotted as a function of the calculated oxygen adsorption energy, ΔE_O. All data are shown relative to Pt. This removes many of the systematic variations in conditions of the different experiments. The sources of the experimental data are marked by: circles[34] (Pt monolayers supported on single-crystal metal electrodes), diamonds[6] (polycrystalline alloys annealed in ultrahigh vacuum before immersion in the electrochemical cell) and crosses[2] (bulk $Pt_3Ni(111)$ alloys annealed in ultrahigh vacuum before immersion). The dashed lines are the theoretical predictions from refs 12,35. We have also included data points for the Pt_3Y (red) and Pt_3Sc (blue) catalysts studied in the present work. **b**, Calculated free energy diagram for the oxygen reduction reaction at 0.9 V (versus the reversible hydrogen electrode) for Pt(111) (solid line) and for Pt overlayers on the $Pt_3Sc(111)$ and $Pt_3Y(111)$ surfaces (dashed). The free energy changes for the formation of OOH (ΔG_1) and the removal of OH (ΔG_2) are indicated. In each case a water bilayer as well as electrical field effects (see ref. 36) are included. Q3

On a given surface, the magnitudes of ΔG_1 and ΔG_2 (and thus the rate of the ORR) are related to the stability of adsorbed OOH, OH and O. Forming a Pt 'skin' on top of a Pt_3X compound is one way to modify the electronic structure of the Pt surface to tune the stability of these critical intermediates. The stabilities of the OOH and OH (and O) intermediates, in turn, scale roughly with the stability of adsorbed O (ΔE_O); hence, this parameter is particularly useful for characterizing both ΔG_1 and ΔG_2[19,20]. If ΔE_O becomes increasingly positive, adsorbed OOH is destabilized, resulting in a larger ΔG_1. Simultaneously, however, ΔG_2 decreases because it becomes easier to break the Pt–OH (and Pt–O) bonds. These opposing effects give rise to the volcano observed in Fig. 1a.

Figure 1a shows both experimental activity data as well as a dashed line indicating predicted activity based on our DFT model. Both the experimental data and the model strongly suggest that a surface that binds O 0–0.4 eV more weakly than Pt(111) should exhibit an ORR activity better than Pt, with the optimum at a binding energy of roughly 0.2 eV weaker than that of Pt. We note that, although all of the computational results in the figure are obtained on perfect, close-packed single crystal surfaces, the experimental data are taken from a mixture of single crystal, vacuum-annealed polycrystalline and Ar-sputtered polycrystalline surfaces. The resulting structural differences do introduce deviations from our single-crystal models, implying modest changes in ORR activity[21], but the differences do not substantially alter the trends described above.

In addition to looking for active skin-type Pt_3X or Pd_3X compounds for the ORR, we also searched for such alloys that are stable using a database developed from DFT calculations[22,23]. In Fig. 2, we show the calculated oxygen adsorption energy on the skins, ΔE_O relative to Pt, as a function of the calculated heat of formation of the bulk alloys, $\Delta E_{alloy} = E(\text{alloy}) - E(\text{constituents})$, where E is the total energy of the alloy and the constituents in metallic form, for a range of alloys.

One pathway to Pt or Pd skin formation is for Pt/Pd in the second layer of the close-packed (111) surface to exchange with X in the first layer; the concentration of X in the second layer then increases from the stoichiometric 25% to 50%[18]. Alternatively, a Pt skin may be formed simply by dissolution of X from the first layer, after which remaining Pt atoms reaggregate to partially heal the surface. This latter process, which would be more likely to result in a stoichiometric (~25%) concentration of X in the layer below the Pt surface, is, in principle, possible for all of the alloys included in Fig. 2 because they have a standard potential for stripping, U_{strip}, which is more negative than, or approximately equal to, the oxide or hydroxide formation potential, U_{ox}. Whether the concentration of X in the second layer is stoichiometric or higher depends on the system and the method by which it is formed.

We have calculated the O adsorption energy for both 25 and 50% X in the second layer for a number of the systems considered. The systems with 50% X in the second layer will only have surface Pt/Pd atoms with X neighbours, whereas systems with only 25% X in the second layer have two inequivalent types of Pt atoms—those with X neighbours in the second layer and those without. Both types will in principle contribute to the activity, but in cases like Pt_3Y, those surface Pt atoms coordinated to purely Pt neighbours in the second layer will bind O too strongly and will be blocked. Only the less reactive sites with second-layer Y neighbours will be active. These sites are equivalent to the active surface sites on the second-layer systems with 50% X. We therefore concentrate in the following analysis on these systems (red points in Fig. 2). Q1

It is clear from Fig. 2 that, of the alloys with ΔE_O values in the optimal range, Pt_3Y and Pt_3Sc stand out as the most stable. In fact, these are the most stable of all the face-centred cubic alloys in a database that consists of more than 60,000 compounds[22]. The common feature of these alloys is that they combine Pt or Pd and an early transition metal. The high stability of these compounds in the bulk can therefore be understood in terms of metal–metal *d* bonds that are approximately half filled (each of the two elements in the bond contribute half of nine *d* electrons for Pt or Pd plus one from X). This means that the bonding states are filled and the anti-bonding states are empty[24].

We note that the favourable bulk heat of formation of Pt_3Y and Pt_3Sc is still not sufficient to make these alloys thermodynamically stable against oxidation or dissolution under the conditions of a cathode in a PEMFC. It is, however, expected to affect the kinetic stability of these compounds. Transport of Y or Sc atoms from the interior of the alloy to the surface, where they may eventually

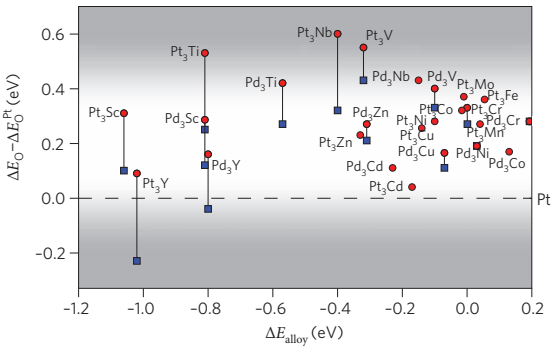

Figure 2 | Output of computational screening procedure, showing the oxygen binding energy, relative to that of Pt, on a Pt or Pd skin surface, as a function of alloying energy. ΔE_{alloy} is the calculated energy of formation of the indicated elements from the appropriate bulk elemental precursors, specified on a per atom basis. For some systems we include results for the cases where there are 50% (circles) and 25% (squares) of the alloying element in the second layer. The range of interesting oxygen adsorption energies where the ORR activity should be higher than that of Pt, according to the model, is highlighted with a greyscale gradient representing the edges of the range to recognize limitations on the accuracy of DFT calculations.

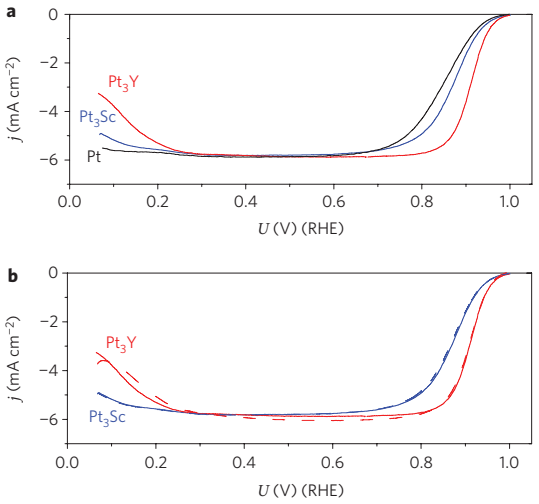

Figure 3 | Anodic sweeps of cyclic voltammograms of Pt, Pt_3Sc and Pt_3Y in O_2-saturated electrolyte. a, The first stable sweep. **b**, A comparison of the first steady cycle (solid lines) and after 90 minutes of cycling (dashed lines), for Pt_3Y and Pt_3Sc only, under the same conditions as **a**. Measurements were taken at 20 mV s^{-1} and 1,600 rpm in 0.1 M $HClO_4$ at 23 ± 2 °C.

dissolve or oxidize, will involve an energy barrier determined in part by the heat of formation of the compound.

Experimental results. In the following, we report an experimental characterization of the two most promising (active and stable) compounds described above, Pt_3Y and Pt_3Sc. The alloys were prepared in bulk, polycrystalline form. To pre-condition the surfaces for electrochemical testing, they were sputter-cleaned and analysed under ultrahigh vacuum conditions, without vacuum annealing (full details of the ultrahigh vacuum characterization can be found in the Supplementary Information). The catalysts' electrochemical activity was measured using a rotating disc electrode assembly. These procedures were similar to those used by Markovic and co-workers in their investigations of other polycrystalline bimetallic Pt alloys[25].

The activity of the catalysts for the ORR was measured by carrying out cyclic voltammograms in an O_2-saturated solution, shown in Fig. 3a. The onset for each electrode starts at ~1 V, and there is an initial exponential increase in the current, characteristic of kinetic control. At lower potentials (~0.7 V < U < ~0.95 V), the current approaches the mixed regime, where mass transport plays an increasingly important role. This potential range is the most interesting for fuel cell applications. At still lower potentials, the current reaches its diffusion-limited value, ~5.8 mA cm^{-2}. In the mixed regime, the ORR activity of different catalysts can be compared by evaluating the half wave potential, $U_{1/2}$ (that is, the potential at which the current reaches half its diffusion-limited value). The ORR activity reported for polycrystalline Pt in this work corresponds well to data reported in the literature[7]. The Pt_3Sc shows a positive shift in $U_{1/2}$ of ~20 mV relative to Pt, whereas the Pt_3Y shows a positive shift of ~60 mV. These data show that both Pt_3Y and Pt_3Sc exhibit significant activity improvements over Pt, in line with our theoretical predictions.

Modern PEMFCs have been designed for efficient delivery of reactive gases, thus mass transport effects are only of secondary importance; electrochemical kinetics are the primary cause of inefficiency[1]. In Fig. 4a, the measured current density is corrected for mass transport to obtain the true kinetic current density, j_k, of the catalyst, as a function of the potential, U. The same catalyst ranking is found as that determined by the half wave potential: activity increases in the following order: Pt < Pt_3Sc < Pt_3Y.

In Fig. 4b, the activity enhancement of Pt_3Sc and Pt_3Y over Pt is plotted as a function of potential. At 0.9 V, Pt_3Sc shows a 50% increase in specific activity over Pt, and Pt_3Y shows an improvement by a factor of six. At 0.87 V, Pt_3Sc shows an 80% increase in activity whereas the activity of Pt_3Y is enhanced by an order of magnitude. Owing to the steep gradient (or Tafel slope) of the polarization curve for Pt_3Y, the activity improvement over Pt should be even more pronounced at potentials below 0.87 V. To the best of our knowledge, the Pt_3Y electrode shows the highest ORR activity measured under these conditions for any bulk, polycrystalline metallic surface. The activity of our Pt_3Y sample is closer to that of single-crystal $Pt_3Ni(111)$[2] than to polycrystalline Pt_3Ni, which is not quite as active[7].

The alloy electrodes are stable under continued cycling, as shown in Fig. 3b. Long-term stability will, however, need to be investigated in membrane electrode assemblies in a fuel cell[26,27].

By combining the experimental activity data from Fig. 4a with the theoretically derived ΔE_O from Fig. 2, we have added the Pt_3Y and Pt_3Sc data points onto the volcano plot shown in Fig. 1a. Clearly, the new data follow the general trends very well. This result indicates that our model, describing trends in the ORR activity of alloys, has true predictive power. In Fig. 1b, we have also included more detailed calculations for the two alloy surfaces. It can be seen that the calculations support the notion that the free energy changes of the rate-limiting steps for Pt_3Y and Pt_3Sc are more favourable than the corresponding changes for Pt.

Discussion

It is highly desirable to find ORR catalysts that are not only more active than Pt but also free from precious metals. The model discussed in the present work suggests two avenues. One is to find alloys of non-precious metals with surface bonds to oxygen in the right range (0.0 to 0.4 eV weaker than Pt). The problem is that such alloys are usually not stable under polymer electrolyte fuel cell conditions[28]. A more radical approach is to find ways of avoiding the constraints of the volcano relationship in Fig. 1a. The volcano is the result of specific scaling relations between the stability of O, OH and OOH. If the structure of the active site is changed relative to the close-packed surfaces of metal alloys considered in the present

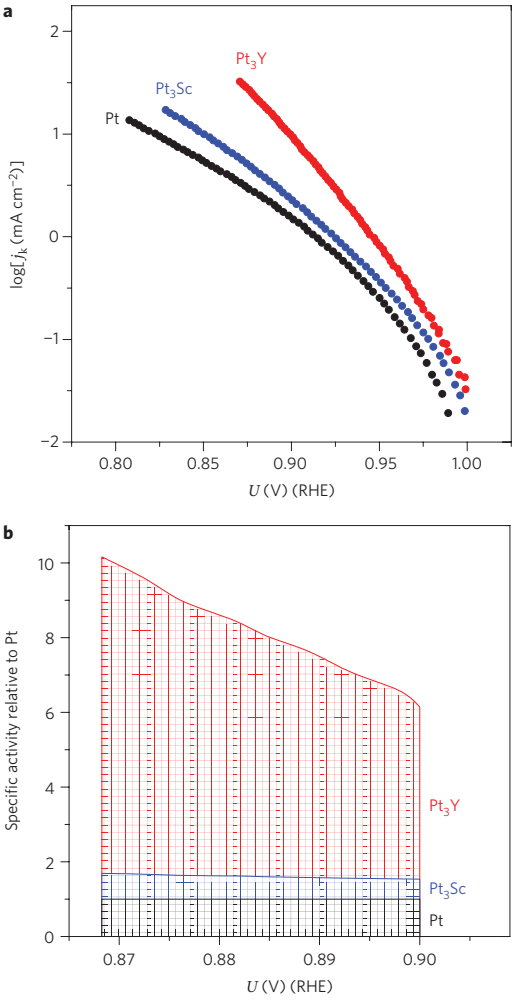

Figure 4 | Activity increase of Pt_3Y and Pt_3Sc versus Pt for the oxygen reduction reaction. a, Specific activity as a function of the electrode potential, U, for Pt, Pt_3Sc and Pt_3Y, expressed as a kinetic current density, j_k. **b**, Activity enhancement relative to Pt (j_k/j_k^{Pt}), from data shown in **a** and plotted on a linear scale. All data were extracted from the voltammograms shown in Fig. 3a.

paper, new scaling relations result and new volcanoes can arise. Rutile oxides have, for instance, been found to have a different volcano[29] and some rutile oxides show ORR activity[30]. The enzymes cytochrome *c* oxidases and multicopper oxidases, which catalyse the ORR with very high specific rates[31], represent interesting structures, and the recently reported iron-based catalysts[32] may represent another such interesting class of materials. However, for the time being the kinetic current densities of the Pt alloys are considerably higher owing to the increased density of active sites[33], and our model offers a reliable path to the discovery of such alloys with useful properties.

Received 2 July 2009; accepted 12 August 2009; published online XX XX 2009

References

1. Gasteiger, H. A., Kocha, S. S., Somappli, B. & Wagner, F. T. Activity benchmarks and requirements for Pt, Pt-alloy, and non-Pt oxygen reduction catalysts for PEMFCs. *Appl. Catal. B-Environ.* **56,** 9–35 (2005).
2. Stamenkovic, V. *et al.* Improved oxygen reduction activity on $Pt_3Ni(111)$ via increased surface site availability. *Science* **315,** 493–497 (2007).
3. Koh, K. & Strasser, P. Electrocatalysis on bimetallic surfaces: modifying catalytic reactivity for oxygen reduction by voltammetric surface dealloying. *J. Amer. Chem. Soc.* **129,** 12624–12625 (2007).
4. Chen, S. *et al.* Origin of oxygen reduction reaction activity on "Pt_3Co" nanoparticles: atomically resolved chemical compositions and structures. *J. Phys. Chem. C* **113,** 1109–1125 (2009).
5. Wakisaka, W., Suzuki, H., Mitsui, S., Uchida, H. & Watanabe, M. Increased oxygen coverage at Pt-Fe alloy cathode for the enhanced oxygen reduction reaction studied by EC-XPS. *J. Phys. Chem. C* **112,** 2750–2755 (2008).
6. Stamenkovic, V. *et al.* Changing the activity of electrocatalysts for oxygen reduction by tuning the surface electronic structure. *Angew. Chem. Int. Ed.* **45,** 2897–2901 (2006).
7. Paulus, U. A. *et al.* Oxygen reduction on high surface area Pt-based alloy catalysts in comparison to well defined smooth bulk alloy electrodes. *Electrochim. Acta* **47,** 3787–3798 (2002).
8. Paulus, U. A. *et al.* Oxygen reduction on Carbon-Supported Pt-Ni and Pt-Co Alloy Catalysts. *J. Phys. Chem. B* **106,** 4181–4191 (2002).
9. Mayrhofer, K. J. J., Juhart, V., Hartl, K., Hanzlik, M. & Arenz, M. Adsorbate-induced surface segregation for core–shell nanocatalysts. *Angew. Chem. Int. Ed.* **48,** 3529–3531 (2009).
10. Koh, S., Leisch, J., Toney, M. F. & Strasser, P. Structure–activity–stability relationships of Pt–Co alloy electrocatalysts in gas-diffusion electrode layers. *J. Phys. Chem. C* **111,** 3744–3752 (2007).
11. Koh, S., Toney, M. F. & Strasser, P. Activity–stability relationships of ordered and disordered alloy phases of Pt_3Co electrocatalysts for the oxygen reduction reaction (ORR). *Electrochim. Acta* **52,** 2765–2774 (2007).
12. Nørskov, J. K. *et al.* Origin of the overpotential for oxygen reduction at a fuel cell cathode. *J. Phys. Chem. B* **108,** 17886–17892 (2004).
13. Nørskov, J. K, Bligaard, T., Rossmeisl, J. & Christensen, C. H. Towards the computational design of solid catalysts. *Nature Chem.* **1,** 37–46 (2009).
14. Strasser, P., Fan, Q., Devenney, M. & Weinberg, W. H. High throughput experimental and theoretical screening of materials—a comparative study of search strategies for new fuel cell anode catalysts. *J. Phys. Chem B* **107,** 11013–11021 (2003).
15. Skulason, E. *et al.* Density functional theory calculations for the hydrogen evolution reaction in an electrochemical double layer on the Pt(111) electrode. *Phys. Chem. Chem. Phys.* **9,** 3241–3250 (2007).
16. Janik, M. J., Taylor, C. D. & Neurock, M. First-principles analysis of the initial electroreduction steps of oxygen over Pt(111). *J. Electrochem. Soc.* **156,** B126–B135 (2009).
17. Greeley, J., Rossmeisl, J., Hellman, A. & Nørskov, J. K. Theoretical trends in particle size effects for the oxygen reduction reaction. *Z. Phys. Chem.* **221,** 1209–1220 (2007).
18. Stamenkovic, V. R. *et al.* Trends in electrocatalysis on extended and nanoscale Pt-bimetallic alloy surfaces. *Nature Mater.* **6,** 241–247 (2007).
19. Rossmeisl, J., Logadottir, A. & Nørskov, J. K. Electrolysis of water on (oxidized) metal surfaces. *Chem. Phys.* **319,** 178–184 (2005).
20. Abild-Pedersen, F. *et al.* Scaling properties of adsorption energies for hydrogen-containing molecules on transition-metal surfaces. *Phys. Rev. Lett.* **99,** 016105 (2007).
21. Stamenkovic, V. R., Mun, B. S., Mayrhofer, K. J. & Ross, P. N., Markovic, N. M. Effect of surface composition on electronic structure, stability, and electrocatalytic properties of Pt-transition metal alloys: Pt-skin versus Pt-skeleton surfaces. *J. Am. Chem. Soc.* **128,** 8813–8819 (2006).
22. Johannesson G. H. *et al.* Combined electronic structure and evolutionary search approach to materials design. *Phys. Rev. Lett.* **88,** 255506 (2002).
23. Bligaard, T. *et al.* Pareto-optimal alloys. *Appl. Phys. Lett.* **83,** 4527–4529 (2003).
24. Ruban, A. V., Skriver, H. L. & Nørskov, J. K. Crystal-structure contribution to the solid solubility in transition metal alloys. *Phys. Rev. Lett.* **80,** 1240 (1998).
25. Stamenkovic, V. R., Schmidt, T. J., Ross, P. N. & Markovic, N. M. Surface composition effects in electrocatalysis: kinetics of oxygen reduction on well-defined Pt_3Ni and Pt_3Co alloy surfaces *J. Phys. Chem. B* **106,** 11970–11979 (2002).
26. Neyerlin, K. C., Srivastava, R., Yu, C. & Strasser, P. Electrochemical activity and stability of dealloyed Pt–Cu and Pt-Cu-Co electrocatalysts for the oxygen reduction reaction (ORR). *J. Power Sources* **186,** 261–267 (2009).
27. Ball, S. C., Hudson, S. L., Theobald, B. R. C. & Thompsett, D. PtCo, a durable catalyst for automotive proton electrolyte membrane fuel cells? *ECS Transactions* **11,** 1267–1278 (2007).
28. Greeley, J. & Nørskov, J. K. Combinatorial density functional theory-based screening of surface alloys for the oxygen reduction reaction. *J. Phys. Chem. C* **113,** 4932–4939 (2009).
29. Rossmeisl, J., Qu, Z.-W., Zhu, H., Kroes, G.-J. & Nørskov, J. K. Electrolysis of water on oxide surfaces. *J. Electroanal. Chem.* **607,** 83–89 (2007).
30. Takasu, Y., Yoshinaga, N. & Sugimoto, W. Oxygen reduction behavior of RuO_2/Ti, IrO_2/Ti and IrM (M: Ru, Mo, W, V) O_x/Ti binary oxide electrodes in a sulfuric acid solution. *Electrochem. Commun.* **10,** 668–672 (2008).

31. Mano, N., Soukharev, V. & Heller, A. A laccase-wiring redox hydrogel for efficient catalysis of O_2 electroreduction. *J. Phys. Chem. B* **110,** 11180–11187 (2006).
32. Lefèvre, M., Proietti, E., Jaouen, F. & Dodelet, J.-P. Iron-based catalysts with improved oxygen reduction activity in polymer electrolyte fuel cells. *Science* **324,** 71–74 (2009).
33. Gasteiger, H. A. & Markovic, N. M. Just a dream—or future reality? *Science* **324,** 48 (2009).
34. Zhang, J. L, Vukmirovic, M. B., Xu, Y., Mavrikakis, M. & Adzic, R. R. Controlling the catalytic activity of platinum-monolayer electrocatalysts for oxygen reduction with different substrates. *Angew. Chem. Int. Ed.* **44,** 2132–2135 (2005).
35. Rossmeisl, J., Karlberg, G. S., Jaramillo, T. F. & Nørskov, J. K. Steady state oxygen reduction and cyclic voltammetry. *Faraday Discuss.* **140,** 337–346 (2008).
36. Karlberg, G. S., Rossmeisl, J. & Nørskov, J. K. Estimations of electric field effects on the oxygen reduction reaction based on the density functional theory. *Phys. Chem. Chem. Phys.* **9,** 5158–5161 (2007).

Acknowledgements

J.G. and T.F.J. are both recipients of H. C. Ørsted Postdoctoral Fellowships from the Technical University of Denmark. Funding by the Danish Council for Technology and Innovation's FTP program and by the Danish Strategic Research Council's HyCycle program is gratefully acknowledged. The Center for Atomic-scale Materials Design is supported by the Lundbeck Foundation. The Center for Individual Nanoparticle Functionality is supported by the Danish National Research Foundation.

Author contributions

J.G., H.A.H., J.R. and J.K.N. contributed to the computational work in this paper. I.E.L.S., A.S.B., T.P.J., T.F.J., and I.C. contributed to the experimental work.

Additional information

Supplementary information accompanies this paper at www.nature.com/naturechemistry. Reprints and permission information is available online at http://npg.nature.com/reprintsandpermissions/. Correspondence and requests for materials should be addressed to J.K.N.

P3

Scaling Relationships for Adsorption Energies on Transition Metal Oxide, Sulfide, and Nitride Surfaces

E. M. Fernandez, P. G. Moses, A. Toftelund, Heine A. Hansen, J. I. Martinez, F. Abild-Pedersen, J. Kleis, B. Hinnemann, J. Rossmeisl, T. Bligaard, and J. K. Nørskov
Angew. Chem. Int. Ed., **47**, 4683-4686 (2008)

DOI: 10.1002/anie.200705739

Surface Adsorption

Scaling Relationships for Adsorption Energies on Transition Metal Oxide, Sulfide, and Nitride Surfaces**

*Eva M. Fernández, Poul G. Moses, Anja Toftelund, Heine A. Hansen, José I. Martínez, Frank Abild-Pedersen, Jesper Kleis, Berit Hinnemann, Jan Rossmeisl, Thomas Bligaard, and Jens K. Nørskov**

There has been substantial progress in the description of adsorption and chemical reactions of simple molecules on transition-metal surfaces. Adsorption energies and activation energies have been obtained for a number of systems, and complete catalytic reactions have been described in some detail.[1–7] Considerable progress has also been made in the theoretical description of the interaction of molecules with transition-metal oxides,[8–19] sulfides,[20–25] and nitrides,[26–29] but it is considerably more complicated to describe such complex systems theoretically. Complications arise from difficulties in describing the stoichiometry and structure of such surfaces, and from possible shortcomings in the use of ordinary generalized gradient approximation (GGA) type density functional theory (DFT).[30]

Herein we introduce a method that may facilitate the description of the bonding of gas molecules to transition-metal oxides, sulfides, and nitrides. It was recently found that there are a set of scaling relationhips between the adsorption energies of different partially hydrogenated intermediates on transition-metal surfaces.[31] We will show that similar scaling relationships exist for adsorption on transition metal oxide, sulfide, and nitride surfaces. This means that knowing the adsorption energy for one transition-metal complex will make it possible to quite easily generate data for a number of other complexes, and in this way obtain reactivity trends.

The results presented herein have been calculated using self-consistent DFT. Exchange and correlation effects are described using the revised Perdew–Burke–Ernzerhof (RPBE)[32] GGA functional. It is known that GGA functionals give adsorption energies with reasonable accuracy for transition metals.[32,33] It is not clear, however, whether a similar accuracy can be expected for the oxides, sulfides, and nitrides, although there are examples of excellent agreement between DFT calculations and experiments, for example, with RuO_2 surfaces.[9] In our study we focused entirely on variations in the adsorption energies from one system to another, and we expected that such results would be less dependent than the absolute adsorption energies on the description of exchange and correlation.

For the nitrides, a clean surface and a surface with a nitrogen vacancy were studied. For MX_2-type oxides or sulfides, an oxygen- or sulfur-covered surface with an oxygen or sulfur vacancy was studied. The structures of the clean surface considered in the present work and their unit cells are shown in Figure 1. The adsorption energies given below are for the adsorbed species in the most stable adsorption site on the surface.

By performing calculations for a large number of transition-metal surfaces of different orientations,[31] it was found that the adsorption energy of intermediates of the type AH_x is linearly correlated with the adsorption energy of atom A (N, O, S) according to Equation (1):

$$\Delta E^{AH_x} = \gamma(x)\Delta E^{A} + \xi \quad (1)$$

Here the scaling constant is given to a good approximation by Equation (2) where x_{max} is the maximum number of H atoms that can bond to the central atom A ($x_{max} = 3$ for A = N, and $x_{max} = 2$ for A = O, S), that is, the number of hydrogen atoms that the central atom A would bond to in order to form neutral gas-phase molecules.

$$\gamma(x) = (x_{max} - x)/x_{max} \quad (2)$$

We have performed similar calculations for the adsorption of oxygen, sulfur, and nitrogen on a series of transition metal oxide, sulfide, and nitride surfaces (Figure 2). We find that scaling relationhips also exist for these systems, which are considerably more complex than the transition-metal surfaces. Such a correlation between the adsorption energies of O and OH has previously been found for the MO_2 oxides.[12] Furthermore, it can be seen that the scaling constant $\gamma(x)$ is given to a good approximation by the same expression [Eq. (2)] as for adsorption on the transition metals. We find that the mean absolute error (MAE) is lower than 0.19 eV for all the species considered here. The nitride surfaces present a poorer correlation than the others, mainly because TiN(100) is a clear outlier.

[*] Dr. E. M. Fernández, P. G. Moses, A. Toftelund, H. A. Hansen, J. I. Martínez, Dr. F. Abild-Pedersen, Dr. J. Kleis, Prof. J. Rossmeisl, Prof. T. Bligaard, Prof. J. K. Nørskov
Center for Atomic-scale Materials Design
Department of Physics, Technical University of Denmark
DK-2800 Lyngby (Denmark)
Fax: (+45) 4593-2399
E-mail: norskov@fysik.dtu.dk
Dr. B. Hinnemann
Haldor Topsøe A/S, Nymøllevej 55, DK-2800 Lyngby (Denmark)

[**] The Center for Atomic-scale Materials Design is funded by the Lundbeck Foundation. We wish to acknowledge additional support from the Danish Research Agency through grant 26-04-0047 and the Danish Center for Scientific Computing through grant HDW-0107-07.

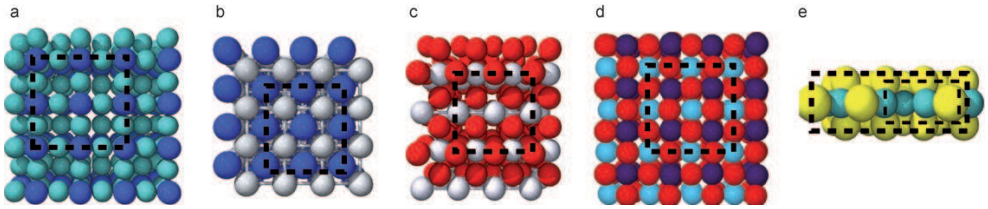

Figure 1. Structures used to describe the surfaces of the transition-metal nitrides, oxides and sulfides. a) Fcc-like structure for the M_2N (100) surface, M = Mo and W. Dark and light blue spheres represent metal and N atoms, respectively. b) Fcc-like rock-salt structure for the TiN (100) surface. Dark blue and gray spheres represent Ti and N atoms, respectively. c) Rutile-like (110) surface for the PtO_2 surface. Red and white spheres represent O and metal atoms, respectively. d) Perovskite structure for the $LaMO_3$ (100) surface, with M = Ti, Ni, Mn, Fe, and Co. Red, purple, and violet spheres represent O, La, and metal atoms, respectively. e) Hcp-like (−1010) surfaces for NbS_2, TaS_2, MoS_2, WS_2, Co-Mo-S, Ni-Mo-S, and Co-W-S. Yellow and green spheres represent S and metal atoms, respectively. The black dashed boxes indicate the unit cell.

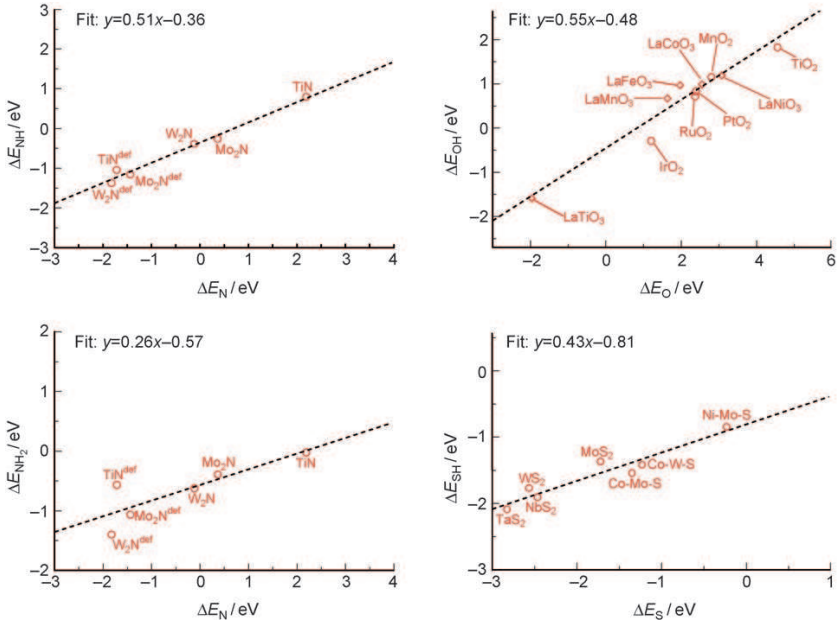

Figure 2. Adsorption energies of NH and NH_2 intermediates over nitrides, an OH intermediate over oxides, and an SH intermediate over sulfides plotted against adsorption energies of N over nitrides, O over oxides, and S over sulfides, respectively. The adsorption energy of AH_x is defined as: $\Delta E^{AH_x} = E(AH_x^*) + (x_{max}-x)/2\,E(H_2) - E(^*) - E(AH_{x_{max}})$ where $E(AH_x^*)$ is the total energy of an AH_x intermediate adsorbed on the most stable adsorption site, $E(^*)$ is the total energy of the surface without the A atom adsorbed, and $E(H_2)$ and $E(AH_{x_{max}})$ are the total energies of the hydrogen molecule and the $AH_{x_{max}}$ molecule in a vacuum, respectively.

It is interesting to compare the results of Figure 2 with the equivalent results for adsorption on the transition metals (Figure 3). It is found that the linear relationships for the nitrides are essentially the same for the two classes of systems. For the oxides, and partially for the sulfides, the results for the compounds are shifted from those on the transition metals. We trace this difference to a difference in the adsorption sites on the two kinds of systems. On the transition-metal surfaces, O and OH are generally found to coordinate with more than one metal neighbor. On the other hand, on the oxide surfaces the O atoms are generally coordinated to a single metal atom. If we use the adsorption energies for O and OH on the transition metals, where they are forced to adsorb in an on-top manner, the results now fall on the same line as for the oxides (Figure 3). For the sulfides, the S atom also adsorbs at a different site than on the transition metal. If the same adsorption site on the metal is considered the data agree, as for the oxides, with the results obtained for adsorption onto the sulfide surface.

The results of Figures 2 and 3 are remarkable and indicate that the nature of the adsorption bond is similar for the transition metals and the compounds. For the transition-metal surfaces, the scaling relationships can be understood within the d-band model.[34–39] The variation in adsorption energies for a given atom or molecule among the transition metals is mainly given by the variations in the strength of the coupling of the valence states of the adsorbate with the d states of the transition metal. The variations in the adsorption energy of an atom A from one transition-metal surface to the next reflect this. If H atoms are now added to atom A, the ability of A to couple to the metal d states decreases, either because the modified A states can couple to fewer d states or because the bonds become longer.[31] The principle of bond-order conservation would indicate that the weakening of the bond strength is proportional to the number of H atoms added, which corresponds to Equation (2).[31] The scaling behavior observed in Figures 2 and 3 indicates that similar arguments should hold for adsorption on transition-metal oxides, sulfides, and nitrides. The key to understanding this can be found in recent work by Ruberto and Lundqvist,[40] in which they show that a suitably modified d-band model can be used to understand trends in adsorption energies on transition-metal carbides and nitrides.

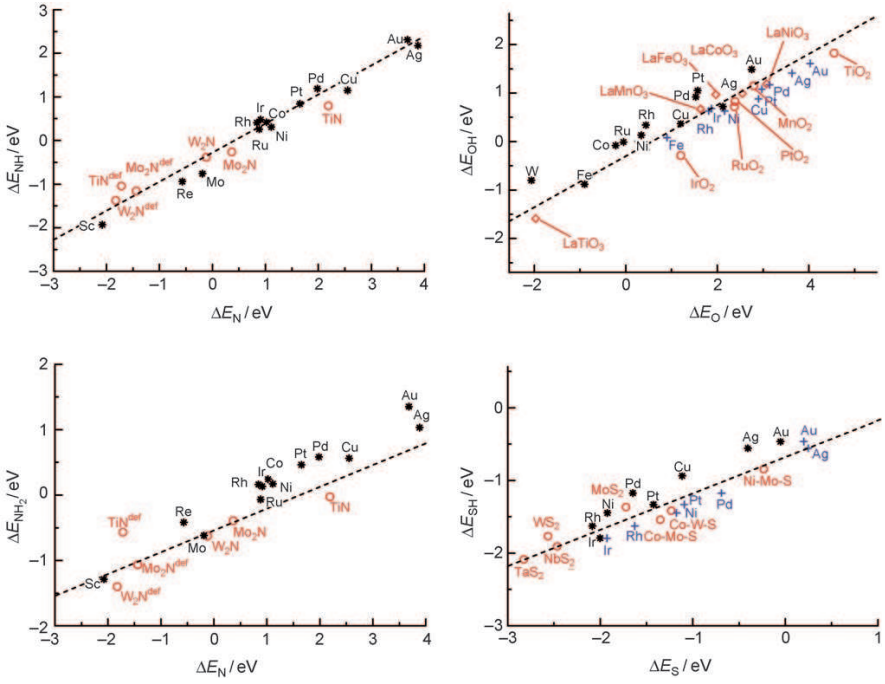

Figure 3. Adsorption energies of NH and NH_2 intermediates on transition metal nitride and transition-metal surfaces, the OH intermediate on transition metal oxide and transition metal surfaces, and the SH intermediate on transition metal sulfide and transition metal surfaces are plotted against the adsorption energies of N, O, and S, respectively. Close-packed surfaces for NH_x and OH_x intermediates, and the stepped surface for SH_x intermediates are considered. The adsorption energies for the OH intermediate on a top site and S intermediates on a bridge site over transition metal centers are included (blue points). The dashed line is the slope $\gamma(x)$ obtained from Equation (2).

The strength of the scaling relationships is shown by the following example. If one has a calculated or an experimental adsorption energy of an adsorbate AH_x ($\Delta E_{M1}^{AH_x}$) for one transition metal or transition-metal compound M1, we can estimate the energy $\Delta E_{M2}^{AH_x}$ of the same intermediate on another system M2 from the adsorption energies of atom A on the two systems, by using Equation (3).

$$\Delta E_{M2}^{AH_x} = \Delta E_{M1}^{AH_x} + \gamma(x)(\Delta E_{M2}^{A} - \Delta E_{M1}^{A}) \quad (3)$$

$\gamma(x)$ is a rational number given by Equation (2). If we have a database of atomic adsorption energies for a number of systems, we may then estimate the adsorption energy of a number of intermediates. This opens the possibility of obtaining an overview of adsorption energies on oxides, sulfides, and nitride surfaces on the basis of a few calculations.

In summary, density functional theory calculations on the adsorption of O, OH, S, SH, N, NH, and NH_2 on a range of transition metal oxide, sulfide, and nitride surfaces have been presented. It is shown that the adsorption energies ΔE^{AH_x} of AH_x intermediates scale with the adsorption energies ΔE^{A} of the A atoms according to the equation $\Delta E^{AH_x} = \gamma(x)\,\Delta E^{A} + \xi$, where the proportionality constant $\gamma(x)$ is independent of the metal and only depends on the number of H atoms in the molecule.

Experimental Section

The results presented herein were calculated using self-consistent DFT. The ionic cores and their interaction with the valence electrons are described by ultrasoft pseudopotentials (soft pseudopotential for S),[41] and the valence wave functions are expanded in a basis set of plane waves with a kinetic energy cut-off of 350–400 eV. The electron density of the valence states was obtained by a self-consistent iterative diagonalization of the Kohn–Sham Hamiltonian with Pulay mixing of the densities.[42] The occupation of the one-electron states was calculated using an electronic temperature of $k_B T = 0.1$ eV (0.01 eV for the molecules in a vacuum); all energies were extrapolated to $T = 0$ K. The ionic degrees of freedom were relaxed using the quasi-Newton minimization scheme, until the maximum force component was smaller than 0.05 eV $Å^{-1}$. Spin magnetic moments for the oxides, Co-Mo-S, Ni-Mo-S, and Co-W-S were taken into account. Exchange and correlation effects are described using the RPBE[32] GGA functional.

We used the periodic slab approximation, and the unit cells considered were modeled by a (2×2) unit cell for the nitrides and perovskite-type oxides, a (2×1) unit cell for PtO_2, a (2×1) unit cell for Co-W-S and MS_2 surfaces with M = Mo, Nb, Ta, and W, and a (4×1) unit cell for the M-Mo-S surface with M = Ni and Co. A four-layer slab for the nitrides and perovskite-type oxides, a four trilayer slab for PtO_2-type oxides, and an 8 or 12 layer slab for sulfides were employed in the calculations. Neighboring slabs were separated by more than 10 Å of vacuum. The results for the MO_2 surfaces with M = Ir, Mn, Ru, and Ti are taken from Refs. [12,15] The adsorbate together with the two topmost layers for the nitrides and perovskite-type oxides, the two topmost trilayers for MO_2 oxides, and all layers for the sulfides were allowed to fully relax. The Brillouin zone of the systems was sampled with a $4\times4\times1$ Monkhorst-Pack grid for the nitride and oxide surfaces and with a $6\times1\times1$ $(4\times1\times1)$ grid for the 2×1 (4×1) supercell of the sulfide surfaces.

Received: December 14, 2007
Revised: March 28, 2008
Published online: May 16, 2008

Keywords: adsorption · density functional calculations · surface chemistry · transition metals

[1] A. Alavi, P. Hu, T. Deutsch, P. L. Silvestrelli, J. Hutter, *Phys. Rev. Lett.* **1998**, *80*, 3650.
[2] A. Eichler, J. Hafner, *Phys. Rev.* **1999**, *59*, 5960.
[3] B. Hammer, *J. Catal.* **2001**, *199*, 171.

[4] A. Logadóttir, J. K. Nørskov, *J. Catal.* **2003**, *220*, 273.
[5] S. Linic, M. A. Barteau, *J. Am. Chem. Soc.* **2003**, *125*, 4034.
[6] S. Ovesson, B. I. Lundqvist, W. F. Schneider, A. Bogicevic, *Phys. Rev. B* **2005**, *71*, 115406.
[7] S. Kandoi, J. Greeley, M. A. Sanchez-Castillo, S. T. Evans, A. A. Gokhale, J. A. Dumesic, M. Mavrikakis, *Top. Catal.* **2006**, *37*, 17.
[8] S. Wendt, R. Schaub, J. Matthiesen, E. K. Vestergaard, E. Wahlström, M. D. Rasmussen, P. Thostrup, L. M. Molina, E. Lægsgaard, I. Stensgaard, B. Hammer, F. Besenbacher, *Surf. Sci.* **2005**, *598*, 226.
[9] K. Reuter K, D. Frenkel, M. Scheffler, *Phys. Rev. Lett.* **2004**, *93*, 116105.
[10] Y. Yanga, M. Sushchikha, G. Mills, H. Metiu, E. McFarland, *Appl. Surf. Sci.* **2004**, *229*, 346.
[11] S. Chrétien, H. Metiu, *Catal. Lett.* **2006**, *107*, 143.
[12] J. Rossmeisl, Z.-W. Qu, H. Zhu, G.-J. Kroes, J. K. Nørskov, *J. Electroanal. Chem.* **2007**, *607*, 83.
[13] M. D. Rasmussen, L. M. Molina, B. Hammer, *J. Chem. Phys.* **2004**, *120*, 988.
[14] Z. W. Qu, G. J. Kroes, *J. Phys. Chem. B* **2006**, *110*, 23306.
[15] J. Rossmeisl, K. Dimitrievski, P. Siegbahn, J. K. Nørskov, *J. Phys. Chem. C* **2007**, 111, 18821.
[16] T. Bredow, G. Pacchioni, *Chem. Phys. Lett.* **2002**, *79*, 753.
[17] M. Abu Halja, S. Guimond, Y. Romansyshyn, A. Uhi, H. Kulenbeck, T. K. Todorova, M. V. Ganduglia-Pirovano, J. Döbler, J. Sauer, H.-J. Freund, *Surf. Sci.* **2006**, *600*, 1497.
[18] G. Pacchioni, C. Di Valentini, D. Dominguez-Ariza, F. Illas, T. Bredow, T. Kluner, V. Staemmier, *J. Phys. Condens. Matter* **2004**, *16*, 2497.
[19] K. M. Neyman, S. P. Ruzankin, N. Rösch, *Chem. Phys. Lett.* **1995**, *246*, 546.
[20] M. Neurock, R. A. van Santen, *J. Am. Chem. Soc.* **1994**, *116*, 4427.
[21] S. Cristol, J.-F. Paul, E. Payen, D. Bougeard, S. Clémendot, F. Hutschka, *J. Phys. Chem. B* **2002**, *106*, 5659.
[22] M. Sun, A.-E. Nelson, J. Aadjaye, *J. Catal.* **2004**, *226*, 41.
[23] M. V. Bollinger, K. W. Jacobsen, J. K. Nørskov, *Phys. Rev. B* **2003**, *67*, 084310.
[24] H. Schweiger, P. Raybaud, H. Toulhat, *J. Catal.* **2002**, *212*, 33.
[25] T. Todorova, R. Prins, T. Weber, *J. Catal.* **2007**, *246*, 109.
[26] A. Vojvodic, C. Ruberto, B. I. Lundqvist, *Surf. Sci.* **2006**, *600*, 3619.
[27] P. Liu, J. A. Rodriguez, *Catal. Lett.* **2003**, *91*, 247.
[28] G. Frapper, M. Pélisser, *J. Phys. Chem. B* **2000**, *104*, 11972.
[29] J. Ren, C.-F. Huo, X.-D. Wen, Z. Cao, J. Wang, J.-W. Li, H. Jiao, *J. Phys. Chem. B* **2006**, *110*, 22563.
[30] O. Bengone, M. Alouani, P. Blöchl, J. Hugei, *Phys. Rev. B* **2000**, *62*, 16392.
[31] F. Abild-Pedersen, J. Greeley, F. Studt, J. Rossmeisl, T. R. Munter, P. G. Moses, E. Skúlason, T. Bligaard, J. K. Nørskov, *Phys. Rev. Lett.* **2007**, *99*, 016105.
[32] B. Hammer, L. B. Hansen, J. K. Nørskov, *Phys. Rev. B* **1999**, *59*, 7413.
[33] J. Greeley, M. Mavrikakis, *J. Phys. Chem. B* **2005**, *109*, 3460.
[34] B. Hammer, J. K. Nørskov, *Surf. Sci.* **1995**, *343*, 211.
[35] B. Hammer, J. K. Nørskov, *Nature* **1995**, *376*, 238 .
[36] B. Hammer, J. K. Nørskov, *Adv. Catal.* **2000**, *45*, 71.
[37] A. Eichler, F. Mittendorfer, J. Hafner, *Phys. Rev. B* **2000**, *62*, 4744.
[38] J. Greeley, M. Mavrikakis, *Nat. Mater.* **2004**, *3*, 810.
[39] A. Roudgar, A. Gross, *Phys. Rev. B* **2003**, *67*, 033409.
[40] C. Ruberto, B. I. Lundqvist, *Phys. Rev. B* **2007**, *75*, 235438.
[41] D. Vanderbilt, *Phys. Rev. B* **1990**, *41*, 1510.
[42] G. Kresse, J. Furthmuller, *Comput. Mater. Sci.* **1996**, *6*, 15.

P4

Formation Energies of Rutile Metal Dioxides Using Density Functional Theory

J. I. Martinez, H. A. Hansen, J. Rossmeisl, and J. K. Nørskov

Phys. Rev. B., **79**, 045120 (2009)

Formation energies of rutile metal dioxides using density functional theory

J. I. Martínez,* H. A. Hansen, J. Rossmeisl,† and J. K. Nørskov
Department of Physics, Center for Atomic-Scale Materials Design, Technical University of Denmark, DK-2800 Kgs. Lyngby, Denmark
(Received 23 October 2008; revised manuscript received 18 December 2008; published 26 January 2009)

We apply standard density functional theory at the generalized gradient approximation (GGA) level to study the stability of rutile metal oxides. It is well known that standard GGA exchange and correlation in some cases is not sufficient to address reduction and oxidation reactions. Especially the formation energy of the oxygen molecule and the electron self-interaction for localized *d* and *f* electrons are known shortcomings. In this paper we show that despite the known problems, it is possible to calculate the stability of a wide range of rutile oxides MO_2, with *M* being Pt, Ru, Ir, Os, Pb, Re, Mn, Se, Ge, Ti, Cr, Nb, W, Mo, and V, using the electrochemical series as reference. The mean absolute error of the formation energy is 0.29 eV using the revised Perdew-Burke-Ernzerhof (PBE) GGA functional. We believe that the reason for the success is due to the reference level being H_2 and H_2O and not O_2 and due to a more accurate description of exchange for this particular GGA functional compared to PBE. Furthermore, we would expect the self-interaction problem to be largest for the most localized *d* orbitals; that means the late 3*d* metals and since Co, Fe, Ni, and Cu do not form rutile oxides they are not included in this study. We show that the variations in formation energy can be understood in terms of a previously suggested model separating the formation energy into a metal deformation contribution and an oxygen binding contribution. The latter is found to scale with the filling of the *d* band.

DOI: 10.1103/PhysRevB.79.045120 PACS number(s): 71.15.Mb

I. INTRODUCTION

Bulk oxides are important in oxidation and reduction reactions, playing a key role in many technological and environmental processes such as corrosion, combustion, metal refining, electrochemical energy conversion and storage, photosynthesis, and photocatalysis.[1] Rutile metal dioxides are particularly well studied. Electron, neutron, and x-ray diffraction experiments have detected a large number of transition-metal dioxides to possess very stable β' rutile crystal phases.[2–19] In addition, some theoretical studies, at different levels of theory, have confirmed the structural results of the experiments, showing enhanced stability of the rutile phase for most metal dioxides.[20–23]

Rutile oxides are interesting in connection with electrochemical and photoelectrochemical water splitting,[24–27] and recently the surface redox processes on, e.g., RuO_2 and TiO_2 have been treated using density functional theory (DFT).[28,29] The question remains whether standard DFT-generalized gradient approximation (GGA) (Refs. 30 and 31) calculations have sufficient accuracy. It has for instance been shown that for a series of (nonrutile) transition-metal oxides the standard GGA treatment of exchange and correlation is not sufficient to describe redox processes.[32–37]

In the present study we compare DFT-GGA calculations of formation energies with experimental values obtained from electrochemical series[38–40] for a large number of rutile metal dioxides MO_2, with *M* being Pt, Ru, Ir, Os, Pb, Re, Mn, Se, Ge, Ti, Cr, Nb, W, Mo, and V, in order to assess the accuracy of such calculations. All these metal oxides are known to form in the rutile structure; however, for some (e.g., Pt) the rutile structure is not the most stable phase. We show that for these oxides it is possible to accurately calculate the electrochemical stability with a mean absolute error (MAE) of 0.29 eV, using the revised Perdew-Burke-Ernzerhof (PBE) (RPBE) GGA functional.[31] We find that, in agreement with experiments, the formation energies decrease with increasing number of *d* electrons in the metal. We show that this trend may be understood based on a simple model first proposed by Gelatt, Jr. *et al.*,[41] where the formation energy is decomposed into two contributions: (i) the energy required to expand the metal lattice of the metal bulk and (ii) the bond energy gained by introducing oxygen into the deformed metal lattice, following the dioxide stoichiometry.

II. METHOD

The plane-wave pseudopotential DFT code DACAPO (Refs. 31 and 42) has been used for the calculation of all the total energies in this study. The bulk structures have been modeled by using periodically repeated unit cells in a supercell geometry to create the crystal conditions. All atom coordinates and lattice vectors are fully relaxed for each structure using the quasi-Newton minimization scheme[43] until the maximum force component is found to be smaller than 0.05 eV/Å. The metal dioxides have been treated in their rutilelike structure, while the most stable crystal phase was chosen for each pure metal bulk except Mn (modeled as pure bcc). The ion-electron interaction is described by using ultrasoft pseudopotentials,[44] and the Kohn-Sham (KS) one-electron valence states are expanded in a basis of plane waves with kinetic energy below 350 eV; a density cutoff of 500 eV is used. The Brillouin zone of all the systems is sampled with an $(8\times8\times8)$ Monkhorst-Pack grid. The convergence of the total energy with respect to the cutoff energies and the **k** points set is confirmed. Exchange and correlation effects are described using the RPBE-GGA functional[31] and the self-consistent RPBE density is determined by iterative diagonalization of the KS Hamiltonian, Fermi population of the KS states (k_BT=0.1 eV), and Pulay mixing of the resulting electronic density.[45] All total energies have been extrapolated to k_BT=0 eV. Spin polarization ef-

fects are included in the reported results for the dioxides in which naturally magnetized metals are present.

We define the calculated formation energy of the rutile metal dioxides as the reaction energies of the following reaction:

$$M(\text{bulk}) + 2H_2O(\text{l}) \rightarrow MO_2(\text{bulk}) + 2H_2(\text{g}), \quad (1)$$

where M is the metal forming the dioxide, H_2 is in the gas phase, and H_2O is in liquid phase. The calculated formation energies for the rutilelike metal dioxides are obtained by evaluating free-energy differences between the subsystems involved in reaction (1) as the following:

$$\Delta G_{\text{form}} = G[MO_2(\text{bulk})] + 2G[H_2(g)] - \{G[M(\text{bulk})] + 2G[H_2O(\text{l})]\}, \quad (2)$$

where G is the free energy of each subsystem involved in reaction (1). The general procedure for calculating the free energy has been presented previously in Ref. 46. For bulk crystals we neglect the entropy (S) and zero-point energy (ZPE) effects.[47] These quantities have been estimated from vibrational analyses for some representative pure metals and metal oxides involved in this study (Ru/RuO_2 and Ir/IrO_2), yielding differences between total DFT and Gibbs free energies below 0.1 eV and below 0.02 eV for the reaction given in Eq. (1) (at room temperature). We include the gas-phase entropy for H_2 and ZPE for H_2 and H_2O. We get the free energy of liquid water by calculating gas-phase H_2O and applying the entropy at the gas/liquid equilibrium pressure (0.035 bar).[48]

We get the experimental change in free energy by considering the related electrochemical reaction

$$MO_2(\text{bulk}) + 4H^+ + 4e^- \leftrightarrow M(\text{bulk}) + 2H_2O(\text{l}). \quad (3)$$

ΔG for this reaction is $-4eU$, with U being the standard potential vs the normal hydrogen electrode. The experimental values for ΔG_{form} [Eq. (2)] can then either be taken directly from the equilibrium potential of reaction (3) listed in electrochemical series[38–40] or via the dissolution potential

$$M(\text{bulk}) \leftrightarrow M^{n+} + ne^-, \quad (4)$$

and

$$MO_2(\text{bulk}) + 4H^+ + (4-n)e^- \leftrightarrow M^{n+} + 2H_2O(\text{l}). \quad (5)$$

Thereby we can obtain the experimental free energy of reaction (1), which can be directly compared to the values calculated theoretically using Eq. (2).

III. RESULTS AND DISCUSSION

Figure 1 shows the calculated ΔG_{form} for a series of rutile metal dioxides as a function of the experimental values extracted from the electrochemical series.[38–40] Two sets of data points are shown: one corresponding to experimental results extracted from Refs. 38 and 39 and other extracted from Ref. 40. The MAE is 0.29 eV. The *one-to-one* correspondence between the DFT-RPBE results and experiments may be surprising, considering the known shortcomings of standard GGAs. Part of this problem is related to describe the oxygen

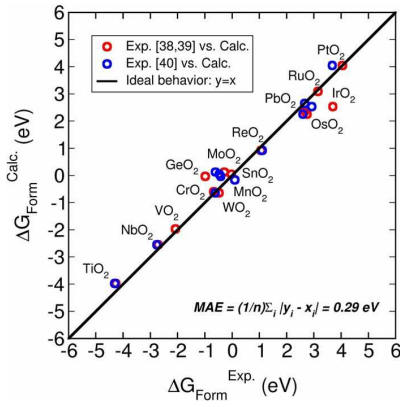

FIG. 1. (Color online) Calculated formation energies of various representative rutile metal dioxides as a function of the experimental values extracted from the electrochemical series (Refs. 38–40). The zero free-energy reference has been taken as the total energy of the metal oxide bulks.

molecule correctly, which is reflected in the calculated formation energy. The deviation from experiment in the reaction $O_2 \rightarrow 2O$ is 1.01 eV for PBE and 0.60 eV for RPBE (Ref. 49); on the contrary, errors on formation energies of H_2O and H_2 are known to be much lower. The deviation introduced in the water formation enthalpy via the reaction

$$2O + 2H_2 \rightarrow 2H_2O \quad (6)$$

is 0.56 eV for PBE and −0.14 eV for RPBE.[49] Therefore, the poor DFT description of the O_2 molecule is totally avoided using the electrochemical formation energy described above, which means using H_2O rather than O_2 as the reference for oxygen on the calculation of the heat of formation.

Another important point is that the values for the formation energies range from around −4 eV for TiO_2 to around 4 eV for PtO_2. This ~8 eV span provides a wide span of energies, making the comparison to experiment looks very good. Investigations in a narrow energy window will in some cases give wrong trends. We test that the findings are robust concerning the choice of GGA-exchange functional by comparing the RPBE with PBE.[30] The RPBE functional appears to have a more accurate inclusion of exchange than PBE, which is important to get reliable adsorption energies.[50,51] We find that while the trends are conserved, PBE systematically overestimates the formation energies by around ~ −0.8 eV. This justifies our choice for the inclusion of the exchange effects (see Table I).

Having established that our DFT calculations give a good representation of the trends on the formation energies, we now turn to the question of the origin of the variation in the heats of oxide formation from one transition metal to the next. The model proposed by Gelatt, Jr. *et al.*[41] to describe the bonding in 4*d* transition-metal compounds in the NaCl structure provides a good starting point. In this model the formation energy is decomposed into two contributions. First, the bulk metal lattice is deformed to the lattice adopted by the metal atoms in the oxide. The deformation energy is

TABLE I. From left to right: experimental formation energies obtained from different sources and PBE and RPBE formation energies for all rutile metal dioxides studied in the present work (all in eV). Beside each oxide label we show references of experiments justifying the existence and stability of the corresponding rutile phase. As superscripts in the experimental values, direct (d) and indirect (i) mean values are extracted from Eq. (3) or from Eqs. (4) and (5), respectively. Only experimental values have been considered from Refs. 38–40.

Rutile system	Reference	ΔG_{form} [a]	ΔG_{form} [b]	$\Delta G_{\text{form}}^{\text{PBE}}$	$\Delta G_{\text{form}}^{\text{RPBE}}$
TiO_2	2	-4.26^{i}	-4.30^{d}	−4.83	−3.97
NbO_2	3 and 4	-2.72^{i}	-2.76^{d}	−3.36	−2.55
VO_2	5	-2.08^{i}		−2.76	−1.97
GeO_2	6 and 7	-0.98^{i}	-0.42^{d}	−0.87	−0.03
CrO_2	8	-0.68^{i}		−1.44	−0.60
WO_2	4 and 9	-0.48^{i}	-0.62^{d}	−1.45	−0.64
MoO_2	4 and 10	-0.29^{i}	-0.61^{d}	−0.29	0.13
SnO_2	5, 11, and 12	-0.03^{i}	-0.47^{d}	−0.75	0.05
MnO_2	13	0.10^{i}	0.10^{i}	−0.87	−0.16
ReO_2	14	1.06^{i}	1.10^{d}	0.05	0.93
PbO_2	15	2.49^{i}	2.66^{i}	1.78	2.65
OsO_2	16	2.75^{i}	2.60^{d}	1.40	2.26
RuO_2	7 and 17	3.15^{i}		2.36	3.10
IrO_2	7, 17, and 18	3.70^{i}	2.92^{d}	1.68	2.53
PtO_2	19	4.05^{i}	3.68^{d}	3.26	4.05

[a]References 38 and 39.
[b]Reference 40.

defined as $G_{\text{deform}}=E_{\text{bulk}}^{\text{expanded}}-E_{\text{bulk}}^{\text{pure}}$, where $E_{\text{bulk}}^{\text{expanded}}$ is the energy per metal atom of the rutile bulk structure without oxygen atoms and $E_{\text{bulk}}^{\text{pure}}$ is the energy per metal atom in the pure metal bulk crystal. This contribution is the energy required to deform the metal lattice from the bulk structure toward the metal lattice in the rutile structure and is expected to be some positive fraction of the cohesive energy. Second, oxygen is introduced into the expanded metal lattice. This results in hybridization between metal d states and oxygen $2p$ states and contributes with a bonding energy $G_{\text{bond}}=G_{\text{deform}}-G_{\text{form}}$, where $G_{\text{form}}=\Delta G_{\text{form}}$ is given by Eq. (2).

When moving through the d series, the d band of the transition metals in each dioxide shifts down in energy, which may affect slightly the hybridization. However, the resulting density of states may often be well described by shifting the bands formed from the hybridization in order to accommodate more electrons into the bands as the number of d electrons is increased through the nd series. The bonding energy thus increases when bonding states are being filled and decreases when antibonding states are being filled.

The octahedral ligand field in the rutile dioxides splits the metal d states into t_{2g} and e_g bands. Based on ligand-field theory, we expect the metal t_{2g} states to be nonbonding or antibonding and the metal e_g states to be clearly antibonding.[52] The bonding orbitals from the nd-O $2p$ hybridization have high O $2p$ character, and they are always filled for the rutile dioxides. Therefore, as the number of d electrons increases, the new d electrons are always added to the antibonding t_{2g} states. Figure 2 shows the formation energy and, separately, its metal bulk deformation and bonding energy contributions, for some representative rutile $4d$ oxides. It is noticeable that the main trend in the formation energies is well captured by the bonding energy alone, meanwhile the deformation energy is rather invariant independently of the transition metal. The bonding energy G_{bond} decreases linearly with the number of d electrons, which suggests a single antibonding band is filled. In accordance with ligand-field theory, the projected density of states shows this band having high t_{2g} character.

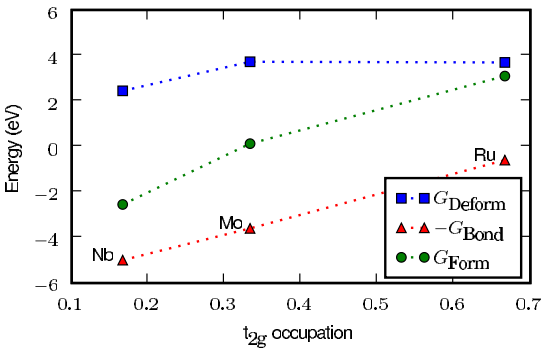

FIG. 2. (Color online) The formation energy, the metal bulk deformation energy, and the bonding energy in the expanded metal lattice as functions of the filling of the metal t_{2g} band for some representative rutile $4d$ metal dioxides (Nb, Mo, and Ru). The variation in formation energy is clearly dominated by the oxygen binding energy.

IV. SUMMARY AND CONCLUSIONS

We have calculated the formation energy of a large number of rutile metal oxides by using the RPBE-GGA functional, comparing the results to experimental values obtained from the electrochemical series. We find that the MAE is 0.29 eV, which is surprisingly low given the well-known limitations of standard DFT-GGA. To explain this we point at a number of points. First, using water (the natural source of oxygen in an electrochemical experiment) as the reference, we avoid calculations of the oxygen molecule. Second, the late 3*d* metals are not included in this study since they do not form rutile oxides. We expect that problems due to self-interaction are largest for those. Finally, the RPBE exchange is more accurate than PBE and Perdew-Wang 91 (PW91) for this kind of problem. We note however that trends are conserved using the PBE exchange. We show that the trends in formation energies can be understood within a simple model originally proposed by Gelatt, Jr. *et al.* The formation energy is split into two contributions: one from the deformation of the metal and one from the binding between metal and oxygen atoms. The latter is the larger of the two, and the variations can be understood by the degree of *d*-band electrons filling the antibonding t_{2g} orbital.

ACKNOWLEDGMENTS

CAMD is funded by the Lundbeck foundation. This work was supported by the Danish Center for Scientific Computing through Grant No. HDW-1103-06 and the STREP EU APOLLON-B Project through Grant No. NMP3-CT-2006-033228.

*jimartinez@fysik.dtu.dk
†jross@fysik.dtu.dk

[1] *Electrochemistry in Transition: From the 20th to the 21st Century*, edited by J. Murphy, S. Srinivasan, and B. E. Conway (Plenum, New York, 1992).
[2] A. Navrotsky, J. C. Jamieson, and O. J. Kleppa, Science **158**, 388 (1967).
[3] A. A. Bolzan, C. Fong, B. J. Kennedy, and C. J. Howard, J. Solid State Chem. **113**, 9 (1994).
[4] N. Jiang and J. C. H. Spence, Phys. Rev. B **70**, 245117 (2004).
[5] M. M. Qazilbash, M. Brehm, B. H. Chae, P. C. Ho, G. O. Andreev, B. J. Kim, S. J. Yun, A. V. Balatsky, M. B. Maple, F. Keilmann, H. T. Kim, and D. N. Basov, Science **318**, 1750 (2007).
[6] V. B. Prakapenka, L. S. Dubrovinsky, G. Shen, M. L. Rivers, S. R. Sutton, V. Dmitriev, H. P. Weber, and T. L. Bihan, Phys. Rev. B **67**, 132101 (2003).
[7] A. A. Bolzan, C. Fong, B. J. Kennedy, and C. J. Howard, Acta Crystallogr., Sect. B: Struct. Sci. **53**, 373 (1997).
[8] B. R. Maddox, C. S. Yoo, D. Kasinathan, W. E. Pickett and R. T. Scalettar, Phys. Rev. B **73**, 144111 (2006).
[9] D. J. Palmer and P. G. Dickens, Acta Crystallogr., Sect. B: Struct. Crystallogr. Cryst. Chem. **35**, 2199 (1979).
[10] F. Werfel and E. Minni, J. Phys. C **16**, 6091 (1983).
[11] S. H. Sun, G. W. Meng, G. X. Zhang, T. Gao, B. Y. Geng, L. D. Zhang, and J. Zuo, Chem. Phys. Lett. **376**, 103 (2003).
[12] Z. Chen, J. K. L. Lai, C. H. Shek, and H. Chen, J. Mater. Res. **18**, 1289 (2003).
[13] C. Poinsignon, E. Djurado, H. Klein, P. Strobel, and F. Thomas, Electrochim. Acta **51**, 3076 (2006).
[14] A. L. Ivanovskii, T. I. Chupakhina, V. G. Zubkov, A. P. Tyutyunnik, V. N. Krasilnikov, G. V. Bazuev, S. V. Okatov, and A. I. Lichtenstein, Phys. Lett. A **348**, 66 (2005).
[15] P. Y. Shen, S. L. Hwang, H. T. Chu, T. F. Yu, C. N. Pan, and W. L. Huang, Eur. J. Mineral. **17**, 543 (2005).
[16] P. C. Yen, R. S. Chen, C. C. Chen, Y. S. Huang, and K. K. Tiong, J. Cryst. Growth **262**, 271 (2004).
[17] R. R. Daniels, G. Margaritondo, C. A. Georg, and F. Lévy, Phys. Rev. B **29**, 1813 (1984).
[18] S. Ono, J. P. Brodholt, and G. D. Price, J. Phys.: Condens. Matter **20**, 045202 (2008).
[19] S. S. Rosenblum, W. H. Weber, and B. L. Chamberland, Phys. Rev. B **56**, 529 (1997).
[20] D. L. Niu and X. J. Xiu, J. Lumin. **122-123**, 155 (2007).
[21] J. H. Xu, T. Jarlborg, and A. J. Freeman, Phys. Rev. B **40**, 7939 (1989).
[22] V. Eyert, Europhys. Lett. **58**, 851 (2002).
[23] T. A. Sasaki, T. Soga, and H. Adachi, Phys. Status Solidi B **113**, 647 (1982).
[24] S. Trasatti, Electrochim. Acta **29**, 1503 (1984).
[25] A. Marshall, B. Borresen, G. Hagen, S. Sunde, M. Tsypkin, and R. Tunold, Russ. J. Electrochem. **42**, 1134 (2006).
[26] E. Guerrini, H. Chen, and S. Trasatti, J. Solid State Electrochem. **11**, 939 (2007).
[27] S. Chretien and H. Metiu, J. Chem. Phys. **129**, 074705 (2008).
[28] J. Rossmeisl, Z. W. Qu, H. Zhu, G. J. Kroes, and J. K. Nørskov, J. Electroanal. Chem. **607**, 83 (2007).
[29] A. Valdes, Z. W. Qu, G. J. Kroes, J. Rossmeisl, and J. K. Nørskov, J. Phys. Chem. C **112**, 9872 (2008).
[30] J. P. Perdew, K. Burke, and M. Ernzerhof, Phys. Rev. Lett. **77**, 3865 (1996).
[31] B. Hammer, L. B. Hansen, and J. K. Nørskov, Phys. Rev. B **59**, 7413 (1999).
[32] A. Svane and O. Gunnarsson, Phys. Rev. Lett. **65**, 1148 (1990).
[33] V. I. Anisimov, J. Zaanen, and O. K. Andersen, Phys. Rev. B **44**, 943 (1991).
[34] W. G. Aulbur, L. Jönsson, and J. W. Wilkins, Solid State Phys. **54**, 1 (2000).
[35] A. B. Shick, W. E. Pickett, and A. L. Liechtenstein, J. Electron Spectrosc. Relat. Phenom. **114**, 753 (2001).
[36] M. Nolan, S. C. Parker, and G. W. Watson, Surf. Sci. **595**, 223 (2005).
[37] L. Wang, T. Maxisch, and G. Ceder, Phys. Rev. B **73**, 195107 (2006).
[38] *CRC Handbook of Chemistry and Physics*, edited by D. R. Lide and H. P. R. Frederikse (CRC, New York, 1996).
[39] M. Pourbaix, *Atlas of Electrochemical Equilibria in Aqueus Solutions* (Pergamon, London/Cebelcor, Brussels, 1966).

[40] S. G. Bratsch, J. Phys. Chem. Ref. Data **18**, 1 (1989).
[41] C. D. Gelatt, Jr., A. R. Williams, and V. L. Moruzzi, Phys. Rev. B **27**, 2005 (1983).
[42] DACAPO homepage, https://wiki.fysik.dtu.dk/dacapo
[43] P. Maragakis, S. A. Andreev, Y. Brumer, D. R. Reichman, and E. Kaxiras, J. Chem. Phys. **117**, 4651 (2002).
[44] D. Vanderbilt, Phys. Rev. B **41**, 7892 (1990).
[45] G. Kresse and J. Furthmuller, Comput. Mater. Sci. **6**, 15 (1996).
[46] J. K. Nørskov, J. Rossmeisl, A. Logadottir, L. Lindqvist, J. R. Kitchin, T. Bligaard, and H. Jonsson, J. Phys. Chem. B **108**, 17886 (2004).
[47] M. V. Bollinger, K. W. Jacobsen, and J. K. Nørskov, Phys. Rev. B **67**, 085410 (2003).
[48] P. W. Atkins, *Physical Chemistry*, 6th ed. (Oxford University Press, Oxford, U.K., 1998).
[49] S. Kurth, J. P. Perdew, and P. Blaha, Int. J. Quantum Chem. **75**, 889 (1999).
[50] F. Abild-Pedersen, J. Greeley, F. Studt, J. Rossmeisl, T. R. Munter, P. G. Moses, E. Skúlason, T. Bligaard, and J. K. Nørskov, Phys. Rev. Lett. **99**, 016105 (2007).
[51] E. M. Fernández, P. G. Moses, A. Toftelund, H. A. Hansen, J. I. Martínez, F. Abild-Pedersen, J. Kleis, B. Hinnemann, J. Rossmeisl, T. Bligaard, and J. K. Nørskov, Angew. Chem. Int. Ed. **47**, 4683 (2008).
[52] J. B. Goodenough, Prog. Solid State Chem. **5**, 145 (1971).

P5

Electrochemical Chlorine Evolution at Rutile Oxide 110 Surfaces
H. A. Hansen, I. C. Man, F. Studt, F. Abild-Pedersen, T. Bligaard and J. Rossmeisl
Accepted for publication in Phys. Chem. Chem. Phys.

Electrochemical Chlorine Evolution at Rutile Oxide 110 Surfaces

Heine A. Hansen,[†] Isabela C. Man,[†] Felix Studt, [†,‡] Frank Abild-Pedersen, [†,‡] Thomas Bligaard[†,§] and Jan Rossmeisl[†]

[†] *Department of Physics, Building 307, Center for Atomic-scale Materials Design, Technical University of Denmark, DK-2800 Kgs. Lyngby, Denmark.*
[‡] *Computational.Materials Design ApS, Fysikvej – Building 307 – DTU, DK-2800 Kgs. Lyngby, Denmark, and*
[§] *Materials Sciences Division, Lawrence Berkeley National Laboratory, Berkeley, CA94720, U.S.A.*

Abstract: Based on density functional theory (DFT) calculations we study the electrochemical chlorine evolution reaction on rutile (110) oxide surfaces. First we construct the Pourbaix surface diagram for IrO_2 and RuO_2 and from this we find the chlorine evolution reaction intermediates and identify the lowest over-potential at which all elementary reaction steps in the chlorine evolution reaction are downhill in free energy. This condition is then used as a measure for catalytic activity. Linear scaling relations between the binding energies of the intermediates and the Oxygen binding energies at cus-sites are established for MO_2 M being (Ir, Ru, Pt, Ti). The linear relations form the basis for constructing a generalized surface phase diagram where two parameters, the potential and the binding energy of oxygen are needed to determine the surface composition. We calculate the catalytic activity as function of the oxygen binding energy giving rise to a Sabatier volcano. By combining the surface phase diagram and the volcano describing the catalytic activity, we find that the reaction mechanism differs depending on catalyst material. The flexibility in reaction path means that the Cl evolution activity is high for a wide range of oxygen binding energies. We find that the required overpotential for chlorine evolution is lower than the overpotential necessary for oxygen evolution.

Introduction

Chlorine represents an essential product for the global chemical industry. Approximately 50% of the total turnover of the chemical industry depends on chlorine and caustic soda.[1] Chlorine production by chlor-alkali processes is one of the largest current technological applications of electrochemistry.[2]

The most active anode catalysts are usually based on RuO_2, however, RuO_2 is barely stable at the high potentials. Therefore RuO_2 is mixed with IrO_2 and additives such as

TiO_2 and SnO_2, in order to improve the stability. The most commonly used electrocatalyst in industrial chlorine processes is the so-called Dimensionally Stable Anodes (DSA®) which is named according to its improved life time compared with earlier used electrocatalysts.[3]

The equilibrium potential for Cl_2 evolution is 1.36V at room temperature and standard conditions, which is slightly larger than the equilibrium potential for oxygen evolution which is 1.23V under the same conditions. This means that under chlorine evolution the simultaneous evolution of oxygen tends to occur as a parasitic side reaction, especially at high current densities. However, depending on the employed catalyst, oxygen evolution usually requires a somewhat larger over-potential than chlorine evolution. Unfortunately, RuO_2 is known to be a good catalyst for oxygen evolution as well as for chlorine evolution. This suggests an overlap of the activity volcanoes for the two reactions and it has in fact been suggested that high catalytic activity for chlorine evolution is fundamentally linked with high oxygen evolution activity.[2]

The anodic chlorine evolution, at the oxide electrodes and especially the chlorine evolution on RuO_2 has been widely studied experimentally. A variety of different reaction mechanisms have been suggested based on indirect experimental quantities such as Tafel slopes and reaction orders.[4] Among the possible reactions are the Volmer-Tafel,[5] the Volmer-Heyvrosky,[6] and the Khrishtalik[7,8] reaction mechanisms. These mechanisms suggest two possible active sites on the rutile (110) surface for chlorine evolution. First the penta-coordinated metal site with unsaturated valence electrons (cus-site) or atop the adsorbed oxygen on the cus-sites of the surface.

Very little is known about the reaction mechanism for chlorine evolution and about the atomic-scale structure of the surface, which depends strongly on catalyst material, electrostatic potential, and electrolyte. Recent developments within density functional theory analysis of electrochemical reactions have opened up the possibilities to study these reactions at the atomic scale.[9] Investigations of especially fuel cell catalysis such as oxygen reduction[10,11,12,13] and methanol oxidation[14,15,16,17] have deepened the insight into reaction mechanisms and surface composition under electrocatalytic reaction conditions. In a previous study the oxygen evolution reaction was investigated.[18] There it was established that it is possible to describe the trends in the oxygen evolving activity using one single descriptor: the adsorption energy of O-atoms on the surfaces. RuO_2 was determined to be the most active rutile (110) surface, which is in good agreement with the experiments. Recently theoretical studies have addressed heterogeneously catalyzed chlorine production by the so-called Deacon process.[19,20] However, in spite of the significant importance of electrochemical chlorine evolution, detailed electronic structure studies of this process have not appeared in literature.

The aim of the present study is to analyze the surface structure and the activity trends underlying electrochemical chlorine evolution over rutile oxides. We start by analyzing IrO_2 and RuO_2 and we construct surface phase diagrams of the rutile (110) surfaces. This allows us to derive plausible mechanisms of the electrochemical chlorine evolution based on the reaction intermediates. We determine the lowest potential

where Cl evolution is possible. Applying adsorption energy correlations we can determine a reduced set of key energetic descriptors for the involved surface reactions and generalize the analysis of IrO_2 and RuO_2 to a trend study where all the material dependence is included in a single descriptor, in this case the oxygen binding energy.

Methods

Calculation details

All electronic structure calculations have been carried out using density functional theory (DFT), with the RPBE functional for exchange and correlation.[21] A periodically repeated 4 layer slab is chosen for the rutile (110) surfaces of RuO_2, IrO_2, TiO_2, and PtO_2. A vacuum layer of 16 Å is used to separate the slab from its periodically repeated images. We use a 2x1 surface unit cell and 4x4x1 Monkhorst-Pack type k-point sampling for slab calculations.[22] The Kohn-Sham equations are solved using a plane wave basis with a cutoff of 350 eV for the eigenstates and the densities are described using a cutoff corresponding to 500 eV. Vanderbilt ultrasoft pseudopotentials are used to deal with the ion cores.[23] A Fermi smearing of 0.1 eV is used and energies are extrapolated to an electronic temperature of 0 K. The two bottom layers of the slab are fixed in their bulk structure, while the two top layers as well as possible adsorbates on it are relaxed until the sum of the absolute forces is less than 0.05 eV/Å. All calculations are performed using the Dacapo and ASE simulation package.[24]

The surface of the unit cell contains two bridge and two cus sites, which means that the total coverage at each type site vary between 50% and 100%. We consider all relevant combinations of adsorption site and adsorbates. We find that adsorbates bind stronger at bridge sites than on cus sites and bridge sites are therefore occupied with oxygen for a large range of conditions. We therefore focus on cus sites throughout this paper. Mixed phases where different kinds of adsorbates are mutually present at the cus sites may exist, however, we find that they are in general only stable in very narrow windows of conditions.

We consider the adsorption of Cl^c, OH^c and O^c at a cus site, ^{c}, as well as the formation of O_2^{cc} and $Cl(O^c)_2$ adsorbed at two cus sites. The adsorption energy of chlorine is calculated using:

$$\Delta E(Cl^c) = E(Cl^c)-E(^c)-1/2E(Cl_2) \quad (1)$$

For oxygen the energy is calculated relative to water

$$\Delta E(O^c) = E(O^c)-E(^c)-E(H_2O)+E(H_2) \quad (2)$$

and for ClO^c we apply the combined reference energy states from above

$$\Delta E(ClO^c) = E(ClO^c)-E(^c)-1/2E(Cl_2)-E(H_2O)+E(H_2) \quad (3)$$

The adsorption energy of O_2^{cc} is defined with reference to water and hydrogen

$$\Delta E\ (O_2^{cc}) = E(O_2^{cc}) - E(2^c) - 2\ E(H_2O) + 2\ E(H_2), \quad (4)$$

and the adsorption energy of $Cl(O^c)_2$ is defined by

$$\Delta E\ (Cl(O^c)_2) = E(Cl(O^c)_2) - E(2^c) - 2\ E(H_2O) + 2\ E(H_2). - ½\ E(Cl_2) \quad (5)$$

The changes in the interaction between the liquid electrolyte and the surface upon adsorption of molecules are expected to be small as long as all hydrogen bonds are saturated and these interactions are therefore neglected. Furthermore, the effect of the local field in the Helmholtz layer is not accounted for. Previously, it has been shown that for metal surfaces the effect of the field is negligible for adsorbates with small dipole moments perpendicular to the surface.[25] For RuO_2 we find that applying a homogeneous external field up to -0.53 V/Å, corresponding to a 1.6 V potential drop across a 3 Å thick Helmholtz layer, changes the relative adsorption energies by less than 0.11 eV.
The above simplifications are expected to be independent on the catalyst material, and therefore the resulting trends in catalytic activity should only be weakly affected by them. Variations in the adsorption energy of e.g. oxygen on the (110) surfaces are several eVs between e.g. IrO_2 and TiO_2, while differences in water interaction and field effects are at least an order of magnitude smaller, and therefore vanish on the adsorption energy scale.

Surface phase diagram

There are four parameters determining the surface composition: the potential, the pH, the concentration of Cl^-, and the electrode material, only the latter is directly available in the simulations, the other three parameters can be included analytically as described below. By applying the computational standard hydrogen electrode[9] it is possible to construct surface Pourbaix diagrams, and identify the most stable structure of the catalyst surface at a range of potentials and pH values.[26] At conditions where oxygen and chlorine evolution are negligible, the structure of the catalyst surface is determined by the equilibrium with water, protons and chloride ions. The oxidation of water may lead to the formation of OH^c or O^c through

$$H_2O(l) + {}^c \leftrightarrow HO^c + H^+(aq) + e^- \leftrightarrow O^c + 2H^+(aq) + 2e^- \quad (6)$$

Chloride ions may be exchanged with the surface via

$$Cl^-(aq) + {}^c \leftrightarrow Cl^c + e^- \quad (7)$$

ClO^c may be formed by first having O^c adsorbed on the surface followed by Cl^- adsorption on top of O^c. At potentials where evolution of Cl_2 or O_2 is appreciable, the surface structure is, however, controlled by the steady state reaction.

At standard conditions (zero pH), $H^+(aq) + e^-$ is in equilibrium with ½ $H_2(g)$ at zero potential vs. the standard hydrogen electrode. At finite pH and potential the chemical potential of a proton and an electron is:

$$\mu(H^+(aq)) + \mu(e^-) = 1/2\mu_{H2(g)} - eU_{SHE} + k_BT \ln(10)\, pH. \quad (8)$$

Similarly $Cl^-(aq)$ is in equilibrium with ½ $Cl_2 + e^-$ at standard conditions at the potential of standard chlorine electrode,

$$Cl^-(aq) \leftrightarrow 1/2Cl_2 + e^- @ U_{SHE} = 1.36V. \quad (9)$$

For an arbitrary potential and activity we therefore obtain

$$\mu(Cl^-(aq)) - \mu(e^-) = ½\,\mu_{Cl2(g)} - e\,(U_{SHE} - 1.36\ V) + k_BT \ln a_{Cl^-}. \quad (10)$$

Equations (8) and (10) allow us to calculate the free energies of O^c, OH^c, Cl^c, and ClO^c adsorbed at a surface site in the electrochemical environment, based on calculations of the gas phase molecules rather than the solvated ions.
The free energy of adsorption for a surface with an adsorbate at U_{SHE} = 0 V, is given by

$$\Delta G = \Delta E + \Delta ZPE - T\Delta S + \Delta G_{ref}, \quad (11)$$

where ΔZPE is the change in zero point energy, T is the temperature, ΔS is the change in entropy upon absorption, and ΔE is the DFT calculated adsorption energies. The zero point energy contribution and the entropy for the adsorbed species are obtained from harmonic vibrational analysis and from tables of thermodynamic properties in the case of gas phase species. The numbers for ΔZPE and -TΔS are listed in the appendix in Tab. 1. The correction ΔG_{ref} is 1.36 eV for Cl^c, ClO^c and $Cl(O^c)_2$ and zero for HO^c and O^c, and is related to the reversible potentials of the chlorine and hydrogen electrodes, respectively (see appendix for details).

To obtain a measure of the activity we apply a simplified estimate: The chlorine evolution reaction is considered possible if and only if all the involved reaction steps are neutral or downhill in free energy. For a given reaction we can determine the lowest potential for which this is the case. Due to the significant challenges in treating reaction barriers for electrochemical processes, we do not include reaction barriers in the present study, and can therefore not directly compare e.g. the relative rates of the

Volmer-Tafel and the Volmer-Heyvrosky reactions. Our approach can thus be viewed as a ”lower-bound over-potential analysis” of the chlorine evolution activity. Since barriers of surface reactions[27] as well as barriers for proton transfer reactions[28] are known to often be linearly dependent on the reaction energy we expect that the trends are conserved even when barriers are included.

Results and discussion

Surface phase diagram for IrO_2

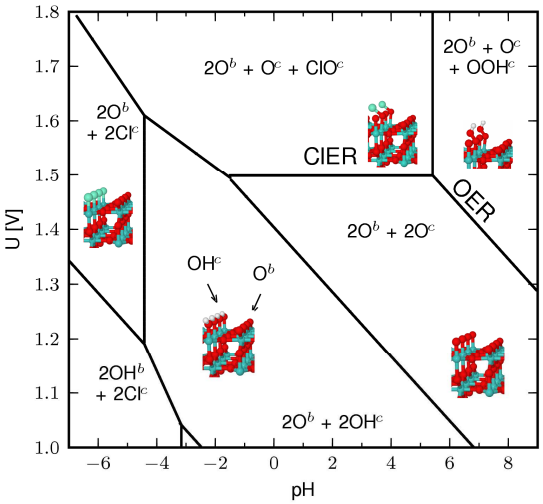

Figure 1: *Surface phase diagram for IrO_2(110) in equilibrium with Cl^-, H^+ and H_2O at 298.15 K and $a_{Cl^-} = 1$. The regions where we expect chlorine or oxygen evolution to become significant has been marked. ^{c} and ^{b} denotes cus site and bridge sites respectively.*

Figure 1 shows the interesting part of the phase diagram of IrO_2. At pH=7 the surface sites are covered by OH and O at most potentials. At low potential, the surface is covered by OH groups (not shown). Increasing the potential oxidizes OH to O first at the bridge sites and then at the cus sites. Eventually formation of OOH becomes thermodynamically favored. When this happens, we expect oxygen evolution to become appreciable[18] and the surface structure is then determined by the kinetics of the steady state evolution of oxygen. The formation of Chlorine adsorbates directly at the cus sites requires pH < -3. Formation of Cl at the bridge sites requires even lower pH.

We would expect that for a good catalyst the formation of the Cl intermediate has $\Delta G \sim 0$ eV near 1.36 V and that there are free sites available for the formation of this intermediate. A mechanism involving Cl adsorbed directly at an Ir cation, does not

fulfill any of these requirements. Instead we see from the phase diagram that a ClO^c intermediate is thermodynamically favored for U > 1.5 V in the pH range from 0 to 3. This suggests the following sequence of intermediates on IrO_2

$$O^c + 2\ Cl^-(aq) \rightarrow ClO^c + Cl^-(aq) + e^- \rightarrow O^c + Cl_2(g) + 2\ e^- \quad (12)$$

as both steps have $|\Delta G| = 0.14$ eV at U = 1.36 V, and a significant amount of O^c sites exist at U > 1.36 V.

Surface phase diagram for RuO_2

The phase diagram for RuO_2 (110) turns out to be a bit more complicated see figure 2. At pH = 7, the surface is dominated by species formed by the oxidation of water. At low potential, only the bridge sites are covered by OH. When the potential is increased, OH is formed at the cus sites, before OH is oxidized to O. We find that oxygen association at the cus sites

$$2\ O^c \rightarrow O_2^{cc} \quad (13)$$

is exothermic by 0.71 eV for the fully O covered surface. The association barrier is only 0.18 eV while desorption of O_2^{cc} is endothermic by 1.16 eV. O_2^{cc} will therefore most likely be present at the surface rather than O^c. Oxygen evolution could happen by further oxidation of the surface

$$H_2O + O_2^{cc} \rightarrow O_2^c + {}^c + H_2O \rightarrow O_2^c + OH^c + H^+ + e^-. \quad (14)$$

The stability of the $O_2^c + OH^c$ structure relative to H_2O and H^+ is indicated in figure 3. Desorption of O_2 from this surface has however $\Delta G = 0.1$ eV, so when $O_2^c + OH^c$ starts to form, we expect oxygen evolution to become important. Additional barriers could exist, we will however not go further into the details of oxygen evolution.

On RuO_2 Chlorine species are formed at pH < 1.3, however, near U=1.36 V oxygen is still the most stable adsorbate. We find that the $2\ O^b + O^c + OCl^c$ intermediate is meta stable relative to a $2\ O^b + Cl(O^c)_2$ structure. The latter structure forms at U > 1.5 V, and we expect this to be the intermediate on RuO_2 (110).

$$O_2^{cc} + 2\ Cl^-(aq) \rightarrow Cl(O^c)_2 + Cl^-(aq) + e^- \rightarrow O^c + Cl_2(g) + 2\ e^- \quad (15)$$

We note in passing that the formation of O_2^{cc} and $Cl(O^c)_2$ depend on the presence of pairs of Ru cus sites at the surface, and it may not be relevant for alloys of e.g. TiO_2 and RuO_2. Neglecting the formation of O_2^{cc} and $Cl(O^c)_2$ and considering the IrO_2 reaction path Eq (12) we find that at U=1.36 V each step has $|\Delta G| = 0.05$-0.12 eV, depending on whether there is O^c or OCl^c adsorbed at the other cus site in the (2x1) unit cell.

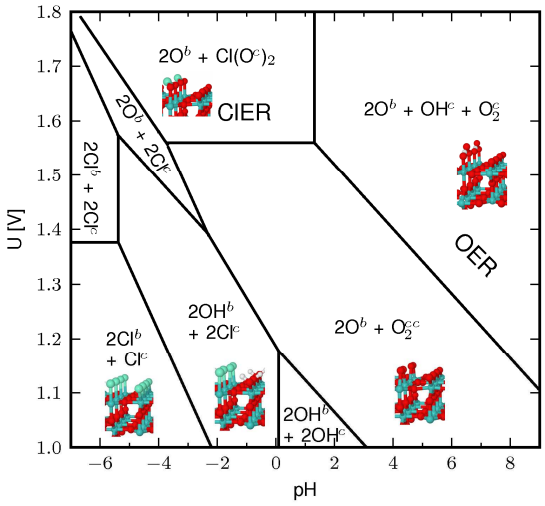

Figure 2. *Surface phase diagram for RuO_2(110) in equilibrium with Cl^-, H^+ and H_2O at 298.15 K and $a_{Cl^-} = 1$. The regions where we expect chlorine or oxygen evolution to become significant have been marked. ^{c} and ^{b} denotes cus site and bridge sites respectively.*

Scaling relations

As mentioned above it is possible to construct the surface phase diagram and reaction intermediate as function of pH, potential and the Cl^- concentration for a given material. The aim is now to generalize the analysis, not studying a single or a few oxide surfaces but rather determine a descriptor which will be a continuous material variable. The starting point of our analysis is to establish correlations between adsorption energies of intermediates on various (110) rutile oxide surfaces. Such relations can be useful in establishing simplified models describing the surface activity and composition, and can be suitable for subsequent screening purposes.[29] In Figure 3 the adsorption energies of Cl^c and ClO^c as defined above are plotted against the O binding at the cus-site with the same environment at the surface. The plot clearly shows that the Cl and O adsorption energies are linearly correlated. Such linear energy relations between adsorption energies of hydrogenated species (CH_x, OH, SH, and NH_x) and the adsorption of the corresponding unhydrogenated atoms: (C, O, S, and N) have previously been shown for transition metals[30,31] and transition metal compounds including oxides.[18,32] The scaling of Cl with respect to O is very similar to scaling of OH with respect to O. This reflects the fact that Cl has a valency of one like the oxygen atom in OH. ClO^c thus also scales as OH (and similar to HOO^c). The present results suggest that the oxygen

adsorption energy is a general measure (a so-called "descriptor") for the reactivity of oxides which has also been suggested for the case of cations in oxides by Pankratiev.[33]

Adsorption of Cl atop O^c is determined by:

$$\Delta E = E(ClO^c) - E(O^c) - 1/2E(Cl_2) = \Delta E(ClO^c) - \Delta E(O^c) \quad (16)$$

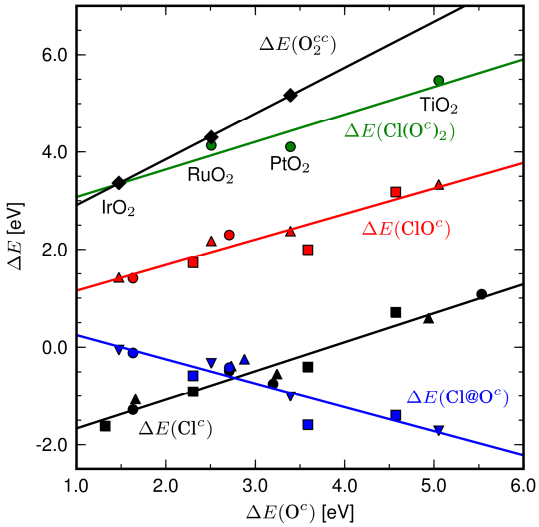

Figure 3. *The adsorption energies of chlorine at cus (black): $\Delta E(Cl^c)=0.59\Delta E(O^c)$ - 2.26 eV (■ – vacant neighboring cus-sites, ▲ - Cl neighbor, ● – O neighbor), the adsorption energy of ClO (red) at cus: $\Delta E(ClO^c)=0.52\Delta E(O^c)$ + 0.62 eV (■ - vacant neighboring cus sites, ● – O neighbor, ▲ – average adsorption energy of ClO for the fully covered surface vs. average adsorption energy for O for fully covered surface), adsorption energy of Cl ontop O at cus (blue): $\Delta E(Cl^c)=-0.48\Delta E(O^c)+ 0.68$ eV (■ – Cl ontop O vs. O with vacant neighboring cus sites , ● – Cl ontop O vs. O with O neighbors, ▲ - Cl ontop O vs. O with ClO neighbors, ▼ – average adsorption energy of Cl ontop O for fully covered surface on vs. average adsorption energy of O for fully covered surface), the adsorption energy of O_2^{cc} vs the average adsorption energy of O^c (yellow): $\Delta E(O_2^{cc})=0.94\Delta E(O^c)$ + 1.96 eV, and the adsorption energy of $Cl(O^c)_2$ vs the average adsorption energy of O^c (green): $\Delta E(Cl(O^c)_2 = 0.56\Delta E(O^c)$ + 2.51 eV . The mean absolute error of the fits are below 0.21 eV.*

The linear scaling relations established above makes it possible to analyze the reaction, not only for a specific metal oxide surfaces, but for potential metal oxide catalyst surfaces with continuously varying reactivity as measured by the adsorption energy of oxygen at the cus-site. The obtained reactivity curves will then be continuous in the oxygen adsorption energy whereas specific oxides (e.g. RuO_2, IrO_2, PtO_2, and TiO_2) will show up as discrete points. The descriptor approach provides a fast overview of

the "phase-space" of materials, but *a priori* leaves the problem of how to find specific materials with the desired descriptor properties unanswered.

Generalized phase diagram

Since the binding energy of all intermediates at the cus sites scales directly with $\Delta E(O^c)$ it is possible to construct a generalized phase diagram showing the most stable phase at potential U as function of the material-dependent descriptor, $\Delta E(O^c)$.

We choose the electrolytic conditions such that when increasing the potential the most stable form of chlorine goes directly from Cl^- to Cl_2, which means that the pH value should be between -1 and 3. HCl(aq) is more stable than Cl^- at pH values below ~ -1, whereas HClO(aq) becomes stable at pH-values higher than ~3. We keep the electrolyte pH and Cl^- concentration fixed (pH = 0, $a_{Cl^-} = 1$) and investigate the surface phase diagram as a function of $\Delta E(O^c)$ and potential. This approach is not a limitation of the method, since other electrolyte conditions can be treated just by changing the free energies accordingly.

This is shown in figure 4. At the limit of weak binding, oxygen association becomes exothermic and barrierless, so phases like ClO^c and $Cl(O^c)_2$ cannot form. From the linear relations we find that

$$O_2^{cc} \rightarrow O_2(g) + 2^c,$$

has $|\Delta G| < 0$ for $\Delta E(O^c) > 2.97$ eV. We therefore chose to consider only OH^c and Cl^c for $\Delta E(O^c) > 2.97$ eV. The free energies of OH^c and Cl^c are within 0.01-0.27 eV depending on the oxide and we expect some coexistence in these regions of phase space. Range of $\Delta E(O^c)$ for some rutile oxides is seen in figure 5. For IrO_2 and RuO_2 the line at lowest $\Delta E(O^c)$ marks the adsorption energy with free neighboring cus sites and the line at highest $\Delta E(O^c)$ marks the adsorption energy with O^c neighbors as calculated in the (2x1) unit cell. For PtO_2 and TiO_2 the line at weakest binding marks the binding energy at high O^c coverage. The variation in adsorption energy with coverage may be seen as an uncertainty arising from neglecting adsorbate-adsorbate interactions. For the considered oxides $\Delta E(O^c)$ is more affected by changing the oxide than changing the O^c coverage. The change of the most stable adsorbate when the potential is increased is qualitatively reproduced for RuO_2 and IrO_2.

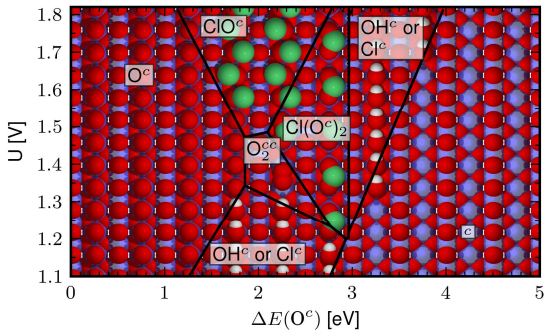

Figure 4. *The most stable surface at pH =0 and a_{Cl^-}=1 as a function of potential, U, and the surface reactivity descriptor, $\Delta E(O^c)$. Metal ions are blue, O atoms red, hydrogen atoms white, and chlorine atoms are green. The regions in the figure are determined by the most stable surface configuration at the given potential. The phase borders are defined by the equilibrium point of the reactions. So for example the border between the surface with O^c on the surface and the surface with ClO^c is defined by: $O^c + Cl^-(aq) \leftrightarrow ClO^c + e^-$, $\Delta G(O^c)-\Delta G(ClO^c)-eU_{SHE} = 0$.*

Chlorine evolution activity

Firstly, we investigate the mechanism involving ClO^c

$$O^c + 2\,Cl^-(aq) \rightarrow ClO^c + Cl^-(aq) + e^- \rightarrow O^c + Cl_2(g) + 2\,e^- \quad (17)$$

The potential at which all steps are neutral or downhill is:

$$U = U^{eq} + |\Delta G(ClO^c)-\Delta G(O^c)| / e, \quad (18)$$

where U^{eq} is the equilibrium potential for chlorine evolution, in this case $1.36V_{SHE}$. Secondly, we investigate the mechanism involving $Cl(O^c)_2$:

$$O_2^{cc} + 2\,Cl^-(aq) \rightarrow Cl(O^c)_2 + Cl^-(aq) + e^- \rightarrow O^c + Cl_2(g) + 2\,e^-$$

The potential at which all steps are neutral or downhill is:

$$U = U^{eq} + |\Delta G(Cl(O^c)_2)-\Delta G(O_2^{cc})| / e. \quad (19)$$

Thirdly we consider a mechanism involving Cl^c adsorbed directly at the metal cus site.

$$2Cl^-(aq) + {}^c \rightarrow Cl^-(aq) + Cl^c + e^- \rightarrow Cl_2(g) + {}^c + 2e^- \quad (20)$$

This mechanism could be relevant for oxides with weaker adsorption energy at the cus site than RuO_2. Our calculations however suggest that this mechanism will be

somewhat poisoned by OH^c formation at the cus sites. The potential where all steps are neutral or down hill is:

$$U = U^{eq} + |\Delta G(Cl^c)| / e, \quad (21)$$

RuO_2 and PtO_2 have $|\Delta G(Cl^c)| < 0.05$ eV for high and low coverage of Cl^c respectively and could in principle work as good catalysts following this path, however for RuO_2, we find the cus sites to be blocked by $O_2{}^{cc}$.

Since the different chlorine evolution potentials all are functions of $\Delta E(O^c)$ the potentials can be plotted directly in the phase diagram as shown in Figure 5 This is similar to the Sabatier activity volcano curves known from heterogeneous catalysis.[34] To have the surface phase diagram in the same plot as the potential volcano directly assures that the activity volcano and the stable surface configuration agrees. In other words, the different activity plots are relevant in different areas of the phase diagram, which are easily obtained by looking at figure 5. The thick black line marks the volcanoes, where the mechanism involves one of the most stable surfaces as an intermediate at the potential where all steps are neutral or downhill in free energy. We note that the surface composition during oxygen and chlorine evolution is not determined by equilibrium, but rather by steady state. However, it seems plausible that the surface composition determined by equilibrium is one of the intermediates during the reaction. Figure 5 also shows the activity of IrO_2 and RuO_2 based on O^c adsorption energy, with the error bars corresponding to the variation of the O^c adsorption energy when going from low to high O^c coverage.

If the accuracy of the linear relations are taken into account, the three investigated mechanisms form a single volcano with a broad plateau for $\Delta E(O^c)$ from 1.5 eV to 3.5 eV. Deviations from the linear relations could be important in this area. The agreement between the detailed analysis for IrO_2 and RuO_2 and the linear relations is therefore surprisingly good.

We find RuO_2 to be at the top of the volcano whereas IrO_2 binds Cl on top O^c too weakly. TiO_2 do not show up on this activity scale. To our knowledge, only a few studies of the relative activity of rutile oxides have been carried out. Kuhn and Mortimer found IrO_2 and RuO_2 to have similar activities and to be more active than TiO_2. Mixtures of TiO_2 with Ir and Ru are more active than mixtures of TiO_2 with Cr, Co, or Pt.[35] Arikado *et al.* found the over-potential to increase in the order $RuO_2 <$ $Ti/PtO_2 < IrO_2$.[36] Kelly *et al.* found the specific activity of Ru sites at $Ru_xTi_{1-x}O_2$ to be 45% more active than the Ir sites at $Ir_xTi_{1-x}O_2$. [4,37] We note the discrepancy between the relative activity of RuO_2, IrO_2, and PtO_2 could be because different preparation methods may lead to different surface roughness factors and different concentrations of residual chlorine in thermally prepared oxides.[4] The high activity of RuO_2 and IrO_2 relative to TiO_2 is in agreement with experiments. The rutile crystal structure of PtO_2 is not the most stable structure for PtO_2, it is however possible that some PtO_2 may be found in the rutile crystal phase if PtO_2 is mixed with oxides that do form the rutile crystal phase.

For comparison the potential for oxygen evolution is also shown in figure 5. It is seen that the potential for chlorine evolution is lower than the potential for oxygen evolution in spite of the lower equilibrium potential for oxygen evolution. This is the reason why electrochemical chlorine evolution is possible. It is also seen that a good oxygen evolution catalyst is also a good chlorine evolution catalyst. A comparison of the experimental potentials for OER and ClER has suggested that the selectivity of oxides does not depend *appreciably* on the catalyst material.[2] The potential of chlorine evolution changes with the potential of oxygen evolution with a slope of 1. Interestingly one of the biggest outliers in the comparison above was a Pt/MnO_2 catalyst in acid where the potential for oxygen evolution was 0.3 eV higher than the potential of chlorine evolution. MnO_2 has an oxygen binding energy around 3.2 eV[38]. Based on Figure 5 we would therefore expect the potential for chlorine evolution to be 0.4 V lower than the potential for oxygen evolution.

Single crystal experiments on RuO_2 find the (110) surface to be less active for Cl_2 evolution than the (101) and the (320) surfaces.[8,39] On polycrystalline RuO_2,[40] mixed RuO_2+TiO_2,[41] and RuO_2 (320)[39] the activity depends on pH, whereas the activity of RuO_2 (110) is independent on pH. The variation of activity with pH has been explained by the reaction

$$OH^c \leftrightarrow O^c + H^+(aq) + e^- \qquad (22)$$

determining the availability of active O^c sites.[7,39,40,42] This clearly requires O^c and HO^c to be near equilibrium at the reaction conditions for Cl_2 evolution. Since the bridge sites and cus-sites on the (110) surface of rutile oxides fulfill the same scaling relations between O and OH adsorption as perovskites [32], it is reasonable to assume the scaling relations are identical for all rutile oxide surfaces. In this case Figure 5 applies for any rutile oxide surface, but with the oxygen adsorption energy depending on the specific surface facet. It has been argued that the binding energy on the stepped (320) surface is stronger than on the (110) surface.[39] If it is assumed the O_2^{cc} and $Cl(O^c)_2$ intermediates form at the (320) surface as well, Figure 5 shows that as $\Delta E(O^c)$ is decreased from ca. 2.6 eV, the OH^c/O_2^{cc} equilibrium shifts to higher potential, which leads to increased blocking of the active sites by OH^c at a fixed overpotential. We note the over-potential at constant current is found to be 80 meV lower on the (320) surface than on the (110) surface,[39] and thus within the vertical error bars indicated in Figure 5.

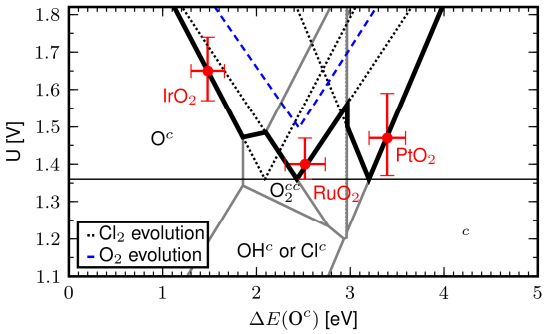

Figure 5: *Sabatier volcanoes (black dotted) for the considered reaction paths involving ClO^c, $Cl(O^c)_2$ and Cl^c (from left to right). The domains of the most stable surface structure as function of potential and oxygen binding energy is marked by gray. To be truly active, the intermediate should form at sites that are stable as this makes the active site abundant. The full black line shows the combined Sabatier volcano taking into account the stability of the active sites for a given mechanism. The Sabatier volcano for oxygen evolution[18] (dashed blue) shows OER always requires a higher potential than ClER. The activity of IrO_2 and RuO_2 are indicated with error bars derived from the variation of the O^c adsorption energy with varying O^c coverage.*

Conclusion

Based on DFT calculations we have established linear scaling relations between Cl, ClO, and O adsorption energies at the cus-sites of rutile oxides. These linear energy relations enable the construction of a generalized surface phase diagram where potential and binding of oxygen are the descriptors determining the surface composition. By applying an electrochemical-thermodynamic approach we can make the first simple theoretical analysis of the electrocatalytic chlorine evolution reaction based on the free energies of the reaction intermediates. A lower-bound to the over-potential required for driving the reaction is thereby determined as function of the oxygen adsorption energy. This approach is an electrochemical analogue to the Sabatier analysis used in heterogeneous catalysis. Combining the surface phase diagram and the Sabatier volcano one obtains a qualified suggestion for the surface structure during reaction condition. The analysis shows that ClO or $Cl(O^c)_2$ will form spontaneously on the cus-sites of IrO_2 and RuO_2 at the potential required for chlorine evolution. This indicates that the Cl_2 evolution occurs through these intermediates on IrO_2 and RuO_2. The potential necessary for Cl_2 evolution is always smaller than the potential for oxygen evolution for oxides exhibiting certain oxygen adsorption energies. This is consistent with experiments[2] and rationalizes experimental findings.

Acknowledgement. The Center for Atomic-scale Materials Design is funded by the Lundbeck Foundation. This work was supported by the Danish Center for Scientific Computing through Grant No. HDW-1103-06, the European Commission (Marie Curie Research Training Network MRTNCT-2006-032474) and The Danish Council for Strategic Research though the HyCycle Center (No. 2104-07-0041).

Appendix

For construction of the surface phase diagrams, we need to calculate the free energy of adsorbates formed by water discharge, e.g. O^c or HO^c:

$$H_2O(l) + {}^c \rightarrow OH^c + H^+(aq) + e^- \quad (A.1)$$

$$H_2O(l) + {}^c \rightarrow O^c + 2\,H^+(aq) + 2\,e^- \quad (A.2)$$

and from adsorption of chloride ions:

$$Cl^-(aq) + {}^c \rightarrow Cl^c + e^- \quad (A.3)$$

The free energy of formation of O^c, defined by (A.2), is

$$\Delta G(O^c)(U,a_{H+}) = G(O^c) + 2\,\mu(H^+) + 2\,\mu(e^-) - \mu(H_2O(l)) - G({}^c), \quad (A.4)$$

Where $G(O^c)$ and $G({}^c)$ is the free energy of the surface with and without O^c respectively. $\mu(H^+) = \mu(H^+)^\ominus + k_BT \ln a_{H+}$ is the chemical potential of protons and $\mu(e^-) = \mu(e^-)^\ominus - e\,U$ is the chemical potential of electrons at the electrode at the potential U. $\mu(e^-)^\ominus$ is an arbitrary reference energy determined by the potential scale.
Throughout this work we reference the potential relative to the standard hydrogen electrode (SHE), which means the hydrogen electrode reaction

$$H^+(aq) + e^- \leftrightarrow \tfrac{1}{2}\,H_2, \quad (A.5)$$

is at equilibrium at zero potential and standard conditions (p_{H2} = 1 bar, pH = 0), from which it follows, that

$$\tfrac{1}{2}\,\mu(H_2)^\ominus = \mu(H^+)^\ominus + \mu(e^-)^\ominus. \quad (A.6)$$

The chemical potential of liquid water is calculated from water vapor in equilibrium with liquid water at 298 K.

$$\mu(H_2O(l)) = \mu(H_2O(g)\ @\ 0.035\ \text{bar and } 298\ \text{K}) \quad (A.7)$$

The formation energy of O^c can therefore be written as:

$$\Delta G(O^c)(U,a_{H+}) = G(O^c) - G({}^c) - \mu(H_2O(g)\ @\ 0.035\text{bar}) + \mu(H_2)^\ominus + 2\,(k_BT \ln a_{H+} - eU),$$
$$= \Delta E_{O^*} + \Delta ZPE - T\Delta S^\ominus + 2\,(k_BT \ln a_{H+} - eU), \quad (A.8)$$

Where $\Delta E(O^c)$ is calculated as described in the section "scaling relations", ΔZPE is the change in zero point energy upon adsorption and is calculated within the harmonic approximation for an adsorbate at the cus-site of RuO_2, and assumed to be constant

from one rutile oxide to the next. ΔS includes the loss of translational entropy of the gas phase molecules upon adsorption on the surface.

An equation similar to (A.8) may be derived for the adsorption of HO^c:

$$\Delta G(HO^c)(U,a_{H+}) = \Delta E(HO^c) + \Delta ZPE - T\Delta S^\ominus + k_B T \ln a_{H+} - eU. \quad (A.9)$$

The free energy of adsorption of chlorine by (A.3) is

$$\Delta G(Cl^c)(U,a_{Cl-}) = G(Cl^c) - G(^c) + \mu(e^-) - \mu(Cl^-)^\ominus - k_B T \ln a_{Cl-}. \quad (A.10)$$

By considering a chlorine electrode at equilibrium at standard conditions

$$Cl^- (aq) \leftrightarrow \tfrac{1}{2} Cl_2 (g) + e^- \quad (A.11)$$

We see that

$$0 = \tfrac{1}{2}\mu(Cl_2)^\ominus + \mu(e)^\ominus - eU_{Cl}^\ominus - \mu(Cl^-)^\ominus, \quad (A.12)$$

where $U_{Cl}^\ominus$ is the standard potential of the reversible chlorine electrode, $U_{Cl}^\ominus$ = 1.36 V at 298 K. We then have

$$\begin{aligned}\Delta G(Cl^c)(U,a_{Cl-}) &= G(Cl^c) - G(^c) + \tfrac{1}{2}\mu(Cl_2)^\ominus - e(U - U_{Cl}^\ominus) - k_B T \ln a_{Cl-} \\ &= \Delta E(Cl^c) + \Delta ZPE - T\Delta S^\ominus - k_B T \ln a_{Cl-} - e(U - U_{Cl}^\ominus). \quad (A.13)\end{aligned}$$

For simplicity we consider the standard conditions $a_{H+} = a_{Cl-} = 1$, and define for notational convenience $\Delta G(Cl^c) = \Delta G(Cl^c)(U=0, a_{Cl-}=1)$, $\Delta G(HO^c) = \Delta G(HO^c)$ (U=0, a_{H+}=1) etc., so that all free energies of adsorption are referenced to the standard hydrogen electrode.

In Table 1, ΔZPE and TΔS for all the relevant reactions are listed at T = 298K. ZPE are obtained from a vibrational calculation within the harmonic approximation. For the adsorbed species the ZPE have been calculated for an adsorbate at the cus-site of RuO_2.

	TS	**TΔS**	**ZPE**	**ΔZPE**	**ΔZPE −TΔS**
H_2O(l)	.67	0	.56	0	0
$H_2O \rightarrow {}^cOH + 1/2H_2$	.20	-.47	.50	-.06	.41
$H_2O \rightarrow {}^cO + H_2$	.41	-.27	.34	-.22	.05
$H_2O \rightarrow 1/2O_2 + H_2$	.73	.05	.32	-.24	-.29
$1/2Cl_2 \rightarrow Cl^c$	-	-.34	-	0.02	.37
Cl_2	.69	-	.06	-	

H_2	.41	-	.27	-
$1/2O_2$	.32	-	.05	-
Cl^c	0	-	.05	-
O^c	0	-	.07	-
OH^c	0	-	.36	-
H^c	0	-	.17	-

Table 1: Zero point energies and entropic corrections at 298 K.

Adsorption energies:

Adsorption Energy (eV)	O on 2 ^{c}	O on O^c + ^{c}	O on Cl^c + ^{c}	O on ClO^c + ^{c}	Average of 2 O on 2 ^{c}
RuO_2	2,30	2,71	2,73	2,8772	2,51
IrO_2	1,32	1,63	1,66		1,48
TiO_2	4,57	5,53	4,94		5,05
PtO_2	3,59	3,20	3,24		3,39

Table 2: Adsorption energy of O at a free cus site (^{c}) for different surface terminations. In all cases the bridge sites are covered with oxygen. The adsorption energy is calculated according to equation (2).

Adsorption Energy (eV)	Cl on 2 ^{c}	Cl on Cl^c + ^{c}	Cl on O^c + ^{c}	Average of 2 Cl on 2 ^{c}
RuO_2	-0,91	-0,38	-0,48	-0,64
IrO_2	-1,62	-1,06	-1,28	-1,347
TiO_2	0,71	0,59	1,08	0,65
PtO_2	-0,40	-0,54	-0,75	-0,47

Table 3: Adsorption energy of Cl at a free cus site (^{c}) for different surface terminations. In all cases the bridge sites are covered with oxygen. The adsorption energy is calculated according to equation (1).

Adsorption Energy (eV)	ClO on 2 ^{c}	ClO on ClO^c + ^{c}	ClO on O^c + ^{c}	Average of 2 ClO on 2 ^{c}
RuO_2	1,73	2,63	2,30	2,18
IrO_2			1,40	1,42
TiO_2	3,18	3,49		3,33
PtO_2	1,99	2,76		2,38

Table 4: Adsorption energy of ClO at a free cus site (*) for different surface terminations. In all cases the bridge sites are covered with oxygen. The adsorption energy is calculated according to equation (3).

Adsorption Energy on top O^c (eV)	Cl on O^c + ^{c}	Cl on 2 O^c	Cl on ClO^c + O^c	Average of 2 Cl on 2 O^c
RuO_2	-0,58	-0,41	-0,24	-0,33
IrO_2		-0,11	0,00	-0,06
TiO2	-1,40			-1,72
PtO_2	-1,60			-1,02

Table 5: Adsorption energy of Cl on top O at a cus site (O^c) for different surface terminations. In all cases the bridge sites are covered with oxygen. The adsorption energy is calculated according to equation (4).

Linear Relations:

In constructing the generalized phase diagram and the Sabatier volcanoes we have used the linear relations below. The mean absolute error (MAE) of the fits is also listed.

$\Delta E(Cl^c)=0.59*\Delta E(O^c)-2.26$ eV, MAE = 0.17 eV

$\Delta E(ClO^c)=0.52*\Delta E(O^c)+0.62$ eV, MAE = 0.16 eV

$\Delta E(O_2{}^{cc})=0.94*\Delta E(O^c)+1.96$ eV, MAE = 0.02 eV

$\Delta E(Cl(O^c)_2) = 0.56*\Delta E(O^c)+2.51$ eV, MAE = 0.21 eV

and the scaling relation between O* and OH* from reference 18:

$\Delta E(HO^c) = 0.61*\Delta E(O^c) - 0.90$ eV

(1) Euro Chlor (representing the chloro-alkali industry, Chlorine Industry Review 2007–2008)
(2) Trasatti, S. *Electrochim. Acta.* **1984**, *29,* 1503-1512.
(3) Trasatti, S. *Electrochim. Acta* **2000**, *45*, 2377-2385.
(4) Kelly, E.J.; Heatherly, D.E.; Vallet, C.E.; White, C.W. *J. Electrochem. Soc.* **1987**, *134,* 1667-1675.
(5) Trasatti, S.; O'Grady, W.E. *Adv. Electrochem. and Electrochem. Engineering* **1981**, *12*, 117-261.
(6) Trasatti, S.; Lodi, G. *"Electrodes of Conductive metallic Oxides"* **1980**, 301-358.
(7) Krishtalik, L.I. *Electrochim Acta* **1981**, *26*, 329.
(8) Hepel, T.; Pollak, F.; O'Grady, W.E. *J. Electrochem. Soc.* **1986**, 133, 69-75.
(9) Nørskov, J.K.; Rossmeisl, J.; Logadottir, A.; Lindqvist, L.; Kitchin, J.R.; Bligaard, T.; Jónsson, H. *J. Phys. Chem. B* **2004**, *108*, 17886-17892.
(10) Lischka, M.; Mosch, C.; Gross, A. *Electrochim. Acta* **2007**, *52*, 2219-2228.

(11) Panchenko, A.; Koper, M.T.M.; Shubina, T.E.; Mitchell, S.J.; Roduner, E. *J. Electrochem. Soc.* **2004**, *151*, A2016-A2026.
(12) Nilekar, A.U.; Mavrikakis, M. *Surf. Sci.* **2008**, *602*, L89-L94.
(13) Rossmeisl, J.; Karlberg G.S.; Jaramillo, T.; Nørskov J.K. *Faraday Discuss.* **2008**, *140*, 337-346.
(14) Liu, P.; Logadottir, A.; Nørskov, J.K. *Electrochim. Acta* **2003**, *48*, 3731.
(15) Cao, D.; Lu, G.Q.; Wieckowski, A.; Wasileski, S.A.; Neurock, M. *J. Phys. Chem. B* **2005**, *109*, 11622.
(16) Ferrin, P.; Nilekar, A.U.; Greeley, J.; Mavrikakis, M.; Rossmeisl, *Surf. Sci.* **2008**, *602*, 3424-3431.
(17) Koper, M.T.M.; Shubina, T.E.; van Santen, R.A. *J. Phys. Chem. B* **2002**, *106*, 686.
(18) Rossmeisl, J.; Qu, Z.-W.; Zhu, H.; Kroes G.-J.; Nørskov, J.K. *J. Electroanal. Chem.* **2007**, *607*, 83-89.
(19) López, N.; Gómez-Segura, J.; Martin, R. P.; Pérez-Ramírez , J. *J. Catal.*, **2008**, 255, 29-39.
(20) Crihan, D.; Knapp, M.; Zweidinger, S.; Lundgren, E.; Weststrate, C. J.; Andersen, J. N.; Seitsonen, A. P.; Over, H. *Angew. Chem. Int. Ed.* **2008**, 47, 2131-2134.
(21) Hammer, B.; Hansen, L.B.; Nørskov, J.K. *Phys. Rev. B* **1999**, *59*, 7413-7421.
(22) Monkhorst, H.J.; Pack, J.D. *Phys. Rev. B* **1976**, *13*, 5188.
(23) Vanderbilt, D. *Phys.Rev. B* **1990**, *41*, 7892-7895.
(24) Open source codes available at http://wiki.fysik.dtu.dk/dacapo and http://wiki.fysik.dtu.dk/ase
(25) Karlberg, G.S.; Rossmeisl, J.; Nørskov, J.K. *Phys. Chem. Chem. Phys.* **2007**, *9*, 5158-5161.
(26) Hansen, H.A.; Rossmeisl, J.; Nørskov. J.K. *Phys. Chem. Chem. Phys.* **2008** DOI: 10.1039/b803956a
(27) Nørskov, J.K.; Bligaard, T.; Logadottir, A.; Bahn, S.; Hansen, L.B.; Bollinger, M.;Bengaard, H.S.; Hammer, B.; Sljivancanin, Z.; Mavrikakis, M.; Xu, Y.; Dahl, S.;Jacobsen, C.J.H. *J. Catal.* **2002**, *209*, 275.
(28) Rossmeisl, J.; Skúlason, E.; Björketun, M.E.; Tripkovic, V.; Nørskov. J.K. *Chem. Phys. Lett.* **2008**, *466*, 68-71.
(29) Nørskov, J.K.; Bligaard, T.; Rossmeisl, J.; Christensen, C.H. *Nature Chemistry* **2009**, *1*, 37-46.
(30) Abild-Pedersen, F.; Greeley, J.; Studt, F.; Rossmeisl, J.; Munter, T.R.; Moses, P.G.; Skulason, E.; Bligaard, T.; Nørskov, J.K. *Phys. Rev. Lett.* **2007**, *99*, 016105.
(31) Rossmeisl, J.; Logadottir, A.; Nørskov, J.K. *Chem. Phys.* **2005**, *319*, 178-184.
(32) Fernandez, E.; Moses, P.G.; Toftelund, A.; Hansen, H.A.; Martinez, J.I.; Abild-Pedersen, F.; Kleis, J.; Hinnemann, B.; Rossmeisl, J.; Bligaard, T.; Nørskov J.K. *Angew. Chem. Int. Ed.* **2008**, *47*, 4683-4686.
(33) Pankratiev, Y.D. *React. Kinet. Catal. Lett.* **1982**, *20*, 255.
(34) Bligaard, T.; Nørskov, J.K.; Dahl, S.; Matthiesen, J.; Christensen, C.H.; Sehested, J. *J. Catal.* **2004**, *224*, 206-217.
(35) Kuhn, A.T.; Mortimer, C.J. *J. Electrochem. Soc.* **1973**, *120*, 231-236.
(36) Arikado, T.; Iwakura, C.; Tamura, H. *Electrochim. Acta* **1978**, *23*, 9-15.
(37) Kelly, E. J.; Vallet, C. E.; White, C. W. *J. Electrochem. Soc.* **1990**, 137, 2482-2491.
(38) J. Rossmeisl, K. Dimitrievski, P. Siegbahn, J.K. Nørskov. **111**, *Phys. Chem. C*. **2007**, 18821-18823
(39) Guerrini, E.; Consonni, V.; Trasatti, S. *J. Solid State Electrochem.* **2005**, *9*, 320-329.
(40) Fernández, J.L.; Gennero de Chialvo, M.R.; Chialvo, A.C. *Electrochim. Acta* **2002**, *47*, 1129-1136.

(41) Erenburg, R.G.; Krishtalik, L.I.; Rogozhina, N.P. *Elektrokhimiya* **1984**, *20*, 1183.
(42) Erenburg, R.G. *Elektrokhimiya* **1984**, *20*, 1602.

P6

Volcano Relation for the Deacon Process over Transition-metal Oxides
F. Studt, F. Abild-Pedersen, H. A. Hansen, I. C. Man, J. Rossmeisl and T. Bligaard
Accepted for publication in ChemCatChem

DOI: 10.1002/cctc.200((will be filled in by the editorial staff))

Volcano Relation for the Deacon Process over Transition-metal Oxides

Felix Studt,[a,b] Frank Abild-Pedersen,[a,b] Heine A. Hansen,[a] Isabela C. Man,[a] Jan Rossmeisl,[a] and Thomas Bligaard*[a,c]

We establish an activity relation for the heterogeneous catalytic oxidation of HCl (the Deacon Process) over rutile transition metal oxide catalysts by combining Density Functional Theory calculations with microkinetic modeling. Linear energy relations for the elementary reaction steps are obtained from the DFT calculations and utilized to establish a one-dimensional descriptor for the catalytic activity. The descriptor employed here is the dissociative chemisorption energy of oxygen. It is found that the commonly employed RuO_2 catalyst is close to optimal, but that there could still be room for improvements. The analysis suggests that oxide surfaces which offer slightly weaker bonding of oxygen should exhibit a superior activity to that of RuO_2.

Introduction

Chlorine is one of the most important compounds for the chemical industry with a worldwide annual production of approximately 50 Mton. It is usually produced from either hydrochloric acid or chloride salts. Electrochemical reduction of either HCl or chloride salts is highly energy demanding and there has thus been growing interest in the heterogeneously catalyzed oxidation of HCl with oxygen using the so-called Deacon process:[1]

$$4HCl(g) + O_2(g) \rightarrow 2Cl_2(g) + 2H_2O(g) \quad (\Delta H^{298K} = -114\ kJmol^{-1}) \quad \mathbf{1}$$

The Deacon process has been known for about 130 years, but industrial production via this route was only established recently by Sumitomo Chemicals using a RuO_2 catalyst supported on TiO_2.[2] Even though the production of chlorine is extremely important to the chemical industry, there have only been few attempts to describe this process theoretically.[3-5] Recently, a density functional theory study (DFT) showed that the most energy demanding step in this reaction is likely to be the recombination of adsorbed chlorine to form Cl_2. All other steps in the reaction pathway were calculated to have significantly lower barriers.[3] In that study, however, it was assumed that the catalytically active surface is RuO_2(110). This assumption was challenged by combined experimental and theoretical studies indicating that the active catalyst should have chlorine atoms sitting in the bridge positions on the (110) surface of RuO_2.[4,5]

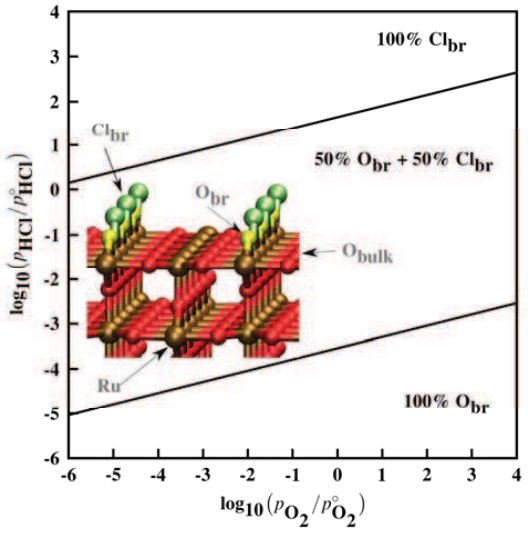

Figure 1. Stability range of the RuO_2 (110) surface for bridge adsorbed 100% O*, 50% O* + 50% Cl*, and 100% Cl* as a function of O_2 and HCl pressures at 573 K.

In this paper, we use DFT calculations to address the underlying principles of the catalytically active surface. Our calculations support that chlorination of the surface does indeed occur under reaction conditions and we analyze how it influences the catalytic performance of the actual catalyst. By comparing the thermodynamics of the reaction on the RuO_2(110) surface with those on TiO_2(110) and IrO_2(110), we find the key parameters determining the activity of the catalytically active surface. By combining Brønsted-Evans-Polanyi (BEP) relations[6-9] and scaling relations[10-12] with a microkinetic model of the reaction, we

[a] *Dr. F. Studt, Dr. F. Abild-Pedersen, M.Sc. H.A. Hansen, M.Sc. I.C. Man, Prof. J. Rossmeisl, Prof. T. Bligaard*
Center for Atomic-scale Materials Design
Department of Physics
Technical University of Denmark
DK-2800 Kgs. Lyngby, Denmark
Fax: (+45) 4593 2399
E-mail: bligaard@fysik.dtu.dk
[b] *Dr. F. Studt, Dr. F. Abild-Pedersen,*
Computational Materials Design ApS
Fysikvej – Building 307 - DTU
DK-2800 Kgs. Lyngby, Denmark
[c] *Prof. T. Bligaard*
Materials Sciences Division
Lawrence Berkeley National Laboratory
Berkeley, CA 94720, U.S.A.

Supporting information for this article is available on the WWW under http://dx.doi.org/10.1002/cctc.200xxxxxx.

furthermore derive a volcano-curve for the activity by which the reaction rate over a given rutile oxide catalyst is described in terms of a single descriptor.

Results and Discussion

It has been shown experimentally that the bridging oxygen atoms of the RuO_2(110) surface will be substituted when the surface is exposed to HCl.[5] In Figure 1 we present a phase diagram for the bridge sites, which we consider as a part of the static surface that is equilibrated with the reaction mixture. Subsequently we consider the coverages of the cus sites through the steady state of the microkinetic modeling. According to the calculated phase diagram in Figure 1, the bridging oxygen atoms on RuO_2(110) will to a large extent be exchanged with chlorine under industrially relevant pressures of oxygen and hydrochloric acid. The situation is different, however, for the two other surfaces considered in this study; neither IrO_2(110) nor TiO_2(110) will be chlorinated at the bridge positions (see Supporting Information for details). The pathway over the RuO_2(110) surface is thus one-dimensional since the adsorbed chlorine atoms do not interact with the hydrogen atoms of the reactant HCl. For the surfaces considered here, bridging oxygen atoms are always energetically more difficult to remove than oxygen atoms bound to the cus sites. Hence, the catalytic reaction on the (110) surfaces will always take place along the free cus sites.[13] The bridging oxygen atoms may bind and release hydrogen, but are unlikely to be exchanged during the reaction.

The free energy diagram of the catalytic cycle for the HCl oxidation is shown in Figure 2 for reaction temperatures of 373 K and 573 K. The first important observation is that the reaction energetics is very similar for the two different ruthenium oxide surfaces. The cycle starts with the dissociative adsorption of HCl on the cus site of the oxygen precovered surface, whereby hydrogen atoms bind to the oxygen and chlorine atoms bind directly to a free cus site. This step is thermodynamically downhill for RuO_2 and IrO_2. As a next step, the dissociative adsorption of molecular oxygen is considered. This process is slightly downhill for RuO_2, significantly downhill for IrO_2 and strongly uphill for TiO_2.[14,15] This reaction is accompanied by a barrier of 0.85 eV for $RuO_{2-x}Cl_x$[16] and 0.11 eV for IrO_2 (see Figure 2, right).

After coadsorption of a second HCl, there are two adsorbed OH-groups and two Cl atoms on the surface. At 373 K, recombination of two chlorine atoms is endergonic for the RuO_2 and IrO_2 surfaces and represents the most free energy demanding step of the catalytic cycle, in agreement with earlier studies.[3] In a last step, two adsorbed OH react to form water and the oxygen precovered surface that was chosen as the starting point of the catalytic cycle.

As shown in Figure 2, an increase in reaction temperature decreases the endergonicity of the chlorine recombination explaining the high temperatures that are needed to run the Deacon process over the RuO_2 catalyst. The overall Deacon process is mildly exothermic (see eq. **1**), and at lower temperatures equilibrium will thus favor the product. An increase in reaction temperature will make the process less exergonic (the exergonicity was calculated to be -0.46 eV at 373 K compared to -0.32 eV at 573 K; see Figure 2). This will lead to a shift in the equilibrium conversion which reduces the final chlorine yield.

There are two steps that primarily determine the activity volcano for the Deacon process. The first is the splitting of molecular oxygen along two cus sites. While this step is feasible over RuO_2 and IrO_2 it becomes very much uphill over TiO_2 thus eliminating its activity completely. The second rate determining step is the recombination of two adsorbed chlorine atoms forming Cl_2. If this step becomes too endergonic, chlorine cannot be removed within a reasonable timescale and poisons the surface, hence affecting the activity of the catalyst. This can be observed for the IrO_2(110) surface where this step is extremely endergonic.

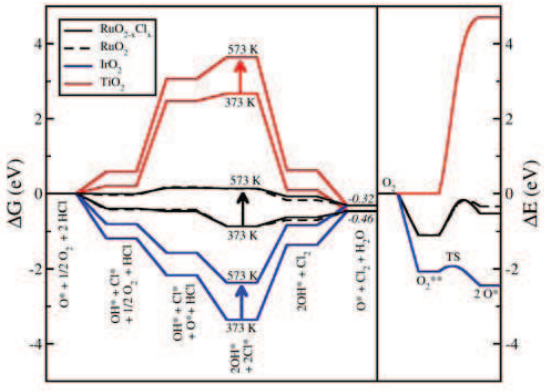

Figure 2. Left: Gibbs free energy diagram obtained from DFT calculations for the Deacon process on the $RuO_{2-x}Cl_x$,[16] RuO_2, IrO_2, and TiO_2 (110) surfaces at 373 and 573 K. Right: Potential energy diagram for the splitting of molecular O_2.

We will now show that the different reaction steps in the catalytic cycle are subject to BEP-relations[6-9] (linear energy relations between reaction energies and reaction barriers) and scaling relations[10,11,12] (linear energy relations between different adsorbates). Figure 3 shows the transition state energy for the splitting of the O-O bond on the Ru cus sites as a function of the dissociative chemisorption energy of O_2 ($\Delta E_{diss}^{O_2}$). For more negative $\Delta E_{diss}^{O_2}$, the barrier for the oxygen dissociation decreases, and at positive $\Delta E_{diss}^{O_2}$ the barrier increases until it falls on the oxygen recombination line (dashed line in Figure 3). Similar BEP relations have been observed for the splitting of diatomic molecules on transition metal surfaces.[7] The existence of such a BEP relation allows the description of the activation energy in terms of $\Delta E_{diss}^{O_2}$.

In Figure 3 the energies ΔE_i of the five elementary reaction steps

$O_2 + 2 * \rightarrow O_2{**}$ (R1)

$O_2{**} \rightarrow 2\ O*$ (R2)

$O* + * + HCl \rightarrow OH* + Cl*$ (R3)

$2\ Cl* \rightarrow Cl_2 + 2 *$ (R4)

$2\ OH* \rightarrow O* + * + H_2O$ (R5)

are plotted as a function of $\Delta E_{diss}^{O_2}$ as well. It can be seen that all reactions ΔE_i (i=1,2,3,4,5) can be described in terms of $\Delta E_{diss}^{O_2}$ within reasonable accuracy. Assuming scaling relations between

$\Delta E_{diss}^{O_2}$ and $\Delta E_{diss}^{Cl_2}$ and taking valency considerations into account, one would expect that Cl* scales with O* with a slope of approximately 0.5 (or -0.5 for chlorine recombination), similar to what has been observed for OH* vs. O* adsorption on transition metal[11] and metal-oxide surfaces.[10,12] This is indeed the case as can be seen for ΔE_4, where the recombination of chlorine is described by a slope of approximately -0.5. Adsorption of the O_2 molecule (ΔE_1) as well as its dissociation into two oxygen atoms (ΔE_2) scales with a slope of approximately 0.5 vs. $\Delta E_{diss}^{O_2}$. For significantly positive $\Delta E_{diss}^{O_2}$ the adsorption of O_2 decreases to zero, so in this regime ΔE_2 is equal to $\Delta E_{diss}^{O_2}$ (dashed line). For the reactions ΔE_3 and ΔE_5 slopes of 0.15 and -0.19 eV are obtained, respectively.

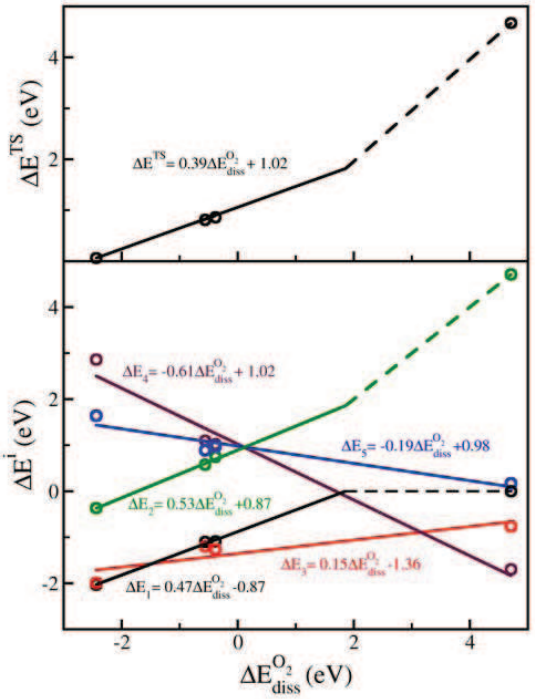

Figure 3. Top: Calculated transition state energies (ΔE^{TS}) as a function of the dissociative chemisorption energy of O_2 ($\Delta E_{diss}^{O_2}$) on different rutile (110) surfaces. Bottom: Calculated energies for the five reactions steps of the Deacon process as a function of $\Delta E_{diss}^{O_2}$. The dashed lines for the O_2-dependent reactions correspond to the regime where O_2 does not associatively adsorb. See text for the labeling of the different reaction steps.

In order to establish a relationship for the Deacon Process activity a microkinetic model was developed. This microkinetic model consists of the five elementary reaction steps (R1)-(R5) described above. The two competing rate determining steps of the overall reaction are the dissociation of molecular oxygen and the chlorine recombination. The overall reaction rate R_{tot} can be written as:

$$R_{tot} = k_2 K_1 p_{O_2} \theta_*^2 (1 - \gamma_2) \qquad 2$$

Where the rate constant, k_2:

$$k_2 = \frac{kT}{h} e^{\frac{-\Delta G^{\ddagger}}{kT}} = \frac{kT}{h} e^{\frac{-\Delta E^{\ddagger}}{kT}} e^{\frac{\Delta S^{\ddagger}}{k}} \qquad 3$$

and the equilibrium constants:

$$K_i = e^{\frac{-\Delta G_i}{kT}} = e^{\frac{-\Delta E_i}{kT}} e^{\frac{\Delta S_i}{k}} \quad (i = 1,2,3,4,5) \qquad 4$$

are determined from the BEP and scaling relations. The entropic contributions, ΔS, to the free energies are calculated in the normal mode approximation, and the pressure of oxygen, p_{O2}, is given by the reaction conditions. The coverage of free sites, θ_*, and the approach to equilibrium (which is the backward rate divided by the forward rate) for R2, γ_2, are obtained from the self-consistent steady-state solution of the microkinetic model. This enables the determination of R_{tot} as a function of $\Delta E_{diss}^{O_2}$ (see Supporting Information for details).

Figure 4 shows the turnover frequency as a function of $\Delta E_{diss}^{O_2}$ for a reaction temperature of 573 K and clearly identifies the ruthenium oxide catalysts as being the closest to the optimal, while the other investigated catalysts, IrO_2 and TiO_2, are on the left and right side of the volcano, respectively. At 573 K, the ruthenium catalyst with oxygen in the bridge position is on top of the volcano. Substitution of the bridged oxygen by chlorine moves the catalytic performance of the material slightly away from the optimum since the dissociative oxygen chemisorption energy increases on these surfaces. The chlorinated catalysts are, however, still close to the top of the volcano. According to the microkinetic model, the Deacon process is estimated to have reaction rates on the order of 10 to 100 s^{-1} at 573K.

The dependence of the Deacon process on the reaction temperature is depicted in Figure 4a. To achieve a turnover frequency (TOF) of about 1 s^{-1} a reaction temperature of at least about 423 K is necessary. The optimal catalyst that runs under these relatively mild conditions, however, would need to have a $\Delta E_{diss}^{O_2}$ that is about 0.5 eV less negative than that of the chlorinated RuO_2 surfaces. An increase in temperature increases the TOF significantly and shifts the top of the volcano to stronger oxygen binding energies, thus making the investigated ruthenium catalysts optimal at temperatures above approximately 700 K.

Figure 4b shows the TOF as a function of the reaction temperature for the RuO_2 catalyst with 50% and 100% chlorine in the bridge position. As can be seen in Figure 4b, chlorine production is found to “take off” at around 500 K (TOF(50%Cl_{br}) = 0.7 s^{-1}; TOF(100%Cl_{br}) = 0.2 s^{-1}). These theoretical TOFs are in remarkably good agreement with experimental data for chlorine production over ruthenium dioxide which show that the reaction starts to take off at approximately 500 K.[3] It can be observed that according to our model, a more optimal choice of the catalyst could theoretically increase the TOF at 500 K to about 20 s^{-1}, thus increasing catalytic activity by more than an order of magnitude. Our analysis also suggests that it would be possible to run the Deacon process with a reasonable TOF at reaction temperatures that are about 100 K lower than those used with RuO_2 catalysts, if one would be able to find an oxide material with the optimal catalytic properties. This would mark a significant improvement since the high reaction temperatures of the deacon process represent one of its major drawbacks.

The above analysis builds on the linear energy relations that again are constructed from density functional theory which has an inherent limitation in accuracy of approximately 0.1-0.2 eV. Since some of the considered energy differences are of that order, one should be cautious. The position of the volcano-curve is rather stable with respect to variations in the underlying linear energy

relations though, and we expect that this activity relation can be used to much more rapidly computationally screen for potentially useful oxide catalysts for the Deacon reaction by pointing to surfaces with the correct dissociative oxygen chemisorption energies.

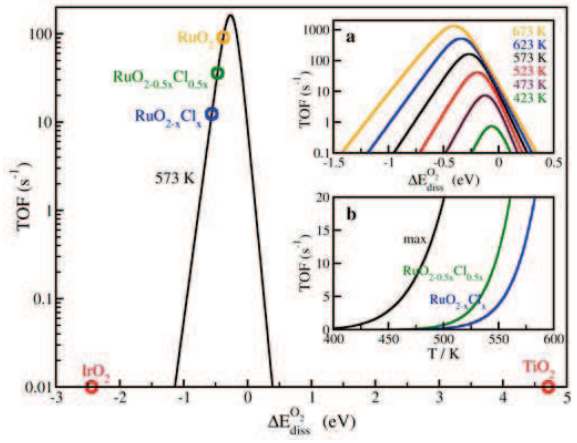

Figure 4. Volcano-curve (turnover frequency as a function of $\Delta E_{diss}^{O_2}$) for the Deacon process at 573 K. Inset: (a) Volcano plots at various temperatures; (b) Turnover frequency as a function of the reaction temperature for $RuO_{2-x}Cl_x$ and $RuO_{2-0.5x}Cl_{0.5x}$[11] The black line represents the theoretically maximal TOF of the Deacon process as given through the BEP and scaling relations and the optimal choice of $\Delta E_{diss}^{O_2}$.

Conclusion

Using the hydrochloride oxidation as an example, we showed that it is possible to apply linear energy relations over rutile metal-oxide surfaces in such a way that a rather complex reaction can be described using one single descriptor. This descriptor was successfully used to establish a reactivity volcano by introducing a detailed microkinetic model. Importantly, the theoretical model is capable to reproduce experimental observations with good accuracy. Linear energy relations combined with microkinetic modeling can thus potentially provide a powerful tool for the computational discovery of new oxide materials for catalytic processes; something that has already proven useful in transition metal heterogeneous catalysis.[17,18] Having established the volcano relationship for the Deacon process, new catalytic materials can now be screened based on the dissociative oxygen adsorption energy alone. This provides a simple and fast way of screening by means of first principles calculations, and could eventually lead to the discovery of improved catalysts. In this respect, RuO_2 is a relatively expensive material, and replacing RuO_2 with cheaper and more abundant materials is therefore highly desirable. For such an extension of this study, other factors such as for example catalyst stability would have to be taken into account.

Computational Methods

Density functional theory calculations were carried out using the dacapo code[19] which uses a plane wave implementation to describe the valence electrons and Vanderbilt ultra soft pseudo-potentials[20] to represent the ionic cores. The kinetic energy cut-off was 350 eV. All calculations were performed using the RPBE generalized gradient approximation (GGA) functional.[21] The self-consistent electron density is determined by iterative diagonalization of the Kohn-Sham Hamiltonian, with the occupation of the Kohn-Sham states being smeared according to a Fermi-Dirac distribution with a smearing factor of k_bT = 0.1 eV, and Pulay mixing of the resulting electron densities.[22] All energies have been extrapolated to k_bT = 0 eV. Slabs consisting of four layers separated by 16 Å of vacuum were periodically repeated in a 1x2 unit cell for the (110) surfaces. The two bottom layers of the slabs were fixed in their bulk structure, while the two top layers as well as possible adsorbates were relaxed until the sum of the absolute forces were smaller than 0.05 eV/Å. A Monkhorst-Pack 4x4x1 *k*-point sampling was applied in order to sample the surface Brillouin zone.[23] The transition state energies were determined by increasing the bond lengths between the two oxygen atoms in small steps (while relaxing all other degrees of freedom) until a saddle point was reached. The vibrational frequencies that were used to determine the zero point energies and the entropy contributions of the adsorbed species were calculated in the harmonic normal-mode approximation.

Acknowledgements

Funding from the Lundbeck Foundation, the Danish National Research Foundation, the Danish Research Councils (STVF), and the Danish Center for Scientific Computing is gratefully acknowledged.

Keywords: Density functional calc. • Cl • Oxides • Catalysts • Oxidation

[1] H. Deacon, US patent **1875**, 165,802.
[2] K. Iwanaga, K. Seki, T. Hibi, K. Issoh, T. Suzuta, M. Nakada, Y. Mori, T. Abe, *Sumitomo Kagaku* **2004**, *1*, 4-12.
[3] N. López, J. Gómez-Segura, R.P. Marín, J. Pérez-Ramírez, *J. Catal.* **2008**, *255*, 29-39.
[4] D. Crihan, M. Knapp, S. Zweidinger, E. Lundgren, C.J. Weststrate, J.N. Andersen, A.P. Seitsonen, H. Over, *Angew. Chem. Int. Ed.* **2008**, *47*, 2131-2134.
[5] S. Zweidinger, D. Crihan, M. Knapp, J.P. Hofmann, A.P. Seitsonen, C.J. Weststrate, E. Lundgren, J.N. Andersen, H. Over, *J. Phys. Chem. C* **2008**, *112*, 9966-9969.
[6] V. Pallassana, M. Neurock, *J. Catal.* **2000**, *191*, 301-317.
[7] J.K. Nørskov, T. Bligaard, A. Logadottir, S. Bahn, L.B. Hansen, M. Bollinger, H. Bengaard, B. Hammer, Z. Sljivancanin, M. Mavrikakis, Y. Xu, S. Dahl, C.J.H. Jacobsen, *J. Catal.* **2002**, *210*, 275-278.
[8] A. Michaelides, Z.P. Liu, C.J. Zhang, A. Alavi, D.A. King, P. Hu, *J. Am. Chem. Soc.* **2003**, *125*, 3704-3705.
[9] T. Bligaard, J.K. Nørskov, S. Dahl, J. Matthiesen, C.H. Christensen, J. Sehested, *J. Catal.* **2004**, *224*, 206-217.
[10] J. Rossmeisl, Z.-W. Qu, H. Zhu, G.-J. Kroes, J.K. Nørskov, *J. Electroanal. Chem.* **2007**, *607*, 83-89.
[11] F. Abild-Pedersen, J. Greeley, F. Studt, J. Rossmeisl, T.R. Munter, P.G. Moses, E. Skúlason, T. Bligaard, J.K. Nørskov, *Phys. Rev. Lett.* **2007**, *99*, 016105.
[12] E.M. Fernández, P.G. Moses, A. Toftelund, H.A. Hansen, J.I. Martínez, F. Abild-Pedersen, J. Kleis, B. Hinnemann, J. Rossmeisl, T. Bligaard, J. K. Nørskov, *Angew. Chem. Int. Ed.* **2008**, *47*, 4683-4686.
[13] K. Reuter, M. Scheffler, *Phys. Rev. B* **2002**, 65, 035406.
[14] S. Wendt, R. Schaub, J. Matthiesen, E.K. Vestergaard, E. Wahlström, M.D. Rasmussen, P. Thostrup, L.M. Molina, E. Lægsgaard, I. Stensgaard, B. Hammer, F. Besenbacher, *Surf. Sci.* **2005**, *598*, 226-245.
[15] S. Crétien and H. Metiu, *J. Chem. Phys.* **2008**, *128*, 044714.
[16] $RuO_{2-x}Cl_x$ ($RuO_{2-0.5x}Cl_{0.5x}$) denotes the RuO_2 (110) surface where 100% (50%) of the bridging oxygen atoms have been replaced by chlorine atoms.
[17] F. Studt, F. Abild-Pedersen, T. Bligaard, R.Z. Sørensen, C.H. Christensen, J.K. Nørskov, *Science* **2008**, *320*, 1320-1322.

[18] J.K Nørskov, T. Bligaard, J. Rossmeisl, C.H. Christensen, *Nature Chemistry* **2009**, *1*, 37-46.
[19] The DACAPO plane wave/pseudopotential code is available as open source software at http://wiki.fysik.dtu.dk/dacapo.
[20] D. Vanderbilt, *Phys. Rev. B* **1990**, *41*, 7892-7895.
[21] B. Hammer, L.B. Hansen, J.K. Nørskov, *Phys. Rev. B* **1999**, *59*, 7413-7421.
[22] G. Kresse, J. Furthmüller, *Comput. Mater. Sci.* **1996**, *6*, 15-50.
[23] H.J. Monkhorst, J.D. Pack, *Phys. Rev. B* **1976**, *13*, 5188-5192.